



The
University
Of
Sheffield.

Investigating the molecular mechanisms in Charcot Marie Tooth disease using human pluripotent stem cells

By:
Larissa Butler

A thesis submitted in partial fulfilment of the requirements for the degree of
Doctor of Philosophy

The University of Sheffield
Faculty of Science
Department of Biomedical Sciences

May 2021

Acknowledgements

The work described in this thesis was only possible with the support of the following people. I offer my deepest gratitude and sincerest thanks to the following:

My supervisor, Dr Ivana Barbaric, many thanks for your continued advice and support. For handling my excited knocks on the office door (pre-covid) with grace. And always being willing to celebrate in the lab with me when I know you were busy with approximately 1 million other things. Thank you for proofing my drafts and being a guiding voice in the story that has been written on these pages.

My Advisors, Dr Andrew Grierson and Dr Anestis Tsakiridis. Thank you for your ideas, insightful discussion and guidance during our advisory meetings. Additionally, Dr Stuart Johnson, thank you for carrying out the electrophysiology of the neurons. The LMF staff, particularly Dr Darren Robinson and Dr Nick van Hateren, for help in setting up the Airyscan so I could carry out my experiments. Thank you both for being on hand whenever the machine began to misbehave, even on a weekend. The cells, the data and my sanity thank you.

The people at CSCB, thank you for graciously handling my multiple Trev pictures and distracted conversations during the lab day. Particularly special mention goes to Dr Chris Price, without whom I can say much of this thesis would have been poorer off. Thank you for always being available in the lab and out of it for support, experimental design help and a laugh.

Thanks to my friends external to the university for your smiles and company when I needed it from either a text or that rare moment outside of the lab.

My family, thanks for putting up with my complaints, my random science facts and jokes and for continually equipping me with everything I needed to carry out this project. Thanks for being available for phone calls at the infamous and ever-changing 'Larissa O'Clock' and dog pics (the fuel of life). Trev, thank you for your constant judgment stares, the blelele of your tongue and the handsomeness of your face. Having a slither in my life for this journey and hopefully much longer is more than I could have expected it to be. Your tolerance of all astounds me. Significantly excellent long boi. Apologies for my constant presence in your life. Love you.

Finally, thanks must go to Dr Esther Allen, Andy Tattersall, the Think Ahead and the Library staff. During the pandemic, you all put on so many writing sessions which brought so many people together when it was easy to feel so alone. These have been instrumental in the writing of my thesis and have made the process much easier. You are some of the unsung heroes of lockdown.

To all mentioned above, none of this would have been possible alone. Thank you for believing in me.

Abstract

Charcot Marie Tooth Disease (CMT) 2A is a progressive peripheral motor and sensory axonal neuropathy caused by point mutations in the *MITOFUSIN 2 (MFN2)* gene. *MFN2* is a protein found on the outer membrane of mitochondria and has functionally important roles controlling mitochondrial fusion, bioenergetics and trafficking. Despite knowledge around *MFN2* function, the cellular cause for CMT2A is not completely understood. Current CMT models struggle to faithfully represent the phenotype variety seen in patients, creating a need for an improved model of disease.

This is, to the best of our knowledge, the first introduction of a CMT2A causing mutation into hPSC to generate a human-based model for the R94Q *MFN2* mutation. Edited and wild-type hPSC were subsequently differentiated in a protocol optimised for the production of the predominantly affected cell type, limb-innervating motor neurons. Comparison of wild-type and edited hPSC derived neurons showed the presence of a mitochondrial transport defect which resulted in a significantly decreased number of mitochondria found further from the cell body but not defects in the number of mitochondria overall. Additionally, no fusion defect was found in this model, in direct contrast to many previous animal studies. The mitochondrial transport defect was alleviated through the addition of ACY738, an HDAC6 inhibitor, indicating further evidence to previous work that this target may be useful in the modulation of CMT2A. This work shows the utility of hPSC in the examination of disease phenotype and can provide the basis for further studies into R94Q pathology and beyond.

List of Abbreviations

Abbreviation	Meaning
ALS	Amyotrophic lateral sclerosis
ANOVA	One-way Analysis of Variance
ATP	Adenosine Triphosphate
BMP	Bone Morphogenic Protein
CMT	Charcot Marie Tooth Disease
CRISPR	Clustered Regularly Interspaced Short Palindromic Repeats
crRNA	CRISPR RNA
DNA	Deoxyribonucleic Acid
DSB	Double Stranded Break
DSD	Dejerine-Sottas Disease
ER	Endoplasmic Reticulum
FACS	Fluorescence-activated cell sorting
GFP	Green Fluorescent Protein
GTP	Guanosine triphosphate
HDR	Homology Directed repair
hESC	human Embryonic Stem Cells
HMSN	Hereditary motor and sensory neuropathy
hPSC	human Pluripotent Stem Cells
HR	Heptad Repeat
ICM	Inner Cell Mass
iPSC	induced Pluripotent Stem Cells
LMC	Lateral Motor Column
MAM	Mitochondrially associated membrane
MEF	Mouse embryonic fibroblasts
MFN	Mitofusin
MNCV	Motor nerve conduction velocity
mtDNA	mitochondrial DNA
NHEJ	Non-homologous End Joining
NHS	National Health Service
NMP	Neuromesodermal Progenitors
PAM	Protospacer Adjacent Motif
qPCR	quantitative Polymerase Chain Reaction
RLS	Roussy-Lévy syndrome
RNA	Ribonucleic acid
sgRNA	specific guide RNA
ssODN	single-stranded Oligonucleotide
tracrRNA	trans-activating CRISPR RNA

Contents

Acknowledgements	3
Abstract	5
List of Abbreviations	6
Table of Figures	13
1) Introduction.....	16
1.1) <i>Neurodegeneration</i>	16
1.1.1) Neurodegeneration and mitochondria.....	16
1.2) <i>Charcot Marie Tooth Disease</i>	22
1.2.1) CMT2A.....	25
1.2.2) MFN2.....	26
1.2.3) Models of CMT2A	28
1.3) <i>Human Pluripotent Stem Cells</i>	31
1.3.1) Derivation of hPSC	31
1.3.2) Differentiation of hPSC	33
1.3.3) Genetic editing strategies	34
1.3.4) Genetic editing in hPSC.....	35
1.3.5) Examples of disease modelling using hPSC	36
1.4) <i>Thesis aims</i>	38
1.4.1) Identification of suitable hPSC cell line for CMT2A modelling and optimisation of hPSC differentiation to limb-innervating motor neurons.....	38
1.4.2) Generation of hPSC clones with a CMT2A patient-relevant mutation.....	39
1.4.3) Characterisation of Mitochondrial Phenotype in Wild-Type and CMT2A hPSC-derived motor neurons.....	39
2) Materials and Methods.....	40
2.1) <i>hPSC Culture</i>	40
2.1.1) Preparation of Culture Vessels	40
2.1.2) E8 Media Preparation	40
2.1.3) E8 Medium.....	41
2.1.4) Stable E8 Medium (S8).....	41
2.1.5) Passaging hPSC.....	41
2.1.6) Freezing hPSC.....	42

2.1.7)	Thawing hPSC.....	42
2.1.8)	Single Cell Dissociation of hPSC	42
2.2)	<i>Karyotyping</i>	42
2.3)	<i>Generation of clones using CRISPR</i>	43
2.3.1)	Guide Design	43
2.3.2)	Introduction of CRISPR components via electroporation.....	43
2.3.3)	Testing of guides	44
2.3.4)	DNA isolation for low cell quantities	44
2.3.5)	Enzymatic digestion-based screen for clones.....	44
2.3.6)	Sanger sequencing	45
2.3.7)	Single-cell cloning on Mouse Embryonic Fibroblasts (MEFs)	45
2.3.8)	hESC media	46
2.4)	<i>Motor Neuron Differentiation</i>	46
2.4.1)	N2B27 Media	46
2.4.2)	Initial protocol for motor neuron differentiation.....	47
2.4.3)	Previously published protocol for motor neuron differentiation	47
2.4.4)	Optimised protocol for motor neuron differentiation	48
2.5)	<i>Sensory Neuron Differentiation</i>	49
2.5.1)	Neural Crest Differentiation	49
2.5.2)	Neural Crest Medium.....	49
2.5.3)	Sensory Neuron Differentiation from Neural Crest.....	49
2.5.4)	Sensory Neuron Base medium.....	50
2.6)	<i>Mitochondrial Assessments</i>	50
2.6.1)	ATP measurements	50
2.6.2)	Mitochondrial DNA qPCR.....	50
2.6.3)	Primers.....	51
2.6.4)	MitoTracker and TMRE FACS	51
2.6.5)	3D Mitochondrial Morphology	51
2.7)	<i>qPCR gene expression analysis</i>	52
2.7.1)	RNA extraction	52
2.7.2)	cDNA production.....	52
2.7.3)	qPCR	52
2.7.4)	qPCR analysis	52

2.8) Primers	53
2.9) FACS analysis	54
2.9.1) Marker staining	54
2.9.2) Primary FACS antibodies	55
2.9.3) Secondary FACS antibodies	55
2.10) Mitochondrial Trafficking	55
2.10.1) Transfection of neurons	55
2.10.2) Tracking experiments	56
2.10.3) Analysis	56
2.11) Western Blot Analysis	56
2.11.1) Protein Lysis	56
2.11.2) Protein Electrophoresis	57
2.11.3) Protein Transfer, Staining and Visualisation	57
2.11.4) Protein Electrophoresis running buffer	57
2.11.5) Protein electrophoresis transfer buffer	57
2.12) Electrophysiology	58
2.13) Imaging and analysis	58
2.13.1) Immunocytochemistry	58
2.13.2) Image analysis	58
2.14) Antibodies	59
2.14.1) Primary Antibodies for Immunofluorescence	59
2.14.2) Primary Antibodies for Western Blot	60
2.14.3) Secondary Antibodies	60
2.15) Solutions and buffers	60
2.15.1) Phosphate-buffered saline	60
2.15.2) 4% (w/v) paraformaldehyde	60
2.15.3) Cell Lysis Solution	61
2.15.4) Laemilli Buffer	61
3) Identification of suitable hPSC cell line for CMT2A modelling and optimisation of hPSC differentiation to limb-innervating motor neurons.....	62
3.1) Introduction	62
3.2) Results	66

3.2.1)	Assessment of hPSC cell lines for the capacity to differentiate into motor and sensory neurons	66
3.2.2)	Assessment of MShel11 karyotype and MFN2 localisation	76
3.2.3)	Assessment of BMP4 and Notch inhibition on motor neuron differentiation efficacy 77	
3.2.4)	Assessment of 3D motor neuron differentiation protocol.....	85
3.2.5)	Alteration of key signalling pathways to increase induction of key motor neuron markers	88
3.2.6)	Characterisation of motor neurons from optimised differentiation protocol ..	98
3.3)	<i>Discussion</i>	100
4)	Generation of hPSC clones with a CMT2A patient-relevant mutation...	104
4.1)	<i>Introduction</i>	104
4.2)	<i>Results</i>	107
4.2.1)	Identification of patient-relevant mutations to model and in silico design of appropriate guide RNAs and repair templates.....	107
4.2.2)	Assessment of sgRNA efficacy	113
4.2.3)	Generation and identification of CRISPR edited hPSC.....	115
4.2.4)	Assessment of Cas9 off-target activity in genetically edited hPSC.....	120
4.2.5)	Assessment of hPSC markers, MFN2 expression and karyotypic identity in genetically edited hPSC	122
4.3)	<i>Discussion</i>	122
5)	Characterisation of Mitochondrial Phenotype in Wild-Type and CMT2A hPSC-derived motor neurons	126
5.1)	<i>Introduction</i>	126
5.2)	<i>Results</i>	132
5.2.1)	R94Q hPSC mitochondrial energetics and morphology	132
5.2.2)	Comparison of MFN2 ^{R94Q/+} cells differentiation ability	137
5.2.3)	Assessment of Mitochondrial Morphology in MFN2 ^{R94Q/+} motor neurons.....	149
5.2.4)	MFN2 ^{R94Q/+} motor neurons have a mitochondrial trafficking defect	154
5.2.5)	Effect of HDAC6 inhibitor on mitochondrial trafficking and morphology	157
5.2.6)	Effect of increasing MFN1 expression on Mitochondrial Trafficking	167
5.3)	<i>Discussion</i>	168
6)	Final discussion and future work.....	174

6.1) <i>A novel model of CMT2A</i>	174
6.2) <i>Mechanistic insights from hPSC based MFN2^{R94Q/+} CMT2A system</i>	174
6.3) <i>Potential for treatments of CMT2A</i>	178
6.4) <i>Closing remarks</i>	180
7) References	181
8) Appendix 1	204

Table of Figures

Number	Figure Title	Page Number
1	Mitochondria and mitochondrial fusion	18
2	Effect of CMT caused axonal degeneration on mean nerve conduction velocity	23
3	MFN2	28
4	Generation of hPSC	32
5	Double-stranded break repair	34
6	The four main Motor Neuron columns <i>in vivo</i> and corresponding axial identity	65
7	Assessment of hPSC lines differentiation to neural crest and sensory neurons	69-71
8	Assessment of hPSC lines differentiation to motor neurons	73- 74
9	Assessment of MFN2 size and localisation in MShef11	76
10	Experimental plan for assessing increased BMP4 and notch inhibition on motor neuron differentiation efficacy	78
11	Assessment of the production of NMP-like cells differentiation	79
12	Assessment of increased BMP4 and notch inhibition on the production of day 14 motor neuron progenitors	80
13	Assessment of increased BMP4 and notch inhibition on the production of day 24 immature motor neuron	82
14	Assessment of increased BMP4 and notch inhibition on the production of day 36 motor neurons	83-84
15	Assessment of 3D motor neuron differentiation protocol	88
16	Assessment of HB9 expression during motor neuron differentiation	90
17	Optimisation of motor neuron differentiation conditions to increase expression of HB9 and HOXC8	91-92
18	Addition of FGF to motor neuron protocol to increase the posterior identity of motor neurons	92-93
19	Assessment of length of FGF signal to induce expression of motor neuron markers	95
20	Initial assessment of optimised motor neuron protocol	97

21	Assessment of biological repeatability in optimised motor neuron protocol	99
22	Surveyor nuclease assay to allow detection of editing and most effective guide sequence.	106
23	Design of sgRNA and repair template for the generation of <i>MFN2</i> R94Q mutation	109
24	Design of sgRNA and repair template for the generation of <i>MFN2</i> T105M mutation	110
25	Design of sgRNA and repair template for the generation of <i>MFN2</i> R364W mutation	111
26	Design of primers to amplify the region of <i>MFN2</i> that would contain the R94Q mutation	112
27	Assessment of R94Q guide efficacy by surveyor nuclease assay	113
28	Assessment of T105M guide efficacy by surveyor nuclease assay	114
29	Generation and screening of MShef11 clones containing CMT2A mutations in <i>MFN2</i>	116-117
30	Confirmation of heterozygous mutation in MShef11 <i>MFN2</i> ^{R94Q/+}	117
31	Identification and screening of potential off-target mutations	119-120
32	Assessment of hPSC markers in genetically edited hPSC	120-121
33	Principles of kymograph generation	129
34	Assessment of mitochondrial content, membrane potential, mtDNA and ATP production in hPSC with <i>MFN2</i> ^{+/+} or <i>MFN2</i> ^{R94Q/+}	133-134
35	Assessment of mitochondrial morphology in hPSC containing <i>MFN2</i> ^{+/+} or <i>MFN2</i> ^{R94Q/+}	136
36	Assessment of <i>MFN2</i> ^{+/+} or <i>MFN2</i> ^{R94Q/+} lines differentiation to neural crest and sensory neurons via qPCR	138
37	Assessment of <i>MFN2</i> ^{+/+} or <i>MFN2</i> ^{R94Q/+} lines differentiation to neural crest and sensory neurons via immunofluorescence	136-137
38	Assessment of Ctrl1 <i>MFN2</i> ^{+/+} and Het2 <i>MFN2</i> ^{R94Q/+} differentiation to neural crest	142-143
39	Assessment of <i>MFN2</i> ^{+/+} or <i>MFN2</i> ^{R94Q/+} lines differentiation to motor neurons via qPCR	144-145
40	Assessment of <i>MFN2</i> ^{+/+} or <i>MFN2</i> ^{R94Q/+} lines differentiation to motor neurons via immunofluorescence	146

41	Assessment of mitochondrial morphology for day 16 motor neurons containing MFN2 ^{+/+} or MFN2 ^{R94Q/+}	148
42	Assessment of mitochondrial spacing and morphology in day 33 neurons containing MFN2 ^{+/+} or MFN2 ^{R94Q/+}	151-153
43	Assessment of mitochondrial transport in day 33 neurons containing MFN2 ^{+/+} or MFN2 ^{R94Q/+}	155-156
44	Investigation in hPSC and motor neurons to determine the appropriate dose of HDAC6 inhibitors to achieve an increase in acetylated tubulin	159
45	Assessment of mitochondrial transport in day 33 neurons containing MFN2 ^{+/+} or MFN2 ^{R94Q/+} in the presence of 100nM HDAC inhibitor ACY738.	160-161
46	Assessment of mitochondrial spacing and morphology in day 33 neurons containing MFN2 ^{+/+} or MFN2 ^{R94Q/+} in the presence of 100nM HDAC inhibitor ACY738	163-165
47	Investigation in motor neurons to determine the appropriate schedule of Leflunomide to increase expression of <i>MFN1</i>	167
48	Proposed model for MFN2 ^{R94Q/+} impact on mitochondrial axonal transport	170
49	Identifying mitochondria within motor neuron axons using automated image analysis	179

1) Introduction

1.1) Neurodegeneration

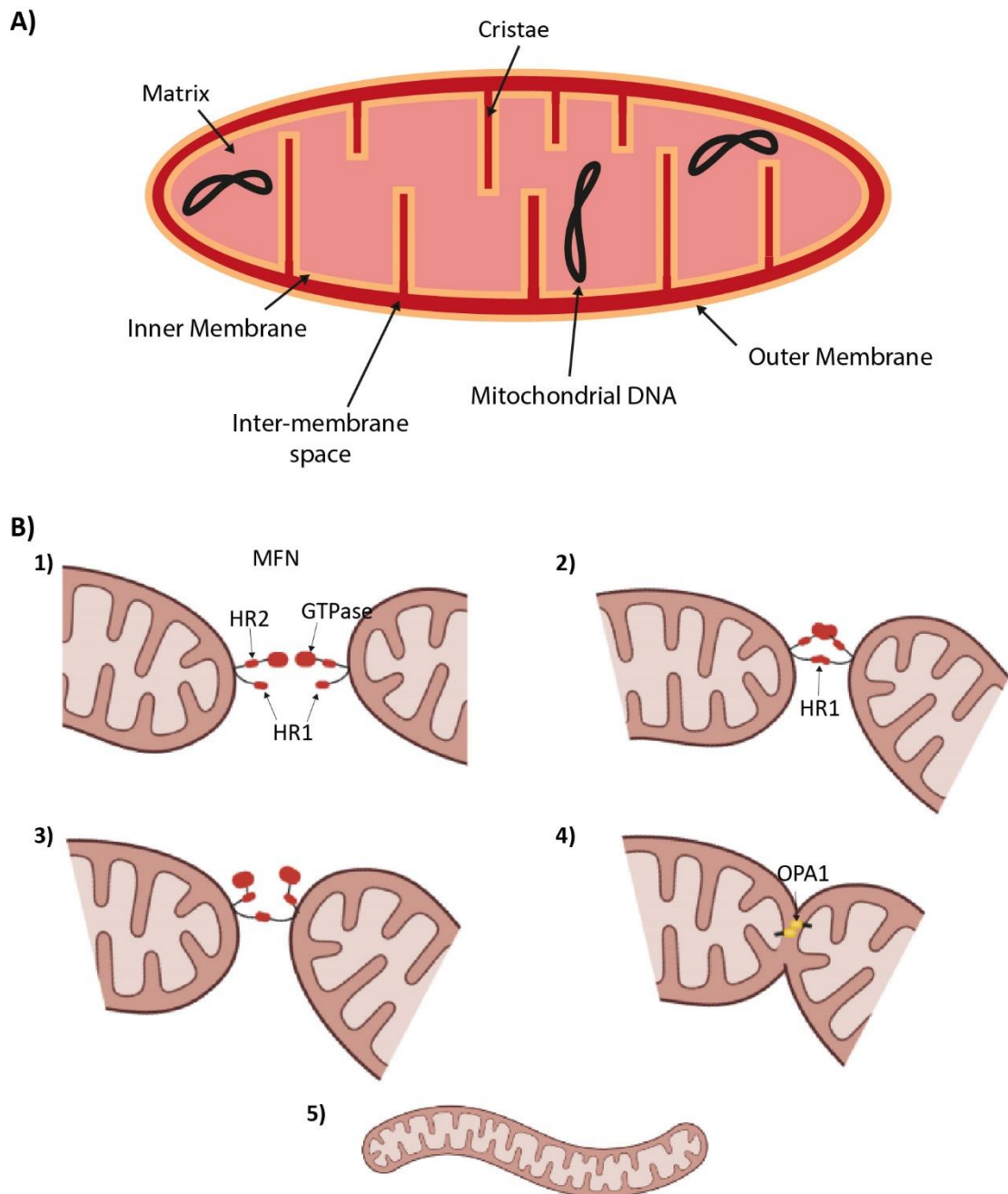
Neurodegeneration is defined as the progressive loss of neuron structure or function and is the hallmark of many diseases known today, such as Parkinson's, Huntington's, Alzheimer's, Amyotrophic lateral sclerosis (ALS) and Charcot Marie Tooth disease (CMT). Without a doubt, neurodegeneration is one of the greatest biological challenges of the current age. Millions of pounds are spent on research to increase understanding and develop potential treatments and therapies which may alleviate symptoms and improve quality of life. Such research has revealed important differences but also similarities found within this umbrella of diseases. Many neurodegenerative diseases have an accumulation of neurotoxic proteins (reviewed in Hetz and Saxena, 2017), dysregulation in calcium signalling (reviewed Müller *et al.*, 2018), increased oxidative stress burden (reviewed in Angelova, Esteras and Abramov, 2021) and bioenergetic disruption (reviewed in Aufschneider *et al.*, 2017). Whilst not every neurodegenerative symptom can be attributed to one cause, many can be aligned with the function of the mitochondria. Furthermore, the accumulation of neurotoxic proteins has been attributed to causing mitochondrial dysregulation, which is now considered a key aspect of many neurodegenerative disease pathologies (reviewed in the following: Baloh, 2008; Aufschneider *et al.*, 2017; Xu, Wang and Tong, 2020). Neurodegenerative diseases are associated with increased mitochondrial fission, altered mitochondrial contact with the endoplasmic reticulum (ER), increased oxidative stress, aberrant mitochondrial transporting, altered mitophagy or increased apoptosis (reviewed in the following: Brini *et al.*, 2014; Aufschneider *et al.*, 2017; Audano, Schneider and Mitro, 2018; Müller *et al.*, 2018; Rieusset, 2018; Xu, Wang and Tong, 2020; Angelova, Esteras and Abramov, 2021). This all makes mitochondria an important target to study in neurodegeneration and a potential avenue for therapeutic opportunities.

1.1.1) Neurodegeneration and mitochondria

Mitochondria are complex organelles that carry out multiple cellular functions essential for life. They have an inner and outer membrane and contain their own DNA (mitochondrial DNA - mtDNA) (Figure 1a). Their inheritance is a little unusual compared with other organelles as mitochondria are not synthesised *de novo*. Instead, they are carefully divided up in cell division to ensure that both daughter cells receive mitochondria via cytoskeletal machinery (reviewed in Mishra and Chan, 2014). The inner membrane of mitochondria is a highly intricate structure composed of cristae which contain the machinery necessary to carry out ATP production via oxidative phosphorylation. The proteins that compose the respiration complexes for oxidative phosphorylation are encoded by mtDNA (reviewed in Taylor and Turnbull, 2005). Mitochondria have transcription and translational machinery meaning

they are capable of localised protein synthesis (reviewed in Greber and Ban, 2016), however, the proteins required for this process are encoded by the nuclear genome and exert regulative effects on mtDNA expression (Ali *et al.*, 2019). This highlights the tight linkage between mitochondria and the rest of the cell. Mitochondria are carefully controlled and regulated to ensure that the cell has everything required for continued existence.

Mitochondria are highly dynamic organelles undergoing fusion and fission to form large networks, the state of which has a significant effect on its functions. The fusion of mitochondria is carried out in two stages. First, mitochondria are tethered together by the mitofusin (MFN) proteins 1 and 2 and GTP hydrolysis can then provide the power-stroke to bring the membranes together (Figure 1b) (Qi *et al.*, 2016; Cao *et al.*, 2017). Following this, OPA1 then carries out the fusion of the inner membrane. It has become apparent that contact with the endoplasmic reticulum (ER) and even lysosomes are capable of marking sites for mitochondrial fission (Friedman *et al.*, 2011; Wong, Ysselstein and Krainc, 2018). Once marked, Dynamin-related protein 1 (Drp1) is recruited and mediates the fission of the inner and outer membrane of the mitochondria (reviewed in Tilokani *et al.*, 2018). Mitochondrial fusion and fission are essential processes for mitochondrial health, allowing for electrochemical coupling and exchange of membranes, proteins and metabolites. Mitochondria alter their shape and distribution dependent on the requirements of the cell, allowing aerobic respiration, calcium homeostasis and production of cellular metabolites to be controlled. Under starvation conditions, mitochondria elongate to produce more energy, whereas fragmented mitochondria produce less. Significant remodelling of the internal cristae also occurs (reviewed Gomes, Benedetto and Scorrano, 2011). This change in shape is also noticeable in human pluripotent stem cells (hPSC) where mitochondria are very fragmented and cells rely predominantly on glycolysis (Varum *et al.*, 2011). Over the course of differentiation, mitochondria become more elongated allowing cells to swap over to oxidative phosphorylation due to their higher energy demands. Excessive fragmentation is a key feature of multiple neurodegenerative diseases including Parkinson's (Martinez *et al.*, 2018) and Alzheimer's (Calkins *et al.*, 2011) which has been seen in animal models and patient brains. In Alzheimer's disease, excessive mitochondrial fragmentation is thought to be driven by upregulation of Drp1 and downregulation of MFN1/2 (reviewed in Aufschnaiter *et al.*, 2017), whereas in Parkinson's excessive fragmentation is Drp1-independent (Martinez *et al.*, 2018). Mitochondrial fragmentation significantly impacts the ability of the mitochondria to meet the bioenergetic requirements of the cell and this is often one of the first indications of neurodegeneration.



Created in BioRender.com bio

Figure 1: Mitochondria and mitochondrial fusion. **A)** A single plane of mitochondria represented showing the outer and inner membrane. Circular mitochondrial DNA is found in the matrix. Cristae are formed from folded inner membrane forming the sites for the electron transport chain and oxidative transport chain. **B)** The fusion of mitochondria is mediated by multiple steps. 1) Outer mitochondrial membrane showing mitofusin proteins. 2) Mitochondrial tethering is achieved by the HR1 domain of mitofusins. 3) GTP hydrolysis causes a conformational change that results in the power stroke required for outer mitochondrial membrane fusion. 4) OPA1 mediates the fusion of the inner mitochondrial membrane. 5) Elongated mitochondria as a result of fusion.

Mitochondria are best known for being the powerhouse of the cell, that is the production of ATP - the energy currency used by most cellular processes. Products from glycolysis are shuttled into the mitochondria and the enzymes found in the mitochondrial matrix carry out the series of reactions known as the Krebs cycle. The Krebs cycle is important for the synthesis of other metabolites that control chromatin modification, DNA methylation, nucleotides, lipids and other proteins (reviewed in Martínez-Reyes and Chandel, 2020). Another key part of the Krebs cycle is the regeneration of coenzymes involved in the electron transport chain. Respiration complexes I-V are encoded within mtDNA and are responsible for carrying out the electron transport chain (with the help of electron carriers such as cytochrome c) on the inner membrane of the mitochondria. The flow of electrons is coupled to the creation of a proton gradient responsible for powering ATP synthase and the generation of ATP (reviewed in Zhao *et al.*, 2019). This process is called oxidative phosphorylation. Carrying out the essential process of oxidative phosphorylation is not without inherent risk. Electron transport chain leakage makes the mitochondria the highest producer of reactive oxygen species (ROS) in the cell (but is not the sole generator). ROS has roles in signalling pathways but overproduction can damage DNA, including mtDNA, oxidise proteins and lipids (reviewed in Zhao *et al.*, 2019). To deal with this, mitochondria are capable of generating mitochondrial-derived vesicles which can package these damaged components and target them to lysosomes (reviewed in Audano, Schneider and Mitro, 2018). In many cases, mitochondria will use fusion and fission to ensure that quality control is maintained. It was shown that function could be restored through the fusion of mitochondria containing two differentially truncated mtDNA (Gilkerson *et al.*, 2008). Mitochondrial fusion is also thought to protect mtDNA levels and fidelity (Chen *et al.*, 2010). If mitochondria are too damaged they can undergo asymmetric fission to eliminate the damaged mitochondrion by mitophagy (Twig *et al.*, 2008). Whilst there are several methods of mitophagy, the best characterised is the PINK1/PARKIN pathway. Normally healthy mitochondria have high membrane potential, these mitochondria import and degrade PINK1. When mitochondria are damaged, they become depolarised, PINK1 import is blocked and therefore it accumulates on the outer membrane. This results in the recruitment of PARKIN, an E3 ubiquitin ligase (reviewed in the following: Jin and Youle, 2012; Whitworth and Pallanck, 2017). Known targets of this protein are MFN1 and MFN2, presumably to prevent mitochondrial fusion and segregate damaged mitochondria. Other mitochondrially localised proteins are also ubiquitinated and ultimately this allows the mitochondria to be targeted to autophagosomes (Gegg *et al.*, 2010). The dysregulation of mitophagy is known to be a key aspect of neurodegenerative diseases such as Parkinson's, indicating the importance of controlling not only energy production but the disposal of damaged mitochondrial components at the right time.

Mitochondria are early targets in apoptotic pathways and often are the point of no return in these cascades. The key role played by mitochondria is mediated through the BCL-2 family of proteins and their functions in mitochondrial outer membrane permeabilization. The most well-known apoptotic proteins are BCL-2 associated X (BAX) and BCL-2 agonist/kill (BAK) (reviewed in Wang and Youle, 2009). Under healthy conditions, BAX is located in the cytosol as a monomer and BAK is found on the outer mitochondrial membrane. During apoptosis, BAX is translocated into the mitochondria and forms oligomers, whilst BAK undergoes conformational changes. The exact mechanism of action is unclear, however, mitochondrial outer membrane permeabilization occurs and cytochrome c is released which is required for caspase activation and ultimately cellular breakdown (reviewed in Wang and Youle, 2009). Apoptosis can occur for any number of reasons, such as DNA damage or ER stress. Mutated forms of Huntington's proteins are known to increase mitochondrial permeability and result in cytochrome c release (Choo *et al.*, 2004). Toxic proteins in Alzheimer's can be targeted to the mitochondria which will result in oxidative stress and which results in cellular death (reviewed in Aufschnaiter *et al.*, 2017). This indicates the mitochondria's sensitivity to detrimental conditions to the cell as well as the connection with other organelles.

The relationship between the ER and mitochondria is extensive and primarily takes place through specialised contact points known as mitochondrially-associated membranes (MAMs) (reviewed in Aufschnaiter *et al.*, 2017). These locations have a highly enriched lipid nature and many proteins are known to be primarily MAM resident. MAM proteins often have roles in the regulation of the contact points as well as responding to the signals from each organelle. The ER is the primary storage of calcium in the cell, through modulation of the strength of MAM contact with ER, the amount calcium transferred to the mitochondria can be altered (reviewed in Müller *et al.*, 2018). Calcium plays an important role in the mitochondria by regulating bioenergetics but must be tightly regulated. If calcium levels increase too much this can result in cell death via the formation of mitochondrial permeability transition pores which can ultimately lead to the release of cytochrome c. In all cells, mitochondria can act as a calcium buffer, preventing extraneous calcium gradients. This is a particularly important role in neurons as calcium is used as a universal second messenger (reviewed in Berridge, 1998). Indeed, motor neurons are considered especially prone to calcium dysregulation as they have lower expression of calcium-binding proteins, parvalbumin and calbindin (reviewed in Ragagnin *et al.*, 2019). Taken together this highlights the reliance of motor neurons on mitochondrial calcium buffering. Disruption of calcium signalling via MAMs is prevalent in many different neurodegenerative diseases. Alzheimer's is associated with increased ER-mitochondria contact resulting in increased calcium entering mitochondria and this is believed to be associated with

neuronal death (reviewed in Müller *et al.*, 2018). Furthermore, calcium dysregulation is a known factor of several ALS forms and Parkinson's due to reduced contact between ER and the mitochondria (Müller *et al.*, 2018; Xu, Wang and Tong, 2020). These findings highlight how important it is for neurons to regulate calcium gradients and how mitochondria play a key role in the maintenance of homeostasis.

In large or polarised cells, such as neurons, mitochondria move to be available to meet localised metabolic and energetic requirements. Mitochondrial distribution in these cells is an active process requiring the use of motor proteins along microtubules which are bound to the outer membrane of mitochondria via adaptor proteins (reviewed in Mandal and Drerup, 2019). Synapses are the site of intense energy demand meaning mitochondria cluster at these locations (reviewed in Mandal and Drerup, 2019). Mitochondria must therefore be trafficked away from the cell body (anterograde transport) and return to the cell body (retrograde transport) by the action of motor proteins such as KINESIN (anterograde transporter) and DYNEIN (retrograde transporter) to fuse and divide with other mitochondria in response to the demands of the cell. It was shown by Misko and colleagues (2010) that MFN2 associates with the Mitochondrial RHO GTPase, RHOT1, (also known as MIRO hereafter referred to as MIRO) and trafficking kinesin protein 1, TRAK1, (also known as MILTON, hereafter referred to as MILTON) complex to facilitate mitochondrial transport (Misko *et al.*, 2010). The MIRO/MILTON complex is known to interact with KINESIN (Misko *et al.*, 2010) and DYNEIN (Pilling *et al.*, 2006; reviewed in Schwarz, 2013), meaning this adaptor complex is important for both directions of travel. Axonal transport of mitochondria is known to be affected in several neurodegenerative diseases, including ALS (Guo *et al.*, 2017; Moller *et al.*, 2017), Alzheimer's (Calkins *et al.*, 2011), Huntington's (Dompierre *et al.*, 2007) and CMT (Benoy *et al.*, 2018; Mo *et al.*, 2018). The number of diseases with mitochondrial trafficking defects indicates the importance of this phenotype in causing degeneration in neurons making it a compelling target for study.

In summary, the mitochondria are a dynamic and highly complex organelle capable of a multitude of functions, not limited to the production of ATP. Its actions are tightly controlled by cellular processes making mitochondria capable of altering molecular priorities as required. This wide range of functions and highly interconnected nature makes mitochondria vulnerable to dysfunction, a particular challenge in neurodegenerative diseases.

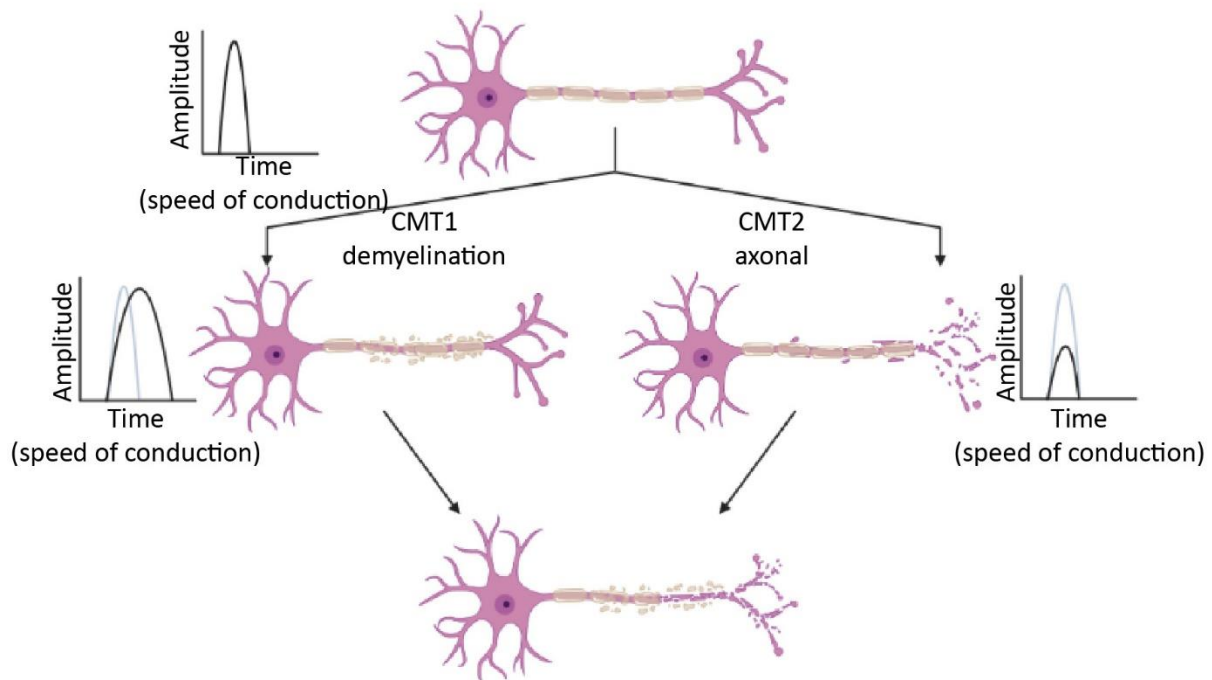
1.2) Charcot Marie Tooth Disease

Charcot Marie Tooth disease (CMT) is one of the most prevalent progressive peripheral motor and sensory neuropathies. The disease is widely considered to affect 1 in 2500 people worldwide, but this can vary greatly depending on the country (Loiseau et al., 2007; Braathen, 2012; Milley et al., 2017). The disease is named after the three scientists who are primarily credited for the initial description of the disease. In 1886, Jean-Martin Charcot and Pierre Marie described a disease with progressive muscular atrophy (Charcot and Marie, 1886). Independently, at the same time, Howard Henry Tooth presented his thesis on several patients also with progressive muscular atrophy. He was also the first to hypothesise this disease was a peripheral nerve disorder (Tooth, 1886). This disease was characterised by muscular atrophy with a severe foot deformity and, in some cases, sensory loss. Now, CMT symptoms listed include muscle weakness and atrophy in longer limbs (particularly legs), foot deformity known as pes cavus, hammertoes and high-arched feet. Similar symptoms can develop in the hands (Szigeti and Lupski, 2009). Sensory symptoms are less common but include sensory loss, numbness and pain in the limbs (Saporta et al., 2011).

After the initial discovery, there was much confusion over the classification of CMT. In 1893, Dejerine and Sottas reported a similar but extremely severe early-onset disease with ataxia, sensory deficit and nerve hypertrophy, later known as Dejerine-Sottas Disease (DSD) (Plante-Bordeneuve and Said, 2002). Similarly, Roussy and Lévy also noted an early childhood disease with extreme symptoms such as foot deformity, muscle wastage and weakness, ataxia and sensory loss. This became known as Roussy-Lévy syndrome (RLS) (Auer-Grumbach et al., 1998). These diseases were considered separate from CMT despite the clear overlap in symptoms. To try and clear up the confusion of this now wide range of diseases, a classification system of hereditary motor and sensory neuropathy (HMSN) were created, with CMT, DSD and RLS appearing in the categories. This system attempts to make sense of these diseases in grouping by clinical presentations.

With the advent of technological advances increasing the ease of sequencing it became apparent that many different HMSN categories had a similar genetic basis. For example, multiple cases of CMT, DSD and RLS had a common cause in duplication of the gene *PMP22* located on chromosome 17p11.2 (Auer-Grumbach *et al.*, 1998; Plante-Bordeneuve and Said, 2002). This gene is now most commonly associated with a form of CMT. Ultimately, DSD, RSL and HSMN are now considered forms of CMT but their exact classification may vary due to an underlying genetic cause. The HSMN classification can still be used to describe clinical presentation in addition to a CMT diagnosis describing the genetic cause

of the disease (Del Bo *et al.*, 2008). Novel classification systems have been proposed but not widely adopted (Magy *et al.*, 2018).



Created in BioRender.com

Figure 2: Effect of CMT caused axonal degeneration on mean nerve conduction velocity. Top) A healthy myelinated motor neuron with corresponding mean nerve conduction velocity. This is shown in all other plots as a light grey for comparison. Left arrow) CMT1 causes demyelination which causes the speed of the conduction time to increase but has not affected the amplitude. Right arrow) CMT2 causes axonal degeneration but the myelin sheath is left intact. This results in a decreased amplitude of conduction with no effect on speed. Bottom) Ultimately both versions of CMT result in axonal degeneration which may be accompanied by demyelination.

CMT now has two main classifications: CMT1 and CMT2. CMT1 is a demyelinating disease resulting in a severe reduction of motor nerve conduction velocity (MNCV). MNCV is measured through the attachment of electrodes to the skin and calculating the time taken for the electronic stimulus to pass through the nerve to the detector (Chouhan, 2016). CMT type 2 is an axonal disease. The MNCV in CMT2 type 2 is normal or slightly reduced but usually has decreased compound motor action potential amplitude (Figure 2). In other words, the speed of the signal is normal but the size of the signal is decreased (Bergamin *et al.*, 2014). At the time of writing, it is known that CMT can be caused by over 1000 different mutations in 80 disease-associated genes (Timmerman, Strickland and Züchner, 2014),

resulting in different onset, progression and severity of the disease. Due to the wide variety of mutations and implicated genes, CMT has every known inheritance mode, autosomal dominant, autosomal recessive and X-linked dominant or recessive. The most common type of CMT is CMT1, comprising around 60% of all CMT cases (Verhoeven *et al.*, 2006). In 60-80% of CMT1 cases of patients, the disease is caused by *PMP22* duplication, and this subtype is known as CMT1A. CMT2 represents only around 18% of CMT cases and is further subdivided into subtypes depending on the underlying genetic cause. CMT2A is the most common subtype of CMT2 comprising ~33% (Verhoeven *et al.*, 2006) of CMT2 cases and is primarily due to mutations in *MITOFUSIN 2 (MFN2)* (Züchner *et al.*, 2004).

CMT is diagnosed through nerve conduction tests and genetic screening at loci of interest depending on family history, though genetic testing is not always necessary or desired (Patzkó and Shy, 2011). Upon diagnosis with CMT, patients are left with relatively few options. There is no treatment approved for use by the NHS. Due to muscle wastage, and associated difficulties, physiotherapy is recommended, along with occupational therapy to allow the continuation of normal daily activities. Depending on the severity, walking aids or even a wheelchair may be necessary. The only pharmacological intervention usually takes the form of pain relief. Surgical intervention is only recommended in the most severe cases where neuropathy has resulted in deformity (NHS England, 2016).

Therapeutic efforts predominantly focus on CMT1A, the most common form of the disease. Most recently PXT3003 (a combination of three drugs currently approved for other indications – baclofen (a chemical derivative of GABA, used in movement disorders), naltrexone (opioid receptor antagonist – used to treat opiate and alcohol addiction) and sorbitol (non-stimulant laxative)) has shown promise in treating CMT1A (Attarian *et al.*, 2014) and has shown positive results in Phase 3 trial (PHARNEXT, 2018). Another potential treatment is ACE-083, a recombinant fusion protein containing a modified form of follistatin and immunoglobulin G2 Fc domain. This acts as a trap for ligands which inhibit skeletal muscle growth and differentiation result in a local increase in muscle volume and force (Glasser *et al.*, 2018). Clinical trials are currently underway for CMT1 and CMTX. However, this is a potential treatment that may have results in multiple forms of CMT which are affected by muscle wastage. However, this drug only alleviates patient symptoms but does not target the molecular pathway involved in disease. Ultimately, despite increased understanding in genetic cause and disease pathology, patients have limited treatment and therapeutic options.

1.2.1) CMT2A

Genetic advancements have increased the understanding of the genetic cause behind the most common form of axonal CMT, CMT2A. Originally, CMT2A was thought to be due to mutations in *KIF1B* (found at 1p36.22) found in a family in Japan and matched to a mouse model of the disease (Zhao *et al.*, 2001). Despite this, there have been no reported additional mutations of this gene and mutation studies in other patients did not confirm *KIF1B* as the cause. Further study showed that *MITOFUSIN 2* (*MFN2*) (also found at 1p36.22), was the main candidate for CMT2A in the majority of patients and produced some of the most severe symptoms, such as optic atrophy leading to the more severe classifications of HSMN (Züchner *et al.*, 2004). Now, CMT2A1 is associated with *KIF1B* mutations and CMT2A2 with *MFN2* mutations. For ease, in this thesis, CMT2A will from herein refer only to *MFN2* mutations. *MFN2* is found in the mitochondria outer membrane and has a large host of implicated functions (see section 1.2.2).

Examination of literature has revealed at least 140 mutations found in various regions of *MFN2* which are known to cause CMT2A (Appendix 1) ranging in age of onset, disease severity and inheritance. Predominantly, the mutations are autosomal dominant, though there are cases of recessive inheritance (Hikiami *et al.*, 2018; lapadre *et al.*, 2018). Additionally, the mutations tend to be point mutations though there are also recorded examples of both inserts (Engelfried *et al.*, 2006), deletions (Verhoeven *et al.*, 2006; Feely *et al.*, 2011; McCorquodale *et al.*, 2011; Bergamin *et al.*, 2014; Antoniadis *et al.*, 2015; Choi *et al.*, 2015) and compound mutations (Nicholson *et al.*, 2008; Calvo *et al.*, 2009; Polke *et al.*, 2011; Bergamin *et al.*, 2014; Kotruchow, Kabzińska and Kochański, 2015). Furthermore, the majority of the mutations cluster in the GTPase domain (Kijima *et al.*, 2005; Brockmann *et al.*, 2008; Chung *et al.*, 2008, 2010; Sitarz *et al.*, 2012) of the protein but are by no means limited to this location (Verhoeven *et al.*, 2006; Ando *et al.*, 2017; Dankwa *et al.*, 2018). This vast range of mutations with varying phenotypes presents a significant challenge to researchers to overcome in understanding this condition.

Axonal degeneration is a hallmark of CMT2A, with biopsied nerves often showing swollen or damaged mitochondria with abnormal clustering (Verhoeven *et al.*, 2006; Calvo *et al.*, 2009). Degeneration of neurons is noted first in the limbs, which is thought to underlie the muscle weakness and wastage in these appendages. In more severe cases of the disease, axonal degeneration can also be accompanied by demyelination of the nerves, including onion bulbs (a histopathological finding indicating repeated cycles of demyelination and remyelination) which are more commonly seen in CMT1 (Vallat *et al.*, 2008; Genari *et al.*, 2011; Hikiami *et al.*, 2018). This underscores the strong variety seen in CMT2A,

which is more often considered to be split into two main categories: early-onset severe disease and late-onset mild disease (Verhoeven *et al.*, 2006; Choi *et al.*, 2015). Typically, the late-onset disease appears at around 40 years of age, but can appear as late as ~60 years of age. It is generally considered a milder form that progresses more slowly. Patients may have difficulty walking but generally do not require assistance (Braathen *et al.*, 2010). The early-onset severe disease tends to appear within the first decade of life and often progresses to include additional symptoms such as optic atrophy (Züchner *et al.*, 2006; Banchs *et al.*, 2008; Brockmann *et al.*, 2008), inability to walk (typically by age 20) (Verhoeven *et al.*, 2006) and brain abnormalities (Brockmann *et al.*, 2008; Chung *et al.*, 2010). This is more commonly associated with specific mutations such as R94Q, which is one of the most common mutations associated with some of the severest additional symptoms (Züchner *et al.*, 2006; Neusch *et al.*, 2007). Despite this attractive grouping of patients into two disparate groups, there is significant cross-over and overlap between symptoms variety, severity and onset, including within individual families which underlies the heterogeneity of this disease (Lawson, Graham and Flanigan, 2005; Kotruchow, Kabzińska and Kochański, 2015).

1.2.2) MFN2

Found on the outer mitochondrial membrane, MFN2 is a nuclear-encoded mitochondrial GTPase. It is essential to embryonic development in mammals due to its involvement in placental development (Chen *et al.*, 2003). The protein contains a GTPase domain, proline-rich domain, a transmembrane domain and two coiled-coil heptad repeats (HR) (Figure 3). There is no current crystal structure for this protein but several now exist for MFN1 (Qi *et al.*, 2016; Cao *et al.*, 2017), with which MFN2 shares 80% similarity. The proline-rich domain is not present in the MFN1 structure and likely plays a role in MFN2 protein-protein interactions. MFN2 can work with MFN1 or alone to cause fusion of the outer mitochondrial membrane. The two proteins have different GTPase activity, with MFN2 being around eight times less active and therefore having a lesser role in the tethering and mitochondrial fusion (Ishihara, Eura and Mihara, 2004). MFN2^{-/-} or MFN1^{-/-} cells show mitochondrial clear fusion defects with highly fragmented mitochondria and some rescue is possible via the overexpression of the other MFN (Chen *et al.*, 2003) suggesting some compensatory mechanisms exist.

MFN2 has diverse roles in apoptosis, mitochondrial trafficking and the regulation of MAMs. It has been shown that BAX can promote mitochondrial fusion between MFN2 mediated homotypic complexes when in the cytosol (Hoppins *et al.*, 2011). It has also been shown by Brooks and colleagues that BAK is capable of interacting with both MFN1 and MFN2, but once apoptosis begins mitochondrial fragmentation occurs. During fragmentation, BAK dissociates from MFN2 and seems to only interact

with MFN1. Mutations of BAK to prevent its association with MFN2 diminished the mitochondrial fragmentation activity (Brooks *et al.*, 2007). MFN2 has been also suggested to have an anti-apoptotic role which may work through ERK signalling (Peng *et al.*, 2015). As mentioned, MFN2 is involved in the binding of mitochondria to the MIRO/MILTON complex, the adaptor for motor protein binding (Misko *et al.*, 2010). It was shown that MFN2 is essential for neuronal differentiation and synapse formation in iPSC-derived neurons (Fang *et al.*, 2016). Given that mitochondria cluster at synapses, MFN2's binding of MIRO/MILTON may be responsible for this defect as mitochondria could not be sufficiently transported to the required cellular locations for axon elongation. MFN2 is a MAM resident protein, also found on the outer membrane of ER at these locations. Initially, MFN2 was thought of as a mitochondrial tether to the ER. De Brito and Scorrano (2008) showed that MFN2 was enriched at MAMs and knocking out *MFN2* caused the two organelles to be in decreased proximity to each other. Added to this, ER shape and Ca²⁺ signalling were altered leading to an increased sensitivity to apoptotic signals (De Brito and Scorrano, 2008). Several papers disputed some of the findings from this study, as they showed that MFN2 ablation increased the localisation of mitochondria to the ER. Nonetheless, all studies agreed that the morphology of the ER was affected and that mitochondria were sensitised to Ca²⁺ related death upon MFN2 ablation (Cosson *et al.*, 2012; Filadi *et al.*, 2015). The discrepancy around MFN2's role in connecting ER and mitochondria was attributed to improvements to the methods used, but it has left the exact details of the relationship uncertain. What is clear, is that MFN2 is involved in mitochondrial contact with the ER and when perturbed this can affect apoptotic sensitivity and calcium homeostasis (Bernard-Marissal *et al.*, 2019).

CMT2A causing mutations are found in every region of MFN2 (Appendix 1), making it difficult to pin down the exact cause of dysfunction. Due to MFN2's wide-ranging roles, mutations may contribute differently to each element of this protein's ability to fulfil necessary functions. A significant proportion of disease-causing mutations cluster in or near the GTPase domain (reviewed in Timmerman, Strickland and Züchner, 2014), such as the most commonly mutated amino acid residue, an arginine at position 94, R94. The most severe of these mutations is R94Q (Züchner *et al.*, 2006), but other variants include R94W (Chung *et al.*, 2006), R94P (Bergamin *et al.*, 2014) and R94G (Ando *et al.*, 2017) making this a clear hotspot for disease potential. Another common mutation T105M, is also located in the GTPase domain, however produces much milder disease in patients (Chung *et al.*, 2006). This indicates that the substitution for a polar side chain to a hydrophobic one in T105M is not as detrimental to protein function as the substitution of positively charged amino acid to a negative one in R94Q. Without a structure of MFN2, it is difficult to conclusively describe the effects these mutations may be having on the amino acid arrangement but this information highlights the

importance of comparing multiple mutations and carefully considering the mechanisms that be involved in their disease interaction.

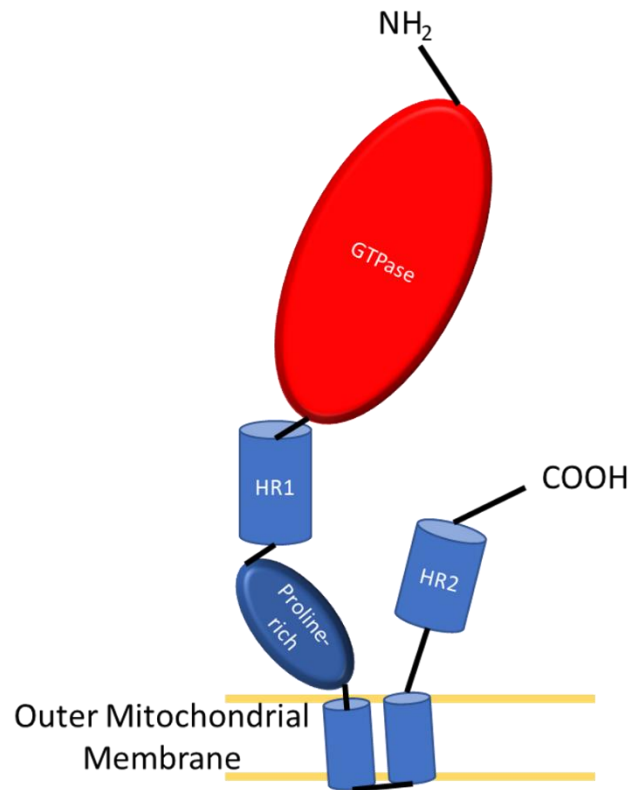


Figure 3: MFN2. Outer mitochondrial membrane resident protein MFN2 contains a GTPase domain, two coiled-coil heptad repeats (HR1 and HR2) and a proline-rich domain. Mutations in this protein are can cause CMT2A. The majority of the mutations cluster in or near the GTPase domain, such as R94Q and T105M. The R364W mutation is found in HR1.

1.2.3) Models of CMT2A

Currently, there are no approved treatments for CMT2A, meaning *in vivo* and *in vitro* modelling still provide important roles in the understanding and development of avenues that can lead to therapies. Many rodent models exist which have various benefits and drawbacks. Notably very few human *in vitro* models exist. The limited nature of models has left the understanding of CMT2A somewhat restricted.

Rodents such as mice and rats are commonly used as *in vivo* models of human disease and CMT2A is no exception but has some unique issues to face when using this model system. *MFN2* knockout mice die mid-gestation due to severe placental defects (Chen *et al.*, 2003). To overcome the lethality of the

knock-out at an early embryonic stage, conditionally inactivated alleles of *MFN2* have been developed (Chen, McCaffery and Chan, 2007). Despite this, a third of the mice died a day after being born and those that survived showed clear defects in movement, posture and size. None of the pups survived past day seventeen (Chen, McCaffery and Chan, 2007). Further rodent models have been generated which have a skeletal specific knockout (Chen *et al.*, 2010), kidney-specific knockout (Gall *et al.*, 2015), heart knockout (Mourier *et al.*, 2015), T105M overexpression (Detmer *et al.*, 2008), R94Q overexpression (Cartoni *et al.*, 2010), R94W knock-in mutations (Strickland *et al.*, 2014) or neuronal-specific R94Q overexpression (Zhou *et al.*, 2019).

Primary embryonic dorsal root ganglia infected with lentivirus to express either WT human *MFN2* or a mutant version was used by Baloh and colleagues (2007) to model several different mutations. Mitochondrial clustering was seen in the majority of mutants tested and mitochondria in mutants were more stationary than in controls, suggesting issues with mitochondrial trafficking (Baloh *et al.*, 2007). This transport defect was a key finding in determining *MFN2*'s role in transporting mitochondria (Misko *et al.*, 2010) and help shed light on why a mutation in *KIF1B*, originally thought to be the cause of *CMT2A* before being confirmed to be *MFN2* (Zhao *et al.*, 2001; Züchner *et al.*, 2004), would produce similar side effects. It was uncovered that *MFN2* is involved in binding to *MIRO/MILTON* complex for axonal transport and more recently, that transport machinery can provide some of the energy required for mitochondrial fusion (Misko *et al.*, 2010; Henrichs *et al.*, 2020). Following this, transport issues have been investigated as a key symptom of *CMT2A* though there is still confusion over the extent of how key of a phenotype this is (Misko *et al.*, 2012; Strickland *et al.*, 2014; Rizzo *et al.*, 2016; El Fissi *et al.*, 2018). A knock-in *MFN2* R94W in mice did not show any axonal transport defects (Strickland *et al.*, 2014), though abnormal clustering was seen in T105M mice (Bannerman *et al.*, 2016) which could be indicative of a transport defect. Taken together it is unclear what role mitochondrial transport has in the generation of *CMT2A* symptoms and whether this is a major player in the onset of disease.

The most common mutation in *CMT2A*, a heterozygous R94Q mutation in *MFN2*, has been modelled several times. A neuronal-specific R94Q overexpression mouse model showed disruption of fusion, widespread axon degeneration and impaired motor function in mice (Zhou *et al.*, 2019). In R94Q overexpression mice, homozygous mice showed severe defects in gait and mitochondrial abnormalities in the axons, but heterozygous mice did not show any phenotype in muscle tests (Cartoni *et al.*, 2010). This model was later reused by researchers who found mitochondrial-ER contact disturbances rendering neurons more vulnerable to oxidative stress and calcium disturbances

(Bernard-Marissal *et al.*, 2019). Further research also showed some visual defects in this model (Picci *et al.*, 2020) which is known to be associated particularly with the R94Q mutation (Züchner *et al.*, 2006). This indicates the importance of selecting relevant criteria for analysis as well as an appropriate model.

The discrepancy in rodent models may come from a species difference that has not yet been fully elucidated. Rodent models typically show limited muscle defects when disease-causing mutations are heterozygous (Detmer *et al.*, 2008; Strickland *et al.*, 2014; Bannerman *et al.*, 2016). Due to the degenerative nature of the disease and the limited time of study or the particular mutation chosen for study full disease phenotype may not yet be apparent. When a homozygous expression is used for disease-causing mutations this often results in death near birth (Strickland *et al.*, 2014) or severe limb defects and a loss of motor axons (Detmer *et al.*, 2008) symptoms which are not seen in patients. These discrepancies highlight the need for a more translational model in CMT2A research.

An obvious *in vitro* model is to take samples from patients who have the disease in question. One of the least invasive ways of doing this is to take a skin tag and culture into primary fibroblasts. However, studies with fibroblasts from patients with heterozygous missense mutations usually show little to no phenotype (Amiott *et al.*, 2008) or a slight decrease in oxidative phosphorylation activity with a normal mitochondrial network (Loiseau *et al.*, 2007; Guillet *et al.*, 2010). Of note, a patient fibroblast model did show altered ER-mitochondria contact (Larrea *et al.*, 2019) but no alteration to the bioenergetics of these cells. Patient fibroblasts are genetically useful tools but cannot replicate the specific vulnerability seen in motor and sensory neurons that generate the phenotypes seen in patients. The particular quality that makes these peripheral neurons susceptible to disease is still a matter of discussion. It has been noted in rodent models, that *MFN1* is less expressed in peripheral neurons than other cellular counterparts (Detmer and Chan, 2007). This may underlie the susceptibility in this case as the compensation provided by this homolog is not as available in peripheral neurons. Indeed, increasing *MFN1* expression has been shown to alleviate numerous defects seen in rodent models (Detmer and Chan, 2007; Misko *et al.*, 2012; Zhou *et al.*, 2019). Whether this applies in human cells has not, to date, been examined meaning the cause of this vulnerability in humans cannot yet be confirmed.

In summary, CMT2A models are lacking a representative translatable model which can describe the patient disease state. The creation of such a model will aid in understanding the cause of axonal degeneration in CMT2A and provide a platform for the development of therapeutic opportunities.

1.3) Human Pluripotent Stem Cells

Human pluripotent stem cells (hPSC) are cells of a human origin that can self-renew and produce more stem cells whilst also retaining the capacity to differentiate into any germ layer or cell type. There are two main types of hPSC: embryonic stem cells (hESC) (Thomson *et al.*, 1998) and induced pluripotent stem cells (iPSC) (Takahashi *et al.*, 2007). hPSC are in a prime position for use in cellular therapies as well as allowing the study of difficult-to-reach cell types. This also makes hPSC particularly attractive for disease modelling due to the wide range of differentiation protocols already established. Furthermore, hPSC are amenable to genetic editing making them valuable tools for the study of genetic diseases and beyond.

1.3.1) Derivation of hPSC

hESC were initially derived in 1998, by Thomson *et al.* They are derived from the inner cell mass (ICM) of the blastocyst (Thomson *et al.*, 1998) which forms 6 days post fertilisation (Figure 4a). The ICM contains the cells which will become the foetus and is isolated by immunosurgery (Figure 4b). This protocol involved the use of antibodies raised to human cells. The trophoblasts cells then died upon exposure to complement and the ICM (which seems to have selective permeability to complement) was separated. This was then plated on to mouse embryonic fibroblasts (MEF), which provide support. The outgrowth from the ICM was dissociated and passaged (Solter and Knowles, 1975; Chen and Melton, 2007). These cell colonies were positive for undifferentiated markers such as SSEA-3 and SSEA-4 and had high telomerase activity (Thomson *et al.*, 1998). In 2006, differentiated mouse cells were reprogrammed using lentiviral induction to an embryonic-like state (Figure 4c). From twenty-four initial genetic candidates, it was found that only four factors were needed. These were: Oct3/4, Sox2, c-Myc and Klf4 (Takahashi and Yamanaka, 2006). The cells produced were termed iPSC. A year later this was done in human cells with the same four factors. The reprogrammed cells were also found to be positive for SSEA-3 and SSEA-4 and have high telomerase activity (Takahashi *et al.*, 2007). iPSC are considered by many to be a more attractive option than hESC as they do not raise all of the same ethical concerns. However, it has been shown that stem cells retain epigenetic memory of their derived cell type (typically skin but now a wide variety of cells can be reprogrammed) (Kim *et al.*, 2010), which has the potential to affect their utility. Many years on from their initial derivation, it is now possible to generate clinical-grade hPSC lines which can be grown in chemically defined xeno-free conditions (Baghbaderani *et al.*, 2015; Ye *et al.*, 2017) allowing more reproducible and consistent results in culture. These advancements have made hPSC a more viable strategy for a wider range of research fields.

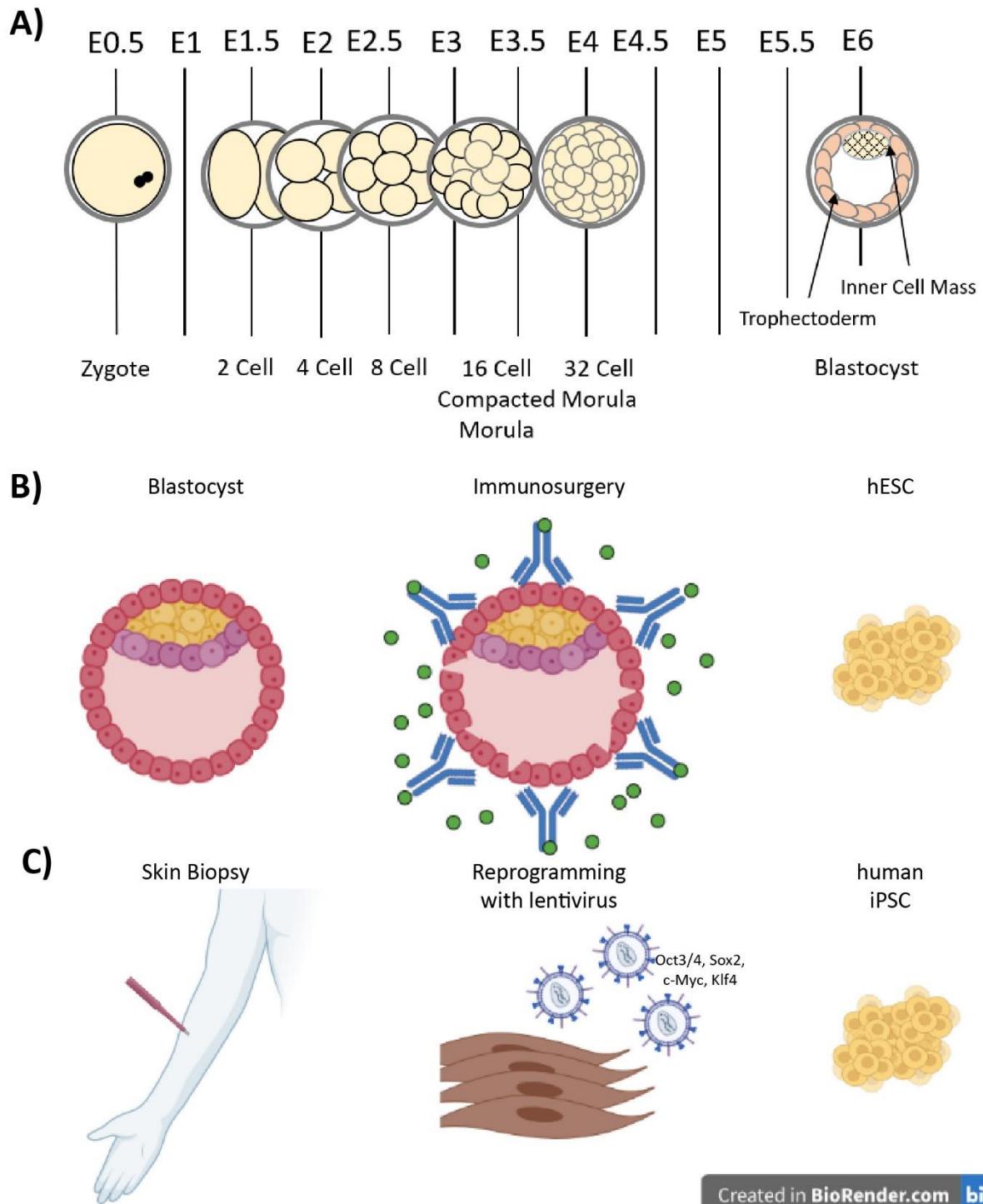


Figure 4: Generation of hPSC. **A)** Development of human embryo to form blastocyst containing trophoblast cells encasing an inner cell mass. Figure adapted from (Cockburn and Rossant, 2010). **B)** Generation of hESC. Blastocyst (left) is subject to immunosurgery (middle) which releases the inner cell mass. These can be cultured to produce hESC (right). **C)** Generation of iPSC. Skin biopsy from an adult (left) to obtain fibroblasts. Fibroblasts can be reprogrammed using lentivirus (middle) containing reprogramming factors: Oct3/4, Sox2, c-Myc and Klf4. Successful reprogramming will produce human iPSC (right).

1.3.2) Differentiation of hPSC

The ability to generate any type of cell has opened up a wide range of cell types previously extremely difficult to obtain from human patients. Using growth factors or the addition of small molecules it is possible to direct the differentiation of hPSC to a particular cell lineage (reviewed in Cohen and Melton, 2011) and, ultimately, to a specific end lineage. It is possible to achieve multiple cell types in far less than the time required for human development *in utero*, though these differentiations do not always produce fully mature cells (Patterson *et al.*, 2012). Co-culture with relevant cell types (Lam *et al.*, 2019; Beauchamp *et al.*, 2020), telomere shortening (Vera, Bosco and Studer, 2016), 3D culture (Beauchamp *et al.*, 2020; Rosa *et al.*, 2020) and different matrices (Sun and Nunes, 2017; Lam *et al.*, 2019) are just some of the multiple strategies researchers have come up with to attempt to overcome this pitfall, however, the majority of differentiated cultures derived from hPSC are still considered immature. Currently, a wide range of directed-differentiation protocols exist for hPSC from retinal pigment epithelia (reviewed in Leach and Clegg, 2015), cardiomyocytes (reviewed in Fujita *et al.*, 2019) to pancreatic beta cells (reviewed in Wesolowska-Andersen *et al.*, 2020). However, these must be often be optimised for particular usage in each cell line, as hPSC are known to have particular inclinations towards differentiation lineage (Osafune *et al.*, 2008; Ramos-Mejia *et al.*, 2010; Wesolowska-Andersen *et al.*, 2020).

Whilst hPSC have the ability to make any cell type, we do not always have the knowledge of which signals are required to achieve this end. A particularly prevalent example exists in the anterior-posterior axis of development. This is controlled by 39 HOX proteins, organised in four genomic clusters (*HOXA*, *HOXB*, *HOXC* and *HOXD*) which are sequentially and co-linearly activated down this axis (reviewed in Deschamps and Duboule, 2017). By default, neuronal differentiations will be cranial (Chambers *et al.*, 2009) meaning further signals are required to a more posterior phenotype. Much work has been done in the elucidation of the signals required for this to occur (Lippmann *et al.*, 2015), but the production of differentiated endpoints from these precursors is still difficult. More recent work has shown that the timing of signals, and not only the presence and absence of signals, may play an important role in their specification (Mouilleau *et al.*, 2021). Work is still required for the relevant cell type to be utilised in the researchers' line of choice but the plethora of protocols available, along with ongoing developments, mean that it is possible to produce a physiologically relevant cell type for most disease models.

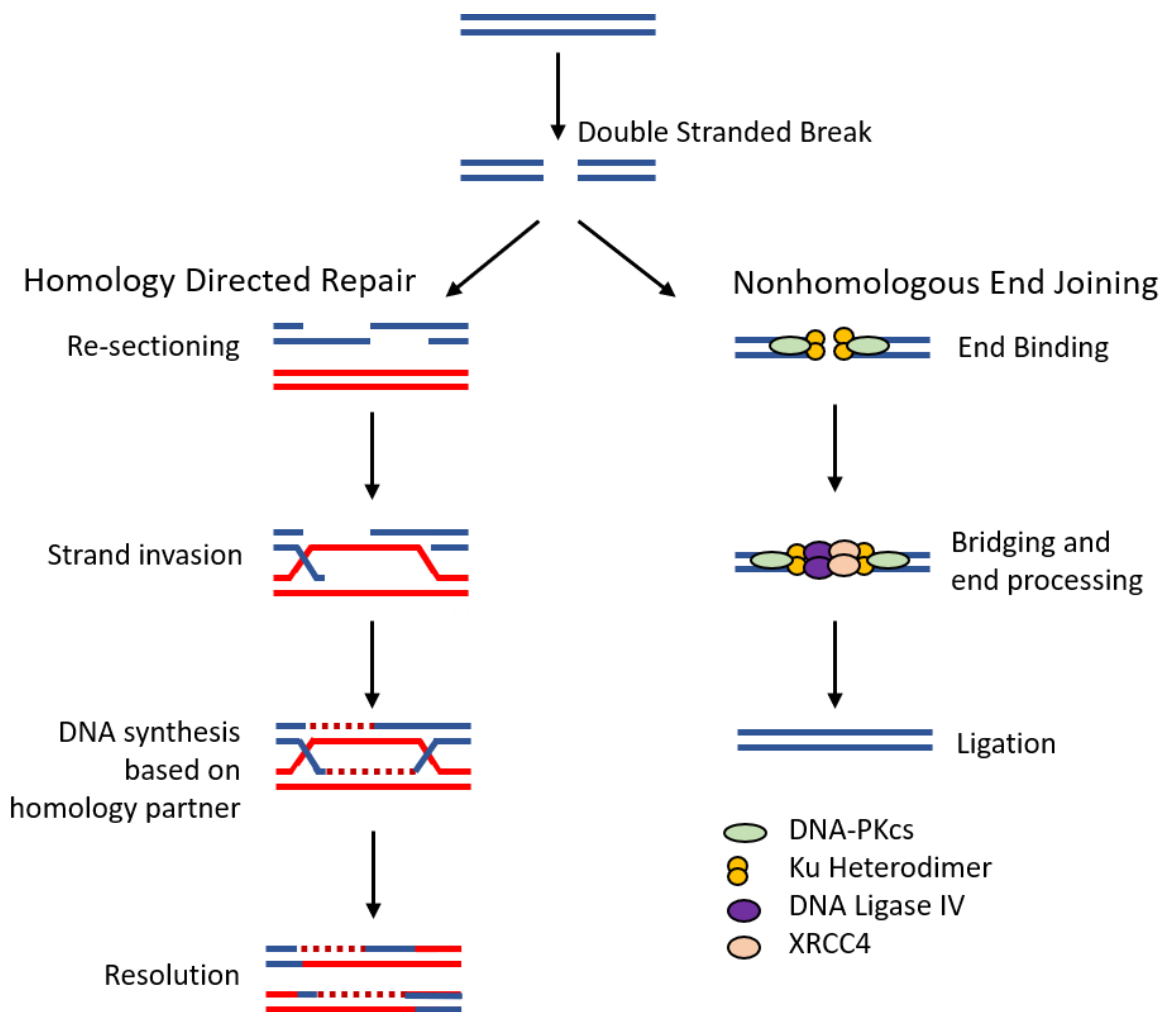


Figure 5: Double-Stranded Break Repair. Non-homologous end-joining (right): Ku heterodimer and protein kinase, DNA-activated process the ends (DNA-PKcs) and recruit the DNA ligase IV-XRCC4 complex to complete ligation (reviewed in Sharma and Raghavan, 2016). Homology directed repair: this involves the generation of a single-stranded region of DNA, followed by strand invasion. DNA synthesis is carried out using the sister chromatid as a template. This can then be resolved in several ways, most commonly, involving cross over of the strands as shown (reviewed in Liu *et al.*, 2019).

1.3.3) Genetic editing strategies

Genetic editing of hPSC for disease models and mechanistic insights requires the creation of double-stranded breaks (DSB). Repair of DSB can be utilised to make desired changes to the wild-type genetic sequence. DSB are repaired in one of two ways: Nonhomologous End Joining (NHEJ) or Homology-Directed Repair (HDR) (Figure 5). NHEJ involves proteins binding to the ends of the DNA to re-join them back together. NHEJ can take place throughout the whole cell cycle, making it more likely to occur than HDR (reviewed in O’Driscoll and Jeggo, 2006). NHEJ is typically thought of as more error-prone than HDR, producing insertions and deletions (indels). This has been utilised to create knockouts

through frameshifts leading to premature stop codons (reviewed in Sharma and Raghavan, 2016). As HDR involves the use of the sister chromatids as a template for repair it takes place between late S-G2 once the chromatids are available. The process involves strand invasion and the formation of a Holliday junction allowing the strands to be successfully resolved and repaired. Through the use of exogenous templates such as single-stranded oligonucleotides (ssODN), this process can be influenced to introduce a specific edit from a small alteration to large-scale alterations (reviewed in Heyer, Ehmsen and Liu, 2010; Liu *et al.*, 2019). In the past targeting to generate DSB has largely been carried out by Transcription Activator-Like Effector Nucleases (TALENs) or Zinc fingers, which are then bound to a non-specific nuclease, such as FOK1 (reviewed in Pabo, Peisach and Grant, 2002). More recently discovered are Clustered Regularly Interspaced Short Palindromic Repeats (CRISPR) and CRISPR associated systems (Cas). CRISPR originates from bacterial and archaea defence systems. They work by integrating part of the invading sequence to the host genome and then creating a small template which, along with other important RNA elements, can be used to guide nucleases systems to the foreign DNA (reviewed in Terns and Terns, 2011). This requires the viral genome to contain a specific recognition sequence known as the protospacer adjacent motif (PAM), the particular sequence identify differs between Cas but is required for targeting (Mojica *et al.*, 2009). The foreign genome can then be silenced through the creation of DSB (reviewed in Bhaya, Davison and Barrangou, 2011). This is very similar to eukaryotic systems such as RNA induced silencing complexes but is an RNA-guided DNA-cutting system. The most well-known of these Cas proteins is Cas9, found in *Streptococcus pyrogens*, which has been used for multiple different eukaryotic editing experiments (reviewed in Bhaya, Davison and Barrangou, 2011). The ease of guide RNA generation to target specific loci makes CRISPR an ideal candidate to use for genomic editing in eukaryotic cells and is now extremely commonly used for genetic editing of all cell types including hPSC.

1.3.4) Genetic editing in hPSC

The ability to edit hPSC has made the generation of isogenic controls an easier task than previously. Many studies have used healthy donor controls which bear no relation to the affected individual (Saporta *et al.*, 2015; Rizzo *et al.*, 2016) and others have generated sibling controls (Ding *et al.*, 2021). Whilst use of previously generated control lines or even sibling controls may be easier than editing hPSC, use of non-isogenic controls leads to questions over the genetic background and whether other genes are affecting disease penetrance. This is particularly prevalent in CMT2A, where the same mutation can have different disease phenotypes even in the same family (Chung *et al.*, 2006; Casasnovas *et al.*, 2010; Dankwa *et al.*, 2018). Since the advent of easier genetic editing, researchers have edited mutations in iPSC lines to generate a wild-type control that has the same genetic

background (Perez-Siles *et al.*, 2020). Additionally, it is possible to generate multiple mutations on the same wild-type background to generate allelic series (Zeltner *et al.*, 2016), thus allowing the comparison of different mutations without concerns of different genetic background.

The availability of CRISPR systems has made hPSC editing increasingly more viable despite being a common bottleneck of hPSC methodology. Indeed, single-cell hPSC cloning typically has low efficiency and require the addition of protein inhibitors (Watanabe *et al.*, 2007), alternative matrixes (Rodin *et al.*, 2014) or even the use of MEFs (Yang *et al.*, 2013) to help overcome this. Additionally, it is known that hPSC are prone to gaining genetic aberrations during culture (Fazeli *et al.*, 2011; Baker *et al.*, 2016; Markouli *et al.*, 2019; Price *et al.*, 2019) and thorough screening should be carried out to ensure any line is free of these issues. Whilst these factors make hPSC challenging to work with, they can usually be mitigated with planning and the necessary capabilities.

1.3.5) Examples of disease modelling using hPSC

The ease of culturing and editing hPSC have made them increasingly more prominent in disease modelling. They do not suffer from species specific translational issues as there is no difference in species but *in vitro* findings may not translate into *in vivo*, making them a complementary partner for such research and not a replacement. Genetic hPSC models are less time consuming to produce than animal models, with less active maintenance and in drug studies will require significantly less compound. Using patient fibroblasts, it is possible to generate induced pluripotent stem cells (iPSC) and then carry out differentiation to the affected cell type for the disease of interest. This allows investigation of a patient's tissue without multiple biopsies, including cells which are more difficult to access. Furthermore, in instances where disease phenotypes are difficult to detect in animals, hPSC can provide a more useful endpoint, as was the case for a chemotherapy-induced peripheral neuropathy drug screen (Rana *et al.*, 2017). In this study, researchers noted disease phenotypes seen in humans that had not previously been noted in animals, as well as, being able to determine particular neuronal defects compared with non-specific cell defect. However, not all positive compounds showed a response in this assay (Rana *et al.*, 2017). It is possible that the cell type examined was not optimal, that another measure was needed to pick up the effect of treatment or that interaction of cell types is required for the neuropathy to develop. With future work, hPSC can cover most of these issues to become a more accurate cell model, but cannot replace an animal in terms of the full system to system interaction.

A study for familial dysautonomia looked at the differences between severe and mild disease, creating an allelic series of hPSC (Zeltner *et al.*, 2016). The different mutations showed differing capabilities to alter specification and neuron survival, indicating that hPSC are sensitive enough to model disease sensitivity and tease apart the contribution of particular mutations. Furthermore, researchers in this study highlighted the importance of genetic background where other genes may be contributing to disease phenotype (Zeltner *et al.*, 2016), thus bringing personalized medicine to the understanding of disease and development of treatments.

Previous studies of CMT2A have involved the issue of patient-derived iPSC rather than the introduction of mutation into hESC. The benefit of using iPSC in this way is that the cells in question are already known to cause disease. In cases where the exact mutation or mutations at fault are in question it can still be possible to study the disease. CMT2A is known to be caused by mutations in *MFN2*, however there is significant variation in phenotype seen within families (Lawson, Graham and Flanigan, 2005; Kotruchow, Kabzińska and Kochański, 2015) leading to questions over disease penetrance and potential contributing factors. However, availability of iPSC derived lines can be somewhat restrictive as only a limited number of mutations have been reprogrammed to generate iPSC. Introducing a desired mutation into hESC is an alternative strategy to model disease which relies on the mutation alone being the causative factor. It can be useful to tease apart different contributing mutations if multiple factors are in play in iPSC derived lines. However, it is possible that epi-genetic factors contribute to disease in which case hESC may not fully characterise the disease phenotype. For hESC edited lines, the control is clearly the unedited line whereas the ideal control for iPSC must be generated through genetic editing. Ultimately this means that no benefit is gained through the lack of editing when generating appropriate isogenic controls. Furthermore, iPSC are known to epigenetically retain an epigenetic phenotype from their previous identity as well as potentially an increased mutational burden in response to re-programming which may affect differentiation potential (Kim *et al.*, 2010; Bar-Nur *et al.*, 2011; Bilic and Belmonte, 2012; Nishizawa *et al.*, 2016). In each case, the use of iPSC and hESC come with significant requirements to optimise any differentiation potential as each line will have particular differentiation bias regardless of origin. Both cell types have utility and must be carefully considered by researchers looking to model disease.

To the best of my knowledge, there are only two studies for CMT2A which have examined iPSC-derived neurons from patient fibroblasts. These two studies modelled different mutations which may account for the confusion between the results. Saporta *et al* found no mitochondrial trafficking in iPSC-derived neurons containing *MFN2*^{R364W/+}. It was noted that neurons had inherent excitability suggesting

calcium dysregulation (Saporta *et al.*, 2015). The other study used iPSC-derived neurons containing MFN2^{A383V/+} and saw mitochondrial transport defects as well as mitochondrial energetic abnormalities (Rizzo *et al.*, 2016). Interestingly, the patient fibroblasts were examined and multiple noted effects were isolated to the neurons (Rizzo *et al.*, 2016), highlighting the importance of testing disease relevant cell types. These studies indicate the benefit that hPSC can provide in understand CMT2A disease pathology, however did not use isogenic controls would have provided a stronger basis for comparison. Taken together this indicates, hPSC have not yet been used to their full potential for the elucidation of disease mechanisms and as a platform for developing therapeutic compounds in CMT2A.

1.4) Thesis aims

The overall aim of my work is to generate a human *in vitro* model for CMT2A and to investigate the molecular mechanism of disease using this model. To do this effectively, I want to use a physiologically relevant cell type that is also human in origin. This means I will need to optimise motor and sensory neuron differentiations for an hPSC line which will later be edited to contain CMT2A causing mutations. I want to focus on a human model as previously developed animal models of CMT2A had significant pitfalls and did not recapitulate patient phenotypes appropriately (Cartoni *et al.*, 2010; Strickland *et al.*, 2014; Bannerman *et al.*, 2016). Moreover, previous use of patient fibroblasts was also not particularly informative (Saporta *et al.*, 2015; Larrea *et al.*, 2019), most likely because CMT2A primarily affects motor and sensory neurons, leaving fibroblasts relatively unaffected by the disease. Patients' motor neurons are experimentally inaccessible; hence, I will utilise hPSC-based technology to: 1) introduce a patient-specific mutation into wild-type hPSC, 2) differentiate mutant and wild-type hPSCs to disease-relevant motor neurons and 3) compare the mitochondrial phenotypes to elucidate any differences caused by the CMT2A causing mutation. To address these goals, the following aims were designed to describe my experimental approach:

1.4.1) Identification of suitable hPSC cell line for CMT2A modelling and optimisation of hPSC differentiation to limb-innervating motor neurons

In my first aim, I focus on choosing a suitable hPSC line for the CMT2A disease model. As motor and sensory neurons are the disease-relevant types for CMT2A, I assess multiple hPSC lines for their ability to differentiate into motor and sensory neurons. From this I will further optimise the differentiation protocols to achieve the most affected, and therefore physiologically relevant, neurons in CMT2A, limb innervating motor neurons.

1.4.2) Generation of hPSC clones with a CMT2A patient-relevant mutation

I will genetically edit wild-type cells to introduce a range of CMT2A causing mutations and obtain isogenic pairs. Clonal lines will be characterised to ensure the lines used faithfully genetically represent CMT2A.

1.4.3) Characterisation of Mitochondrial Phenotype in Wild-Type and CMT2A hPSC-derived motor neurons

Bringing together the previous two aims, I will investigate the effect of CMT2A mutation on motor neurons. To this end, I will examine the different aspects of neuronal physiology and mitochondrial phenotype and function. If a defect is found, I will attempt pharmacological manipulation of my model system to attempt to alleviate this defect.

2) Materials and Methods

2.1) hPSC Culture

hPSC lines used in this study were MasterShef4 (Thompson *et al.*, 2020), MasterShef7 (derived by Professor Harry Moore at the Centre for Stem Cell Biology in University of Sheffield) and MasterShef11 (Thompson *et al.*, 2020). For routine maintenance, hPSC were kept at 37°C in a humidified atmosphere containing 5% CO₂. Cells were cultured on vessels coated with either, Vitronectin (VTN-N) (Life Technologies, A14700) or Geltrex (Gibco, A1413201), as detailed below, in E8 (Chen *et al.*, 2011) or S8 (in-house) medium.

2.1.1) Preparation of Culture Vessels

Upon purchase, VTN-N was thawed and aliquoted before storage of aliquots at -80°C. Aliquots were thawed at room temperature and diluted 1:100 in sterile phosphate-buffered saline (PBS). The culture vessel was covered with an appropriate amount of vitronectin (for example, for T12.5, 1.5ml of diluted VTN-N was used) and incubated at room temperature for 1 hour. Vessels were either used immediately or stored at 4°C for up to one week. Vitronectin was aspirated just before plating cells.

Upon purchase, Geltrex was thawed overnight at 4°C and aliquoted on ice before storage of aliquots at -20°C. Aliquots were thawed overnight at 4°C and diluted 1:100 in fridge-cold DMEM F-12 (Sigma, D6425). The culture vessel was covered with an appropriate amount of diluted Geltrex and incubated at room temperature for 1 hour. Vessels were either used immediately or stored at 4°C for up to two weeks. Geltrex was aspirated just before plating cells.

2.1.2) E8 Media Preparation

Essential 8 (E8) media was prepared in-house using a recipe adapted from (Chen *et al.*, 2011) (2.1.3). Batches of 50X E8 supplements were prepared and stored as 10ml aliquots at -20°C. To prepare 1X E8 media, 10ml aliquots were defrosted overnight at 4°C and added to 490ml of DMEM/F12. This was then filtered using 0.22µm filter (Millipore, S2GPU05RE) and kept at 4°C for a maximum of 14 days.

2.1.3) E8 Medium

Component	50X Concentration	Final Concentration per 1 litre E8	Supplier	Catalogue Reference
DMEM-F12			Sigma	D6425
L-ascorbic acid	3.2g/L	64mg/L	Sigma	A8960
Sodium Selenium	700µg/L	14µg/L	Sigma	S5261
Insulin	970mg/L	19.4mg/L	Thermofisher	A11382
NaHCO ₃	27.15g/L	543mg/L	Sigma	S5761
Transferin	535mg/L	10.7mg/L	Sigma	T0665
Glutamax	50x	1x	Gibco	35050038
FGF-2	5mg/L	100µg/L	Peprotech	100-18B
TGFB1	100µg/L	2µg/L	Peprotech	100-21

2.1.4) Stable E8 Medium (S8)

Stable E8 Medium (S8) is an in-house adjustment to the E8 medium, which entailed increasing NaHCO₃ to a final concentration of (1383mg/L) and replacing FGF-2 with Heat Stable Recombinant Human bFGF (Gibco, PHG0368).

2.1.5) Passaging hPSC

Cells grown on either VTN-N or Geltrex were passaged using ReLeSR (Stem Cell Technologies, 05873) an enzyme-free human stem cell selection and passaging reagent.

To passage the cells, media was removed from the culture vessel and cells washed once with PBS. Cells were then incubated with 100µl/cm² ReLeSR at room temperature for 30 seconds. ReLeSR was aspirated and the culture vessel was further incubated at room temperature for 3-6 minutes, depending on colony density and vessel coating. Following the addition of fresh E8 media, the culture vessel was tapped gently to ensure proper detachment of cells from the culture flask. The cell suspension was pipetted up and down gently using a 10ml stripette to break colonies into small

clumps. Colonies were seeded into new flasks at various split ratios from 1:3-1:8 depending on the desired confluence.

2.1.6) Freezing hPSC

hPSC cultures of approximately 70% confluence were harvested using the method described in 2.1.5). At the final step, instead of resuspension of cell pellet in culture media, cells were resuspended in a freezing media, consisting of 90% foetal bovine serum (FBS) (HyClone, SV30160.03) supplemented with 10% DMSO (Sigma, D4540). Aliquots of 0.5ml cells in freezing media were pipetted into cryovials using a 10ml stripette and placed into Mr Frosty (Nalgene) at -80°C overnight. The following day, cryovials were transferred to liquid nitrogen for long term storage.

2.1.7) Thawing hPSC

Cryovials were removed from liquid nitrogen and placed into a 37°C water bath until thawed. The cells were transferred to a 15ml falcon tube containing 4ml DMEM-F12 pre-warmed to 37°C. The cells were then centrifuged at 155g for 4 minutes. The supernatant was aspirated and the cell pellets were gently resuspended in E8 containing 10µM Rho kinase inhibitor (Y-27632, Generon, 1596-1).

2.1.8) Single Cell Dissociation of hPSC

To dissociate hPSC colonies into single cells, media was removed from culture vessel before washing cells once with PBS. Cells were incubated with 100µl/cm² TrypLE (Gibco, 12604021) at 37°C for 4 minutes. Flasks were then gently tapped to ensure proper detachment of the cells from the culture flask. TrypLE was diluted by the addition of fresh DMEM-F12 at a ratio of 4:1 into the culture vessel. Cells were transferred to an appropriate size falcon tube and centrifuged at 300g for 4 minutes. Cell pellets were resuspended in the appropriate medium, counted using a haematocytometer and diluted to desired cell number per millilitre.

2.2) Karyotyping

Karyotyping was performed by a Genetic Technologist and checked by a Clinical Scientist at the Sheffield Diagnostic Genetics Service. Typically, 20-30 metaphases were analysed by G-banding per sample (as described in Price et al 2019). Genotyping was also carried out via a qPCR analysis (as described in Baker et al., 2016; Laing et al., 2019).

2.3) Generation of clones using CRISPR

2.3.1) Guide Design

Guides were designed *in silico* using Dharmacon CRISPR tool (now Horizon - <https://horizondiscovery.com/products/tools/CRISPR-Targeted-Gene-Designer>) to correct exons of *MFN2* to generate a cut specific for the knock-in to occur. Three different guides were designed for each region. Repair template was designed *in silico* using Dharmacon CRISPR (now Horizon - <https://horizondiscovery.com/products/tools/Edit-R-HDR-Donor-Designer-oligo>) which would not only input the desired change but also edit the sequence such that Cas9 would not be able to re-cut the same location. Relevant primers were designed to amplify the region surrounding the intended edit to allow for Sanger sequencing using primerBLAST (<https://www.ncbi.nlm.nih.gov/tools/primer-blast/>). Settings in primerBLAST were altered to aim for amplified regions that were ~500bp long. All primers and repair templates were ordered from IDT as DNA oligos. For the CRISPR guides, ALT-R® CRISPR-Cas9 crRNA (IDT) were ordered.

2.3.2) Introduction of CRISPR components via electroporation

Upon purchase, crRNA and ALT-R® CRISPR-Cas9 tracrRNA (IDT, 1072532) were diluted to 100µM in Nuclease-Free Duplex Buffer (IDT, 11-01-03-01), aliquoted and stored at -20°C. Aliquots of crRNA and tracrRNA were mixed in equimolar concentrations in a sterile tube and heated at 95°C for 5 minutes to form the crRNA:tracrRNA duplex (this is the sgRNA) before being allowed to cool to room temperature. The ALT-R® S.p. HiFi Cas9 Nuclease V3 (IDT, 1081060) was diluted in Resuspension Buffer R (part of kit 10µl electroporation kit, Invitrogen, MPK1025) to 36µM and incubated at room temperature in a 50:50 mix with the crRNA:tracrRNA duplex to form the ribonucleoprotein (RNP) complex. The repair template was resuspended to 100µM in Nuclease-Free Duplex Buffer, aliquoted and stored at -20°C. For use in experiments, 100µM stock was diluted to 10.8µM in Resuspension Buffer R.

To introduce the CRISPR components into cells, cells were dissociated to a single cell suspension, as described in 2.1.8), and pelleted. The cell pellet was resuspended in the Resuspension Buffer R at 2.2×10^7 cells/ml. For each electroporation, 1µl of RNP complex, 9µl cell suspension and 2µl of repair template (replaced with R buffer if not used) was mixed and pipetted into a 10µl Neon electroporation tip (Invitrogen, MPK1025). Electroporation was carried out on DigitalBio Microporator (ThermoFisher) with the following settings: 1400V, 20ms, 1 pulse.

Cells were transferred to a prepared and prewarmed plate coated with vitronectin, containing E8 supplemented with 10 μ M Y-27632. Cells were fed fresh media 24 hours later and used for further experiments the following day.

2.3.3) Testing of guides

DNA was isolated from transfected cells using Qiagen DNeasy Blood and Tissue Kit (Qiagen, 69504). 100ng of DNA was used for each PCR reaction. The region of interest was amplified using Platinum Taq DNA Polymerase High Fidelity (Invitrogen, 11304011) with the following cycle parameters: 94°C for 2 minutes, then 30 cycles of 94°C for 15 seconds, 58°C for 30 seconds, 68°C for 35 seconds. Surveyor Kit (IDT, 706020) was used according to manufacturer's instructions. In brief, the PCR product (containing putatively edited DNA) was hybridised to control DNA before incubation with Surveyor Nuclease for 1 hour at 42°C. Samples were run on 1% agarose gel at 100V for 40-80 minutes. Editing could be seen through the presence of extra bands, indicating the nuclease had cleaved at a mismatch of the hybridised DNA.

2.3.4) DNA isolation for low cell quantities

Cells were pelleted at 252g for 4 minutes and kept at -20°C until analysis. Cells were resuspended in 0.4ml cell lysis buffer, as detailed in 2.15.3), and incubated at 55°C overnight. An equal volume of phenol/chloroform was added to the tube and inverted several times. The sample was centrifuged at 8,000g for 5 minutes to allow separation of the phases. The aqueous phase was transferred to a fresh Eppendorf tube and 40 μ l 3M NaAC and 1ml 100% ethanol was added. The tube was inverted at least 10 times to facilitate mixing followed by centrifugation at 10,000g for 5 minutes to pellet the DNA. The supernatant was removed and DNA was washed with 1ml 70% ethanol before centrifugation was repeated. Ethanol was removed and DNA was resuspended in 20 μ l of TE and left for several hours to dissolve. Concentration and purity were analysed on a Nanodrop Lite (ThermoFisher).

2.3.5) Enzymatic digestion-based screen for clones

To allow a rapid screen to identify correctly edited clones, the genomic region with *MFN2* intended for editing was examined for potential changes in restriction sites as a result of correct editing. For the MFN2-R94Q intended edit, one extra restriction site was generated due to the nucleotide change, for the enzyme BseMII (ThermoFisher, ER1401). Potential clones had DNA extracted using protocol 2.3.4) and the region was amplified using Platinum Taq DNA Polymerase High Fidelity with the following cycle parameters: 94°C for 2 minutes, then 30 cycles of 94°C for 15 seconds, 58°C for 30 seconds, 68°C for 35 seconds. 100ng of DNA was used for each PCR reaction BseMII (ThermoFisher, #ER1401) was

incubated with 3µl of PCR product along with the relevant buffers supplied with the enzyme at 55°C for 2 hrs. The product was run on a 1% agarose gel and bands examined for changes compared to control. Samples of interest were then sent for sequencing.

2.3.6) Sanger sequencing

PCR products were cleaned up using a PCR clean up kit (Macherey-Nagel, 740609) according to the manufacturer's instructions and sent to Source Bioscience for sequencing. Alternatively, PCR clean-up and sequencing were outsourced to the University of Sheffield Medical School where clean-up was carried out via a magnetic bead method and sequenced using Applied Biosystems' 3730 DNA Analyser.

2.3.7) Single-cell cloning on Mouse Embryonic Fibroblasts (MEFs)

To aid with the survival of hPSC upon dissociation to single cells, cloning of hPSC was performed on a layer of mitotically inactivated mouse embryonic fibroblasts (MEFs). To this end, 96 well plates (Greiner, M0812-100EA) were coated with 0.1% (v/v) gelatin in PBS and incubated for 1 hour at room temperature. MEFs were defrosted and resuspended in DMEM containing 20% FBS (HyClone, SV30160.03). Gelatin was aspirated from the plates and MEFs were seeded at a density of 10,000 cells/cm². Plates were placed in an incubator at 37°C with 10% CO₂ overnight before their use.

On the day of cloning, the medium from the plates was replaced with either hESC medium (section 2.3.8)) supplemented with 10µM Y-27632 or a mix of hESC medium and MteSR (#85850, Stem Cell Tech) medium at an equal ration, supplemented with 20µM cholesterol and 10µM Y-27632.

Cells at 48 hours post-transfection were dissociated from the plate as described in 2.1.8). Cells were sorted using the FACS Jazz (BD Biosciences) to ensure a single cell was deposited in each well. Machine settings were checked using individual fluorescent beads sorted into 96 well plates and confirming bead number on checking on the Incell (GE Healthcare). Immediately after sorting plates were centrifuged at 252g for 15 seconds to aid attachment of the cells to the feeder layer.

After approximately 14 days, hPSC colonies were passaged in the following way: the medium was aspirated from the well and a 200µl pipette tip containing 200µl fresh medium supplemented with Y-27632 was used to detach the colony off the plate. This was pipetted up and down to ensure that the colony was broken into smaller pieces and that all cells were captured from the well. A third of the well contents were transferred to the new culture vessel and the remaining sample was taken for DNA analysis.

2.3.8) hESC media

Component	Concentration	Manufacturer	Catalogue Reference
DMEM-F12		Sigma	D6425
Knockout Serum Replacement	20%	Thermofisher	10828028
Glutamax	1:100	Gibco	35050038
Non-essential Amino Acids	1:100	Gibco	1114035
Beta-mercaptoethanol	200nM	Gibco	31350010
FGF-2	4ng/ml	Peprotech	100-18B

2.4) Motor Neuron Differentiation

2.4.1) N2B27 Media

All protocols used N2B27 medium as a base for experiments. Media was made in advance and kept at 4°C for up to 2 weeks until use.

Component	Concentration	Manufacturer	Catalogue Reference
DMEM-F12	50:50 mix with neurobasal	Sigma	D6425
Neurobasal	50:50 mix with DMEM-F12	Gibco	21103049
N2	1:100	Gibco	17502001
B27	1:50	Gibco	17504001
Glutamax	1:100	Gibco	35050038
Non-essential Amino Acids	1:100	Gibco	1114035
Beta-mercaptoethanol	1:1000	Gibco	31350010

2.4.2) Initial protocol for motor neuron differentiation

hPSC were plated on day 0 at 52,700 cells/cm² on to vitronectin coated surface in N2B27 media with 10µM Y-27632, 20ng/ml FGF-2 (R & D systems, 233-FB/CF), 0.1µM LDN193189 (Tocris, 6053), 3µM Chir99021 (Tocris, 4423). Cells were fed the following day with the same medium as day 1, without Y-27632. At day 3, cells were dissociated to single cells with Accutase (Gibco, A110501) at 37°C for 4 minutes before being counted and re-plated at 47,400 cells/cm² on to a Geltrex coated surface in N2B27 media containing FGF-2 100ng/ml, 3µM Chir99021, 0.1µM retinoic acid (all-*trans* retinoic acid (Sigma R2625)), 0.5µM SAG (Tocris, 4366), 1µM Purmorphamine (Tocris, 4551). Media was changed every two days unless otherwise stated. At day 10, cells were dissociated as previous and re-plated at 40,000 cells/cm² on to Geltrex coated surface in N2B27 media containing 20ng/ml BDNF (Peprotech, 450-02), 200µM L-Ascorbic Acid (Sigma, A4403), 0.1µM Retinoic acid, 0.5µM SAG and 1µM Purmorphamine. Cells were re-plated into identical conditions if they reached confluence. At day 24, media was changed to contain 20ng/ml BDNF, 20ng/ml GDNF (Peprotech, 450-10), 200µM L-Ascorbic Acid in N2B27 media. Cells were re-plated into identical conditions if they reached confluence. Cells were used for experiments at days 3, 8, 14 and 36.

2.4.3) Previously published protocol for motor neuron differentiation

This protocol was altered from (Maury *et al.*, 2015; Guo *et al.*, 2017). Changes from published protocol include the addition of PVA for the initial formation of the embryoid body (EB), use of accutase over trypsin and use of an Eppendorf shaker to dissociate EBs.

The protocol was carried out as follows: 3000 hPSC were plated on day 0 in 96 well U-bottomed low attachment plates (Greiner, 650185) in N2B27 media containing, 5µM Y-27632, 0.2µM LDN193189, 3µM Chir99021, 40µM SB431542 (Tocris, 1614) and 0.05% PVA (Sigma, P8136). Plates were spun at 400g for 4 minutes to ensure that cells were at the bottom of the well. All medium changes within this plate were replacing only 50% of the media to ensure the EB was not disturbed, media was changed every two days unless otherwise stated. At day 2 medium was changed to contain 0.1µM retinoic acid and 0.5µM SAG. At day 7 medium contained 0.1µM retinoic acid, 0.5µM SAG, 10ng/ml BDNF and 10ng/ml GDNF. At day 9 EBs were pooled together and dissociated using accutase and an Eppendorf shaker (Eppendorf ThermoMixer C) set at 37°C at increasing speeds from 800rpm to 1400rpm for 30 minutes. Speeds increased by 200rpm every 5 minutes after EBs were manually pipetted up and down. Once at single cells, they were re-plated at 52,000cells/cm² in media containing which 10µM DAPT (Tocris, 2634) 10ng/ml BDNF, 10ng/ml GDNF, 0.1µM retinoic acid and 0.5µM SAG. Plates were prepared with Poly-L-Ornithine (Sigma, P4957) for 30 minutes at 37°C, followed by washing three with PBS and then coated with Geltrex as described in 2.1.1). Media changes were now 50% every three

days, with media added gently to the side of the well. At day 14, retinoic acid and SAG were removed from the culture media and DAPT was increased to 20 μ M. At day 16, 10ng/ml CNTF (Peprotech, 450-13) was added to the culture media. On day 17, DAPT was removed from the media. From this point on media contained only BDNF, GDNF, CNTF at 10ng/ml and is defined as motor neuron maintenance media. Cells were used for experiments on day 16 or 33 as stated.

2.4.4) Optimised protocol for motor neuron differentiation

Due to optimisation carried out in experiments the protocol in 2.4.3) was optimised to contain changes as detailed below.

The optimised protocol was carried out as follows: 3000 hPSC were plated on day 0 in 96 well U-bottomed low attachment plates (Greiner, 650185) in N2B27 media containing, 20ng/ml FGF-2, 5 μ M Y-27632, 0.2 μ M LDN193189, 4 μ M Chir99021, 40 μ M SB431542 (Tocris, 1614) and 0.05% PVA (Sigma, P8136). Plates were spun at 400g for 4 minutes to ensure that cells were at the bottom of the well. All medium changes within this plate were replacing only 50% of the media to ensure the EB was not disturbed, media was changed every two days unless otherwise stated. At day 2 medium was changed to contain 20ng/ml FGF-2, 0.2 μ M LDN193189, 4 μ M Chir99021, 40 μ M SB431542, 1 μ M retinoic acid and 0.5 μ M SAG. At day 4 medium contained 1 μ M retinoic acid and 0.5 μ M SAG. At day 7 medium contained 1 μ M retinoic acid, 0.5 μ M SAG, 10ng/ml BDNF and 10ng/ml GDNF. At day 9 medium was changed to contain 10 μ M DAPT 10ng/ml BDNF, 10ng/ml GDNF, 1 μ M retinoic acid and 0.5 μ M SAG. At day 13 EBs were pooled together and dissociated using accutase and an Eppendorf shaker (Eppendorf ThermoMixer C) set at 37°C at increasing speeds from 800rpm to 1400rpm for 30 minutes. Speeds increased by 200rpm every 5 minutes after EBs were manually pipetted up and down. Once at single cells, they were re-plated at 52,000cells/cm² in media containing which 10 μ M DAPT (Tocris, 2634) 10ng/ml BDNF, 10ng/ml GDNF, 0.1 μ M retinoic acid and 0.5 μ M SAG. Plates were prepared with Poly-L-Ornithine (Sigma, P4957) for 30 minutes at 37°C, followed by washing three with PBS and then coated with Geltrex as described in 2.1.1). Media changes were now 50% every three days, with media added gently to the side of the well. At day 14, retinoic acid and SAG were removed from the culture media and DAPT was increased to 20 μ M. At day 16, 10ng/ml CNTF (Peprotech, 450-13) was added to the culture media. On day 17, DAPT was removed from the media. From this point on media contained only BDNF, GDNF, CNTF at 10ng/ml and is defined as motor neuron maintenance media. Cells were used for experiments on day 16 or 33 as stated.

2.5) Sensory Neuron Differentiation

2.5.1) Neural Crest Differentiation

At day 0, hPSC were plated on Geltrex coated surface at 30,000 cells/cm² in neural crest media (2.5.2), containing Y-27632 (10μM). Y-27632 was removed at day 2. Media was changed on day 2 and 4. Cells were used for further experiments on day 5.

2.5.2) Neural Crest Medium

Media was made in advance and kept at 4°C for up to 2 weeks until use.

Component	Concentration	Manufacturer	Catalogue Reference
DMEM-F12		Sigma	D6425
N2	1:100	Gibco	17502001
Glutamax	1:100	Gibco	35050038
Non-essential Amino Acids	1:100	Gibco	1114035
SB431542	2μM	Tocris	1614
Chir99021	1μM	Tocris	4423
DMH1	4μM	Tocris	4126
BMP4	15ng/ml	Gibco	PHC9534

2.5.3) Sensory Neuron Differentiation from Neural Crest

Neural Crest cells were dissociated using accutase at 37°C for 5 minutes and re-plated on a Geltrex coated surface at 100, 000 cells/cm² in Sensory neuron base media containing Chir99021 (3μM), SU5402 (Tocris, 3300) (1μM) and DAPT (2.5μM) and 10μM Y-27632. Y-27632 was removed from the media the following day. Two days after, media was changed to contain sensory neuron base media and BDNF, GDNF and NGF (Peprotech, 450-01) each at 10ng/ml. Media was changed every other day. Cells were used for further experiments 7 days later.

2.5.4) Sensory Neuron Base medium

Media was made in advance and kept at 4°C for up to 2 weeks until use.

Component	Concentration	Manufacturer	Catalogue Reference
BrainPhys		Stem Cell Tech	05790
N2	1:100	Gibco	17502001
B27	1:50	Gibco	17504001
Glutamax	1:100	Gibco	35050038
Non-essential Amino Acids	1:100	Gibco	1114035

2.6) Mitochondrial Assessments

2.6.1) ATP measurements

Cells were dissociated to single cells as described in section 2.1.8) and plated at 90,000 cells/cm² in 96 well plate (Greiner μ CLEAR, 655087) in E8 supplemented with 10 μ M Y-27632. Duplicate plates were generated for each experiment. One plate was used for the ATP measurements using the ATPlite assay (Perkin-Elmer, 6016943) and the values obtained were normalised against cell numbers assess from the duplicate plate.

For the ATPlite assay, the day following plating of cells, 50 μ l of cell lysis buffer was added to the ATPlite plate before shaking at 700rpm for 5minutes in the dark (On Varioskan plate reader (Thermofisher)) . Then 50 μ l of substrate solution was added to the wells and the plate was shaken again for 5 minutes at 700rpm in the dark and the luminescence measured using a Varioskan plate reader (Thermofisher). All ATPlite reagents were warmed to room temperature before use and protected from light as appropriate.

To assess cell numbers, cells in the second plate using 4% PFA for 15 minutes before being washed thoroughly with PBS. Cells were then stained with Hoechst 33342 (Thermofisher, H3570) before imaging in the Incell analyser (GE Healthcare). Acquired images were processed and cells counted using Cell Profiler (Carpenter *et al.*, 2006). Values obtained from the ATPlite assay were normalised against cell numbers.

2.6.2) Mitochondrial DNA qPCR

DNA was extracted using the Qiagen DNeasy kit (Qiagen, 69506) according to the manufacturer's instructions. DNA was eluted in TE buffer and quantified on a Nanodrop Lite (Thermofisher). 20 μ l

reactions were set up in triplicate in 384 well plates. Each qPCR reaction contained the following: 20ng template DNA, 200nM forward primer, 200nM reverse primer, 1x Rox low, 1X KAPA SYBER FAST qPCR MASTER MIX (Kapa Biosystems, KK4601) and water. PCR reactions were run on a QuantStudio 12K Flex Thermocycler (Life Technologies, 4471087) with the following cycle parameters: 50°C for 2 minutes, 95°C for 2 minutes, then 40 cycles of 95°C for 3 seconds, 60°C for 2.5 seconds.

2.6.3) Primers

Primers were generated to several mitochondrial DNA genes as based on (Abril *et al.*, 2008) whilst GAPDH was used as genomic DNA controls. For analysis, a ratio of cycle times is generated between genomic/mitochondrial DNA.

Target	Forward Primer	Reverse Primer
GAPDH	AGCCACATCGCTCAGACAC	GCCCAATACGACCAAATCC
MT-CO2	CTGAACCTACGAGTACACCG	TTAATTCTAGGACGATGGGC
12S/MT-RNR1	CTCCCAATAAAGCTAAAA	GCTATTGTGTGTTTCAGATAT
MT-ND2	GCCCTAGAAATAAACATGCTA	GGGCTATTCTAGTTTTATT

2.6.4) MitoTracker and TMRE FACS

200,000 per well hPSC were plated in a 24 well plate in E8 supplemented with 10µM Y-27632. The following day the media was aspirated. MitoTracker Green (Invitrogen, M7514) was added to the appropriate wells at 20nM and incubated for 20 minutes. TMRE-mitochondrial membrane assessment potential assay kit (Abcam, ab113852) was carried out according to the manufacturer's instructions. Cells were harvested using the method as described in section 2.1.8) and placed into FACS tubes analysis on BD FACS Jazz. Baseline fluorescence was set using unstained controls and analysed using the following settings (Mitotracker, 530/40, TMRE, 610/40)

2.6.5) 3D Mitochondrial Morphology

Glass coverslips were placed in 24 well plates and coated with vitronectin for hPSC or with Geltrex if for neurons using differentiation protocol in 2.4). For hPSC, these cells were plated 100,000 per well in E8 and Y-27632. They were fixed using 4% PFA for 15 minutes before being washed thoroughly with PBS. For neurons, these cells were plated at 100,000 per well in the appropriate media for that stage of the differentiation. Cells were fixed at the necessary time point using the same method.

Slides were stained with ATPB and Hoeschst 33342 (Thermofisher, H3570), using the method as described in section 2.13.1) and mounted onto glass slides before imaging on the LSM880 AiryScan Confocal (Zeiss) using Fast-Scan mode and Z-stacking to visualise the entire mitochondrial network. At least 10 images were taken per slide. Images were analysed from maximum projections using ImageJ thresholding and analyse particles to generate form factor and aspect ratio.

2.7) qPCR gene expression analysis

2.7.1) RNA extraction

Cells of interest were pelleted in as described in section 2.1.8) before storage at -80°C. RNA was extracted from these pellets using either the Qiagen RNA easy plus (Qiagen, 74134) and QIAshredder (Qiagen, 79654) kits or the Norgen Total RNA Purification Plus Kit (Norgen, 48300) according to the manufacturer's instructions. RNA was eluted in the appropriate buffer and quantified using the Nanodrop Lite (Thermofisher).

2.7.2) cDNA production

RNA was reverse transcribed into cDNA using High Capacity Reverse Transcriptase (Applied Biosystems, 4368813) according to the manufacturer's instructions. In brief, each 20µl cDNA reaction contained; 1X RT buffer, 1x dNTP mix, 1X RT random primers, 1 unit Reverse Transcriptase, nuclease-free water and 2000ng, 1000ng, or 500ng of RNA.

2.7.3) qPCR

Each 10µl qPCR reaction contained 1x TaqMan Fast Universal Master Mix (ThermoFisher, 4352042), 100nM of forward primer, 100nM of reverse primer, 100nM of probe from the universal probe library (Roche, 4683633001) and 10ng of genomic DNA. This was run on QuantStudio 12K Flex Thermocycler (ThermoFisher) with the following parameters: 50°C for 2 minutes, 95°C for 10 minutes, then 40 cycles of 95°C for 15 seconds, 60°C for 1 minute.

2.7.4) qPCR analysis

The analysis was carried out by using the 1/Delta CT method. In brief, control gene cycle time was subtracted from the cycle time of the gene of interest generate Delta CT. 1 divided by this number generates 1/Delta CT which was plotted.

2.8) Primers

Primers were generated using The Universal Probe Library Assay Design Center (Roche, https://lifescience.roche.com/en_gb/brands/universal-probe-library.html)

Target	Probe	Forward Primer	Reverse Primer
<i>GAPDH</i>	#60	AGCCACATCGCTCAGACAC	GCCCAATACGACCAAATCC
<i>LHX1</i>	#80	atgcaacctgaccgagaagt	caggtcgctaggggagatg
<i>LHX3</i>	#12	gttcaggaggggcaggac	ctcccgtagaggccattg
<i>FOXP1</i>	#84	tgacaaacaaccagctctca	tgagggctcagcacttgtt
<i>HOXA10</i>	#32	gttttgacacaagaaatgtcagc	gacattgttgggataatttgg
<i>HOXD10</i>	#2	ctgaggtctccgtgtccagt	Gctggttggtgatcagacttg
<i>OCT4</i>	#35	AGCAAAACCCGGAGGAGT	CCACATCGGCCTGTGTATATC
<i>BRACHYURY (T)</i>	#23	aggtaccaaccctgagga	gcaggtgagttgtcagaataggt
<i>SOX1</i>	#37	ACCAGGCCATGGATGAAG	CTTAATTGCTGGGGAATTGG
<i>PAX6</i>	#12	AGGGCAACCTACGCAAGA	CGTTGGAAGTATGGAGTTG
<i>SOX2</i>	#35	ttgctgcctctttaagactagga	taagcctggggctcaaact
<i>OLIG2</i>	#12	agctcctcaaatcgcattcc	atagtcgtcgcagctttcg
<i>ISLET1</i>	#83	GCAGCCCAATGACAAAATAA	CCGTCGTGTCTCTCTGGACT
<i>HB9</i>	#50	ttacctgacttatgaaactgaaacc	cccagagacgtaagcataaacc
<i>HOXA1</i>	#9	gacgaccgcttcttagtgg	tcccggaagtctgtaggta
<i>HOXA2</i>	#5	caagaaaaccgcacttctgc	tgtgttggtgtaagcagttctca
<i>HOXB3</i>	#3	agctgctgaactgtccgttt	ccaggtccacgatgattttt
<i>HOXA4</i>	#20	gttgccaccaagagagaac	ccaagtagtcttctcaggtatcc

<i>HOXC5</i>	#25	cccgatgtacagtcagaa	gcctgctcctttgatctc
<i>HOXB6</i>	#12	tggaagctgaagaagaaactgaa	gccgggttatgatttgtg
<i>HOXC8</i>	#86	tcccagcctcatgtttcc	tgataccggctgtaagttgc
<i>HOXC9</i>	#70	tcctagcgtccaggtttcc	gctacagtcggcaccaa
<i>HOXC10</i>	#19	aggagagggccaaagctg	agccaatttctgtggtgtt
<i>SOX9</i>	#61	gtaccgcacttgacacaac	tctcgtctcgttcagaagtc
<i>PAX3</i>	#13	aggaggccgactggaga	cttcatctgattgggtgct
<i>TfAPB</i>	#49	cctgcactcccgaagaata	gcgccagtagatccgtaaat
<i>SNAI1</i>	#11	gctgcaggactctaaccaga	atctccggaggtgggatg
<i>SNAI2</i>	#7	tggttgcttcaaggacacat	gcaaatgctctgttgacgtg
<i>MSX1</i>	#7	ctcgtcaaagccgagagc	cggttcgtctgtgtttgc
<i>POU4F1</i>	#78	ctccctgagcacaagtacc	ctggcgaagaggttgctc
<i>PRPH</i>	#63	ggatgagattgagttcctcaaga	ctggctctccacactcacct
<i>SCN9A</i>	#1	aaaaagaagcagccctgaga	ctcctcacataagaggcttgc
<i>P2X3</i>	#15	gcgcccttacttctgtgg	aaacttctggctttgtactgctc
<i>CDX2</i>	#34	atcacatccggaggaaag	Tgcggttctgaaaccagatt
<i>HOXC6</i>	#87	tgaattcctacttcactaaccttc	atcataggcgggtggaattga

2.9) FACS analysis

2.9.1) Marker staining

Cells were harvested using the method as described in section 2.1.8) and placed into FACS tubes (Falcon, 352053), resuspended in FACS buffer (PBS supplemented with 10% FCS).

Cells were stained with primary for 15 minutes at 4°C before washing with 4ml FACS buffer. Cells were centrifuged at 312g for three minutes and the supernatant aspirated. Cells were resuspended in FACS buffer and secondary antibody added at appropriate dilution for 15 minutes 4 °C in the dark. Cells

were washed as previously before cells were carefully resuspended before analysis on BD FACS Jazz. Baseline fluorescence was set using the primary antibody control P3X which does not show expression on human cells (Köhler and Milstein, 1975).

2.9.2) Primary FACS antibodies

Target	Manufacturer	Catalogue Number	Reactivity	Dilution
TRA-1-85	In-house hybridoma	(Williams <i>et al.</i> , 1988)	Mouse	1:10
TRA-1-81	In-house hybridoma	(Andrews <i>et al.</i> , 1984)	Mouse	1:10
P3X	In-house hybridoma	(Köhler and Milstein, 1975)	Mouse	1:10
SSEA3	In-house hybridoma	(Shevinsky <i>et al.</i> , 1982)	Rat	1:10
P75	In-house hybridoma	(Ross <i>et al.</i> , 1984)	Mouse	1:10

2.9.3) Secondary FACS antibodies

Target	Manufacturer	Catalogue Number	Dilution
Mouse Secondary (647)	Strattech	115-605-044-JIR	1:200

2.10) Mitochondrial Trafficking

2.10.1) Transfection of neurons

At day 13 of differentiation protocol in 2.4.3) or 2.4.4), cells were plated at 170,000 cells per 35µm dish (Ibidi, 81156) in the appropriate media. Differentiation continued as normal. At day 33 of differentiation protocol neurons were transfected using Lipofectamine LTX with Plus Reagent (ThermoFisher, 15338100) and Opti-MeM (Gibco, 31986062) as indicated in the manufacturer's instructions. Plasmids p-Cag GFP and ds-RedMito plasmid (red fluorophore with mitochondrial targeting sequence, under CMV promotor, produced by TanakaBio, 632421) were used in a ratio: 7:3. Transfection components were incubated with cells for 5 hours before media was replaced with fresh

motor neuron maintenance media. Neurons were used within 24-48 hours of transfection. If neurons were to be dosed with compound, they were fed motor neuron maintenance media after the transfection end and dosed 1 hour after with relevant compound.

2.10.2) Tracking experiments

Zeiss LSM880 AiryScan Confocal chamber and insert were heated so that the media remained at approximately 37°C. A bottle of water was placed within the chamber to ensure a stable temperature and humidified environment. Neurons were located using 40X objective using the GFP plasmid, then checked for ds-RedMito. Suitable neurons, transfected by both plasmids, were imaged at an appropriate location using the Fast-Scan mode where an image was taken every 3 seconds for 6 minutes. After this, the entire neuron was imaged using both channels Fast-Scan mode and z stacks to visualise the entire length of the neuron, where possible.

2.10.3) Analysis

The axon was traced using the GFP image as a guide, and then 'resliced' and the stack collapsed using 'max projection' in FIJI (Schindelin *et al.*, 2012) producing a kymograph (space-time plots) where time is measured on the y axis and distance is measured on the x-axis. Anterograde and retrograde travelling mitochondria were noted for each kymograph. Mitochondrion speed was measured by tracing the line of the travelling mitochondria. The width of the line was the distance covered by the mitochondria and the height was converted to seconds allowing velocity to be calculated.

Images taken along the axon length were stitched together using the FIJI plugin 'Stitching' 'Pairwise Stitching' (Preibisch, Saalfeld and Tomancak, 2009) to produce a composite image of a neuron. This axon was then traced using the green channel and the FIJI plugin 'Simple Neurite Tracer' (Longair, Baker and Armstrong, 2011). The axon path was transferred to the FIJI region of interest manager. The axon path could then be highlighted on the red channel (showing the ds-RedMito) and was straightened with a width of 50 pixels for the axon path. This could then be analysed as previous mitochondrial morphology using 'Analyse Particles' on a thresholded image to measure individual mitochondria.

2.11) Western Blot Analysis

2.11.1) Protein Lysis

Cells to be harvested for protein lysis were washed with PBS before 1x Laemilli Buffer was added to the cells and harvested by scraping and placed in a 0.5ml Eppendorf. Samples were incubated at 95°C

for 10 minutes to denature proteins before being snap-frozen in dry ice and stored at -80°C until future analysis. Protein quantification was carried out using a Nanodrop Lite.

2.11.2) Protein Electrophoresis

Each sample was diluted into protein buffer (Bio-Rad, 161-0791) and heated at 95°C for 5 minutes. 15µg of protein was loaded to a 10% separating gel at 200V for approximately 40 minutes in a Mini Trans-Blot Cell (Bio-Rad) with pre-stained ladder precision plus protein (BioRad, 161-03475).

2.11.3) Protein Transfer, Staining and Visualisation

Protein was transferred on to PVDF (Millipore, IPVH00010) or nitrocellulose membrane (BioRad, 1620115) using a Mini Trans-Blot Cell (Bio-Rad) for 90 minutes at 240A. The membrane was blocked in 5% milk in PBS in a 50ml falcon tube and incubated for 45 minutes on shaking platform. Primary antibodies were made in 3% P/BSA and incubated overnight on a rolling platform at 4°C. The next day the membrane was transferred to a new 50ml falcon tube and washed for 5 minutes in PBS on a rolling platform 3 times. The secondary antibody was made up in 3% P/BSA and incubated in the dark for 1 hour on a rolling platform at room temperature. The membrane was washed as previously before being placed within two pieces of filter paper to dry, in the dark. This was then imaged using a LiCor Odyssey (LiCor).

2.11.4) Protein Electrophoresis running buffer

For 10x SDS

Component	Concentration	Manufacturer	Catalogue Reference
Trizma Base	30.28g/l	Sigma	A71503
Glycine	144.13g/l	Sigma	G7407
Sodium dodecyl sulphate	1g/l	Sigma	71729
ddH ₂ O			

2.11.5) Protein electrophoresis transfer buffer

Component	Concentration	Manufacturer	Catalogue Reference
Trizma Base	11.252g/l	Sigma	A71503
Glycine	3.026g/l	Sigma	G7407
Methanol	200ml per litre	Merck	67-56-1
ddH ₂ O			

2.12) Electrophysiology

Patch-clamp experiments were carried out and analysed by Stuart Johnson.

2.13) Imaging and analysis

2.13.1) Immunocytochemistry

Cells were washed with PBS before 4% PFA was added and incubated for 15 minutes at room temperature. The cells were washed with PBS twice to ensure PFA was removed. At this point, cells could be stored at 4°C in PBS and stained with antibodies at a later date. To permeabilise the cells and block the non-specific antibody interactions PBS supplemented with 0.2% Triton X-100 (Sigma, T8787) and 10% FCS was added for to the cells 1hr at room temperature. Primary antibodies were diluted in staining buffer which contained PBS supplemented with 10% FCS and 0.1% Tween 20 (Sigma, P9416). These were then incubated with samples at 4°C overnight. Cells were washed three times with PBS and secondary antibodies were incubated for 1-2 hours at room temperature in the dark. Cells were washed three times with PBS. Hoechst (Thermofisher, H3570) or Draq5 (Abcam, ab108410) were diluted 1:5000 in secondary antibody mix. Samples were then imaged using either the Incell (GE Healthcare) or LSM880 AiryScan Confocal (Zeiss) as appropriate.

2.13.2) Image analysis

Images were analysed using Cell Profiler (Carpenter *et al.*, 2006) using custom made protocols for identification of cells and thresholding against control samples to identify positive signal.

2.14) Antibodies

2.14.1) Primary Antibodies for Immunofluorescence

Target	Manufacturer	Catalogue Number	Reactivity	Dilution
ChAT	Abcam	AB144P	Goat	1:100
Islet1/2	DSHB	39.4D5	Mouse	1:200
Nfh	Abcam	Ab8135	Rabbit	1:500
ATPB	Abcam	Ab128743	Mouse	1:500
TuJ1	Abcam	Ab7807	Mouse	1:500
TuJ1	Biologend	802001	Rabbit	1:1000
Brn3a	Millipore	AB5945	Rabbit	1:200
Peripherin	Abcam	Ab4666	Rabbit	1:1000
Sox10	CST	D5V9L	Rabbit	1:200
Sox9	CST	D8G8H	Rabbit	1:200
HB9	DSHB	81.5C10	Mouse	1:50
Olig2	R&D	AF2418	Goat	1:200
Sox1	R&D	AF3369	Goat	1:100
HoxC9	Abcam	Ab50839	Mouse	1:50
Acetylated Tubulin	Sigma Aldrich	T6793	Mouse	1:5000
Tubulin	CST	2144	Rabbit	1:25
MFN2	CST	D2D10	Rabbit	1:200
FoxP1	R&D	MAB45341-SP	Mouse	1:50

2.14.2) Primary Antibodies for Western Blot

Target	Manufacturer	Catalogue Number	Reactivity	Dilution
Acetylated Tubulin	Sigma Aldrich	T6793	Mouse	1:5000
Tubulin	CST	2144	Rabbit	1:1000

2.14.3) Secondary Antibodies

Target	Manufacturer	Catalogue Number	Dilution
Goat Secondary (594)	Invitrogen	A-11058	1:200
Mouse Secondary (488)	Invitrogen	A-21202	1:200
Rabbit Secondary (647)	Invitrogen	A-31573	1:200
Rabbit Secondary (594)	Invitrogen	A-21207	1:200
Mouse Secondary (800)	ThermoFisher	A32730	1:20000
Rabbit Secondary (680)	ThermoFisher	A32734	1:20000

2.15) Solutions and buffers

2.15.1) Phosphate-buffered saline

10x PBS (Sigma, D1408) was diluted to 1x in ddH₂O. This was autoclaved before use and stored at room temperature.

2.15.2) 4% (w/v) paraformaldehyde

Paraformaldehyde (Sigma, 158127) was mixed with 800ml PBS, stirred and heated to approximately 60°C to aid dissolving. After several hours, the pH was raised through the addition of 5M NaOH until the solution was clear. The pH was corrected to 6.9 using HCl and volume was adjusted to 1L with PBS. The 4% PFA solution was then filtered using a 0.22µm filter (Millipore, S2GPU05RE) before aliquoting and storage at -20°C.

2.15.3) Cell Lysis Solution

Cell lysis solution was used for DNA extractions and made according to the table below. This solution was made and stored at room temperature. Proteinase K was stored independently at -20°C at 20mg/ml and was added to lysis buffer to generate a final of concentration of 400µg/ml on the day of use.

Component	Final Concentration	Manufacturer	Catalogue Reference
SDS	0.5%	Sigma	71729
EDTA pH 8	10mM	ThermoScientific	AM9261
Tris-HCl pH 7.4	10mM	Sigma	93362
NaCl	10mM	Sigma	
dH ₂ O			

2.15.4) Laemilli Buffer

Laemilli buffer was prepared as a 2x stock and stored as 1ml aliquots at -20°C. This buffer was defrosted and diluted to 1x using ddH₂O before use.

Component	Final Concentration	Company	Catalogue Reference
SDS	4%	Sigma	71729
Glycerol	20%	Sigma	G5516
Tris-HCl pH 6.8	125mM	Sigma	93362
Bromphenol Blue	0.004%	Sigma	
ddH ₂ O			

3) Identification of suitable hPSC cell line for CMT2A modelling and optimisation of hPSC differentiation to limb-innervating motor neurons

3.1) Introduction

The accurate study of CMT2A using hPSCs requires the selection of a cell line suitable for modelling. The choice of the cell line is based on several key criteria. Firstly, the hPSC line should be capable of differentiation into the cell types affected by CMT2A, i.e. motor and sensory neurons. As symptoms of CMT2A mainly manifest in the limbs, particularly the legs, generation of the limb subpopulation of motor and sensory neurons is important to accurate modelling of CMT2A. Secondly, the chosen cell line should be karyotypically normal. Finally, prior to editing, the chosen hPSC line should possess a wild-type sequence of *MFN2*.

Identification of a karyotypically normal line is necessary due to the propensity of stem cells to gain small and large genetic aberrations over the course of culture (Baker *et al.*, 2016). These genetic changes can lead to a multitude of effects including changes to growth, apoptosis and differentiation (Fazeli *et al.*, 2011; Baker *et al.*, 2016; Markouli *et al.*, 2019; Price *et al.*, 2019). Ultimately, if an advantage is provided by the mutation the culture can be overtaken by these aberrant lines (Price *et al.*, 2019), making it important to ensure a line is normal before editing and to routinely assess for changes via karyotypic or PCR screening (Laing, Halliwell and Barbaric, 2019). Ensuring that the cell line has normal *MFN2* size and localisation allows confidence that any phenotype seen is caused by intended genetic editing.

It is necessary to assess multiple cell lines for their differentiation capacity as stem cells have been shown to have different propensities to differentiate into particular cell lineages (Osafune *et al.*, 2008; Ramos-Mejia *et al.*, 2010; Wesolowska-Andersen *et al.*, 2020). Whilst CMT2A mutations are not known to affect differentiation capacity (Saporta *et al.*, 2015; Rizzo *et al.*, 2016), it is important to ensure cellular differentiation is robust in any chosen cell line, otherwise there may not be adequate population to examine for a cellular phenotype. Furthermore, if a defect in differentiation is found then subsequently it may be interrogated as a potential phenotype.

Sensory neurons cover a wide range of nerve cells allowing the individual to respond to environmental stimuli such as light, heat or pressure. When these signals may be harmful, sensory neurons, known as nociceptors, signal this as pain which normally serves as a warning. In CMT2A, patients can

experience pain and loss of feeling, indicating the involvement of nociceptors and mechanoreceptors (pressure sensation) making them interesting neuronal subtypes to study. *In vivo*, sensory neurons arise from neural crest, which is specified to the neural plate by opposing gradients of BMP4/WNT from the roof plate and Shh from the floor plate and notochord (reviewed in Stifani, 2014). Neural crest particularly requires a precise interplay of BMP4 agonism and antagonism for production, which has led to wide variability in the efficiency of *in vitro* protocols (Hackland *et al.*, 2017). Neural crest cells are an important source of multiple cell fates, including the enteric nervous and peripheral nervous systems, making it an important target for diseases like Hirschsprung's, which affects gut innervation, as well as sensory neuronal disorders such as CMT (Chambers *et al.*, 2012; T Frith *et al.*, 2018). A previously defined method known as 'top-down inhibition' has been successful at tightly controlling the BMP4 levels through inhibition of BMP type 1 receptor and then saturating the cultures with recombinant BMP4 (Hackland *et al.*, 2017). Use of the top-down inhibition method produces neural crest cultures typified by key neural crest markers such as PAX3, SOX9, SOX10 and P75 (Betters *et al.*, 2010; Hackland *et al.*, 2017). Peripheral sensory neurons can be characterised by the expression of BRN3A, ISLET1 and PERIPHERIN (Chambers *et al.*, 2012). Nociceptors can be identified through the expression of *SCN9A* encoding for sodium channel Na(V)1.7 (Estacion *et al.*, 2009) and *P2X3* (Wang *et al.*, 2018). *In vitro*, nociceptor-like cells can be generated from neural crest through the use of several small molecular inhibitors (Chambers *et al.*, 2012; Hackland *et al.*, 2017).

Motor neurons are involved in relaying signals from the brain to muscle fibres or glands allowing the secretion of hormones or causing contraction of muscle fibres. In CMT2A, skeletal muscle is atrophied and patients can have difficulty moving their limbs due to axonal degradation of the motor neurons innervating the extremities (Reilly *et al.*, 2011). Motor neurons are also specified from the neural plate, but use the opposing gradients of BMP4/WNT and shh to generate five exclusive progenitor domains. The progenitor domains ultimately lead to the production of interneurons and the motor neuron progenitor domain (reviewed in Stifani, 2014). Using knowledge about the combination of *in vivo* signals at play, protocols have been developed producing motor neuron progenitor cells expressing NKX6.1, PAX6 and OLIG2, CHAT, for the production of their neurotransmitter acetylcholine, and ISLET1/2 (reviewed in Davis-Dusenbery *et al.*, 2014). *In vitro*, modulation of BMP4 signalling is usually achieved via ALK inhibition (LDN193189) and often combined with another ALK inhibitor (SB431542) in a method known as dual SMAD inhibition (Chambers *et al.*, 2009). Dual SMAD inhibitors form the basis for many neuronal differentiation protocols (Chambers *et al.*, 2012; Amoroso *et al.*, 2013; Maury *et al.*, 2015; Zeltner *et al.*, 2016) due to their ability to produce high quantities of the immature pan-motor neuron marker, OLIG2 (Mizuguchi *et al.*, 2001). OLIG2 expression leads to the expression of

post-mitotic motor neuron marker, HB9 (reviewed in William, 2003), through activation of pro-neural basic-helix-loop-helix proteins which initiate HB9 transcription (Lee and Pfaff, 2003). HB9 is typically viewed as pan-motor neuron marker and is commonly monitored as a measure of successful motor neuron generation (Amoroso *et al.*, 2013; Kiskinis *et al.*, 2014; Maury *et al.*, 2015). However, HB9 is not present in all motor neuron populations (Amoroso *et al.*, 2013) and may be down-regulated in mature neurons depending on dorsal/ventral limb targeting which can also be identified by the presence of LHX1 (Figure 6) (reviewed in Stifani, 2014). For studies in diseases, such as ALS, where all spinal motor neurons are affected, limb motor neurons are one of the first affected groups of neurons. This indicates that limb motor neurons may have some unique vulnerability (Frey *et al.*, 2000), making them an interesting target for study in multiple neurodegenerative diseases.

Motor neurons are organised into one of five main columns (Figure 6) depending on their function and which muscle group the axons will innervate. The five columns are median motor column (MMC), lateral motor column (LMC), hypaxial motor column (HMC), spinal accessory column (SAC) and the preganglionic column (PGC). Limb innervating motor neurons are found in the LMC, this found in brachial and lumbar sections targeting to the arms and legs, respectively. Brachial neurons are typified by the expression of HOX5-8 and lumbar neurons by the expression of HOX10-12 (Figure 6) (reviewed in Stifani, 2014). LMC motor neurons are specifically characterised by high FOXP1 expression and expression of RALDH2 (Dasen *et al.*, 2008; Rousso *et al.*, 2008). Acquisition of LMC identity is not fully understood but has been linked highly with the Shh signalling gradient as shown in a notable protocol which was successful in producing a large population of FOXP1⁺ neurons (Amoroso *et al.*, 2013). However, production of LMC neurons was unexpected as previous differentiations had resulted in MMC populations as characterised by the presence of LHX3 (Figure 6). Through use of an embryoid body (EB) method and high Shh signalling (with the use of SAG (smoothed receptor agonist) and Purmorphamine), LMC motor neurons were found to be of a primarily brachial rostral identity, as determined by HOX identity (HOX5-8). Despite this, the protocol developed by Amoroso *et al.* only generated ~50% motor neurons with FOXP1⁺ motor neurons taking up only ~68% of that, indicating the need for further optimisation.

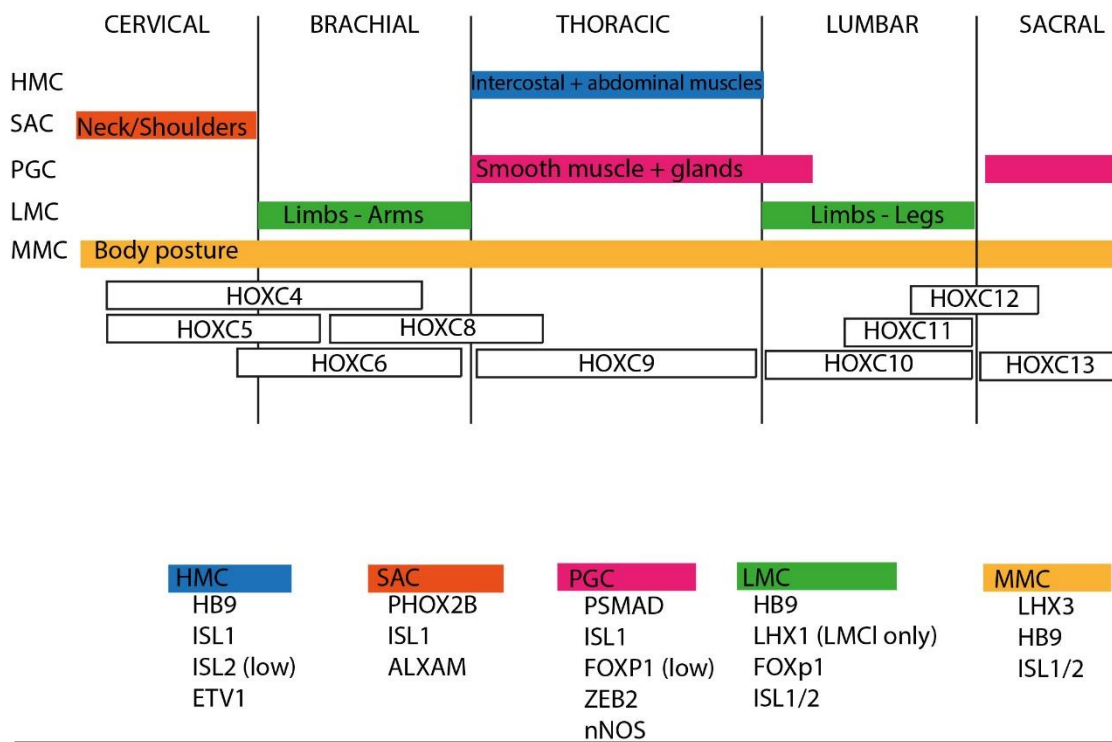


Figure 6: The four main Motor Neuron columns *in vivo* and corresponding axial identity. Motor neurons are organised into four main columns according to their function. The four columns are median motor column (MMC), lateral motor column (LMC), hypaxial motor column (HMC), spinal accessory columns (SAC) and the preganglionic column (PGC). These columns span the anterior-posterior axis of the body and different levels can be identified through the expression of various HOX genes (simplified for this schematic). Below schematic key markers for columnar identification are listed.

Differentiation of stem cells toward neuronal fate is a well-established phenomenon and can be precisely modulated to direct this differentiation to specific neuronal fates. As mentioned, motor neuron differentiation can be successfully achieved via dual SMAD inhibition, however, this typically results in anterior neurons (Chambers *et al.*, 2009) and requires the presence of extraneous factors *In vivo* generation of posterior cell populations is achieved via axial extension by neuromesodermal progenitors (NMPs), a bipotent source of stem cells capable of producing cells from both neural and mesoderm lineages (Gouti *et al.*, 2014). WNT agonism (e.g. via GSK3 inhibition with CHIR9927) shows important roles in the generation of OLIG2⁺ cells (Maury *et al.*, 2015), but has been shown to affect the acquisition of posterior fate (Nordström *et al.*, 2006; Cunningham *et al.*, 2015), which makes it of particular importance for the *in vitro* generation of NMPs and *in vivo* axial extension. NMPs-like cells can be differentiated with the use of FGF and WNT and show expression of HOXC9 (Gouti *et al.*, 2014), a marker of thoracic neurons. Whilst HOXC9 is not an LMC marker, the use of FGF to promote its

expression reveals important insights into the signalling pathways required for axial extension. Indeed, expression of HOX genes occurs in response to the modulation of several interacting signal gradients of which FGF is one (Liu, Laufer and Jessell, 2001; Nordström *et al.*, 2006; Lippmann *et al.*, 2015). Cranial and upper brachial HOX genes respond to increasing levels of RA to produce an increasingly posterior phenotype (HOX1-5). For brachial and thoracic HOX genes RA concentration decreases down the posterior axis and FGF concentration increases (HOX6-9). Finally, for lumbar and sacral regions, FGF concentration continues to increase and GDF11 increases down the posterior axis (HOX10-13) (Liu, Laufer and Jessell, 2001; Nordström *et al.*, 2006; Lippmann *et al.*, 2015). RA also has an important role in arresting the progressive activation of increasingly posterior HOX genes to transition the cells to a fixed rostral-caudal position (Lippmann *et al.*, 2015). This indicates importance not only for the concentration but the timing of RA, a finding recently confirmed for both RA and FGF induction (Mouilleau *et al.*, 2021). *In vivo*, undifferentiated somites along the neural tube express RALDH2 to generate RA and RALDH2 also a marker of limbs during development, underlining RA as a key player in the acquisition of LMC identity (Niederreither *et al.*, 1997; Patani *et al.*, 2011).

It is well understood that HOX genes interact with transcription factors which will determine final motor neuron state. Of particular note is the interaction between HOX genes and FOXP1, where the of ablation HOX genes relevant for LMC production will significantly decrease the amount of LMC motor neurons and FOXP1⁺ cells (Dasen *et al.*, 2008; Rousso *et al.*, 2008). On the other hand, ablation of FOXP1 results in no LMC generation at all and a more randomised targeting of motor neurons and instead produce an increased amount of HMC neurons (Dasen *et al.*, 2008). These findings show that whilst HOX genes are not the only 'gatekeepers' to differentiation they are an important step consideration when generating particular neuronal subtypes.

Choosing a suitable line with the necessary properties to model CMT2A is the essential first step towards generating a model. The following chapter describes the assessment of stem cell lines for further modelling based on their differentiation capability as well as optimisation of protocols to produce both sensory and motor neurons for future modelling of CMT2A.

3.2) Results

3.2.1) Assessment of hPSC cell lines for the capacity to differentiate into motor and sensory neurons

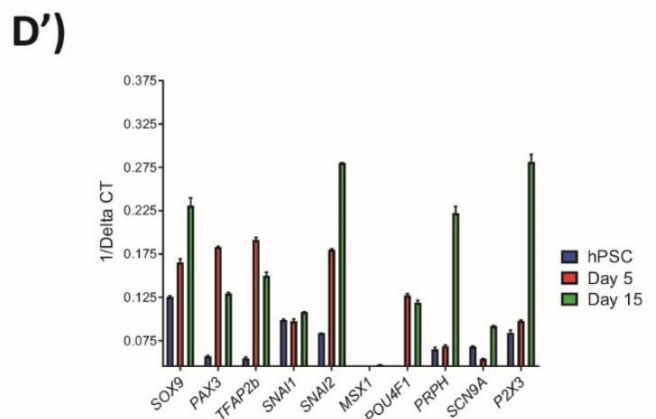
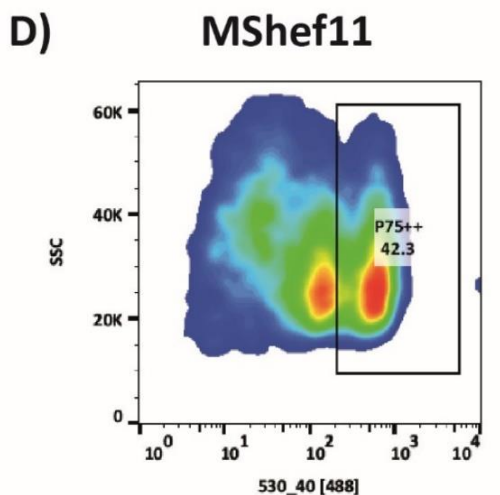
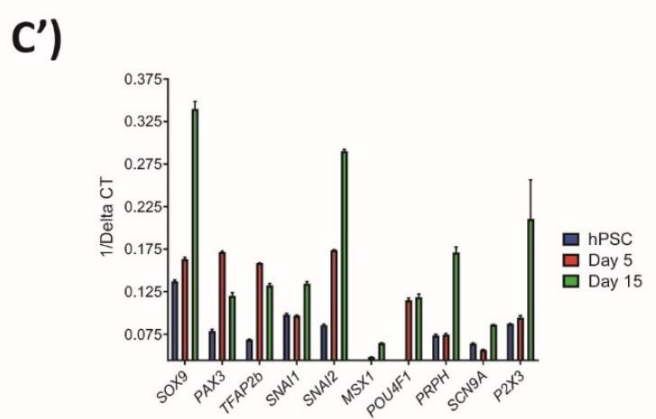
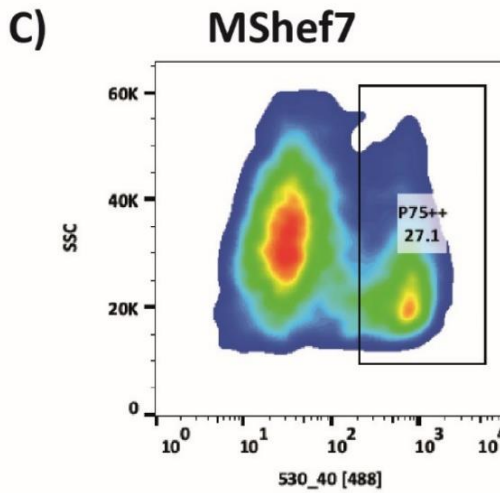
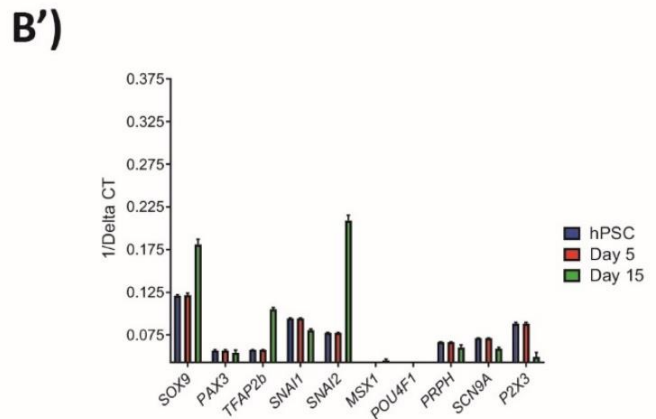
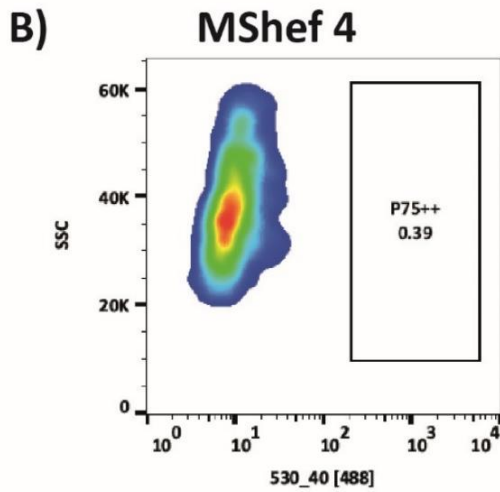
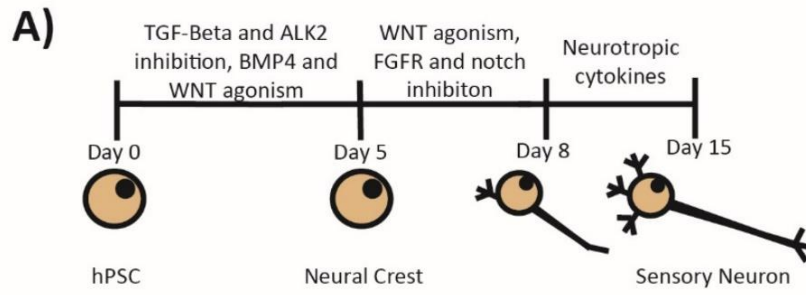
The cell line used to generate a CMT2A model would be required to show the capacity to differentiate into both motor and sensory neurons. Therefore, I chose three different stem cell lines to test, these

were: MShef4, MShef11 and MShef7 (Canham *et al.*, 2015). All three hPSC lines chosen had recently been subject to full genome sequence (Thompson *et al.*, 2020), which could allow me to interrogate the sequences for abnormalities.

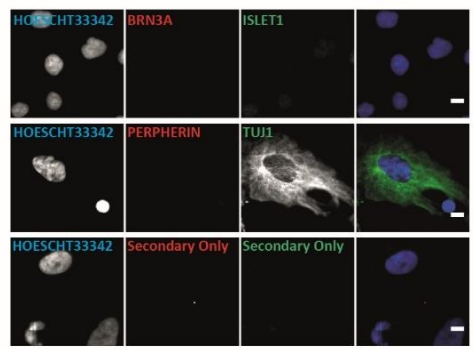
The first differentiation I chose to investigate was of hPSC to sensory neurons as a suitable protocol had already been developed in our laboratory (Hackland *et al.*, 2017; T Frith *et al.*, 2018). CMT2A patients are affected by pain and numbness (reviewed in Saporta *et al.*, 2011), therefore I decided to assess this protocol for nociceptor-like cells markers and compare the cell lines in their efficacy of generating this type of neuron.

Differentiation of sensory neurons involved the generation of neural crest and from this sensory neurons were generated via a previously established protocol (Hackland *et al.*, 2017)(Figure 7A). Cell lines were measured via FACS analysis for the highest expression of P75 (P75⁺⁺) (Betters *et al.*, 2010) at day 5 of differentiation. MShef11 showed the highest P75⁺⁺ population out of the three cell lines at 43.2%, whereas MShef4 and MShef7 showed only 0.39% and 27.1%, respectively (Figure 7B, 7C, 7D). Further analysis of neural crest differentiation was carried out by qPCR expression for relevant markers (*SOX9*, *PAX3*, *TFA2B*, *SNAI1*, *SNAI2*, *MSX1* (Betters *et al.*, 2010; Hackland *et al.*, 2017; T Frith *et al.*, 2018)). All three lines showed upregulation of neural crest markers compared to undifferentiated stem cells (Figure 7B', 7C', 7D'). MShef11 and MShef7 produced significantly more *SOX9* expression than MShef4 (Figure 7E), indicating that MShef11 was able to produce neural crest with higher efficacy than the other two lines. From neural crest, sensory neurons can be produced with the application of WNT, FGF receptor inhibition and Notch inhibition (Chambers *et al.*, 2012). I assessed the sensory neurons on day 15 of differentiation for expression of key sensory neuron markers such as *PRPH* (encoding for PERIPHERIN, only found in nerves of the peripheral nervous system) and *POU4F1* (encoding for BRN3A) (Chambers *et al.*, 2012). Additionally, nociceptor-specific genes were investigated (*SCN9A*, encoding for sodium channel Na(V)1.7 expressed in nociceptors (Estacion *et al.*, 2009), and *P2X3*, a major receptor for nociceptors in the dorsal root ganglia (Wang *et al.*, 2018)). MShef11 and MShef7 both showed strong upregulation of sensory neuron and nociceptor markers (Figure 7C', 7D'), whereas MShef4 did not (Figure 7B'), further indicating a defect in differentiation for this cell line. The expression of nociceptor markers indicates there may be some nociceptor-like cells present in the differentiation. Expression of *PRPH* (Figure 7F) and *POU4F1* (Figure 7G) were significantly higher in both MShef7 and MShef11 than MShef4. MShef11 expression of *PRPH* was also found to be significantly higher than MShef7, further suggesting MShef11 may be more capable of producing sensory neurons than the other cell lines. Immunofluorescence was used to

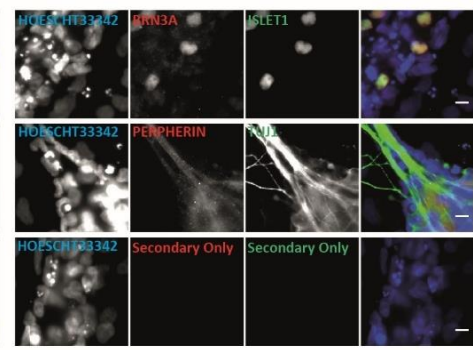
confirm protein expression of key sensory neuron markers BRN3A and PERIPHERIN. Additionally, ISLET1 was co-stained with BRN3A as this co-expression is a key marker of sensory neurons (Chambers *et al.*, 2012) and axonal marker TUJ1 was checked to indicate the presence of axons not stained via PERIPHERIN. MShef7 and MShef11 both successfully whereas MShef4 did not (Figure 7B''). MShef11 produced significantly more BRN3A⁺ and ISLET⁺ cells than the other cell lines (Figure 7H, 2H') and showed clear expression of PERIPHERIN within the axons (Figure 7D''). Taken together these data suggest that MShef11 was the most capable of successfully producing sensory neurons based on the highest expression of relevant neural crest and sensory neuron markers.



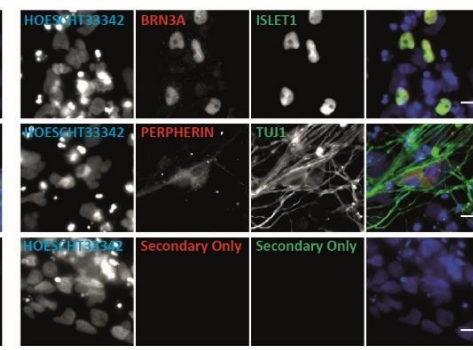
B'') MShef4



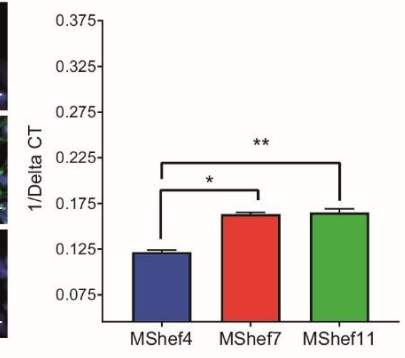
C'') MShef7



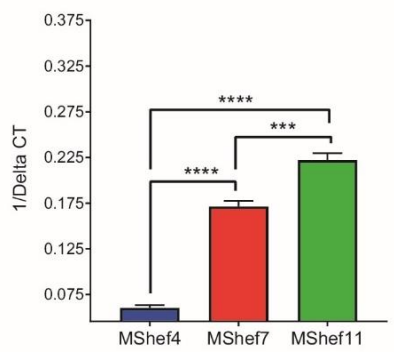
D'') MShef11



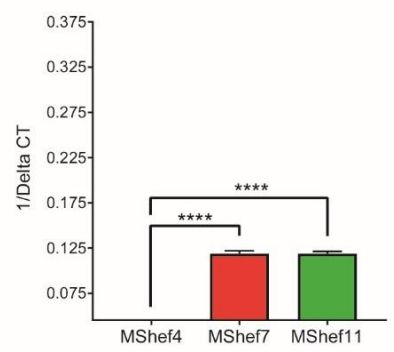
E)



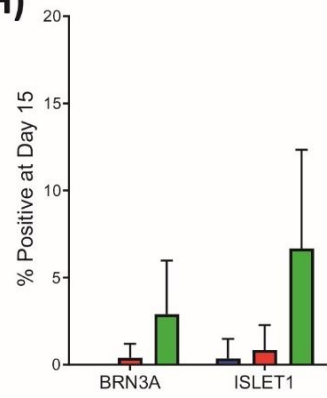
F)



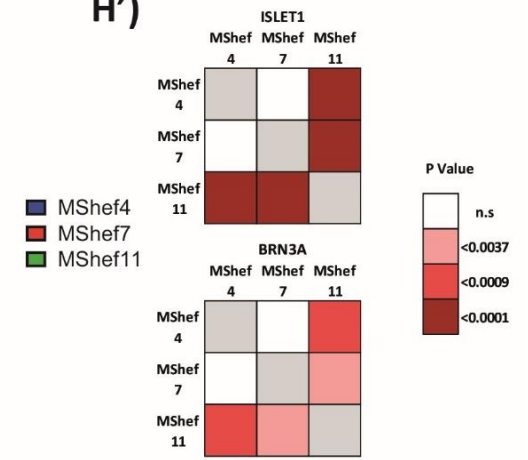
G)



H)

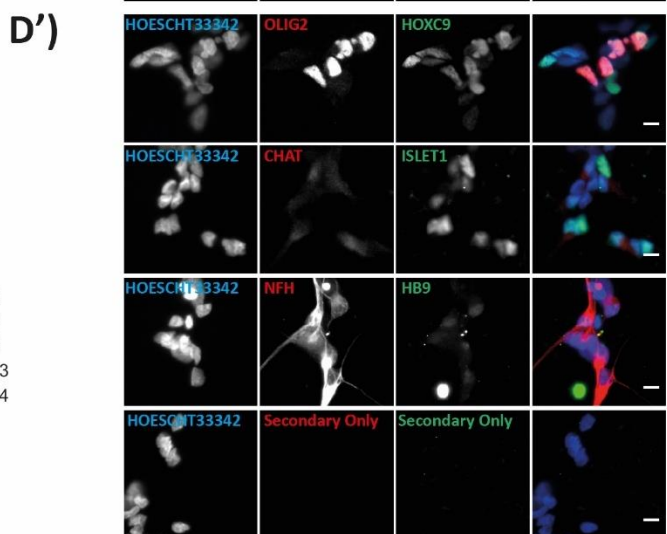
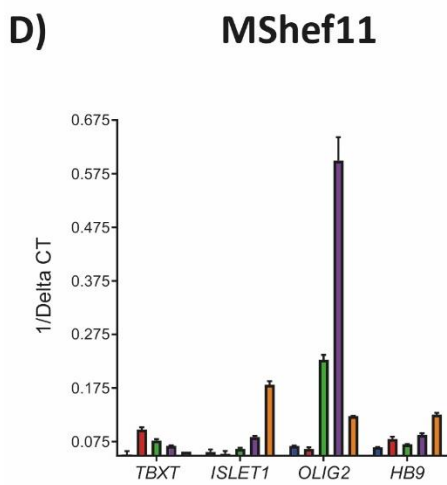
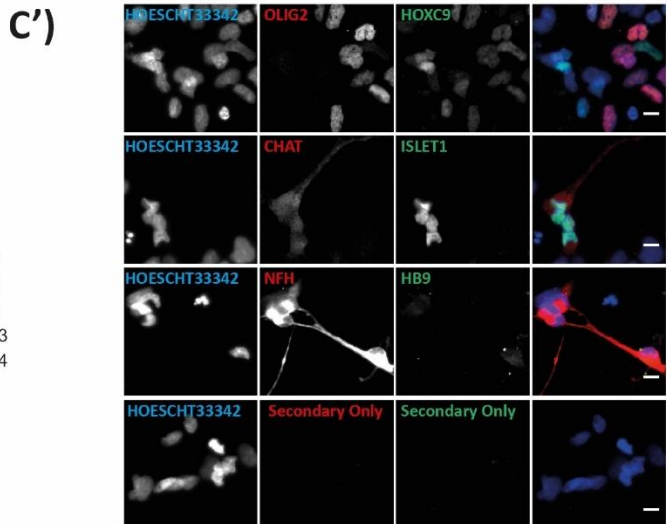
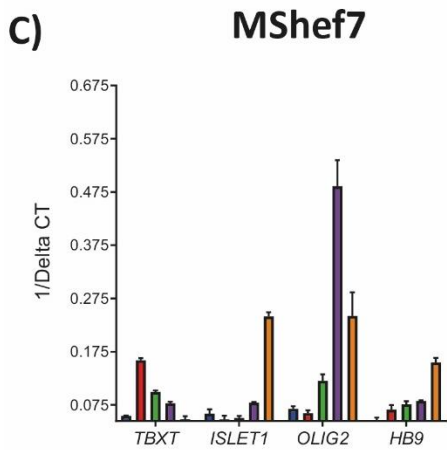
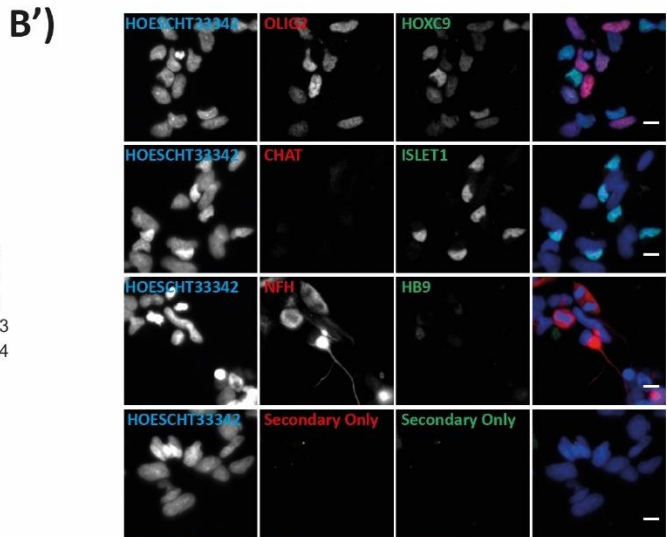
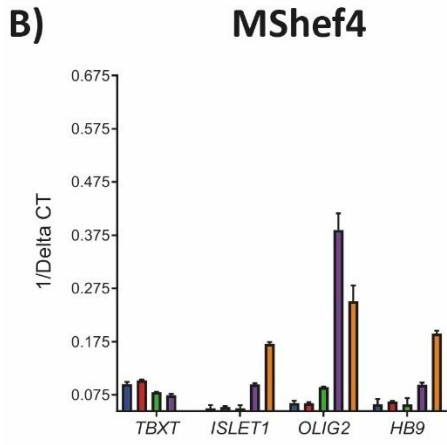
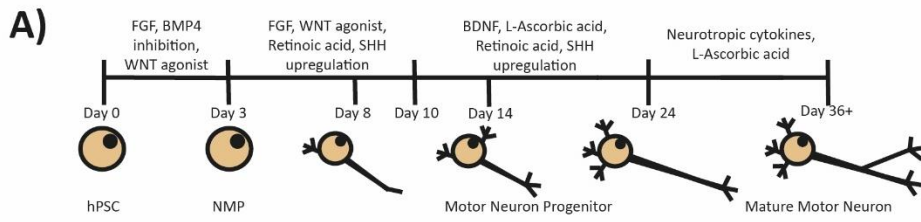


H')



(Previous pages) Figure 7: Assessment of hPSC lines differentiation to neural crest and sensory neurons. **A)** Differentiation of hPSC to sensory neurons through neural crest. Protocol from (Hackland *et al.*, 2017; T. Frith *et al.*, 2018). **B)** FACS plot for Mshf4 at day 5 of differentiation. Boxed area represents P75++ population which is the population of putative neural crest cells. **B')** Expression of neural crest markers (*SOX9*, *PAX3*, *TFAP2b*, *SNAI1* *SNAI2*, *MSX1*), sensory neuron marker (*POU4F1* which encodes for BRN3A), peripheral nervous system axonal marker (*PRPH* which encodes for PERIPHERIN) and nociceptor markers (*SCN9A*, *P2X3*) over the course of differentiation for MShf4 cells. Data shown are the mean \pm SD N = 3 technical repeats. **B'')** Staining of sensory neuron markers (BRN3A, ISLET1), peripheral nervous system axonal marker (PERIPHERIN) and axonal marker (TUJ1) for MShf4 cells at day 15 of the differentiation protocol. Nuclei are counterstained with Hoechst33342. Scale bar: 10 μ m. **C)** Fluorescence intensity for MShf7 at day 5 of differentiation. Boxed area represents P75++ population which is the population of putative neural crest cells. **C')** Expression of neural crest markers (*SOX9*, *PAX3*, *TFAP2b*, *SNAI1* *SNAI2*, *MSX1*), sensory neuron marker (*POU4F1* which encodes for BRN3A), peripheral nervous system axonal marker (*PRPH* which encodes for PERIPHERIN) and nociceptor markers (*SCN9A*, *P2X3*) over the course of differentiation for MShf7 cells. Data shown are the mean \pm SD N = 3 technical repeats. **C'')** Staining of sensory neuron markers (BRN3A, ISLET1), peripheral nervous system axonal marker (PERIPHERIN) and axonal marker (TUJ1) for MShf7 cells at day 15 of the differentiation protocol. Nuclei are counterstained with Hoechst33343. Scale bar: 10 μ m. **D)** Fluorescence intensity for MShf11 at day 5 of differentiation. Boxed area represents P75++ population which is the population of putative neural crest cells. **D')** Expression of neural crest markers (*SOX9*, *PAX3*, *TFAP2b*, *SNAI1* *SNAI2*, *MSX1*), sensory neuron marker (*POU4F1* which encodes for BRN3A), peripheral nervous system axonal marker (*PRPH* which encodes for PERIPHERIN) and nociceptor markers (*SCN9A*, *P2X3*) over the course of differentiation for MShf11 cells. Data shown are the mean \pm SD N = 3 technical repeats. **D'')** Staining of sensory neuron markers (BRN3A, ISLET1), peripheral nervous system axonal marker (PERIPHERIN) and axonal marker (TUJ1) for MShf11 cells at day 15 of the differentiation protocol. Nuclei are counterstained with Hoechst33343. Scale bar: 10 μ m. **E)** Comparison of expression of *SOX9* between cell lines at day 5 of differentiation. Data shown are the mean \pm SD N = 3 technical repeats. **F)** Comparison of expression of *PRPH* between cell lines at day 15 of differentiation. Data shown are the mean \pm SD N = 3 technical repeats. **G)** Comparison of expression of *POU4F1* between cell lines at day 15 of differentiation. Data shown are the mean \pm SD N = 3 technical repeats. **H)** Summary of image analysis at day 15 of differentiation for sensory neuron markers (BRN3A, ISLET1) of MShf4, MShf7 and MShf11. Data shown are the mean \pm SD N = 3 technical repeats. **H')** Statistical analysis of H.

After assessment of the sensory neuron differentiation, I investigated the capacity of the cell lines to differentiate into the predominantly affected cell type found in CMT2A which are motor neurons. For this, I utilised another protocol under development in our laboratory which required differentiation into NMP-like cells through the addition of FGF, BMP4 inhibition and WNT agonism before the addition of RA and ventralisation using Shh upregulation (Figure 8A). Motor neuron progenitors were then maintained with the addition of L-Ascorbic acid and neurotrophic cytokines until maturation. Differentiation efficacy was assessed via gene expression analysis at key time points (day 3 (NMP-like stage), day 8 (neural progenitor), day 13 (motor neuron progenitor), day 24 (mature motor neuron)) for markers relevant to NMP (*TBXT* – encoding for BRACHYURY an NMP marker (Gouti *et al.*, 2014)) and motor neurons (*ISLET1*, *OLIG2*, *HB9* (reviewed in Stifani, 2014)). MShef7 and MShef11 showed an increase in expression of *TBXT* at day 3 which then decreased over the rest of the differentiation, indicating the upregulation of NMP genes before onset to further specification (Figure 8C, 8D). MShef4 did not appear to upregulate *TBXT* as this was already comparatively highly expressed in the undifferentiated hPSC (Figure 8B). All of the hPSC lines upregulated *ISLET1*, *OLIG2* and *HB9* by day 13, indicating the presence of motor neurons in culture. MShef11 expressed significantly more *OLIG2* (Figure 8E) than the other lines at day 13 suggesting the strongest motor neuron induction. However, MShef11 expressed significantly less *HB9* than the other lines on day 24 with MShef4 expressing the highest amount of *HB9* (Figure 8F). Protein expression was assessed at day 24 of differentiation by immunofluorescence for *OLIG2*, *CHAT*, *ISLET1*, *HB9*, *HOXC9* and axonal marker, neurofilament heavy chain (NFH). As NMP-like cells were used as a basis for the protocol, I believed it necessary to assess for *HOX* genes of thoracic identity (such as *HOXC9*) as previous work in our laboratory had indicated the NMPs would be thoracic. All lines showed expression of *HOXC9* (Figure 8B, 8C, 8D, 8G, 8G') (MShef4: 48% (± 16), MShef7: 74% (± 18), MShef11: 71% (± 17)), with MShef7 and MShef11 expressing significantly more *HOXC9* than MShef4, indicating these cells had a thoracic identity and that this protocol would require further optimisation to result in neurons with an LMC identity. All lines also showed expression of *OLIG2*, an immature motor neuron marker, (MShef4: 21% (± 16), MShef7: 14% (± 9), MShef11: 11% (± 10)) (Figure 8B, 8C, 8D, 8G, 8G'). For neurons to still be showing an immature marker at day 24 of the protocol could suggest a failure for the motor neurons to mature. Neuronal immaturity was further indicated by the overall low expression of *HB9* (MShef4: 2% (± 2), MShef7: 10% (± 12), MShef11: 5% (± 12)) and *ISLET1* (MShef4: 23% (± 12), MShef7: 32 (± 10), MShef11: 27 (± 10)). Expression of neurotransmitter enzyme *CHAT* was low for all lines (MShef4: 0% (± 0), MShef7: 18% (± 9), MShef11: 9% (± 9)), with MShef7 producing significantly more than MShef4.



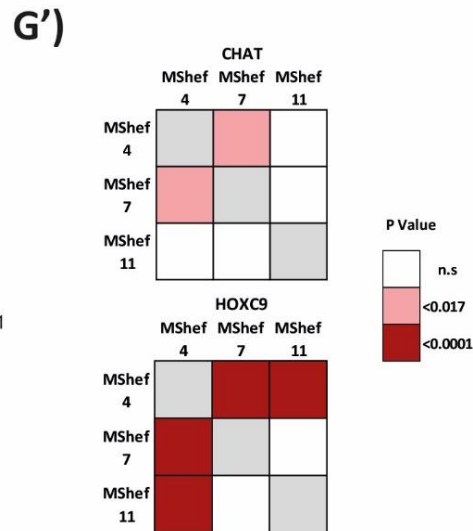
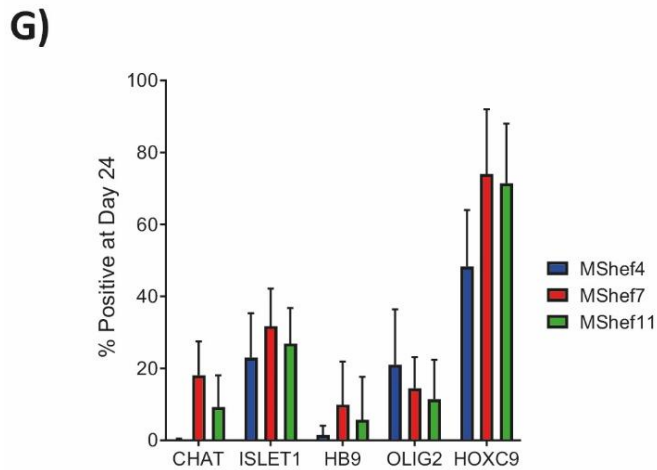
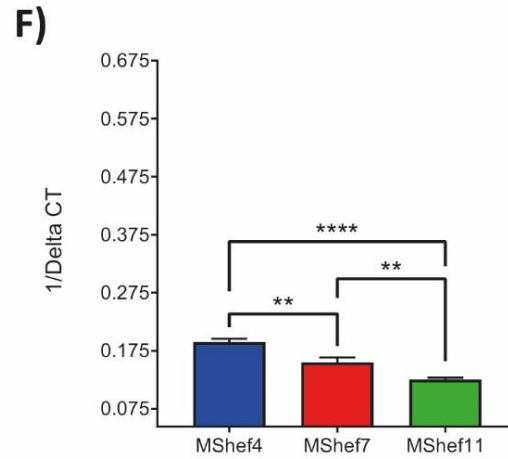
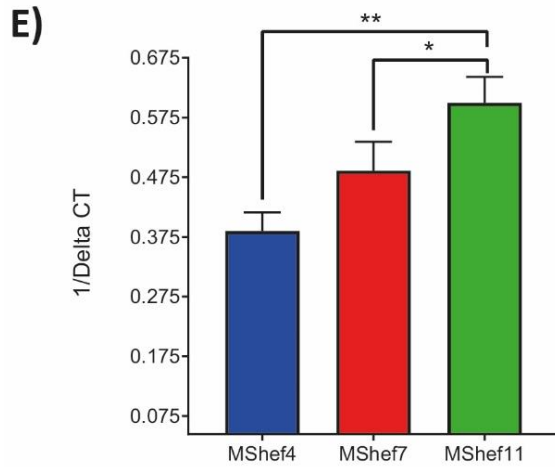


Figure 8: Assessment of hPSC lines differentiation to motor neurons. **A)** Protocol for differentiation of hPSC to motor neurons. **B)** qPCR showing expression of NMP marker (*TBXT* which encodes for BRACHYURY), early motor neuron marker (*OLIG2*), motor neuron marker (*ISLET1*) and post-mitotic marker (*HB9*) over the course of differentiation for MShef4 cells. Data shown are the mean \pm SD N = 3 technical repeats. **B')** Staining of early motor neuron marker (OLIG2), postmitotic motor neuron marker (HB9), motor neuron neurotransmitter (CHAT), motor neuron marker (ISLET1), axonal marker (NFH) and trunk positional marker (HOXC9) for MShef4 cells at day 24 of the differentiation protocol. Nuclei are counterstained with Hoechst33343. Scale bar: 10 μ m. **C)** Expression of NMP marker (*TBXT* which encodes for BRACHYURY), early motor neuron marker (*OLIG2*), motor neuron marker (*ISLET1*) and post-mitotic marker (*HB9*) over the course of differentiation for MShef7 cells. Data shown are the mean \pm SD N = 3 technical repeats. **C')** Staining of early motor neuron marker (OLIG2), postmitotic motor neuron marker (HB9), motor neuron neurotransmitter (CHAT), motor neuron marker (ISLET1), axonal marker (NFH) and ...

...**Cont.** trunk positional marker (*HOXC9*) for MShef7 cells at day 24 of the differentiation protocol. Nuclei are counterstained with Hoechst33343. Scale bar: 10 μ m. **D)** Expression of NMP marker (*TBXT* which encodes for BRACHYURY), early motor neuron marker (*OLIG2*), motor neuron marker (*ISLET1*) and post-mitotic marker (*HB9*) over the course of differentiation for MShef11 cells. Data shown are the mean \pm SD N = 3 technical repeats. **D')** Staining of early motor neuron marker (*OLIG2*), postmitotic motor neuron marker (*HB9*), motor neuron neurotransmitter (*CHAT*), motor neuron marker (*ISLET1*), axonal marker (*NFH*) and trunk positional marker (*HOXC9*) for MShef11 cells at day 24 of the differentiation protocol. Nuclei are counterstained with Hoechst33343. Scale bar: 10 μ m. **E)** Comparison of expression of *OLIG2* between cell lines at day 13 of differentiation. Data shown are the mean \pm SD N = 3 technical repeats. **F)** Comparison of expression of *HB9* between cell lines at day 24 of differentiation. Data shown are the mean \pm SD N = 3 technical repeats. **G)** Summary of image analysis at day 24 of differentiation for early (*OLIG2*) and post-mitotic (*HB9*) motor neuron markers, motor neuron neurotransmitter (*CHAT*), motor neuron marker (*ISLET1*) and trunk positional marker (*HOXC9*) of MShef4, MShef7 and MShef11. Data shown are the mean \pm SD N = 3 technical repeats. **G')** Statistical analysis of G.

Overall, MShef4 did not produce motor neurons in this protocol as shown by a failure to generate any *CHAT*⁺ cells, whereas MShef7 and MShef11 both produced cells with were *CHAT*⁺, *ISLET*⁺ or *OLIG2*⁺, suggesting they were both able to differentiate into motor neurons.

Upon review of the cell lines capability to differentiate into both motor and sensory neurons, I chose to prioritise MShef11 due to it having the strongest performance in the sensory neuron protocol and performing comparably to MShef7 in the motor neuron protocol. MShef11 did produce less *HB9* expression when comparing with MShef7, indicating there may be a specific bias in this line towards a particular type of motor neuron which was not *HB9*⁺. However, as not all LMC motor neurons express *HB9*, I decided that MShef11 was a suitable line to proceed with. Additionally, the protocol itself produced a low amount of *CHAT*⁺ cells and would, therefore, require further optimisation to increase motor neuron specification and maturation.

In summary, of the cell lines examined, MShef11 possessed the greatest efficacy in differentiating to both motor and sensory neurons. Therefore, my results showed that MShef11 was an appropriate cell line for use in further differentiation optimisation and ultimately in CMT2A modelling.

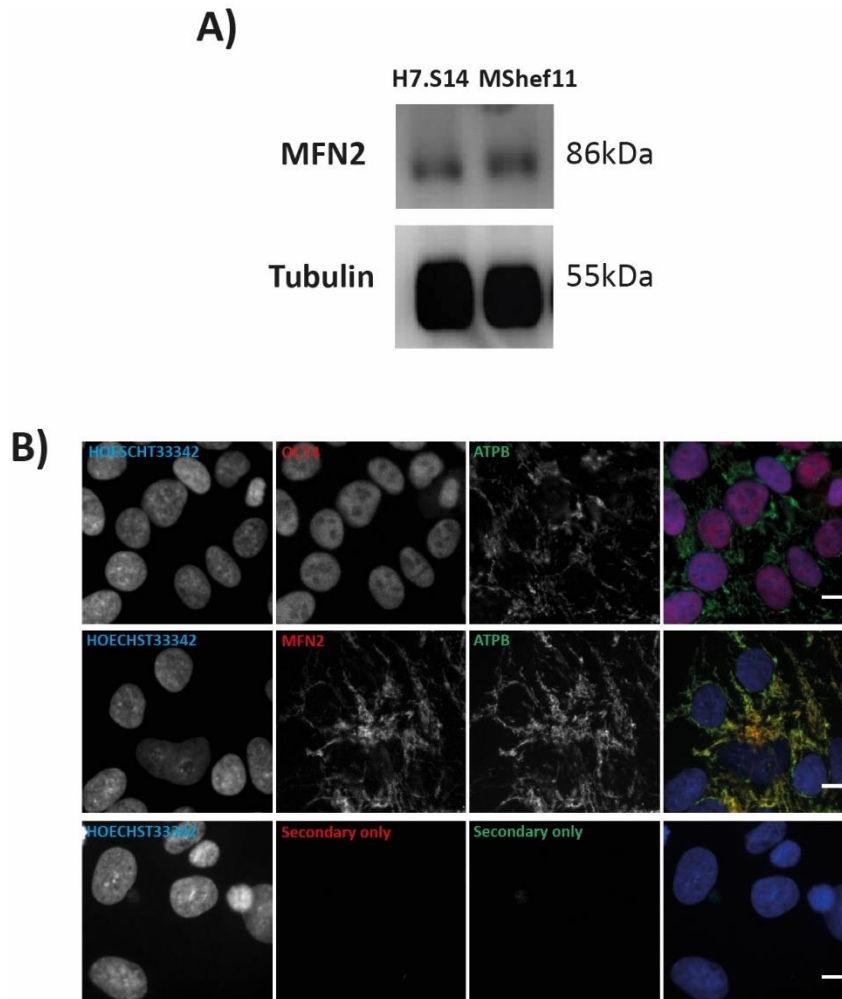


Figure 9: Assessment of MFN2 size and localisation in MShef11. A) Western blot of MFN2 in MShef11 alongside another hPSC line H7S14. B) Staining of mitochondrial markers (ATPB, MFN2) stem cell marker (OCT4) to identify undifferentiated cells. Nuclei are counterstained with Hoechst33343. Scale bar: 10µm

3.2.2) Assessment of MShef11 karyotype and MFN2 localisation

Stem cells can gain genetic aberrations during the course of normal passaging and culture which can lead to alterations to growth, apoptosis and differentiation (Baker *et al.*, 2016; Markouli *et al.*, 2019; Price *et al.*, 2019). MShef11 was karyotypically assessed and found to be normal and was routinely monitored throughout culture in order to confirm this did not change (data not shown).

Before the introduction of mutations to MFN2 capable of modelling CMT2A, it was necessary to confirm that MFN2 was of the expected size of 86kDa and had a mitochondrial localisation in MShef11. MFN2 size was examined using Western Blotting and compared to a subclone of H7 (Thomson *et al.*, 1998), known as H7.s14 (Harrison *et al.*, 2009). MFN2 size in MShef11 was found to be comparable to H7.s14 (Figure 9A). The localisation of MFN2 was examined through immunofluorescence and

comparing localisation of ATPB, a subunit of ATP synthase. Simultaneously, MShef11 was examined for expression of undifferentiated stem cell marker OCT4 (Mouilleau *et al.*, 2021) to ensure that identified cells investigated had an undifferentiated identity. MShef11 hPSC were found to express OCT4 (Figure 9B) and MFN2 appeared to co-localise with ATPB, suggesting undifferentiated MShef11 possessed MFN2 localised to the mitochondria.

In summary, of the cell lines examined, MShef11 possessed the greatest efficacy in differentiating to both motor and sensory neurons, expressed MFN2 of the correct size and localisation and was found to be karyotypically normal. Therefore, my results showed that MShef11 was an appropriate cell line for use in further differentiation optimisation and ultimately in CMT2A modelling.

3.2.3) Assessment of BMP4 and Notch inhibition on motor neuron differentiation efficacy

My previous data (Figure 8) had shown persistence of OLIG2⁺ cells late in the differentiation and a lack of mature marker HB9 in both protein and expression, meaning the neurons may be immature. Notch inhibition has been shown to cause maturity of all neuronal subtypes (Maury *et al.*, 2015) and therefore I decided to test the effect of Notch inhibition (RO4929097) on this protocol to achieve a more mature phenotype during the later stages of the protocol. Additionally, the cultures generated contained many non-neuronal cell types (Figure 8) which indicated a lack of specification to the neural plate. Motor neuron development *in vivo* is dependent on BMP4 and Shh signalling gradients which lead to the generation of the five neuron progenitor domains (reviewed in Stifani, 2014). As Shh was already highly upregulated by both SAG and Purmorphamine in this protocol, I decided to focus on the BMP4 inhibition (using LDN193189). I postulated that lengthening the presence of LDN193189 until day 14 of differentiation would increase the specification of motor neurons as shown by OLIG2 expression. LDN193189 and RO4929097 were tested alone and in combination during the protocol (Figure 10A, 10B). The efficacy of the first stage of differentiation to NMP-like cells was assessed at day 3 using immunofluorescence for key NMP markers, SOX2 and BRACHYURY (Gouti *et al.*, 2014). MShef11 produced a highly SOX2⁺ culture (99% (± 1)), however, BRACHYURY was notably weak, being detected in less than 1% of cells (Figure 11A). To confirm the onset of relevant markers, I measured the gene expression on day 3 of *TBXT* and Brachial/Thoracic HOX genes (*HOXC6-HOXC9*). Expression of *TBXT* was significantly upregulated compared to hPSC (Figure 11B), suggesting mesoderm genes were successfully upregulated as part of differentiation. Whilst upregulation of mesoderm genes is not necessary for neural differentiation, it does indicate the presence of NMPs due to their bi-potent capacity. Gene expression analysis by qPCR showed significant upregulation of both *HOXC8* and *HOXC9* compared to hPSC, suggesting the NMPs may be predominantly a thoracic population.

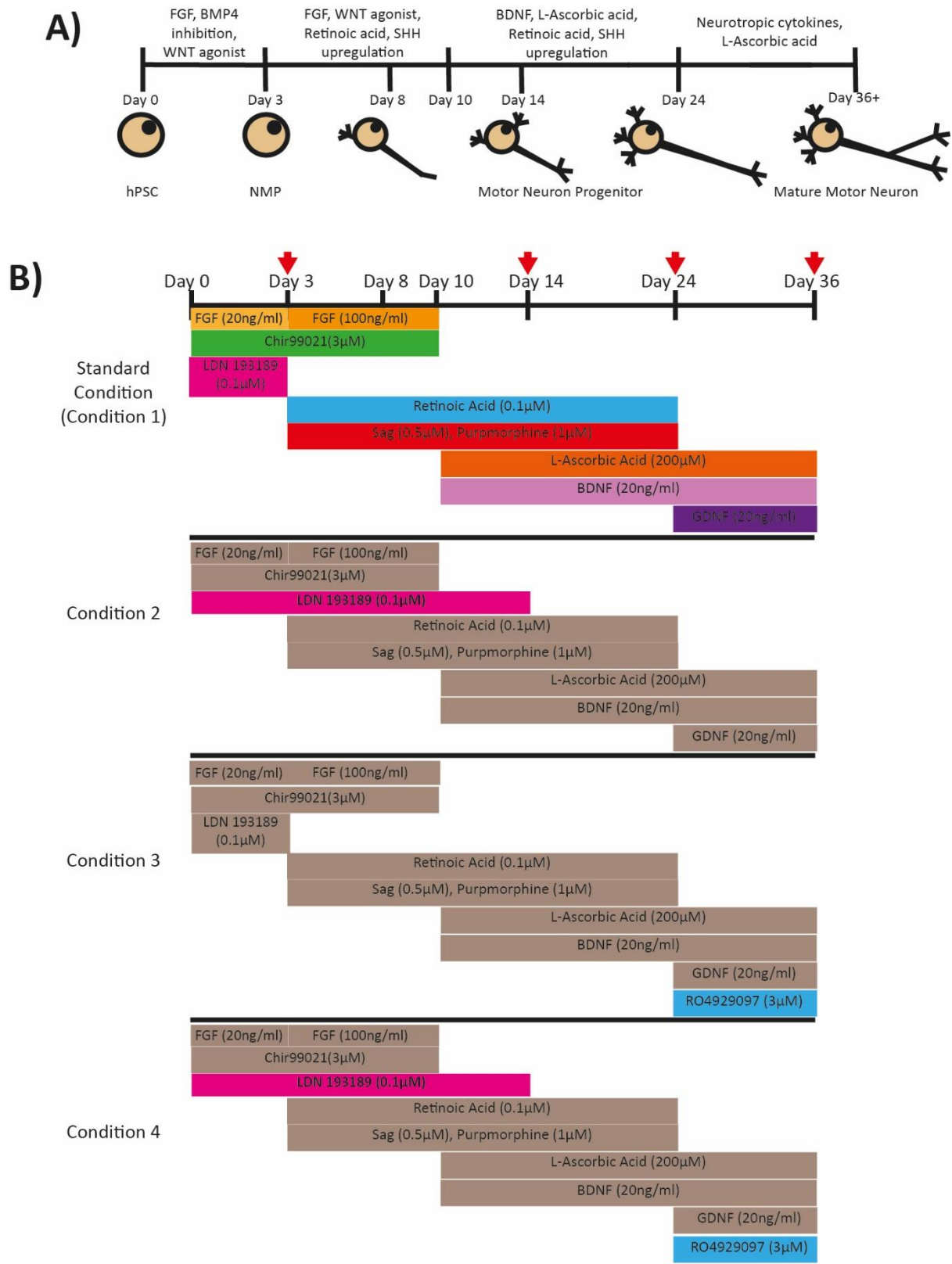


Figure 10: Experimental plan for assessing increased BMP4 and notch inhibition on motor neuron differentiation efficacy. A) Differentiation of hPSC into motor neurons. B) Conditions tested in comparison to the standard protocol. Cells were taken for analysis at time points indicated by the arrows.

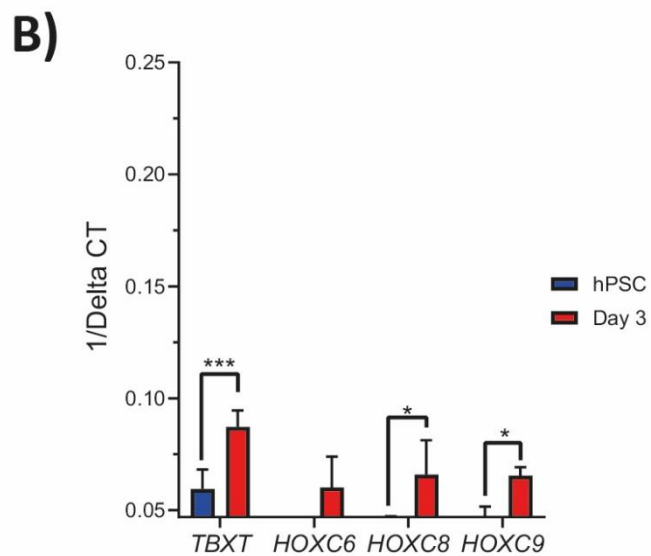
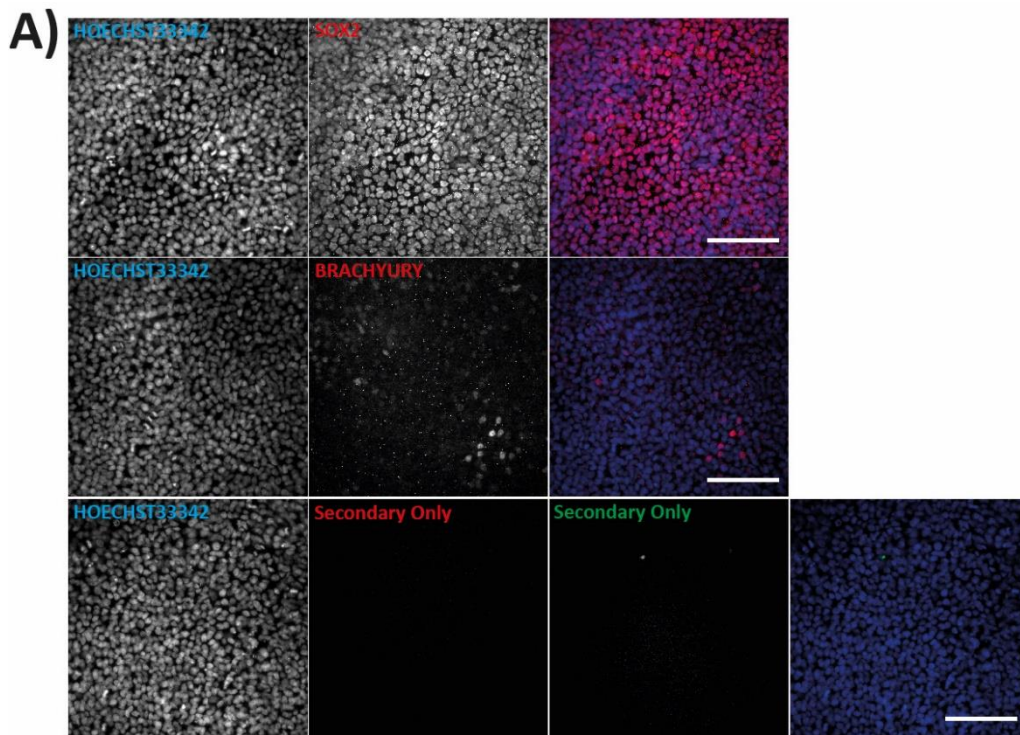


Figure 11: NMP Assessment of the production of NMP-like cells differentiation. A) Staining of markers of NMP (BRACHYURY, SOX2) and trunk positional marker (HOXC9) at day 3 of the differentiation protocol. Nuclei are counterstained with Hoechst33343. Scale bar: 100µm. **B)** Expression of *BRACHYURY* and *HOXC9* compared to hPSC at day 3 of differentiation. Data shown are the mean \pm SD N = 4 biological repeats. (** - $P \leq 0.01$, *** - $P \leq 0.001$, 2-way ANOVA)

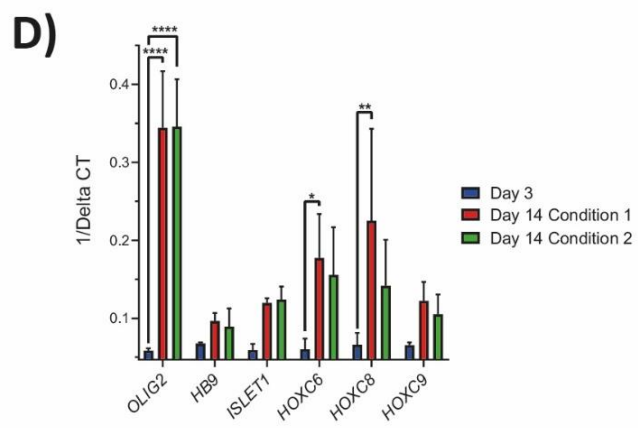
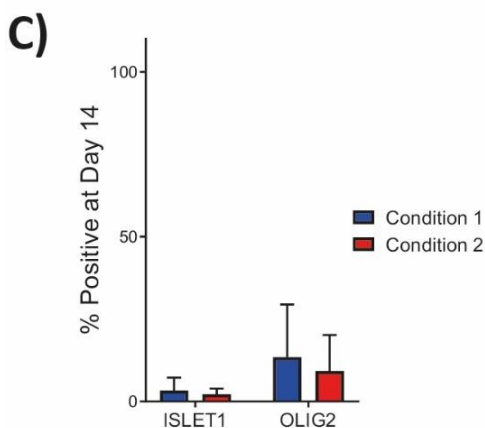
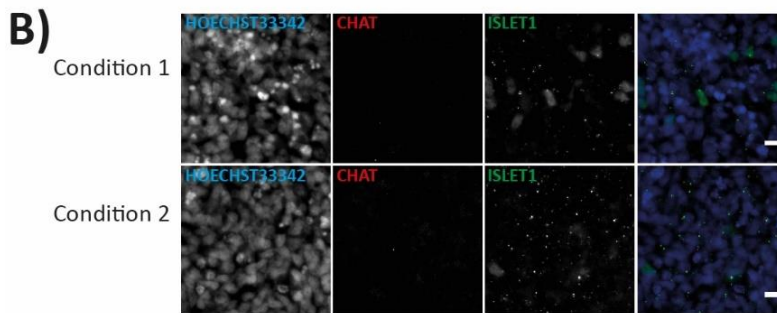
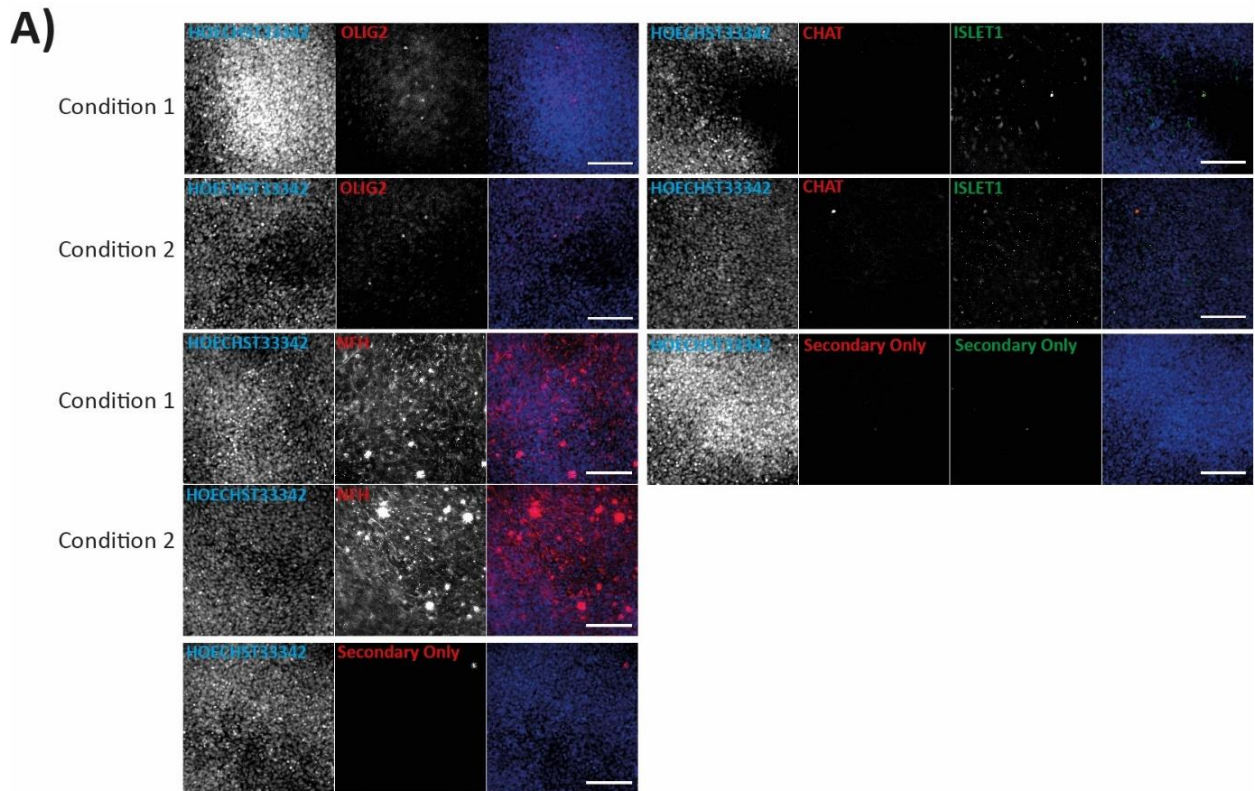


Figure 12: Assessment of increased BMP4 and notch inhibition on the production of day 14 motor neuron progenitors. A) Staining of early motor neuron marker (OLIG2), motor neuron neurotransmitter (CHAT), motor neuron marker (ISLET1), axonal marker (NFH) and trunk positional marker (HOXC9) at day 14 of the differentiation protocol. Nuclei are counterstained with Hoechst33343. Representative images are shown for each condition. Scale bar: 100µm. ...

...**Cont.** . **B)** Enlarged section of staining for CHAT and ISLET at day 14 of the differentiation protocol. Nuclei are counterstained with Hoechst33343. Scale bar: 10 μ m **C)** Summary of image analysis of HOXC9 and ISLET1 staining at day 14 of differentiation. Data shown are the mean \pm SD N = 4 biological repeats. **D)** Expression of motor neuron markers (*OLIG2*, *HB9*, *ISLET1*) and trunk positional marker (*HOXC9*) comparing the two conditions at day 14 of differentiation. Data shown are the mean \pm SD N = 4 biological repeats.

Condition 1 carried out the motor neuron differentiation as seen previously (section 3.2.1), whereas condition continued BMP4 inhibition until day 14 when the cells should have characteristics of motor neuron progenitors. Cells were assessed via immunofluorescence for expression of immature marker OLIG2, the presence of CHAT, ISLET and NFH. Both condition 1 and 2 produced a similar amount of OLIG2⁺ (condition 1: 27% (\pm 5), condition 2: 18 (\pm 3)) and ISLET⁺ (condition 1: 3% (\pm 3), condition 2: 2 (\pm 1)) cells (Figure 12A, 12C) with no significant differences between them. No CHAT expression was detected in either culture at day 14 (Figure 12B). In order to investigate the onset of differentiation further, I measured gene expression on day 14, examining *OLIG2*, *HB9*, *ISLET* and Brachial/Thoracic HOX genes (*HOXC6-HOXC9*). *OLIG2* expression was significantly higher compared with day 3 of differentiation, though there was no difference between the conditions (Figure 12D), indicating LDN193189 extension of the protocol had not increased specification to the motor neuron progenitor state. Expression of HB9 and ISLET1 was not significantly upregulated in either condition compared with day 3, further supporting that the neurons were still immature. Unexpectedly, expression of *HOXC6* and *HOXC8* were significantly increased in condition 1 compared with day 3. This data may indicate that condition 1 was more adept at generating brachial motor neurons than condition 2, but would require further investigation to be sure as the two conditions were not significantly different.

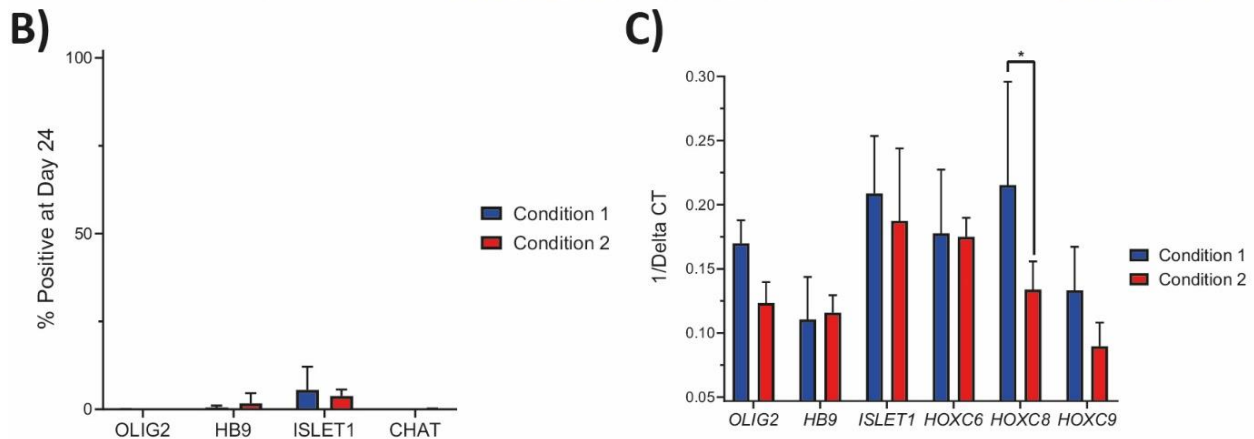
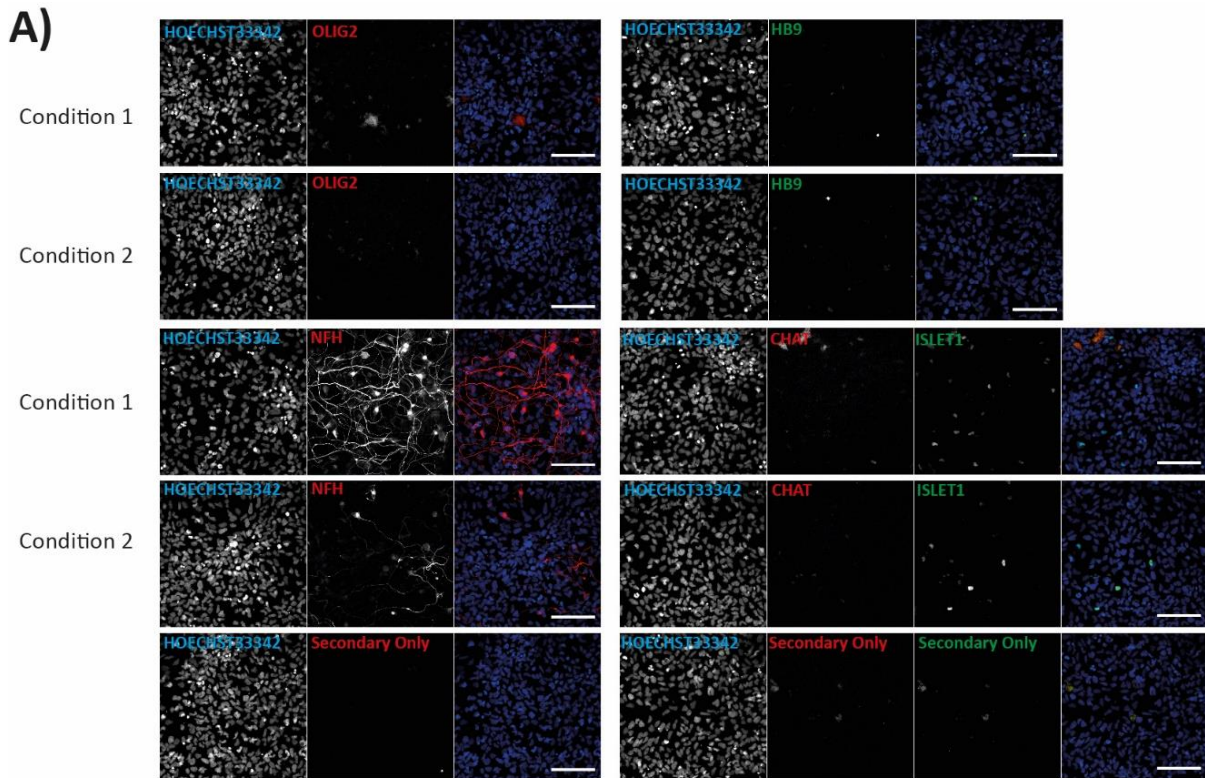
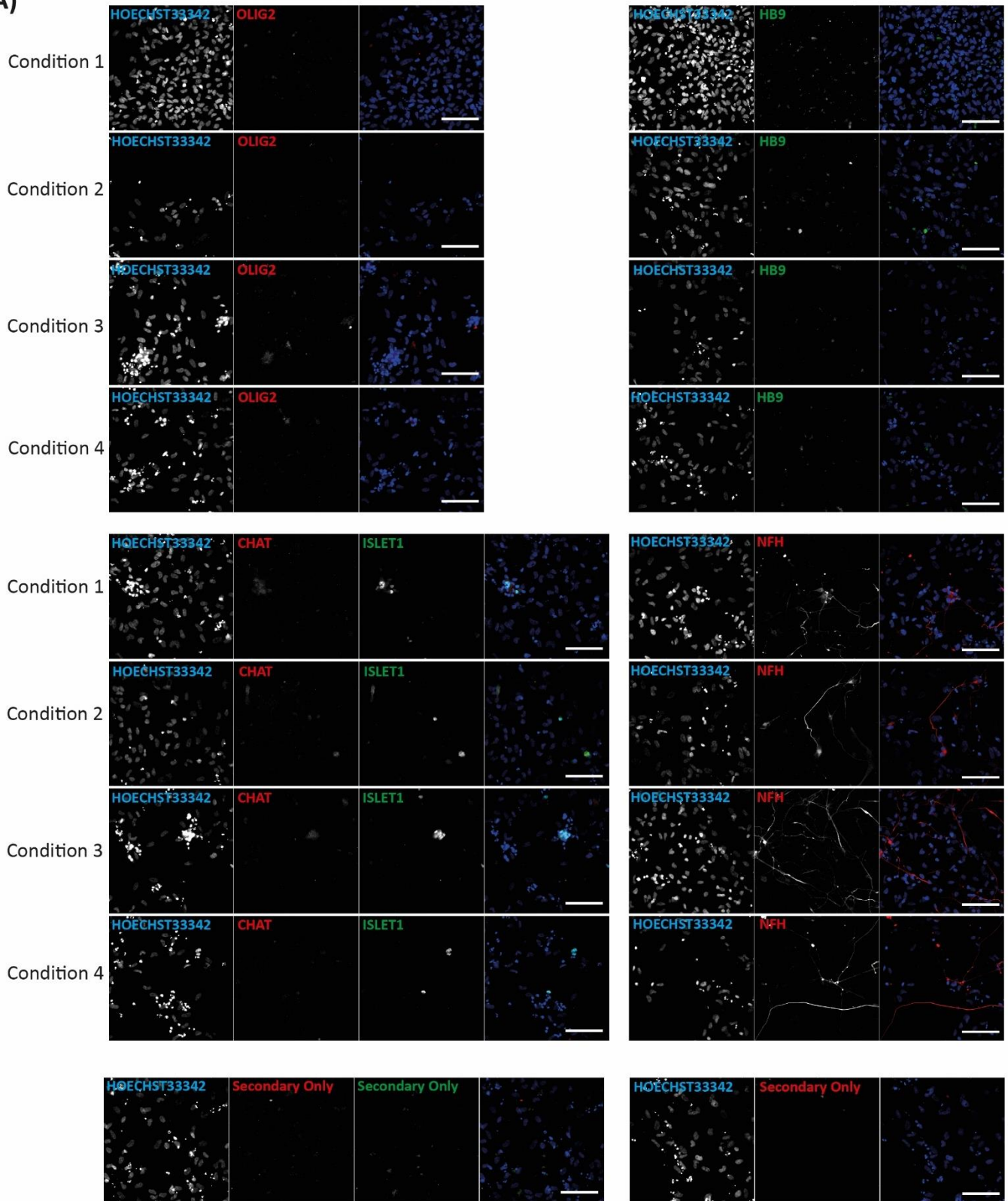


Figure 13: Assessment of increased BMP4 and notch inhibition on the production of day 24 immature motor neuron A) Staining of early motor neuron marker (OLIG2), postmitotic motor neuron marker (HB9), motor neuron neurotransmitter (CHAT), motor neuron marker (ISLET1), axonal marker (NFH) and trunk positional marker (HOXC9) at day 24 of the differentiation protocol. Representative images are shown for each condition. Nuclei are counterstained with Hoechst33343. Scale bar: 100 μ m. **B)** Summary of image analysis of OLIG2, HB9, ISLET1 and HOXC9 staining at day 24 of differentiation. data shown are the mean \pm SD. N=4 biological repeats. **C)** Expression of motor neuron markers (OLIG2, HB9, ISLET1) and trunk positional marker (HOXC9) comparing the two conditions at day 24 of differentiation. Data shown are the mean \pm SD N = 4 biological repeats. (* - P \leq 0.05, t-test).

A)



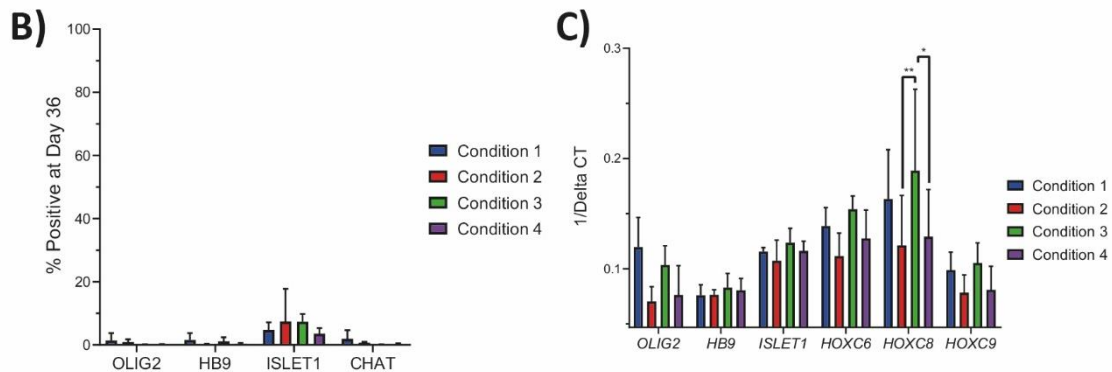


Figure 14: Assessment of increased BMP4 and notch inhibition on the production of day 36 motor neurons. **A)** Staining of early motor neuron marker (OLIG2), postmitotic motor neuron marker (HB9), motor neuron neurotransmitter (CHAT), motor neuron marker (ISLET1), axonal marker (NFH) and trunk positional marker (HOXC9) at day 36 of the differentiation protocol. Nuclei are counterstained with Hoechst33343. Representative images are shown for each condition. Scale bar: 100 μ m. **B)** Summary of image analysis of OLIG2, HB9, ISLET1 and HOXC9 staining at day 36 of differentiation. Data shown are the mean \pm SD N = 4 biological repeats. **C)** Expression of motor neuron markers (*OLIG2*, *HB9*, *ISLET1*) and trunk positional marker (*HOXC9*) comparing the four conditions at day 36 of differentiation. Data shown are the mean \pm SD N = 4 biological repeats. (* - $P \leq 0.05$, ** - $P \leq 0.01$, 2-way ANOVA)

To see if the extra BMP4 inhibition had a delayed affected neuronal maturation efficacy of differentiation was assessed again at day 24 by immunofluorescence for the expression of OLIG, HB9, CHAT, ISLET and NFH. Both condition 1 and 2 produced a similar amount of ISLET⁺ (condition 1: 5% (\pm 4), condition 2: 4% (\pm 2)) and HB9⁺ (condition 1: >1%, condition 2: 2% (\pm 2)) cells (Figure 13A, 13B). Additionally, the expression of CHAT was still not detected on day 24, suggesting that motor neurons were either still immature or not being successfully produced despite the onset of OLIG2 and neuronal populations (as indicated by the presence of NFH). In order to further investigate the efficacy of differentiation, I measured gene expression on day 24 of *OLIG2*, *HB9*, *ISLET* and Brachial/Thoracic HOX genes (*HOXC6-HOXC9*). Expression of *OLIG2* had decreased compared with day 14 conditions (Figure 12D, 13C) and expression of *HB9* and *ISLET1* had increased, however, no significant differences were noted between condition 1 and 2 for motor neuron markers, indicating that the presence of LDN193189 had not altered the patterning of these cells to a more motor neuron-like identity and that cells may still possess an immature phenotype or not differentiating correctly. Expression of *HOXC8* was significantly higher in condition 1 than condition 2, indicating that LDN193189 had continued to affect the HOX patterning of these cells.

Inhibition of Notch has been shown to increase the maturity of neurons (Borghese *et al.*, 2010), therefore I decided to assess the effect of the addition of Notch inhibitor, RO4929097, on the cultures from day 24 of the differentiation. Including \pm Notch inhibition conditions expanded the number of conditions from two to four (Figure 10B). On day 36 of differentiation, motor neuron production was assessed by immunocytochemistry for OLIG2, HB9, CHAT, ISLET and NFH. Less than 1% of cells were found to be CHAT⁺, HB9⁺ or OLIG2⁺ (Figure 14A, 14B), indicating that despite the production of neurons (indicated by the presence of NFH), motor neuron cells had not been generated from this protocol. The number of ISLET1⁺ cells on day 36 was similar to that found on day 24 (condition 1: 4% (\pm 1), condition 2: 7% (\pm 7), condition 3: 7% (\pm 2), condition 4: 3% (\pm 1)) and no significant differences were noted in the detected levels of ISLET1. In order to further investigate the efficacy of differentiation, I measured gene expression for day 36 of *OLIG2*, *HB9*, *ISLET* and Brachial/Thoracic HOX genes (*HOXC6-HOXC9*). Expression of motor neuron markers (*OLIG2*, *HB9*, *ISLET1*) was not significantly altered across the conditions (Figure 14C) and expression of *HB9* and *ISLET1* did not appear elevated from the previous day 24 (Figure 13C, 14C). *HOX6-9* expression showed a similar pattern as at day 24. *HOXC8* was significantly decreased in conditions which contained the extended LDN193189, suggesting that the increased BMP4 inhibition altered the expression of HOX genes.

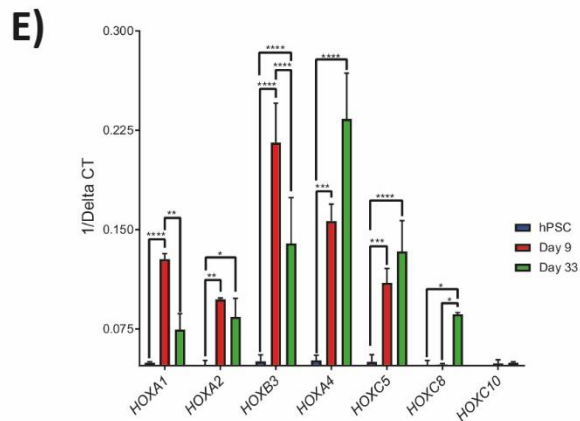
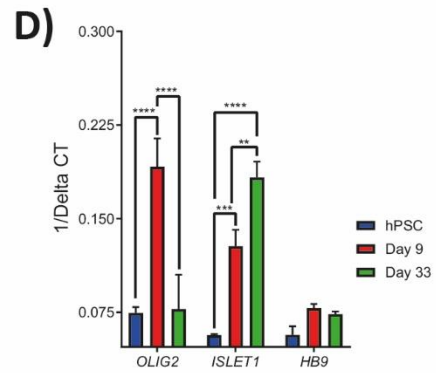
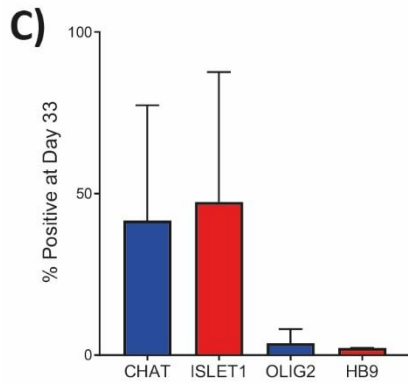
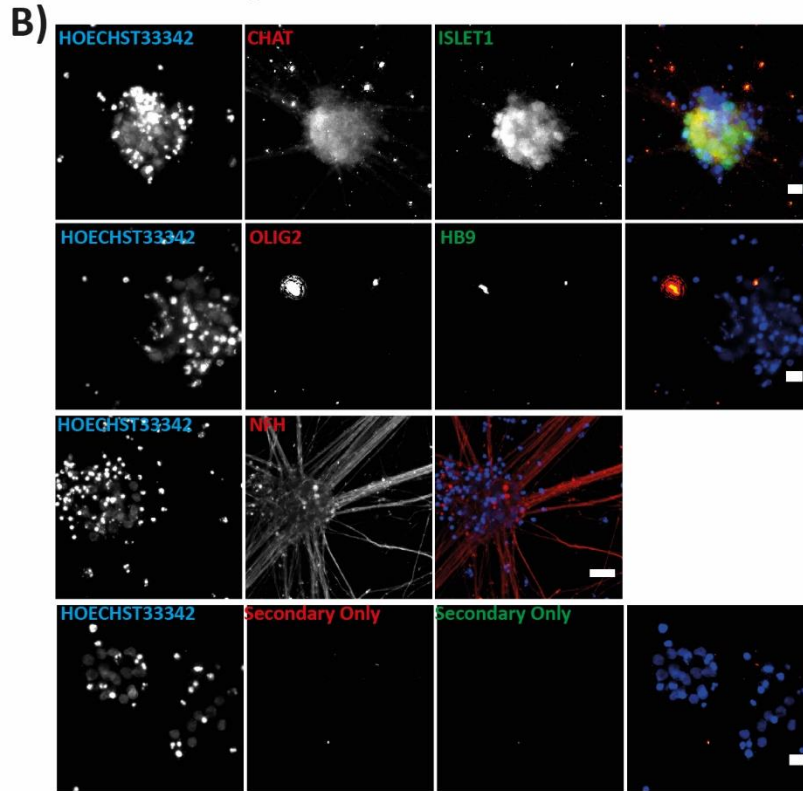
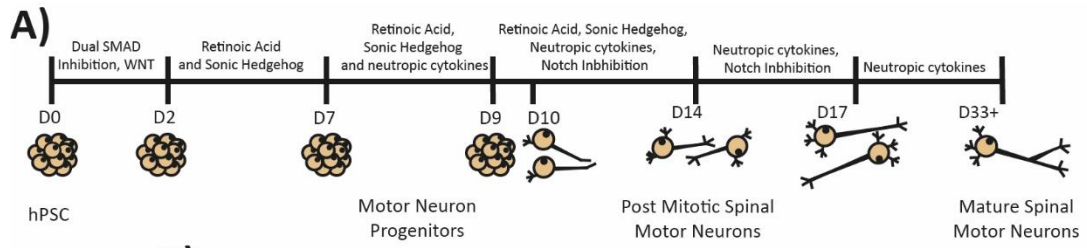
In summary, the described protocol ultimately failed to produce motor neurons, as shown by the lack of CHAT⁺ cells detected. Previously, the protocol had successfully produced CHAT⁺ cells (Figure 8D' vs 13A), indicating high variability in the protocol. The Notch inhibition and extended BMP4 inhibition did not increase the number of motor neurons generated but the latter may have affected HOX gene expression. The protocol produced a large number of non-neuronal cells indicating poor specification to the neural plate. The presence of non-neuronal cells meant that multiple passaging steps were necessary which may have affected motor neuron survival. Significant further optimisation would be required in order generate the LMC motor neurons using this protocol. Due to time constraints, I decided it would be beneficial to investigate alternative protocols which may provide a stronger starting point to optimise from.

3.2.4) Assessment of 3D motor neuron differentiation protocol

A literature search of a different motor neuron differentiation protocols capable of generating LMC motor neurons revealed a protocol, using an EB method, initially developed by Maury *et al.* This protocol was subsequently adapted by Guo *et al.* to produce HB9⁺ motor neurons to model ALS (Maury *et al.*, 2015; Guo *et al.*, 2017). For this protocol, I used the dual SMAD method whilst including WNT

and RA (Figure 15A). Cranial and brachial HOX genes are responsive to RA, meaning it was likely these could be brachial neurons rather than thoracic or lumbar. After 9 days, I dissociated the EB and progenitor neurons were plated with Notch inhibition (DAPT) for maturation before being maintained with neurotropic cytokines. Dissociation of the EB was the only plating step, meaning no further passaging of the neurons would be required which I hypothesised would help neuronal survival and potentially decrease the number of non-neuronal cells in the culture.

MShf11 was differentiated using the new protocol (Figure 15A) and motor neuron production was assessed by immunocytochemistry for OLIG2, HB9, CHAT, ISLET and NFH at day 33. CHAT⁺ (42% (± 25)) and ISLET1⁺ (47% (± 28)) cells (Figure 10B, 10C) were found, indicating a culture enriched with motor neuron cells; however, variability was high between repeats. As expected, the overall number of non-neuronal cells was decreased and there was a large network of branching axons, as seen by NFH staining. By day 33, there was only 4% (± 3) OLIG2⁺ cells, suggesting motor neurons may have matured, however, this had not resulted in population that was enriched for HB9⁺ cells (2% ($\pm >1$)). The lack of HB9⁺ cells could indicate a specific subpopulation of LMC (that does not express HB9) or incorrect columnar or axial positioning. To investigate the identity of the neurons, I carried out gene expression analysis looking at motor neuron genes (*OLIG2*, *ISLET1* and *HB9*) during the protocol. *OLIG2* expression was significantly increased at day 9 of differentiation compared with hPSC (Figure 15D), indicating a strong onset of early motor neuron genes, which was then decreased again at day 33, indicating maturation. *ISLET1* expression significantly increased at each time point measured, further confirming successful neuronal production. *HB9* expression was not significantly increased at any time point measured. Making it more likely that incorrect columnar or axial identity was the cause. I examined the expression of *HOX* genes (*HOX1-10*) in order to investigate whether axial identity was a causative factor in the lack of HB9 expression. By day 9 of the differentiation, expression of cranial *HOX* genes (*HOX1-4*) were significantly upregulated whilst *HOXC8* was not. The lack of *HOXC8* at day 9 indicates the neurons were predominantly anterior prior to the addition of the DAPT maturation signal. As this population appeared to be predominantly anterior and HB9⁺ cells do not arise in the cranial region this could explain the lack of HB9 upregulation and HB9⁺ cells found in the culture. By day 33, *HOXC8* was significantly upregulated, indicating a more brachial culture suggesting some heterogeneity in the culture and this population of cells may be responsible for the small amount of HB9⁺ cells seen.



((Previous page) Figure 15: Assessment of 3D motor neuron differentiation protocol. A)

Differentiation of hPSC into motor neurons using embryoid body method. Protocol adapted from Maury et al., 2015 and Guo et al., 2017. **B)** Staining of early motor neuron marker (OLIG2), postmitotic motor neuron marker (HB9), motor neuron neurotransmitter (CHAT), motor neuron marker (ISLET1) and axonal marker (NFH) at day 33 of the differentiation protocol. Nuclei are counterstained with Hoechst33343. Representative images shown. Scale bar: 15µm. **C)** Summary of image analysis of CHAT, OLIG2, HB9 and ISLET1 staining at day 33 of differentiation. Data shown are mean ±SD N = 2 biological repeats. **D)** Expression of motor neuron markers (*OLIG2*, *HB9*, *ISLET1*) at day 33 of differentiation. Data, shown are mean ±SD N = 2 biological repeats. (** - P ≤ 0.01, *** - P ≤ 0.001, **** - P ≤ 0.0001, 2-way ANOVA) **E)** Expression of positional HOX markers at day 33 of differentiation. *HOXA1* – *HOXA4* are cranial markers, *HOXC5* is a cervical/brachial marker, *HOXC8* is a brachial/thoracic marker and *HOXC10* is a lumbar marker. Data shown are mean ±SD N = 2 biological repeats. (* - P ≤ 0.05, - ** - P ≤ 0.01, *** - P ≤ 0.001, **** - P ≤ 0.0001, 2-way ANOVA)

In summary, the EB protocol tested showed the production of motor neurons containing the expression of CHAT, ISLET1 and OLIG2 at appropriate time points. However, the neurons produced were not LMC motor neurons, therefore the protocol would require further optimisation to produce the relevant neurons for the modelling of CMT2A.

3.2.5) Alteration of key signalling pathways to increase induction of key motor neuron markers

Multiple EB based motor neuron differentiation protocols exist in the literature and I noted many of these had the EB dissociation after the addition of the DAPT (Klim *et al.*, 2019; Thams *et al.*, 2019). Furthermore, motor neuron survival can be increased when they are plated at high density (Qu *et al.*, 2014). Based on these findings from the literature, I chose to perform the EB dissociation in my protocol from day 9 to day 13 (Figure 16A). I postulated that this would allow the start of the neuronal maturation to take place within the EB at a high density before being dissociated which may lead to increased neuronal survival post replating. I examined motor neuron production by immunocytochemistry for OLIG2, HB9, CHAT, ISLET and NFH at day 33. Levels of CHAT⁺ (52% (±26)) and ISLET⁺ (52% (±10)) cells (Figure 16B, 16C) were unaffected by this change, indicating motor neuron differentiation was successful. Unexpectedly, OLIG2⁺ cells were detected in some cultures at day 33 (21% (±36)), indicating either a lack of maturation for some cells or prolonged/delayed OLIG2⁺ expression. Despite this, the number of HB9⁺ cells were low at day 33 (5% (±4)). As not all LMC motor neurons express *HB9* on maturation, but all do during development (reviewed in Stifani, 2014), I decided to investigate a time course from the point DAPT was added to the culture (day 9) in order to

determine if *HB9* was ever expressed in the differentiation. Along with *HB9*, I examined *OLIG2* to confirm the downregulation of immature motor neuron expression and *ISLET1* as a more general motor neuron marker. *OLIG2* expression showed a decrease on day 11 (Figure 16D), 48 hours after DAPT addition, and continued to decrease after this. A very slight increase in *HB9* expression was seen at day 11, however, it decreased again at day 12. *ISLET1* expression increased after the addition of DAPT, showing the strongest expression on day 11. The dual SMAD method is known to produce predominantly anterior neurons (Chambers *et al.*, 2009), therefore I decided to confirm if this was the reason I was not seeing the expression of *HB9* in culture by examining the expression of *HOX* genes 1-5 across the same time course. *HOXA1* and *HOXB3* were highly expressed throughout the entire time course with *HOXA4* and *HOXC5* expression increasing over time, indicating the presence of a cranial population due to known the cross repression of *HOXC5* and *HOXC8* (Dasen, Liu and Jessell, 2003). From this data, it seemed likely that the lack of *HB9* expression in these cells was due to the neurons having a cranial identity, indicating the protocol would need to be modified in order to generate more posterior neurons.

Dual SMAD inhibition and WNT signalling work in combination to increase specification to the neural plate and motor neuron progenitor domain (Maury *et al.*, 2015). WNT signalling has been shown to have a role in the posteriorisation of motor neurons in addition to its role in their specification (Nordström *et al.*, 2006; Cunningham *et al.*, 2015). Added to this, *HOX1-6* are responsive to increasing levels of RA (Liu, Laufer and Jessell, 2001), *HOX6* being a brachial (and therefore able to produce LMC) *HOX* gene. Using the combination of this knowledge, I decided to increase the length of the dual SMAD inhibition and WNT signalling from the first 2 days of the protocol to the first 4 (Figure 17B). Additionally, I increased the concentration of CHIR99021 (3 μ M to 4 μ M) and RA (0.1 μ M to 1 μ M) to promote expression of more posterior *HOX* genes. The conditions were tested alone or in combination during the first 14 days of differentiation (Figure 17A, 17B) and gene expression for motor neuron marker *HB9* and brachial *HOX* gene *HOXC8* were analysed on day 10, day 12 and day 14 of differentiation. Condition 5, which contained both increased dual SMAD and CHIR99021, as well as the increase in CHIR99021 concentration resulted in the highest increase in *HB9* expression (Figure 17C), leading to the strongest expression on day 12. *HOXC8* expression was not as dramatically affected, leading to only a small increase in conditions 4 and 5. As condition 4 showed the strongest induction of *HB9* expression and a marginal increase in *HOXC8* expression, it was chosen as the basis for further optimisation

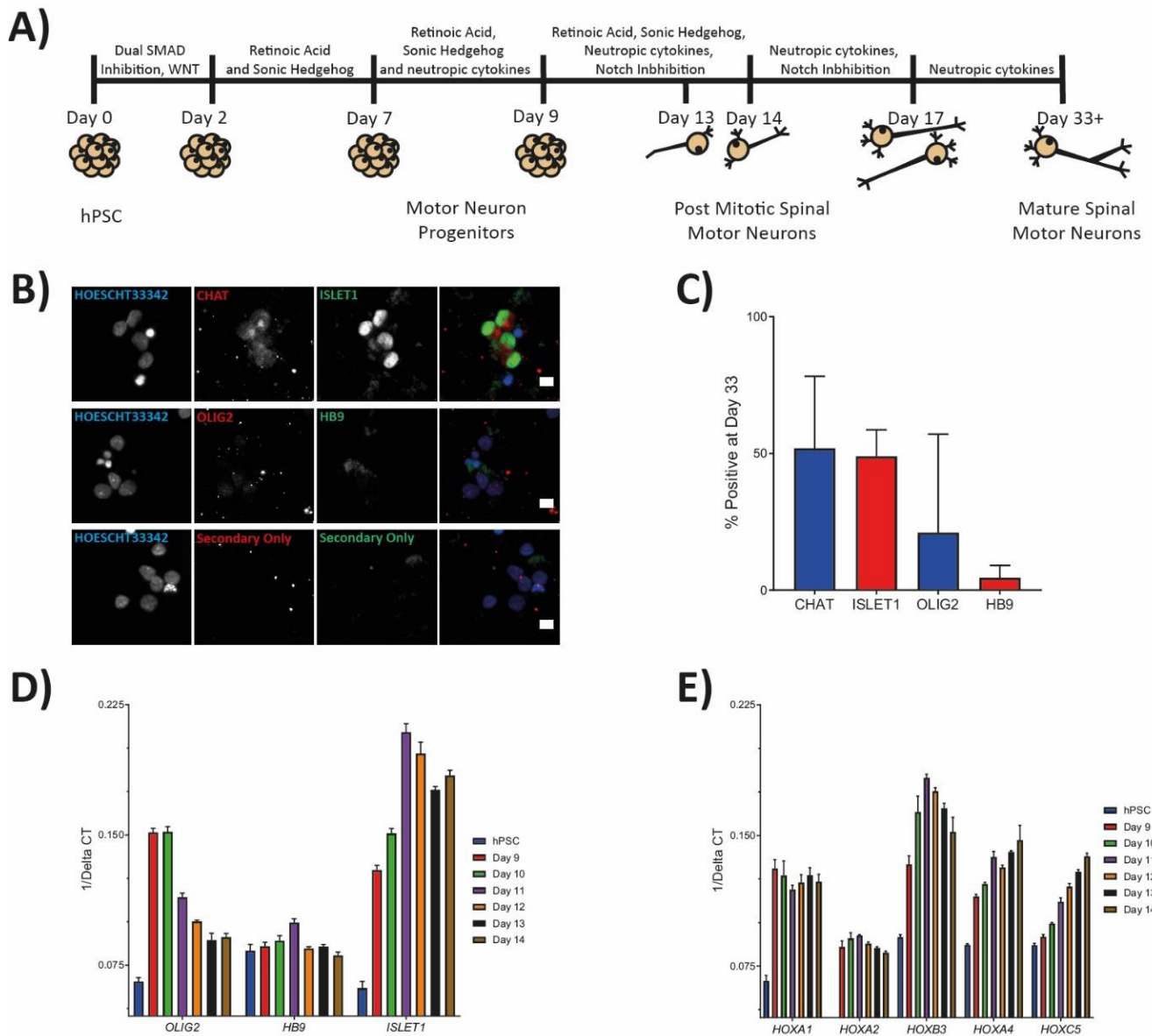
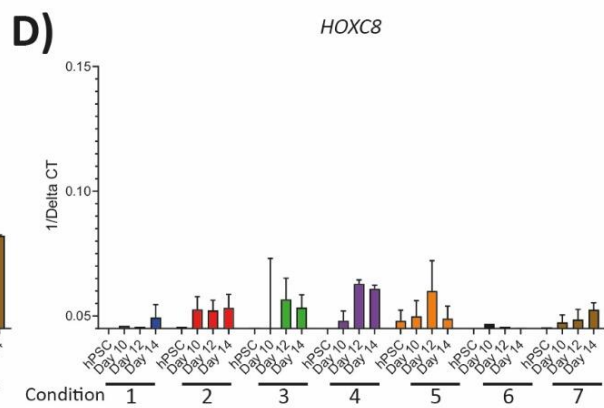
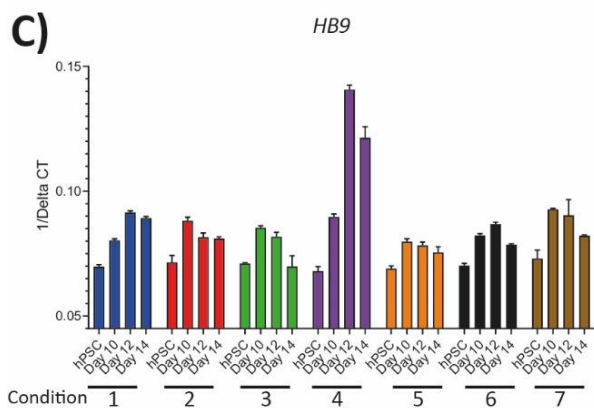
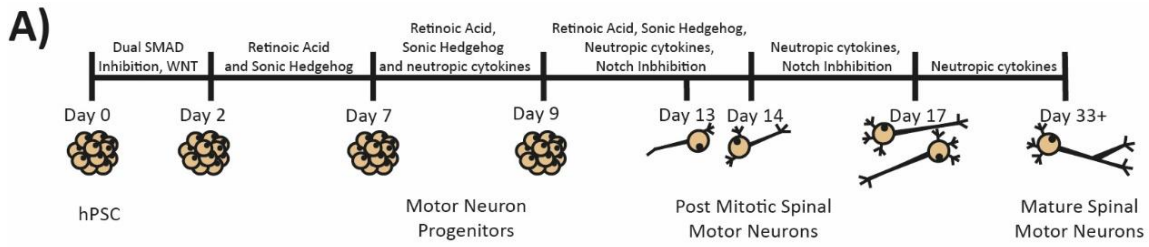


Figure 16: Assessment of HB9 expression during motor neuron differentiation. A) Differentiation of hPSC into motor neurons using embryoid body method. Protocol adapted from Maury et al., 2015 and Guo et al., 2017. **B)** Staining of early motor neuron marker (OLIG2), postmitotic motor neuron marker (HB9), motor neuron neurotransmitter (CHAT) and motor neuron marker (ISLET1) at day 33 of the differentiation protocol. Nuclei are counterstained with Hoechst33343. Representative images are shown. Scale bar: 10 μ m. **C)** Summary of image analysis of CHAT, OLIG2, HB9 and ISLET1 staining at day 33 of differentiation. Data shown are the mean \pm SD N = 3 technical repeats. **D)** qPCR showing expression of motor neuron markers (*OLIG2*, *HB9*, *ISLET1*) over the course of the differentiation from day 9 to day 14. Data shown are the mean \pm SD N = 3 technical repeats. **E)** qPCR showing expression of positional HOX markers over the course of the differentiation from day 9 to day 14. *HOXA1* – *HOXA4* are cranial markers. Data shown are the mean \pm SD N = 3 technical repeats.

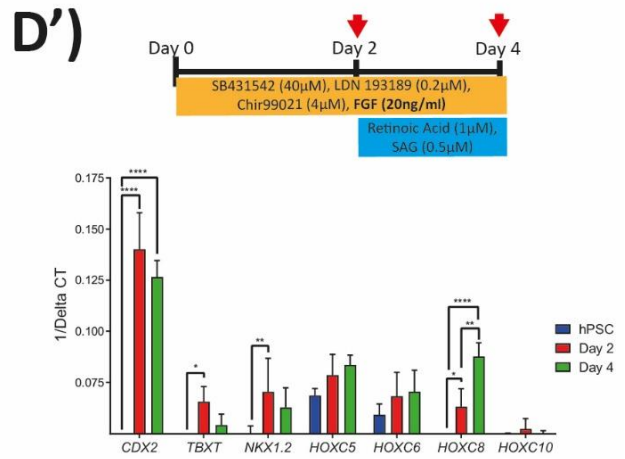
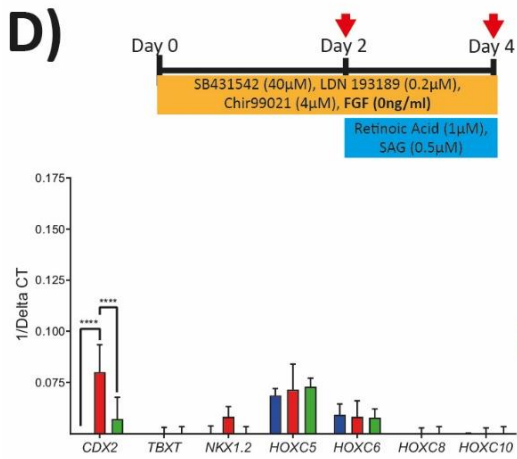
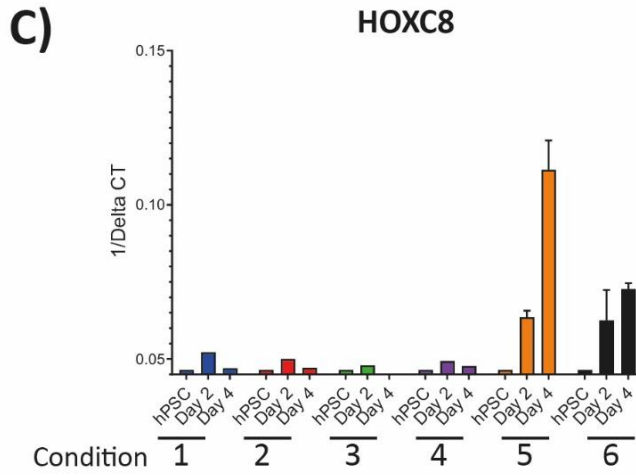
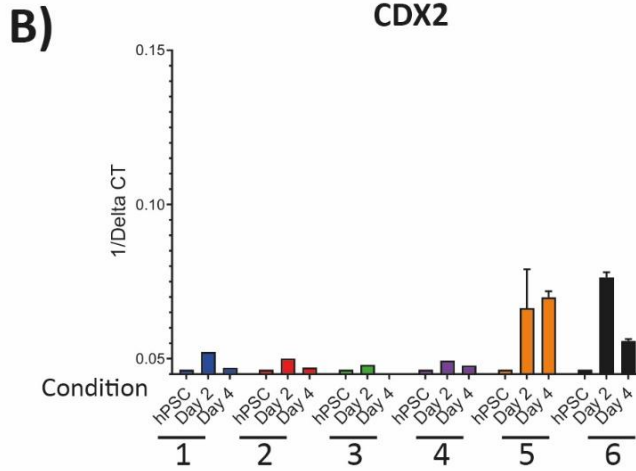


(Previous page) Figure 17: Optimisation of motor neuron differentiation conditions to increase expression of HB9 and HOXC8. **A)** Differentiation of hPSC into motor neurons using embryoid body method. Protocol adapted from Maury et al., 2015 and Guo et al., 2017. **B)** Conditions tested in comparison to the standard protocol. Cells were taken for analysis at time points indicated by the arrows. **C)** Expression of post-mitotic motor neuron marker, *HB9*, in the conditions tested. Data shown are the mean \pm SD N = 3 technical repeats. **D)** Expression of the positional marker *HOXC8* in the conditions tested. Data shown are the mean \pm SD N = 3 technical repeats.

FGF is required *in vivo* to induce expression of more posterior HOX genes and performs this function for brachial/thoracic genes in combination with RA (Liu, Laufer and Jessell, 2001; Dasen, Liu and Jessell, 2003). Additionally, RA has a key role in transitioning cells to a fixed rostral-caudal position (Lippmann *et al.*, 2015) as well as in the acquisition of LMC identity (Niederreither *et al.*, 1997; Patani *et al.*, 2011). Based on these key pieces of information, I chose to investigate the effect of increasing FGF concentrations (5ng/ml, 10ng/ml, 20ng/ml) with two concentrations of RA (0.1 μ M to 1 μ M) (Figure 18A) on the induction of *CDX2* expression. *CDX2* interacts with HOX expression to help control axial development and is transiently expressed in more posterior populations (reviewed in (Deschamps and Duboule, 2017)). *CDX2* is also known to be involved in NMP development (Gouti *et al.*, 2014). I also chose to analyse the expression of *HOXC8* to determine the axial identity cells produced. Samples were examined at day 2 and 4 of differentiation. *CDX2* and *HOXC8* expression were only induced when the FGF was present at 20ng/ml in conditions 5 and 6 (Figure 18B, 18C), reinforcing the finding that FGF was necessary to induce the expression of more posterior markers but interestingly, that the FGF signal could be present at the same time as the dual SMAD inhibition and still produce a more posterior axial identity. *CDX2* was expressed most transiently at 1 μ M RA and hence, I chose this concentration of RA for further protocol development. The expression of *CDX2* led me to postulate that it was possible NMP-like cells were being produced in the EB and could be the cause of this increased posterior population. To investigate the presence of NMP-like cells, I chose to examine a *HOX5-10* in order to confirm the anterior-posterior identity of this population with greater accuracy and the induction of NMP genes (*TBXT*, *NKX1.2*). In the presence of FGF 20ng/ml, NMP genes were significantly upregulated at day 2, indicating that NMP-like cells may be present in the EB at this time. Moreover, expression of *HOXC8* and *CDX2* was significantly increased at both days 2 and 4 of the high FGF cells compared to hPSC and compared to the non-FGF condition indicating that the presence of FGF had produced cells with a more posterior axial identity. Finally, I sought to examine the length of FGF signalling required to ensure that the *HOX* identity was fixed in the correct rostral-caudal position. I tested the inclusion of FGF for 4, 9 or 12 days and examined the expression of *OLIG2*, *HB9*, *HOXC6* and *HOXC8* at days 10, 12 and 14 of differentiation (Figure 19A). Expression of *OLIG2*

remained high when FGF was included for 12 days (Figure 19B''), which indicated the persistence of the immature signal, or that cells were differentiating into a non-motor neuron cell type (such as oligodendrocytes which is typified by extended *OLIG2* expression (Hu, Du and Zhang, 2009)). *HOXC8* was expressed most highly in condition 2 (FGF for 9 days) (Figure 19B'), however, *HOXC6* expression did not appear to be increasing. The lack of *HOXC6* indicated cells may be progressing towards a thoracic fate instead of brachial. Expression of *OLIG2* was highest at day 10 for condition 1 (Figure 19B) and decreased towards day 14. Additionally, *HOXC6* expression increased throughout the time course, alongside *HOXC8*. Taken together, this data suggests that the neurons were obtaining a brachial fate during their differentiation. Expression of *HB9* was slightly increased at day 10, however, whether this translated into the expression of HB9 protein would need to be further investigated.

(Next page) Figure 18: Addition of FGF to motor neuron protocol to increase the posterior identity of motor neurons. A) Conditions tested in comparison with the standard condition. Cells were taken for analysis at the time points indicated by the arrows. **B)** Expression of the early posterior marker, *CDX2*, in the conditions tested. Data shown are the mean \pm SD N = 3 technical repeats. **C)** Expression of the positional marker, *HOXC8*, in the conditions tested. Data shown are the mean \pm SD N = 3 technical repeats. **D)** Expression of NMP markers in the absence (D) and presence (D') of FGF. Top: schematic showing the experimental condition of the experiment. Cells were taken for analysis at time points indicated by the arrows. Bottom: Gene expression profiling by qPCR of NMP markers (*CDX*, *TBXT*, *NKX2.3*) and positional markers (*HOXC5*, *HOXC6*, *HOXC8*, *HOX10*). Data shown are the mean \pm SD N = 3 technical repeats.



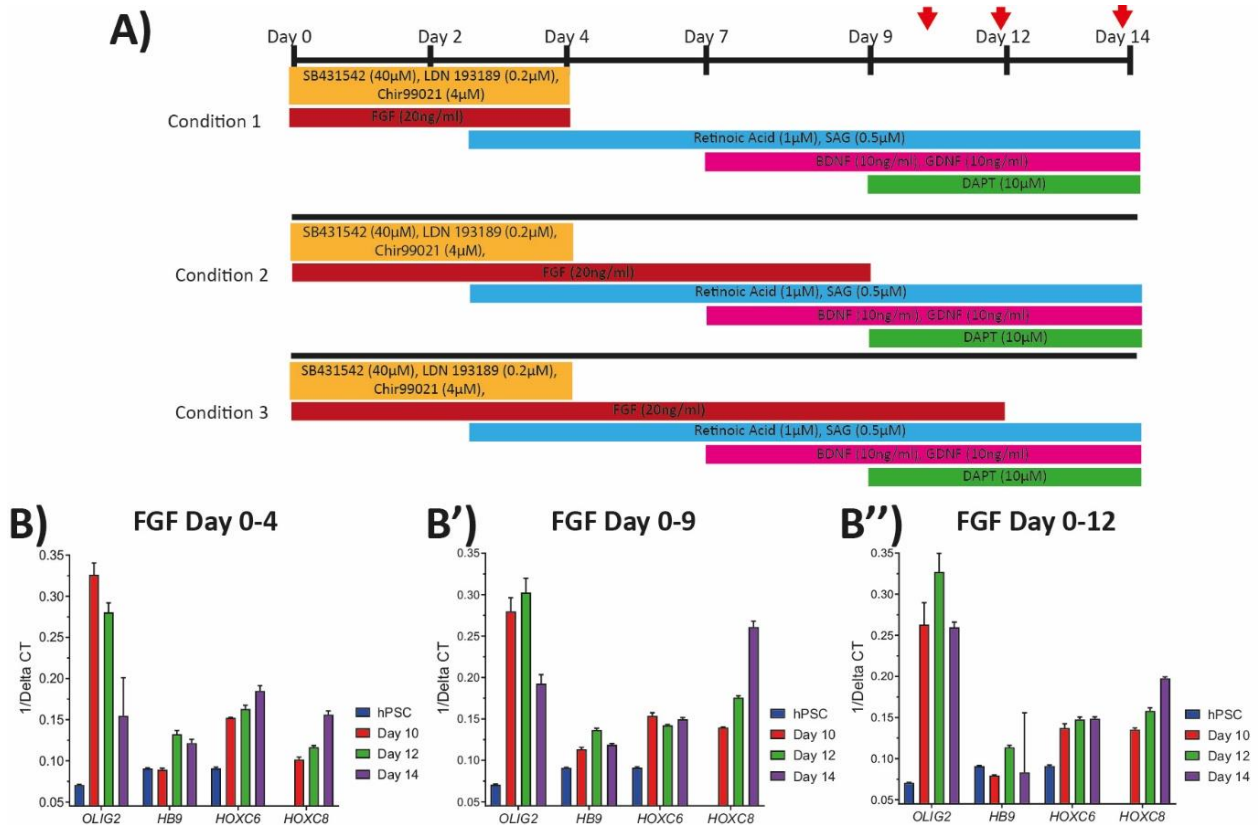


Figure 19: Assessment of length of FGF signal to induce expression of motor neuron markers. A) Conditions tested in comparison with the standard condition. Cells were taken for analysis at the time points indicated by the arrows. **B)** Expression of motor neuron markers (*OLIG2*, *HB9*) and positional markers (*HOXC6*, *HOXC8*). FGF was added for the indicated number of days, 0-4 (B), 0-9 (B') or 0-12 (B''). Data shown are the mean \pm SD N = 3 technical repeats.

Combining the data previously generated (Figures 17-19), I attempted the full version of the protocol, including an extended dual SMAD inhibition, extended and increased CHIR99021 concentration, increased concentration of RA and inclusion of FGF for the first four days of the protocol (Figure 20A). Differentiation was assessed by immunocytochemistry for expression of CHAT, ISLET1, HB9 and axonal marker TUJ1 at day 16 and day 33. At day 16 of differentiation, CHAT⁺ (62%) and ISLET⁺ (64%) (Figure 20B) cells represented the majority of the population and HB9⁺ cells consisted of just under half (47%) of the population. At day 33 of differentiation, the marker composition (CHAT⁺ (44%), ISLET⁺ (57%) and HB9⁺ (50%)) (Figure 20B, 20C) was similar to that seen at day 16, indicating successful differentiation to motor neurons had been achieved. Large axonal projections were also highly visible throughout the culture as seen by axonal marker TUJ1 (Figure 20D), with few non-neuronal cell types present in the population. To confirm correct columnar identity, expression of neuronal markers *OLIG2*, *ISLET1* and *HB9* and columnar markers (Figure 6) *LHX1*, *LHX3* and *PHOX2B* were investigated in

the middle and at the end of the differentiation. Expression of immature marker *OLIG2* peaked at day 13 and was low again at day 33 (Figure 20E), *ISLET1* expression increased throughout the protocol and *HB9* expression increased at day 13 and remained relatively high at day 33, indicating differentiation had proceeded successfully. Expression of *LHX1*, *LHX3* and *PHOX2B* was highest at day 13 and decreased again on day 33. This indicates that the cells were not MMC (due to the lack of *LHX3* on day 33) and the lack of *LHX1* indicates the population may be medial LMC (as *LHX1* is only found in the LMC on the lateral side) (Figure 6). However, it is difficult to draw definitive conclusions on the LMC identity of these neurons given that previous work has suggested that *in vitro* conditions may not provide full maturation of these neurons (Amoroso *et al.*, 2013). Expression of *PHOX2B* remained somewhat elevated at day 33, which may indicate that a population of neurons failed to induce posterior *HOX* genes and retained a cervical state. Alternatively, there may be a contaminating population of sensory neurons present in the culture (Chambers *et al.*, 2012; Stifani, 2014). To investigate the possibility of contaminating sensory neurons, I checked the expression of *BRN3A* via immunofluorescence and found the cells to be negative (Figure 20F). This indicates that there are not mature sensory neurons contaminating the culture and does not explain the finding of *CHAT*⁻ neurons in the culture. Expression analysis of *HOX* genes 1-10 was carried out by qPCR to determine the axial identity of the culture. *HOXC6* and *HOXC8* expression rose by day 13 in culture, suggesting that neurons had a caudal brachial identity (Figure 15G). *HOXC5* expression was also high indicating that the population was likely heterogeneous in its axial identity. This was further supported by the presence of some *HOXC10* expression at day 33 indicating a small lumbar population may also be present.

In summary, the data shown indicates the optimised protocol is capable of generating the desired limb innervating LMC spinal motor neuron population from MShef11 hPSC, as required for further modelling of CMT2A.

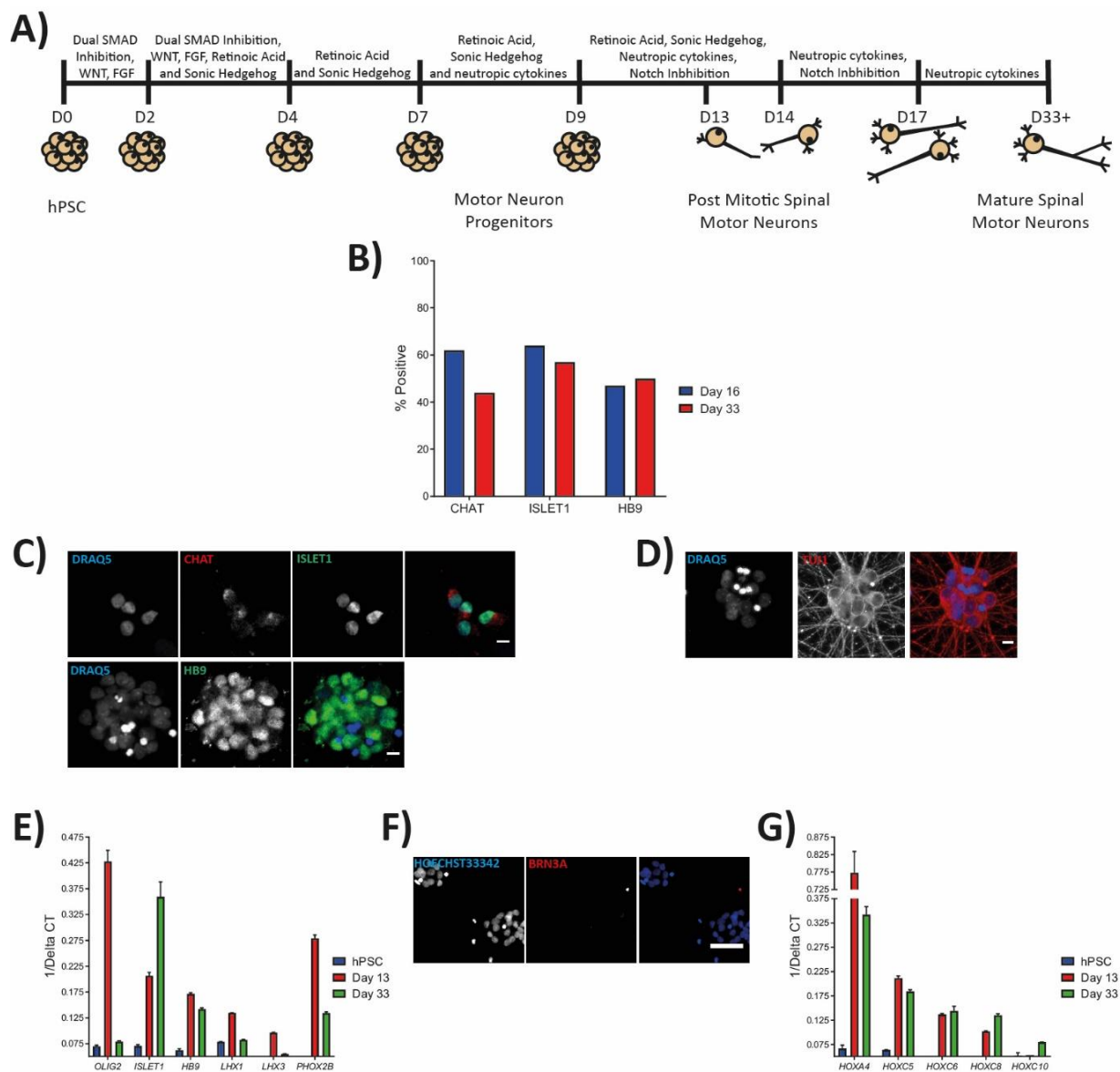


Figure 20: Initial assessment of optimised motor neuron protocol. **A)** Optimised differentiation protocol of hPSC into motor neurons using embryoid body method. Protocol adapted from Maury et al., 2015 and Guo et al., 2017. **B)** Quantification of motor neuron marker (CHAT, ISLET, HB9) expression at days 16 and 33. **C)** Staining of motor neuron markers (CHAT, ISLET, HB9) at day 33 of the differentiation protocol. Nuclei are counterstained with DRAQ5. Scale bar: 10µm. **D)** Staining of axonal marker (TUJ1) at day 33 of the differentiation protocol. Nuclei are counterstained with DRAQ5. Scale bar: 100µm. **E)** Expression of relevant motor neuron markers (*OLIG2*, *ISLET1*, *HB9*) and relevant columnar identity markers (*LHX1*, *LHX3*, *PHOX2B*). Data shown are the mean \pm SD N = 3 biological repeats. **F)** Staining of sensory neuron marker (BRN3A) at day 33 of the differentiation protocol. Nuclei are counterstained with Hoescht33342. Scale bar: 50µm. **G)** Expression of HOX markers from anterior/cranial (*HOXA4*), to posterior/lumbar (*HOXC10*). Data shown are the mean \pm SD N = 3 biological repeats.

3.2.6) Characterisation of motor neurons from optimised differentiation protocol

Protocol variability would render modelling of CMT2A difficult as it would be difficult to confirm if phenotypic effects were seen from the mutation or simply inefficient differentiation. MShef11 was differentiated using the optimised protocol a further three times and motor neuron differentiation was assessed at day 16 and 33 by immunofluorescence for CHAT, ISLET and HB9. At day 16, over 50% of the population was CHAT⁺ (67% (± 18)), ISLET1⁺ (53% (± 9)), OLIG2⁺ (85% (± 16)) or HB9⁺ (51% (± 23)) (Figure 21A), indicating high levels of successful differentiation that was fairly robust and strong marker expression found in the percentage of positive cells at day 33 (CHAT⁺ 81% (± 13), ISLET1⁺ 76% (± 10) or HB9⁺ 92% (± 5)) (Figure 21B). To confirm LMC identity, neurons were stained for FOXP1 and a large proportion of cells were found to be highly FOXP1⁺ (77% (± 20)) (Figure 21B and 21C). To further confirm neuronal identity, expression of neuronal markers *OLIG2*, *ISLET1* and *HB9* and columnar markers *LHX1*, *LHX3* and *PHOX2B* were investigated in the middle and at the end of the differentiation. Expression of *OLIG2* was significantly increased and then decreased as differentiation progressed (Figure 21C), indicating successful motor neuron specification and maturation. *ISLET1* expression increased significantly over the course of differentiation. *HB9* expression was significantly higher in cells at day 13 and day 33 of the differentiation protocol compared to undifferentiated hPSCs, indicating the presence of post-mitotic motor neurons from day 13 which persisted in culture. Expression of columnar markers *LHX1*, *LHX3* and *PHOX2B*, were as found previously (Figure 20E vs 21D). Expression analysis of *HOX* genes 1-10 was carried out by qPCR to determine the axial identity of the neurons in culture. Expression of *HOXA4*, *HOXC6* and *HOXC8* was significantly increased at both day 13 and day 33 of differentiation compared to hPSC (Figure 21D), this combined with the lack of significant increase of expression with *HOXC5* indicates the presence of a caudal brachial population. Finally, neurons were found to be electrophysiologically active and produce relevant action potentials (data not shown). Taken together, these results show the successful production of hPSC-derived motor neurons consisting of a predominantly brachial limb-innervating.

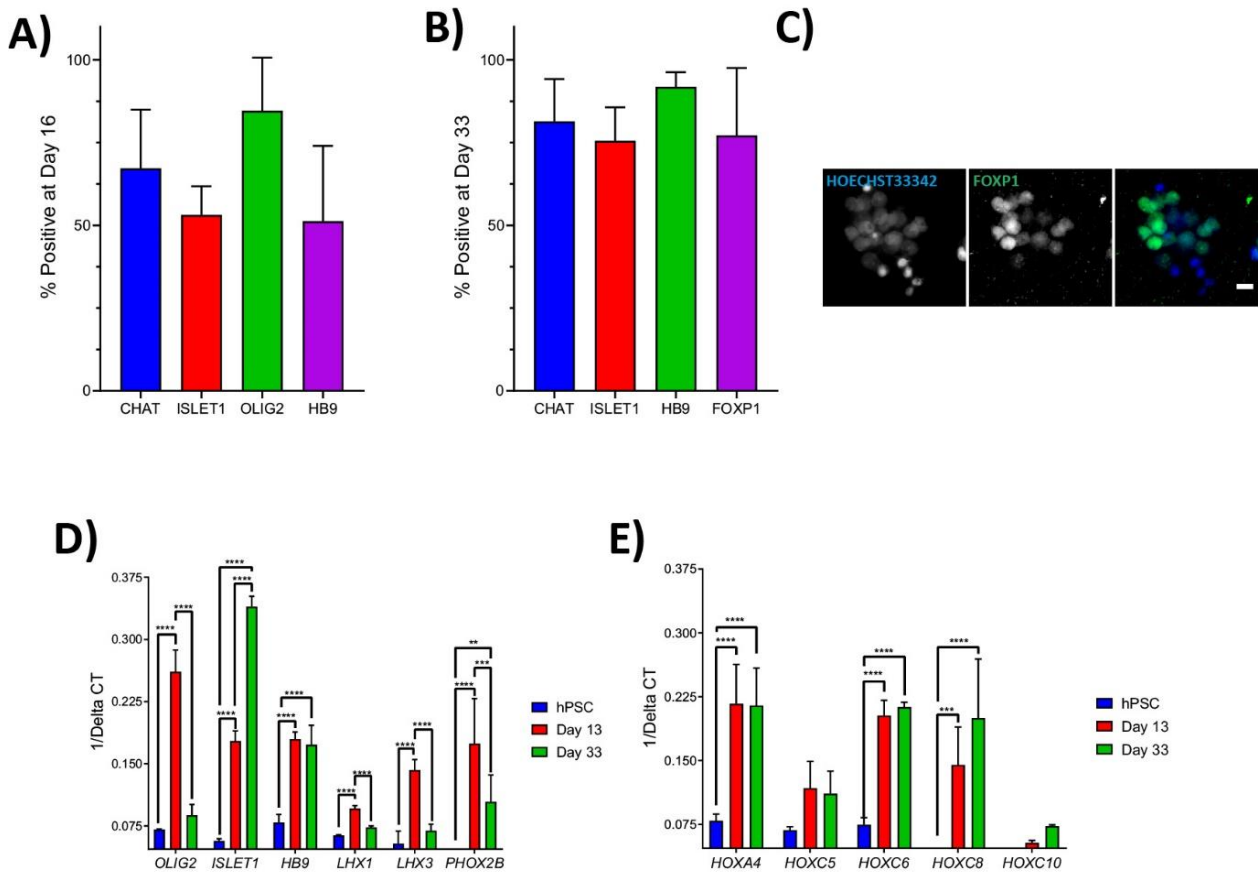


Figure 21: Assessment of biological repeatability in optimised motor neuron protocol. A) Summary of image analysis at day 16 of differentiation for post-mitotic (HB9) motor neuron markers, motor neuron neurotransmitter (CHAT) and motor neuron marker (ISLET1). Data shown are the mean \pm SD N = 3 biological repeats. **B)** Summary of image analysis at day 33 of differentiation for post-mitotic (HB9) motor neuron markers, motor neuron neurotransmitter (CHAT) and motor neuron marker (ISLET1). Data shown are the mean \pm SD N = 3 biological repeats. **C)** Staining of LMC marker (FOXP1) at day 33 of the differentiation protocol. Nuclei are counterstained with Hoescht33342. Scale bar: 10 μ m **D)** Expression of relevant motor neuron markers (*OLIG2*, *ISLET1*, *HB9*) and relevant columnar identity markers (*LHX1*, *LHX3*, *PHOX2B*). Data shown are the mean \pm SD N = 3 biological repeats. **E)** Expression of HOX markers from anterior/cranial (*HOXA4*), to posterior/lumbar (*HOXC10*). Data shown are the mean \pm SD N = 3 biological repeats.

3.3) Discussion

In summary, this work details the identification of MShef11 to model CMT2A through analysis of karyotype, MFN2 expression and differentiation capacity. MShef11 is capable of differentiating into both neuronal cell types affected in CMT2A and a protocol allowing for the generation of LMC motor neurons was optimised for this line. Several iterations of both 2D and 3D protocols were required to achieve the intended result and have allowed increased understanding in the signals necessary to lead to the generation of this highly specific subtype of motor neurons.

Initially, I tested the differentiation capacity of multiple stem cell lines to determine which was the preferred line to work with. This work further underpins the finding that different stem cell lines have varying propensities to differentiate to particular lineages. This was particularly prevalent with MShef4, which failed to differentiate in the neural crest protocol. These changes are likely the result of either epigenetic or smaller mutational changes in the cell lines themselves (Bock *et al.*, 2011; Nishizawa *et al.*, 2016; Thompson *et al.*, 2020). Whilst it is known that genetic aberrations can cause a difference in differentiation capacity (Fazeli *et al.*, 2011; Markouli *et al.*, 2019), cultures were tested for karyotypical abnormalities during culture and are therefore unlikely to have been present at sufficient quantities to impact on differentiation capacity.

CMT2A affects both motor and sensory neurons, therefore it was necessary to test protocols capable of producing both types of neurons. The sensory neuron protocol was capable of producing neural crest and sensory neurons in MShef11 and MShef7. The end population of sensory neurons was very heterogenous and was not subjected to extensive characterisation. Whilst a significant part of clinical symptoms, sensory symptoms are not considered the primary focus of the clinical presentation. To this end, the protocol was not further developed or expanded upon. Sensory markers PERIPHERIN and BRN3A are present in the culture with indications of a nociceptor phenotype (as shown by expression of *SCN9A* and *P2X3*) but the type of sensory neurons present is likely heterogeneous. Additionally, there are many non-neuronal cells present in the culture, which could have several different identities as neural crest is a high multipotent source of cells in the body.

Beginning with a 2D protocol for motor neuron differentiation, I looked into the modulation of BMP4 and Notch signalling to increase specification and maturation of the neurons. The protocol was not yielding CHAT⁺ neurons in the subsequent differentiation, despite previous success in all cell lines and increase in the BMP4 modulation. It is known that cells produce endogenous factors which differ from passage to passage and can interfere with differentiation (Hackland *et al.*, 2017). This intrinsic

difference may lead to the variability seen within this protocol, rendering the increase in LDN193189 ineffective. Despite this, increase modulation of BMP4 signalling is still a likely target for optimisation of this protocol, though other changes would likely also be needed to overcome the variability.

The addition of RO4929097 did not have any effect on the expression of key markers. Notch inhibition is a known method of maturing multiple different neuronal populations but has shown to be most effective when used early in the protocol in ensuring commitment to the emerging fate (Maury *et al.*, 2015). From this, it is likely the RO4929097 was added too late in the protocol to have any effect as the immature marker OLIG2 had already reduced in expression. It is possible that adding it earlier would have been more beneficial and could have led to a decrease in non-neuronal cells present in the culture.

Differentiation of motor neurons using a 3D EB method provided a population of highly neuronal cells. The protocol did not require multiple passaging steps which improved ease of use and removed neuronal loss upon seeding which seems to have affected the 2D protocol in the later stages of differentiation. EB methods have gained popularity as it allows for many of the benefits of 3D culture (such as increased cell-cell interaction) without some of the drawbacks (such as expensive matrix/scaffolds). Indeed, it is suggested that 3D methods are more adept at producing longer axons than their 2D counterparts regardless of the cell line (Chandrasekaran *et al.*, 2017). Whilst using the EB method, I found that increasing the length of dual SMAD signalling and the length and concentration of CHIR99021 led to an increase in motor neuron markers. This is likely due to the increase in neural plate specification signals coming from the dual SMAD inhibition, additionally, WNT signalling plays a role in both specification of neuronal fate and elongation of the posterior axis (Nordström *et al.*, 2006; Gouti *et al.*, 2014; Cunningham *et al.*, 2015). Addition of FGF increased the expression of more posterior HOX genes due to its combinatorial role with WNT signalling and RA (Dasen, Liu and Jessell, 2003; Nordström *et al.*, 2006; Mouilleau *et al.*, 2021). The use of FGF to induce a posterior fate is not a novel concept and has been utilised in the generation of NMPs previously (Gouti *et al.*, 2014), however, the use of FGF in combination with the dual SMAD inhibition in the way described in this thesis indicates that the neural specification in this population can take place at the same time as the acquisition of the posterior identity. Increasing the WNT agonism as I have described was seen as a necessary step in work by Mouilleau and colleagues during their investigations, however, whilst an important part of their experimental design, FGF was still used after the initial dual-SMAD differentiation had taken place (Mouilleau *et al.*, 2021). My work indicates the staggering of these

signals is not necessarily important for the generation of some brachial cell types and raises questions around how the timing of these signals interact.

When I attempted to utilise a protocol found in the literature, it did not yield the same results in MShef11 as those found in the paper. Coupled with the knowledge that without the presence of extraneous signals neuronal differentiation has an anterior forebrain identity (Liu, Laufer and Jessell, 2001), MShef11 may have additional requirements to the H9 or iPSC lines used by Guo et al in order to produce sufficiently posterior neurons. *HOXA5* was the most posterior HOX gene examined from the protocol in the literature (Guo *et al.*, 2017), and is found on upper brachial motor neurons but also in lower cervical motor neurons (reviewed in Stifani, 2014). Together this may suggest MShef11 was not producing the correct columnar identity instead of the wrong axial identity. This is supported by the finding that not all the neurons are HB9⁺ or FOXP1⁺ in the final protocol, even though posterior HOX expression is largely increased. Furthermore, there are still neuronal cells found within the culture that are not CHAT⁺, suggesting the presence of non-motor neuronal cells. *PHOX2B*, a marker found in cervical neurons is also highly expressed in sensory neuron populations, which would be CHAT⁻, however no BRN3A⁺ cells were found by immunofluorescence. This suggests the possibility that the high expression of *PHOX2B* is from cervical motors but leaves unanswered questions as to the identity of contaminating motor neuron populations. Further investigation into relevant markers would help gain an understanding of the neuronal types present.

CMT2A primarily affects limb innervating neurons and the most severe symptoms are typically seen in the legs. Generation of these particular neurons is not well-established and would likely require the presence of GDF11 in combination with FGF to cause expression of the lumbar HOX genes (HOX10-12) (Liu, Laufer and Jessell, 2001; Mouilleau *et al.*, 2021). This type of protocol is much less well characterised than other neuronal differentiations meaning it would likely require more time and further optimisation. I focused on attempting to generate a brachial population. In the final population, *HOXA4*, *HOXC6* and *HOXC8* expression are significantly upregulated, suggesting that enriched for brachial neurons. The population is likely to be caudal brachial due to the low expression of *HOXC5* and high expression of *HOXC8* (Dasen, Liu and Jessell, 2003). Future work may shed light on the differences between the two groups of LMC motor neurons and provide further insight into the particular vulnerability of these neurons.

Protocols leading to a specific generation of limb innervating are of particular importance to many diseases other than CMT, such as ALS and Parkinson's. The protocol described produced a large

population of HB9⁺ and FOXP1⁺ neurons indicative of LMC motor neurons. Production of high proportions of LMC neurons may allow further studies into the particular the defining characteristics of these neurons and why they are so preferentially affected compare with others. For many neurodegenerative diseases the regulation of ER/mitochondrial contacts (Sassano, van Vliet and Agostinis, 2017; Xu, Wang and Tong, 2020), calcium gradients (reviewed in Brini *et al.*, 2014) and lipid synthesis (Aufschnaiter *et al.*, 2017) are coming more into focus, indicating there many more commonalities for neurodegenerative diseases than previously thought. Therefore, the work described on CMT may provide utility to other researchers working in these fields to advance understanding of disease.

In summary, the data presented in this chapter demonstrates the differences in hPSC lines to successfully generate particular differentiated lineages. Additionally, this work describes the optimisation of a differentiation protocol to more specifically generate LMC motor neurons through a 3D dual-SMAD and FGF combined approach.

4) Generation of hPSC clones with a CMT2A patient-relevant mutation

4.1) Introduction

CMT2A is caused by over 100 mutations in *MFN2*, the majority of which cluster near the GTPase domain and cover a wide range of phenotypic severity and onset (reviewed in (Stuppia *et al.*, 2015)). The majority of these mutations are dominant heterozygous point mutations which means the generation of genetically relevant hPSC lines for disease modelling would require the introduction of a precise mutation. To model CMT2A, I chose to introduce patient-relevant *MFN2* mutations into the previously characterised hPSC line MShef11 (as described in Chapter 3).

CRISPR-Cas9 has been utilised to edit multiple different cell types due to its high versatility, which comes from the use of a specific guide RNA (sgRNA) allowing targeting to the desired genomic location. CRISPR is now available for use with a wide range of existing protocols even in previously difficult-to-edit cell types. hPSCs have also been widely used in conjunction with Cas9 (reviewed in Zhang *et al.*, 2017) to model various diseases including familial dysautonomia (Zeltner *et al.*, 2016) and kidney disease in organoids (Freedman *et al.*, 2015). Cas9 introduces double-stranded breaks (DSB) to DNA as directed by the sgRNA. This induces the cell's repair pathways to fix the damage. Repair can be carried out through either NHEJ or HDR. NHEJ involves proteins binding to the ends of the DNA in order to re-join them back together. This is a more common and more error-prone pathway, often used to create knockouts through frameshifts leading to premature stop codons (reviewed in Sharma and Raghavan, 2016). HDR involves the use of the sister chromatids as a template for repair. Through the use of exogenous templates such as single-stranded oligonucleotides (ssODN), this process can be influenced to introduce a specific edit from a small alteration to large-scale alterations (reviewed in Heyer, Ehmsen and Liu, 2010; Liu *et al.*, 2019).

Whilst the presence of Cas9 is essential for the introduction of double-stranded breaks (DSB) to induce the desired repair pathways, the persistence of Cas9 can be either beneficial or not, depending on the desired mutation. Cas9 vector takes longer than mRNA to be expressed as the cell must transcribe and translate the sequence, but also remains present for longer which can lead to repeated cutting of the DNA (Kim *et al.*, 2014). Plasmid-based systems can also lead to stable integration of the Cas9 vector which can be useful for genome-wide studies (Ihry *et al.*, 2018; Ross-Thriepland *et al.*, 2020). Transfection with Cas9 protein removes much of the need for initial processing (transcription and

translation of Cas9), but also leads to faster clearance, which can be beneficial where re-cutting is a concern. Additionally, it has allowed higher efficiency of editing some difficult-to-transfect cell types that are particularly sensitive to the introduction of large plasmids (Kim *et al.*, 2014; Liang *et al.*, 2015).

Careful design of CRISPR-Cas9 components can enhance the likelihood of HDR occurring over NHEJ, as well as making the desired edit easier to find. Components amenable to design include the sgRNA, the repair template, the ssODN (if in use) and even the Cas9 enzyme itself. Increasing the proximity of the sgRNA to the repair site has shown to increase precise editing (Liang *et al.*, 2017), indicating the need to test multiple guides for both their on-target and off-target activities. Altering guide length from the typically 20nt remains somewhat controversial. Guides longer than 20nt appear to be processed down (Ran *et al.*, 2013) suggesting they may not provide much benefit. On the other hand, shorter sgRNA have been shown in some cases to decrease off-target activity without sacrificing on-target activity (Fu *et al.*, 2014) and in others have shown a more severe effect on Cas9 activity (Zhang *et al.*, 2016). The sgRNA can also be subject to sequence or chemical modifications which are intended to increase the efficiency of editing (Yin *et al.*, 2017; Filippova *et al.*, 2019; Scott *et al.*, 2019). This level of modification has been extended to the Cas9 enzyme itself with several versions of Cas9 being available, including high fidelity (Kleinstiver *et al.*, 2016; Vakulskas *et al.*, 2018), nickases (which only cut one strand instead of two) (Ran *et al.*, 2013), Cas9 with linked enzymes (including deaminase, where the Cas9 is dead and is only used to target) (Gaudelli *et al.*, 2017), GFP linked (for ease of locating cells containing Cas9) (Freedman *et al.*, 2015) and generation of Cas9 active only during S/G2 (through the fusion of Cas9 and the first 110 amino acids of Geminin) (Gutschner *et al.*, 2016). Furthermore, chemical enhancement may be used in order to increase the likelihood of HDR (Li *et al.*, 2017; Riesenberger and Maricic, 2018) or inhibit NHEJ enzymes (Maruyama *et al.*, 2015). For the repair template, altering the length of the homology arms depending on the size of the edit required can provide increased efficacy (Liang *et al.*, 2017).

For ease of creating multiple edits, it is possible to produce the sgRNA as two separate parts known as CRISPR RNA (crRNA) and trans-activating CRISPR RNA (tracrRNA). The crRNA is the stretch of RNA which guides Cas9 to the intended location to create the DSB. The tracrRNA is the constant region involved in binding the RNA to Cas9. These two stretches of RNA must be successfully combined and associated with Cas9 in a Cas9:Duplex either outside the cell or after production within the cell for the enzyme to target correctly to the desired location.

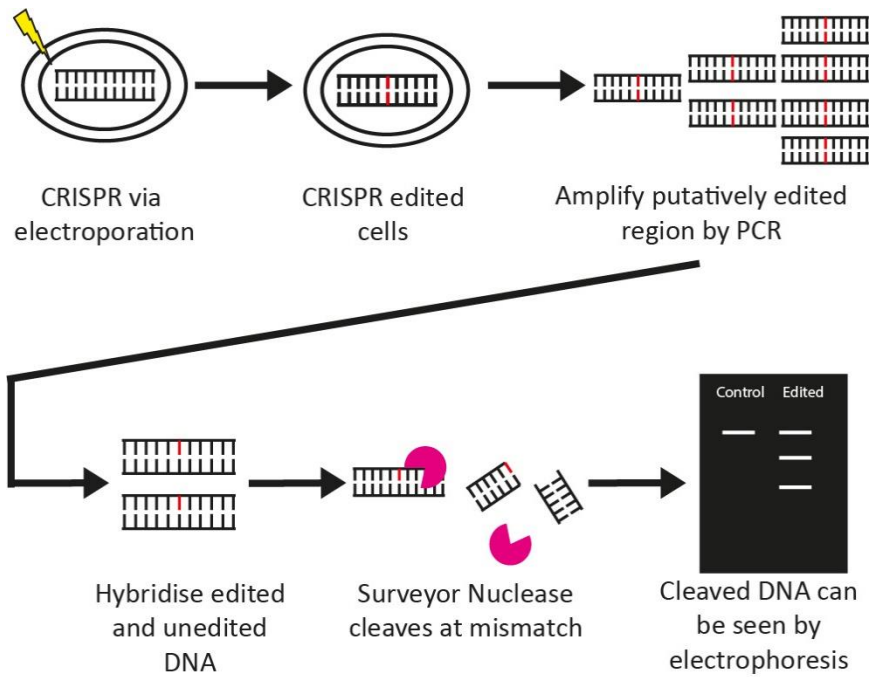


Figure 22: Principles of surveyor nuclease assay. Mismatch detection allows examination of editing efficiency and selection of the most effective guide sequence.

Ultimately, for genetic editing to be successful, Cas9 and associated components must be delivered to the cells in sufficient quantity. Two commonly used methods for hPSC are electroporation and lipid-based transfection. However, particular success appears to be cell line dependent (Singh, 2019), thus adding another element to the list of factors requiring optimisation for successful editing.

Once cells have been putatively edited, it is necessary to identify cells which have been successfully edited to contain the desired mutations and check that they do not contain any off-target mutations. In cases where Cas9/sgRNA have been delivered by plasmid antibiotic selection can be utilised, however, when Cas9 protein is used this kind of selection is not possible. The creation of indels can be measured using enzymes involved in mismatch detection such as surveyor (CEL1 from plants) (Voskarides and Deltas, 2009) and T7E1 (bacterial) (Hye *et al.*, 2009; Cho *et al.*, 2013). Mismatch detection enzymes rely on the hybridisation of putatively edited DNA to control (un-edited) DNA and cleavage of mismatches found (Figure 22). If the guide has allowed sufficient Cas9 targeting to the region DSB will have formed which can be repaired either by NHEJ or HDR. Some NHEJ repairs will have been inefficient leading to mismatches between any hybridised edited and unedited strands that can be recognised by the surveyor nuclease and cleaved, visualisation of these extra DNA fragments can be achieved via gel electrophoresis. In the case of specific editing, it may be possible to create or destroy a restriction site which can be identified through enzymatic digestion or careful primer design.

Eventually, confirmation of the exact mutation is required through sequencing and confirmation of expression.

Introduction of unwanted mutations at sites with sequence similarity remains a problem for all genetic editing technologies and must be carefully evaluated to ensure the success of a model. For CRISPR, mismatches appear to be tolerated better at the 5' end of the guide (reviewed in Zhang *et al.*, 2015) and whilst multiple systems exist for prediction of these unintended cleavage events (Gaj, Gersbach and Barbas, 2013; Singh *et al.*, 2015), the reasons for them are not fully understood making finding off-target mutations through prediction alone very difficult. Use of high fidelity Cas9 (Kleinstiver *et al.*, 2016; Vakulskas *et al.*, 2018) and careful design of CRISPR components can alleviate some concerns but cannot completely remove the risk of off-target activity. Screening a small number of likely individual sites for potential mutation is a relatively simple way to investigate the propensity of the system for the generation of off-target activity. Choosing to investigate only a small number of sites, however, is subject to significant bias though may be preferable to the more expensive exome, or even full genome, sequencing. Further to mutations gained through the CRISPR process, stem cells are particularly prone to the gain of genetic aberrations during culture (Baker *et al.*, 2016) and therefore, must be analysed to ensure DNA integrity. Additionally, retention of stem cell characteristics such as expression of key stem cell markers and pluripotency are essential to ensure that the cell line properties have not been unduly altered as a result of the genetic editing.

The following chapter describes the *in-silico* design and testing of CRISPR guides capable of editing *MFN2* and the ultimate generation of MShf11 *MFN2*^{R94Q/+} lines with no detected off-target mutations that retain stem cell markers.

4.2) Results

4.2.1) Identification of patient-relevant mutations to model and in silico design of appropriate guide RNAs and repair templates

Upon review of literature, I chose three different mutations known to cause CMT2A, including one of the most severe mutations (R94Q) (Züchner *et al.*, 2004), a mutation associated with a mild form of the disease (T105M) (Lawson, Graham and Flanigan, 2005) and mutation associated with a moderate to severe form of the disease (R364W) (Züchner *et al.*, 2006). CRISPR-Cas9 systems are particularly adept at producing highly precise double-stranded breaks (DSB), which can be repaired to incorporate base changes (Cong *et al.*, 2013). This made CRISPR-Cas9 an obvious first choice to use for the

generation of MShef11 lines containing CMT2A relevant mutations. To ensure Cas9 cuts at the correct locus, I sought to design sgRNA to the region of interest and a single-stranded oligonucleotide (ssODN) which would serve as a repair template for the HDR pathway. Various online tools exist for the generation of sgRNA and repair templates for CRISPR-based editing. I used Horizon's (previously known as Dharmacon) CRISPR design tool, which requires input of several parameters such as the human reference genomes and CRISPR enzyme in use. I chose human reference genome (hg38), *Streptococcus pyogenes* Cas9 and *MFN2* (gene id reference 9927). The R94Q mutation is found within exon 3 of *MFN2* (Figure 23A), and hence in the CRISPR design tool, I selected this region and the nucleotide that would need to be edited to cause the desired mutation (Figure 23B). The software generated several guides to this region which were ranked according to their functionality (1-7) and coloured according to their specificity (high/medium). I prioritised guides which had strong functionality and specificity and that were close to the intended repair site. Using these guidelines, I selected up to three potential guides for each location. Using these sequences and the Horizon HDR Donor Designer tool, I designed the ssODN for the repair template. This tool uses the sgRNA sequence to locate the region of cutting. I selected the exact nucleotide I wished to alter and the desired change would be (Figure 23C) and from this, I created the ssODN which would allow the point mutation to take place (Figure 23D). As the intended edit was only a single nucleotide, the ssODN length did not need to exceed 80bp (larger arms are needed for larger edits) with homology arms of ~30bp on either side. A similar process was carried out for T105M located in exon 4 (Figure 24A, 24B, 24C, 24D) and R364W located in exon 10 (Figure 25A, 25B, 25C, 4D), however only two guides were designed for both of these regions as high specificity guides were more easily available than for the R94Q site. For R364W a secondary mutation was added to the ssODN to ensure that Cas9 was not capable of re-cutting the site (Figure 25D). The addition of a secondary mutation is essential as re-cutting of the same location would increase the chance that indels would form (as NHEJ is more likely to occur than HDR) (Maruyama *et al.*, 2015). The particular mutation chosen is a silent mutation which would remove the PAM sequence, but other mutations suggested would impede the binding of the sgRNA itself.

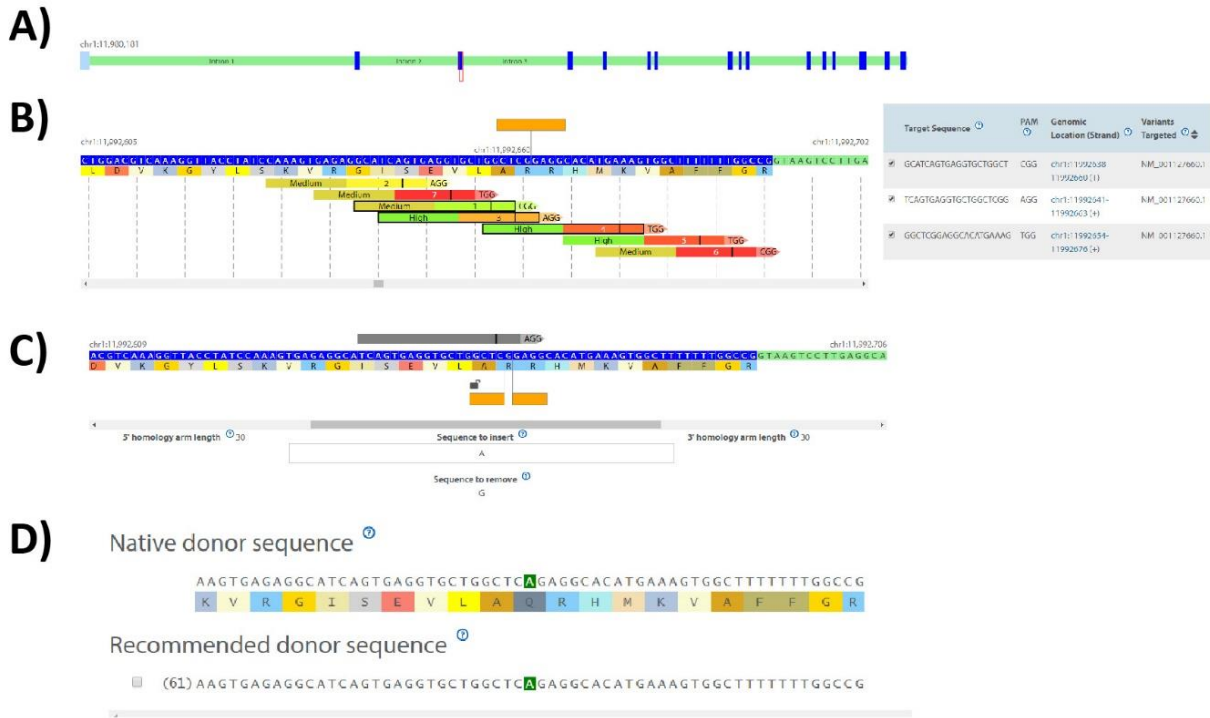


Figure 23: Design of sgRNA and repair template for the generation of *MFN2* R94Q mutation. A) *MFN2* on chromosome 1 in Horizon Cas9 Design Tool. Green regions indicate noncoding intronic regions. Dark blue regions indicate exons. Light blue regions outer regions of *MFN2* coding sequence. The red box indicates a section containing the site to be edited for production of R94Q mutation and viewed in B). **B)** A zoomed-in region of *MFN2* including the chromosomal location in Horizon Cas9 Design Tool. The genomic sequence can be seen along with the corresponding protein-coding sequence. The yellow bar at the top indicated intended cut site for Cas9 to allow the production of R94Q mutation. Below are suggested guides to enable Cas9 targeting to this region. Guides are coloured according to their specificity (high/medium) and ranked on their functionality (1-7). Guide PAM sequences are also shown. Guides selected have a black outline, sequences for these guides are shown on the right. **C)** A zoomed-in region of *MFN2* including the chromosomal location in HDR ssODN design tool. The genomic sequence can be seen along with the corresponding protein-coding sequence. The guide used for Cas9 targeting shown as grey above the genomic sequence. Yellow bars below protein-coding sequencing indicate the area which is intended to be edited by HDR to produce R94Q mutation. Below is the intended changed nucleotide. **D)** Design outputs from HDR ssODN design tool. Intended edited nucleotide highlighted in green, output protein-coding sequence is displaced beneath which shows codon containing the highlighted nucleotide will now produce glutamine instead of arginine.

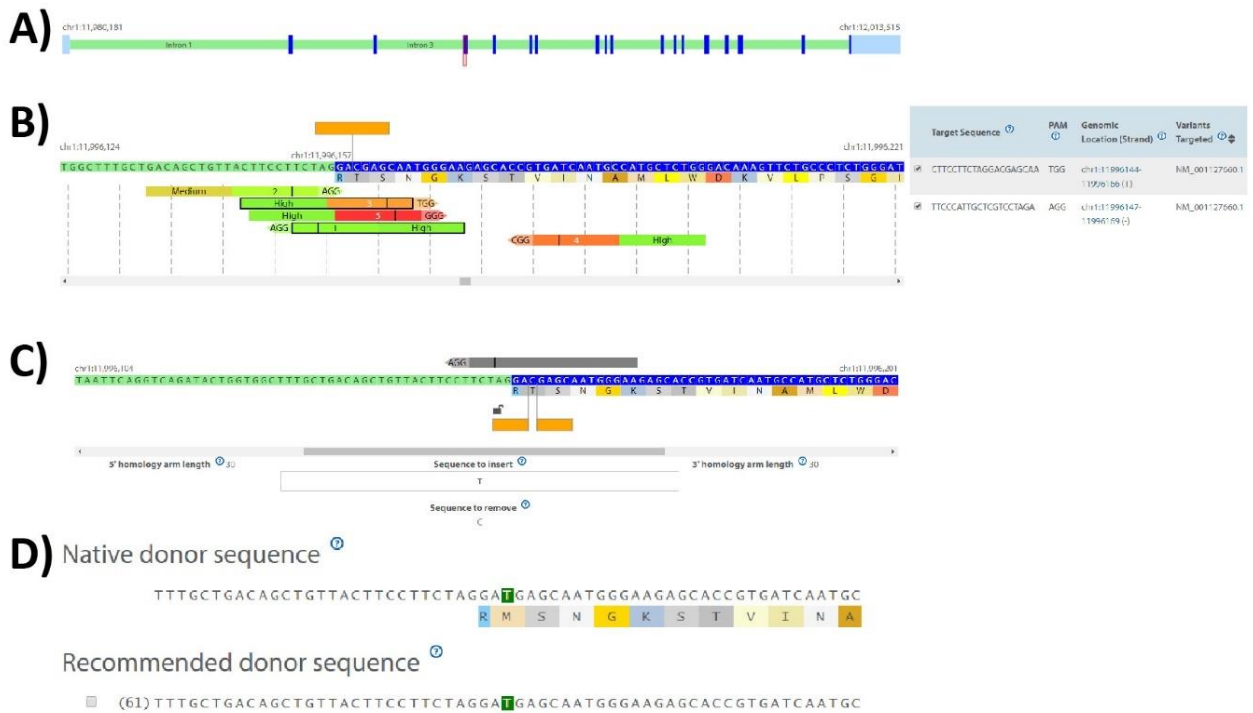


Figure 24: Design of sgRNA and repair template for the generation of *MFN2* T105M mutation. A) *MFN2* on chromosome 1 in Horizon Cas9 Design Tool. Green regions indicate noncoding intronic regions. Dark blue regions indicate exons. Light blue regions outer regions of *MFN2* coding sequence. The red box indicates a section containing the site to be edited for production of T105M mutation and viewed in B). **B)** A zoomed-in the region of *MFN2* including the chromosomal location in Horizon Cas9 Design Tool. The genomic sequence can be seen along with the corresponding protein-coding sequence. The yellow bar at the top indicated intended cut site for Cas9 to allow the production of T105M mutation. Below are suggested guides to enable Cas9 targeting to this region. Guides are colour according to their specificity (high/medium) and ranked on their functionality (1-5). Guide PAM sequences are also shown. Guides selected have a black outline, sequences for these guides are shown on the right. **C)** A zoomed-in region of *MFN2* including the chromosomal location in HDR ssODN design tool. The genomic sequence can be seen along with the corresponding protein-coding sequence. The guide used for Cas9 targeting shown as grey above the genomic sequence. Yellow bars below protein-coding sequencing indicate the area which is intended to be edited by HDR to produce T105M mutation. Below is the intended changed nucleotide. **D)** Design outputs from HDR ssODN design tool. Intended edited nucleotide highlighted in green, output protein-coding sequence is displaced beneath which shows codon containing the highlighted nucleotide will now produce methionine instead of threonine.

... cont. secondary cutting. To this end, multiple alternative silent mutations are displayed below.

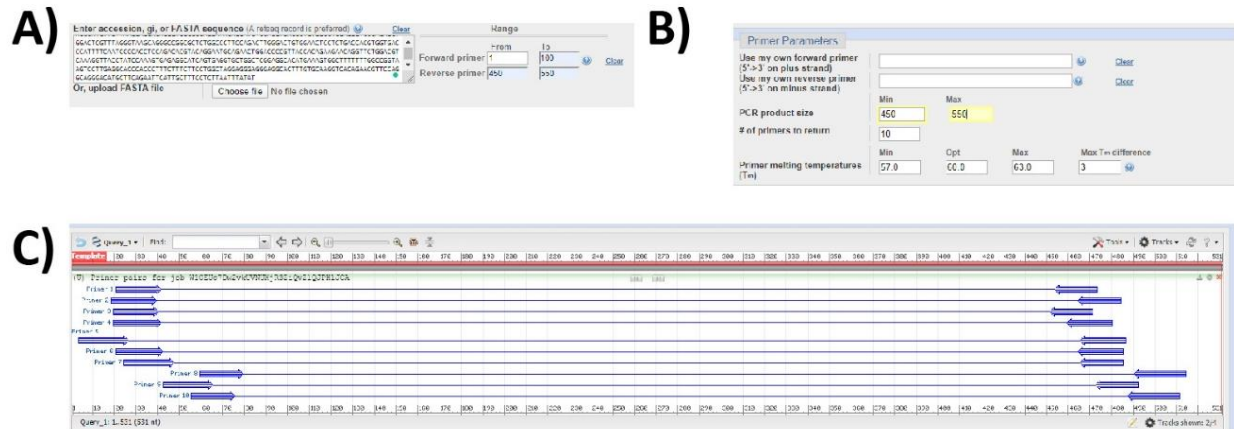


Figure 26: Design of primers to amplify the region of *MFN2* that would contain the R94Q mutation.

A) Input for primer design on Primer-BLAST of the region of *MFN2* containing the sequence required to be edited for R94Q mutation. **B)** Alteration of settings for primer generation on Primer-BLAST to product a smaller product than the default. **C)** The output of Primer-BLAST settings showing potential primer pairs.

As successful editing of cell lines would need to be confirmed via Sanger sequencing, I required primers capable of amplifying each region of *MFN2*, which could be interrogated for sequence changes. I designed primers using PRIMERBLAST where the sequence for amplification was added to the software (Figure 26A) and adjusted so it could produce a PCR product of ~500bp (Figure 26B). The primers were designed so that the edited region would be at least 100-150 bp away from either primer to ensure that it could be seen clearly after sequencing. Examples of primers output are shown (Figure 26C).

In summary, sgRNA, ssODN and accompanying primers were designed *in silico* for the future production of hPSC lines containing CMT2A-causing *MFN2* mutations R94Q, T105M and R364W.

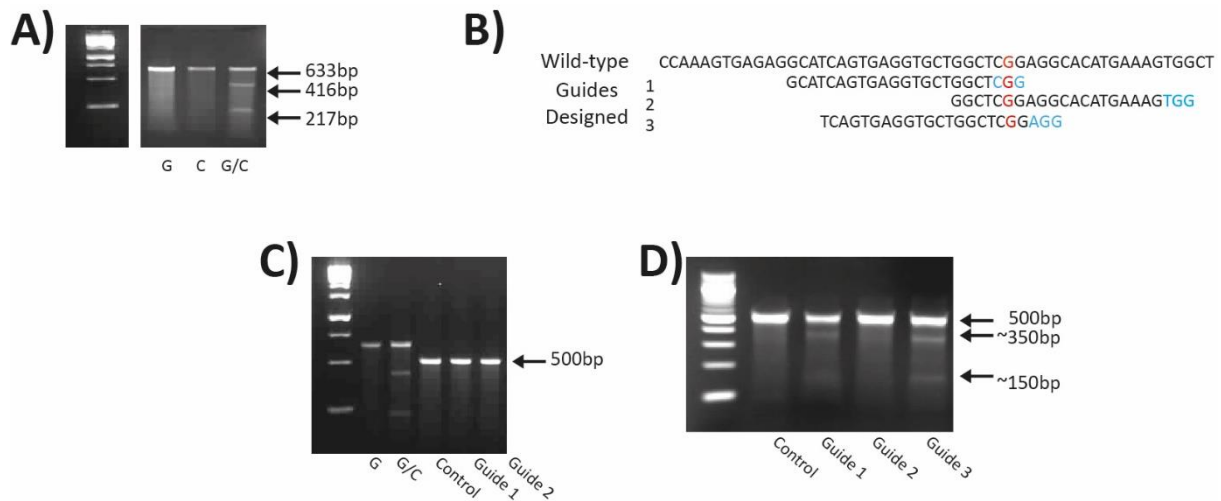


Figure 27: Assessment of R94Q guide efficacy by surveyor nuclease assay. A) Surveyor assay test. G and C are control DNA sequences supplied with the kit that when hybridised should produce the intended bands as shown. **B)** Sequence of intended edit location and guides designed to target this area. PAM is indicated in blue, nucleotide to be edited is shown in red. **C)** Unsuccessful CRISPR editing using STEMCELL Technologies Cas9 kit. Control DNA was not edited with CRISPR. **D)** Successful CRISPR editing using IDT ALT-R CRISPR as shown by the presence of extra bands. Control DNA was not edited with CRISPR.

4.2.2) Assessment of sgRNA efficacy

For all the mutations I had chosen to model, HDR would be required to introduce the specific mutation meaning the creation of indels would need to be minimised. To minimise the chances of off-target cutting (Kim *et al.*, 2014) and on target-recutting, I chose to use Cas9 as a protein and to bind it to the sgRNA in a Cas9:Duplex prior to transfection. Guides were ordered as separate crRNA and tracrRNA which have to be combined to form the sgRNA itself, increasing the flexibility of the system allowing the testing of multiple guides and ultimately editing of multiple regions. To identify which of the *in-silico* designed guides had the highest efficiency of introducing DSB, I utilised the Surveyor assay to screen for mismatched DNA. Initially, to confirm the assay was capable of showing the presence of mismatched DNA, I tested the built-in controls named G and C which when hybridised and cleaved should produce bands at 416bp and 217bp (Figure 27A). Previous work in our

laboratory had optimised electroporation for hPSC lines, therefore I chose to use this method to introduce the previously designed crRNA for MFN2^{R94Q} (Figure 27B) as made by STEMCELL Technologies, and ArciTect Cas9-GFP (with tracrRNA) to HeLa cells. I utilised HeLa cells to optimise the process due to their ease of growing and transfection. Additionally, I chose to use a GFP tagged Cas9, as this would make it possible to sort cells containing Cas9 after transfection, therefore, helping in the identification of putatively edited CRISPR clones. After hybridisation and digestion, I assessed the

production of extra DNA fragments by gel electrophoresis and found the samples containing CRISPR and sgRNA to have no extra bands, suggesting indels were not present in these samples (Figure 27C). This may have been due to poor transfection, poor targeting or poor Cas9 activity or poor detection



Figure 28: Assessment of T105M guide efficacy by surveyor nuclease assay. A) Sequence of wild-type *MFN2* sequence along with several guides designed to allow Cas9 targeting to this region. Nucleotide to be edited in order to generate T105M mutation highlighted in red. PAM sequence indicated in light blue. **B)** Successful CRISPR editing using IDT ALT-R CRISPR. Control DNA was not edited with CRISPR.

by the surveyor nuclease.

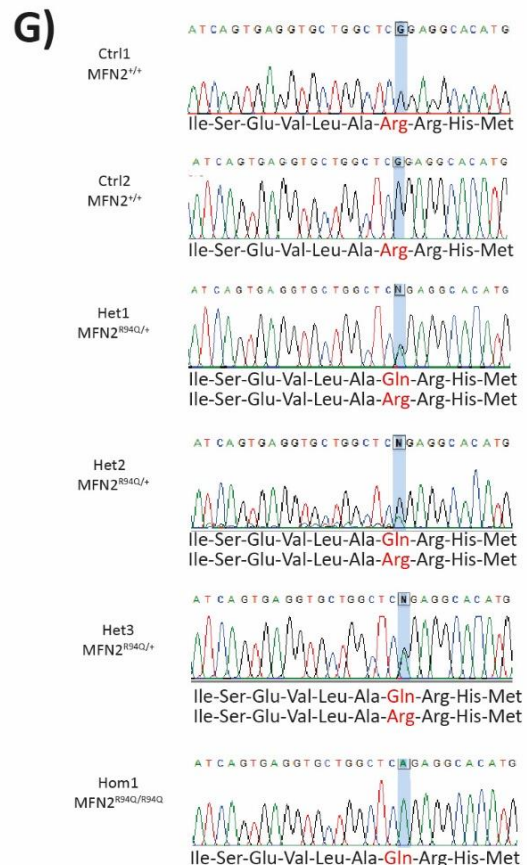
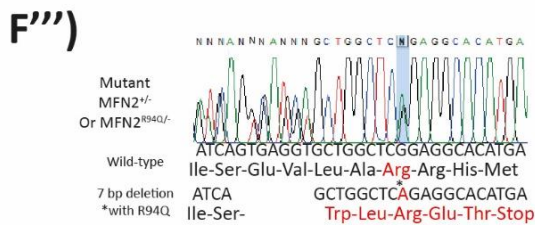
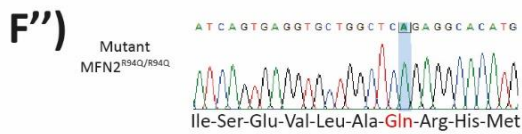
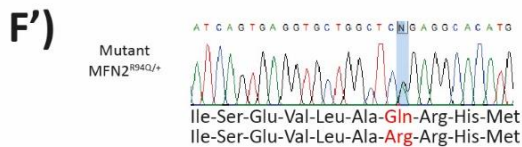
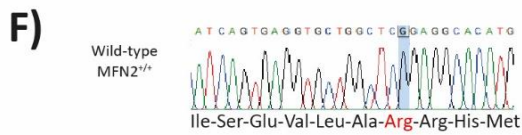
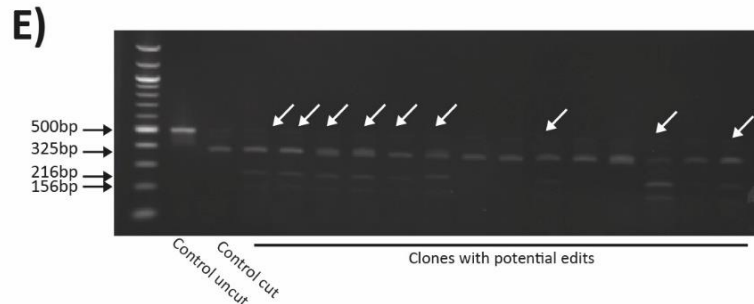
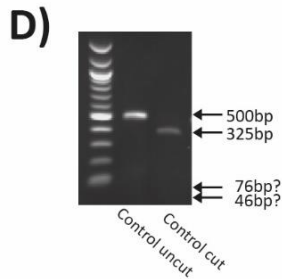
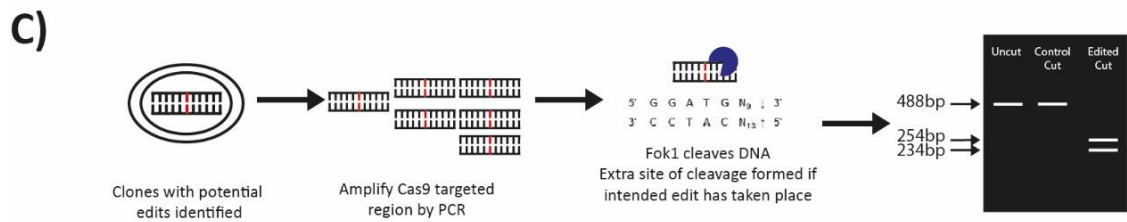
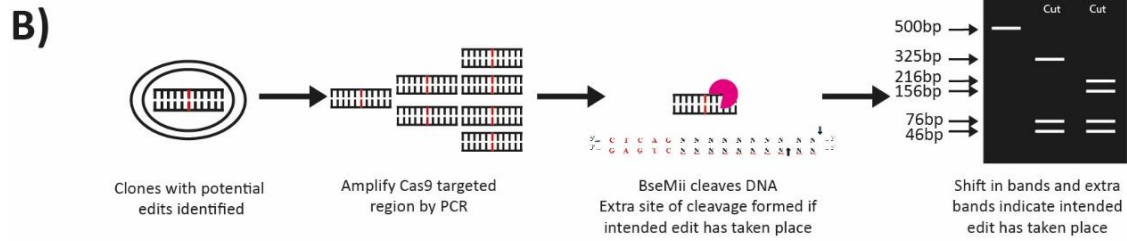
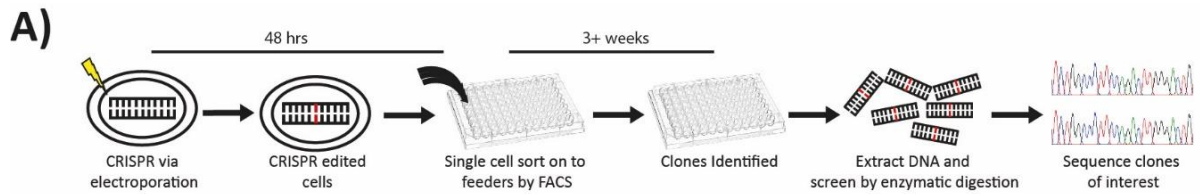
The settings utilised for the transfection were previously optimised for another hPSC cell line, therefore I began to use MShef11 in preference to HeLa cells as I wanted to optimise the entire editing process specifically for this line. I designed a third guide for *MFN2*^{R94Q} (Figure 27B) to assess if the guide targeting was an issue. Additionally, I tested a different version of Cas9 due to reagent availability, this was IDT Alt-R Hi-Fi Cas9 and related crRNA/tracrRNA. The Alt-R Hi-Fi Cas9 is a high-fidelity version of Cas9 which has been designed to reduce off-target cutting and increase on-target activity (Vakulskas *et al.*, 2018), however, this enzyme did not have a GFP tag which would increase the number of clones I would be required to screen later in the process. I carried out the same editing and assessed efficacy of DSB generation via the surveyor assay and electrophoresis. Extra bands can be seen on the gel for both guide 1 and guide 3 (Figure 27D), suggesting successful indel production had occurred in these samples. Guide 3 had the brightest extra bands, indicating it to be the more efficacious of the three crRNA and so was chosen to be the crRNA used for generation of *MFN2*^{R94Q} mutations. This process was also carried out for crRNA designed to generate *MFN2*^{T105M} (Figure 28A) and assessment with the surveyor assay and electrophoresis showed a single extra band present on the gel for each guide (Figure 28B). This band appears to be ~250bp suggesting the DSB may have occurred near the centre of the amplified sequence resulting in two approximately equal-size fragments which were not sufficiently separated during electrophoresis. Guide 2 had the brightest band, indicating it to be the more efficacious of the two crRNA and so was chosen to be the crRNA

used for generation of MFN2^{T105M} mutations. Due to the expense of guide generation, MFN2^{R364W} crRNA has not yet been tested in this way.

In summary, the efficacies of multiple crRNAs targeted to exon 3 and exon 4 of *MFN2* were tested in MShef11 through the use of the surveyor assay. For each location, the highest performing guide was indicated through the production of mismatched DNA cleaved by the surveyor nuclease and could be used for the future generation of specifically edited hPSC.

4.2.3) Generation and identification of CRISPR edited hPSC

As HDR is a rarer form of DNA repair for DSB compared with NHEJ (Maruyama *et al.*, 2015), it would be necessary to screen many colonies to identify cells that have been edited correctly. Additionally, as I had chosen to utilise a protein-based Cas9 enzyme, I could no longer select via antibiotic resistance nor via fluorescence as I had optimised transfection using a non-GFP tagged Cas9. I instead investigated DNA-based methods that could be used to detect the presence of edited DNA in MShef11. To this end, I set out to design an enzymatic digestion screen (Figure 29A) that would rely on the introduction of the desired nucleotide change generating a new enzymatic restriction site. For both MFN2^{R94Q} and MFN2^{T105M}, an extra restriction site is generated if the mutation is present and can be cleaved by *BseMIII* for MFN2^{R94Q} (Figure 29B) and *FokI* for MFN2^{T105M} (Figure 29C). Cleavage of this extra site would produce additional bands on a gel when separated by electrophoresis. However, using the enzymatic digestion assay would not distinguish between homozygous, heterozygous and indels also containing the intended edit, meaning it would be necessary to sequence all colonies positive in this screen. In order to ensure that lines were clonal, it was necessary to introduce a single-cell cloning step into the procedure which would take 3 weeks for the cells to grow back from (Figure 8A). To maximise chances of producing a successful model, I chose to focus on the MFN2^{R94Q} mutation as it is the most severe of the mutations optimised the process for and arguably had the highest chance of mimicking the disease phenotype. In order to confirm the principle of the enzymatic digestion, I digested an unedited sample of MShef11 DNA and assessed band production via gel electrophoresis. The size of the bands was smaller in the digested sample and approximately matched the size of bands predicted *in silico* (Figure 29B, 29D). However, some of the smallest predicted fragments were not present on the gel, this may have been due to their small size having either allowed them to move off the gel or due to being too faint to detect with the equipment available to me.



(Previous page) Figure 30: Generation and screening of MShef11 clones containing CMT2A mutations in *MFN2*. **A)** CRISPR editing protocol with single-cell cloning of hPSC to identify pure populations of cells with *MFN2* R94Q mutation. **B)** Proposed result of the enzymatic digestion screening method for *MFN2*^{R94Q} mutants. **C)** Proposed result of the enzymatic digestion screening method for *MFN2*^{T105M} mutants. **D)** Test of BseMii enzyme on unedited DNA. A shift in band size can be seen, however, small bands cannot be identified. **E)** Example output of enzymatic screen of putatively edited cells. Arrows indicated samples with extra bands suggesting the presence of the *MFN2*^{R94Q} mutation. **F)** Sanger sequencing output from the enzymatic screen in (E). Sample with no extra bands produced wild-type result (F). Samples with extra bands, indicating the presence of the desired mutation, returned several results, heterozygous (F'), homozygous (F'') or indel containing R94Q mutation (F'''). **G)** Sanger sequencing of the panel of lines for ongoing work.

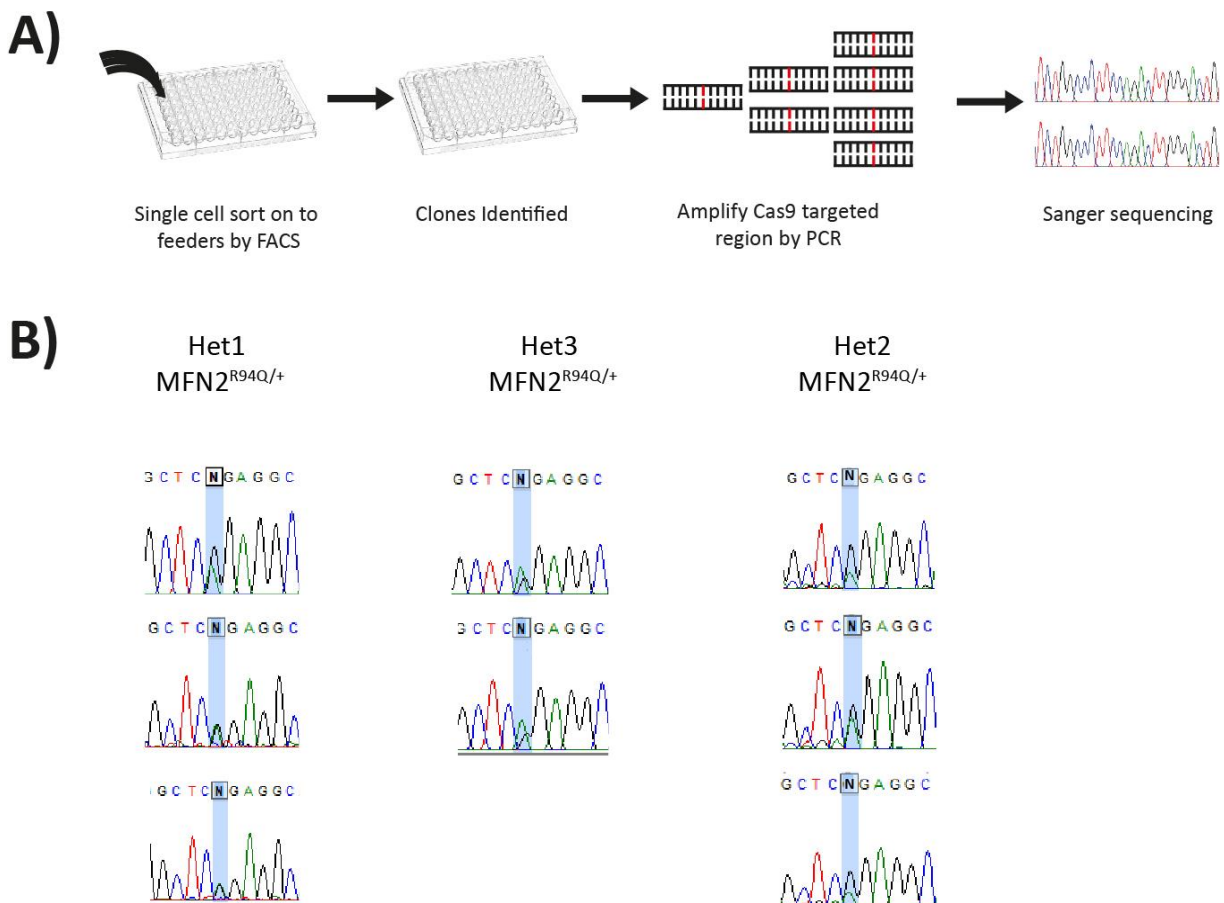


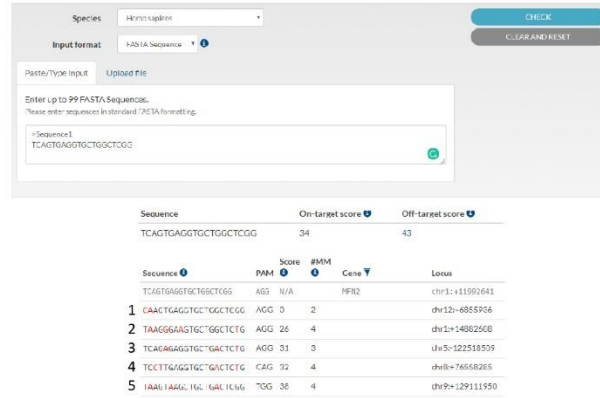
Figure 29: Confirmation of heterozygous mutation in MShef11 *MFN2*^{R94Q/+}. **A)** Single-cell sorting of clones method to confirm heterozygosity. **B)** Sanger sequencing from multiple clones of mutant *MFN2*^{R94Q/+} lines.

Having optimised all the necessary parts of the protocol, I carried out the CRISPR electroporation, along with the ssODN, and the cloning process as described in Figure 8A. After the growth period, clones were assessed for the presence of MFN2^{R94Q} in the enzymatic digestion screen. Many samples showed extra DNA fragments suggesting the presence of an extra restriction site and, therefore, MFN2^{R94Q} (Figure 29B, 29E). As previously noted, the smallest bands were still not present on the gel (Figure 29D). DNA was extracted from clones of interest and sent for Sanger sequencing. Several different types of edited clones were identified including MFN2^{R94Q/+} (Figure 29F'), MFN2^{R94/R94Q} (Figure 29F'') and indels which also contained the mutation (either heterozygous or homozygous, however, it is not possible to tell in the former case which strand the mutation is on) (Figure 29F'''). To confirm the accuracy of the enzymatic screen, several samples which did not show the presence of extra fragments upon digestion were also sent for sequence and showed a wild-type MFN2^{+/+} sequence (Figure 29F) indicating the screen to be successful. From the sequenced clones, I chose clone 3F5 as an MFN2^{+/+} control, three MFN2^{R94Q/+} clones 7G7, 3E9, 1E2 and one MFN2^{R94Q/R94Q} clone 7G10 for further analysis. From this point lines will be referred to in the following way, control lines (parental line MShef11 and 3F5) will be Ctrl1 MFN2^{+/+} and Ctrl2 MFN2^{+/+} respectively, heterozygous lines (7G7, 3E9, 1E2) will be referred to as Het1 MFN2^{R94Q/+}, Het2 MFN2^{R94Q/+} and Het3 MFN2^{R94Q/+} and the homozygous line will be referred to as Hom1 MFN2^{R94Q/R94Q} (Figure 29G).

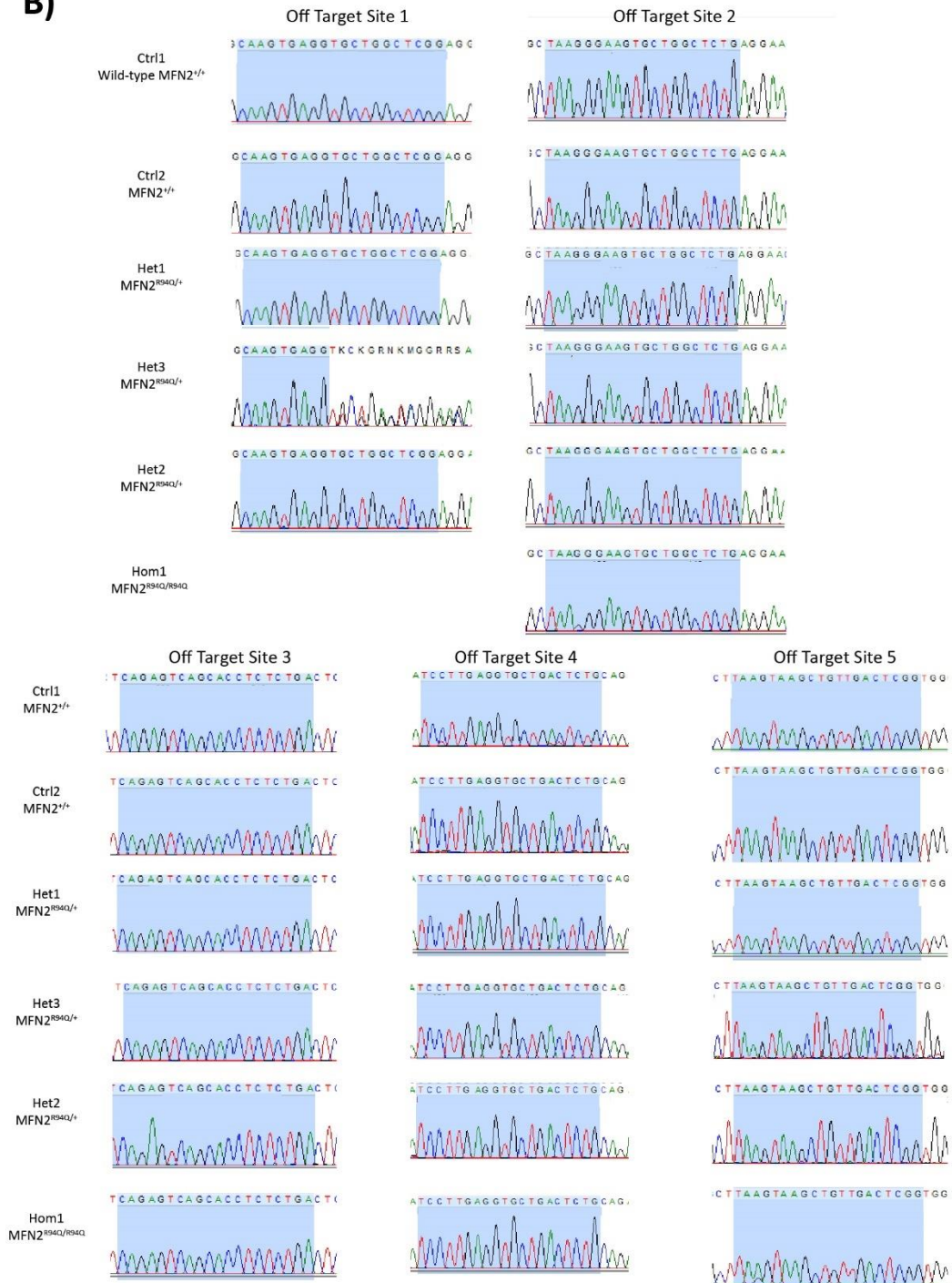
The populations sequenced were sorted by FACS to single cells, however the Sanger sequencing data obtained was from an average of cells of each clone, meaning a signal showing MFN2^{R94Q/+} could in actuality be a mix of any combination of normal/heterozygous/homozygous as this would appear identically on the sequencing readout. This could happen if the single-cell sort was not accurate or if the generation of DSB and subsequent repair took place after sorting (creating a mixed population within the well). In order to confirm that MFN2^{R94Q/+} lines were truly heterozygous populations they were re-cloned via FACS (Figure 30A) and surviving colonies were sequenced confirming their heterozygous genotype (Figure 30B). Confirmation of clone identity as possessing MFN2^{R94Q/+} means I have successfully generated hPSC lines containing a CMT2A relevant mutation.

In summary, this data indicates I have successfully edited and cloned MShef11 MFN2^{R94Q/+} lines. Additionally, I have produced MFN2^{R94Q/R94Q} lines and MFN2^{+/+} control lines which will allow for the robust characterisation of the cellular phenotype carried by this mutation in MShef11 hPSCs and their differentiated derivatives.

A)



B)

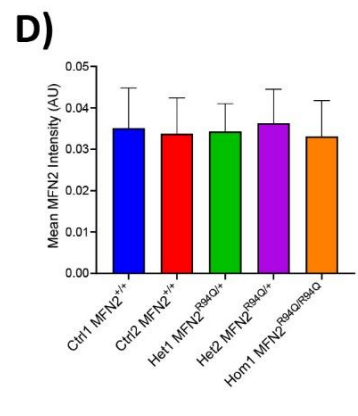
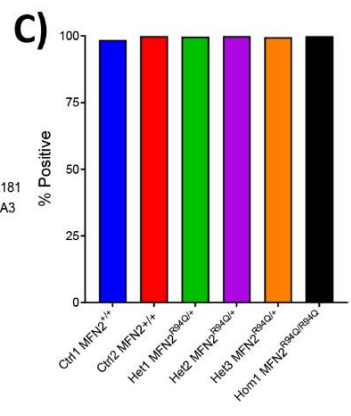
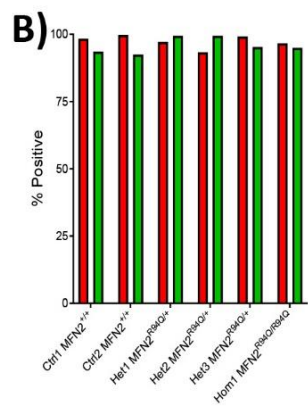
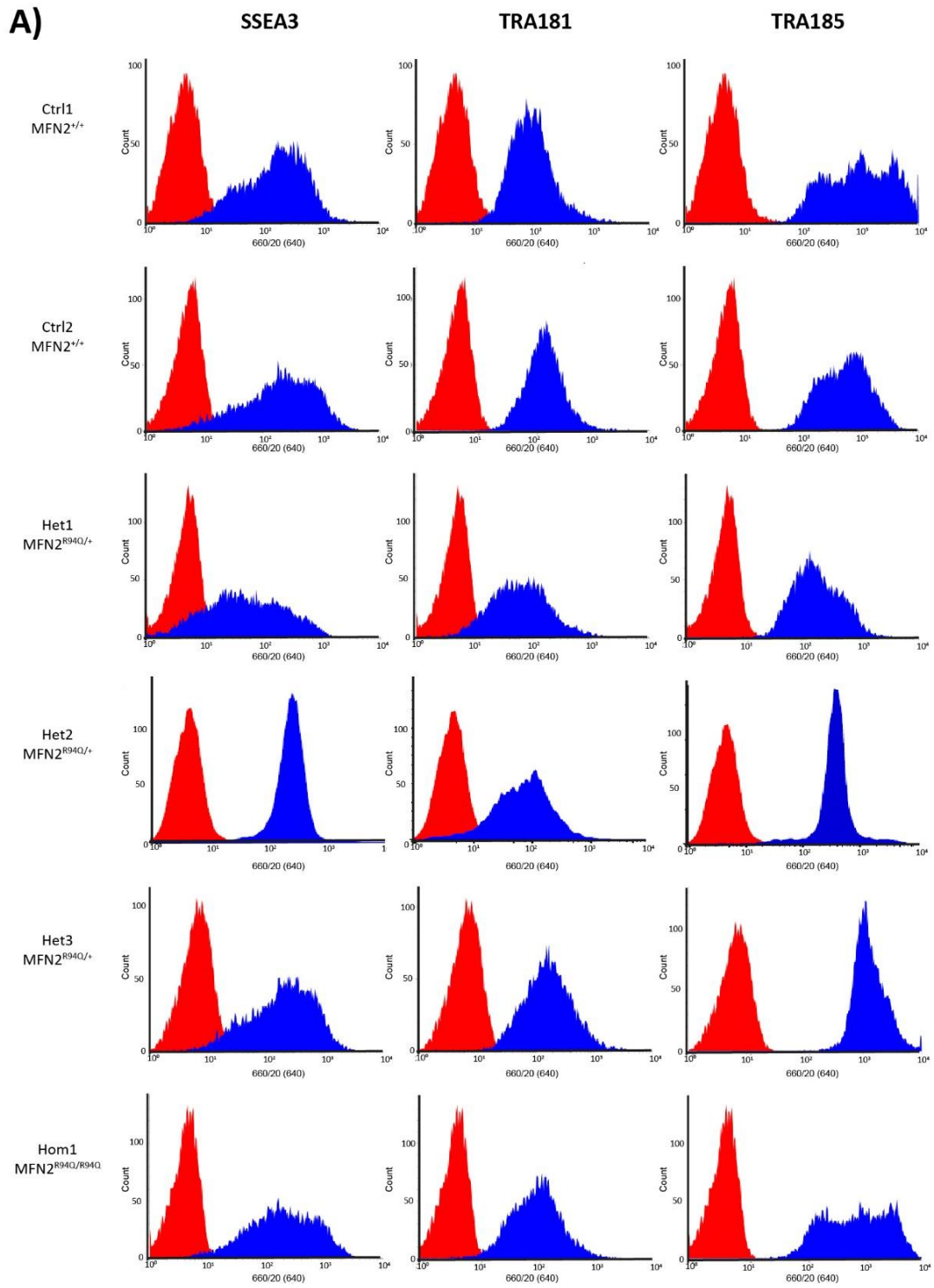


(Previous page) Figure 31: Identification and screening of potential off-target mutations. A) IDT CRISPR guide checker tool to analyse the potential off-target hits of the R94Q guide identified as the best from the previous surveyor assay. Potential off-target hits have a score depending on their likelihood to hit the site (lower indicated higher likelihood) and the number of mismatches (MM) noted. The gene name is only present if the site is in a coding region. **B)** Sanger sequencing results for each off-target location for each line tested.

4.2.4) Assessment of Cas9 off-target activity in genetically edited hPSC

CRISPR-based editing systems are known to have specificity issues leading to the generation of unintended DSB (Zhang *et al.*, 2015) which may produce phenotypic effects unrelated to intended mutation. As an initial step, I chose to use a high fidelity Cas9 which would limit the risk, however not removing it completely. To confirm the chosen clones were free from unintended editing, I investigated the top most likely target locations for the sgRNA used for clone generation. I utilised the IDT Guide checker to generate a list of potential mismatched locations where the MFN2^{R94Q} crRNA may be likely to bind. From this list, I chose to investigate the top 5 most likely sites and designed primers to amplify and sequence these regions (Figure 31A). All clones were analysed and compared to Ctrl1 MFN2^{+/+}. Sites 2-5 were free of mutation, however, Het3 MFN2^{R94Q/+} showed an indel at site 1 (Figure 31B). This was the most difficult site to sequence, due to its high similarity to the intended edit site and the highly repetitive sequence in the surrounding area. Therefore, this clone was used for several experiments before this discovery, but its usage stopped once this finding became clear. This off-target site is in intron 3 of *USP5* and it is not known how this may affect cellular phenotypes.

(Next page) Figure 32: Assessment of hPSC markers in genetically edited hPSC. A) Fluorescence intensity for wild-type and edited MShef11 lines for stem cell markers SSEA3, TRA-1-81 and the pan-human marker TRA-1-85. **B)** Summary of SSEA3 and TRA-1-81 geometric mean data analysis of (A). **C)** Summary of TRA-1-85 geometric mean data analysis of (A). **D)** Summary of image analysis for mean MFN2 intensity. Data shown are the mean \pm SD. N=10 images, technical repeats.



4.2.5) Assessment of hPSC markers, MFN2 expression and karyotypic identity in genetically edited hPSC

Single-cell cloning of hPSCs is typically a bottleneck in the generation of genetically edited hPSC due to poor survival rate (Watanabe *et al.*, 2007; Barbaric *et al.*, 2014). Additionally, it is known that stem cells can gain genetic changes which can increase their chance of survival in this process (Draper *et al.*, 2004; Price *et al.*, 2019) therefore I checked for genetic aberrations via karyotype and qPCR analysis (Baker *et al.*, 2016; Laing, Halliwell and Barbaric, 2019). All lines were assessed and found to be karyotypically normal (data not shown).

Undifferentiated hPSC can be identified through the presence of immature undifferentiated markers such as SSEA3 (Shevinsky *et al.*, 1982) and TRA-1-81 (Badcock *et al.*, 1999). As a control, the pan-human marker TRA-1-85 (Williams *et al.*, 1988) was also utilised. In order to ensure that the cloning process had not caused them to lose their stem cell characteristics, stem cell markers were assessed via FACS analysis. All lines were found to be >91% SSEA3⁺ (Figure 32A, 32B), >93% TRA-1-81⁺ and 100% TRA-1-85⁺ (Figure 32A, 32C). Together this data indicates that the hPSC lines retained their markers of undifferentiated state after genetic editing, which make makes them viable candidates for further differentiation and modelling of CMT2A.

As *MFN2* is not typically found to be differentially expressed in CMT2A (Amiott *et al.*, 2008; Larrea *et al.*, 2019), I decided to check the levels of expression to investigate if the editing process had altered *MFN2* expression. I stained plated control and edited stem cells with an antibody targeting *MFN2* and compared the expression of *MFN2* using the intensity of the *MFN2* stain. The average mean intensity of the cells did not show any differences (Figure 32D) indicating there is no difference in the expression of *MFN2* across the population.

4.3) Discussion

In summary, this chapter details the successful generation of MShel11 clones containing *MFN2*^{R94Q/+} mutation which have no detected off-target mutations and have retained relevant stem cell characteristics. Further to this, *MFN2*^{R94Q/R94Q} lines and lines containing a variety of indels were also generated which could prove useful for further study of *MFN2* function and its role in CMT2A.

To date, this is the only reported production of CMT line through the editing of genetically normal hPSC. Previous work has been focused on the use of patient iPSC and the generation of isogenic or sibling controls (Saporta *et al.*, 2015; Kim *et al.*, 2016; Rizzo *et al.*, 2016; Kitani-Morii *et al.*, 2017; Juneja

et al., 2018; Shi *et al.*, 2018). As iPSC are known to epigenetically retain an epigenetic phenotype from their previous identity, which can affect differentiation (Kim *et al.*, 2010; Bar-Nur *et al.*, 2011; Nishizawa *et al.*, 2016), production of iPSC lines can make downstream differentiation, modelling and comparisons more difficult. The generation of lines via the introduction of disease-causative mutations allows comparison of different mutations and, ultimately, may help answer questions around disease penetrance which differs among families with the same mutation (Nakhro *et al.*, 2013; Choi *et al.*, 2015).

Initially, I intended to produce an allelic series of CMT2A mutations which would allow the study of them in series to see how each mutation contributed to cellular phenotype. Due to time constraints, I chose to prioritise the generation of MFN2^{R94Q/+}, which is one of the most phenotypically severe mutations found in CMT2A patients. The first attempt to generate DSB with CRISPR involved the use of the ArciTect Cas9 system from STEMCELL but did not show the successful generation of indels when analysed by the surveyor assay. This was potentially due to poor transfection as settings were previously optimised for hPSC lines rather than HeLa cells, which whilst comparatively easy to transfect when compared with stem cells, still require their own optimised settings. Additionally, HeLa cells are known to have a far more complex karyotype than the normal diploid karyotype (Harris *et al.*, 2003), which may have resulted in difficulty targeting or identifying mutations in these cells. As guide 1 was shown to be successful in MShef11 when used in combination with the Alt-R Hi-Fi Cas9 system (suggesting this guide was capable of targeting to MFN2) it is possible that whilst this guide may have been successful in HeLa cells the surveyor assay was not sensitive enough to pick up the mutations. Utilization of T7E1 over surveyor, which is reported to be more sensitive (Vouillot, Th  lie and Pollet, 2015), or TIDE sequencing to locate indels may have provided increased sensitivity (Vouillot, Th  lie and Pollet, 2015; Sentmanat *et al.*, 2018) to understand what was happening in the HeLa system and which guide was optimal in MShef11. Use of these systems may also help understand the presence of only one extra band for the T105M mutation as the sequence of the indels would be visible. Ultimately, MFN2^{R94Q} sgRNA 3 clearly showed the highest activity despite being only three bases in nucleotide sequence different from guide 1, indicating the importance of testing multiple guides to gain the best on-target activity.

When introducing point mutations, it is often necessary to create a secondary mutation to prevent the repeated cutting of Cas9. This mutation is intended to be silent but can often have unintended consequences such as changing the substrate affinity (Kimchi-Sarfaty *et al.*, 2007), mRNA stability (Duan *et al.*, 2003) and intron retention (Yadegari *et al.*, 2016). This has led to the need for ‘scarless

editing' where secondary mutations are removed in a second round of CRISPR. MFN2^{R94Q} mutant lines did not require this second round of mutations as the point mutation itself would prevent further binding to that allele. However, if I had proceeded with making MFN2^{R364W} this would have been a necessary step and should be carefully considered for any future work.

In the assessment of off-target activity of guide 3, I checked only five specific locations for the presence of indels and found activity at one of the sites for clone Het3 MFN2^{R94Q/+} which also possessed the MFN2^{R94Q/+} mutation. The work described here indicates that despite careful design and the use of a high fidelity Cas9 enzyme off-target mutation is still a significant issue for CRISPR based systems. Previous studies have shown that titration of guide concentration can reduce off-target effects faster than on-target effects (Zhang *et al.*, 2015) or more novel CRISPR enzymes include inbuilt 'proofreading' capabilities (Chen *et al.*, 2017) may have helped reduce the chance of off-target activity. However, there may be off-target hits in other clones generated in this work that were not investigated, meaning it may be important to carry out full exome sequencing or even full genome sequencing. Additionally, this leaves the use of CRISPR for therapeutic applications in genetic diseases, such as CMT2A, as still somewhat distant and underlies the importance of the generation of genetically accurate models to increase understanding until such treatments may be considered viable and safe.

Although HDR is less likely to be the repair pathway involved in the repair of DSB, multiple instances of MFN2^{R94Q} mutation were found from the surviving clones. Indeed, more homozygous clones were found than heterozygous and many clones contained indel mutations indicating multiple cutting events took place in the cells. This further supports the importance of careful sgRNA and ssODN for editing as MFN2^{R94Q} sgRNA 3 was only a few base pairs from the intended altered nucleotide and the ssODN had short homology arms which may have contributed to their strong activity (Liang *et al.*, 2017). Ultimately, this design made finding a solely heterozygous mutant more challenging and therefore it may have been more beneficial to have used a less efficient guide, such as guide 1, or to have titrated the guide concentration down to reduce the amount of Cas9 targeting. Increasing the rate of HDR through the use of small molecular enhancers or use of an alternative Cas9 may have decreased the number of indels picked up in the screening step, however, this may have further complicated the difficulty generating the heterozygosity required for accurate modelling of CMT2A. Whilst MFN2^{R94Q/R94Q} is not a mutation found in patient populations, further study in a cellular setting may help increase understanding of the contribution of the mutation to disease phenotype especially when used in conjunction with the MFN2^{R94Q/+} model.

In summary, this chapter describes the generation of MShf11 lines containing the CMT2A mutation MFN2^{R94Q/+} along with wild type control lines and even MFN2^{R94Q/R94Q}. Additionally, conditions were optimised for the transfection of MShf11 which could allow the generation of MFN2^{T105M} lines or with further work, MFN2^{R364W} lines. The generation of these lines allows the study of the cellular phenotypes at work in CMT2A and aids in the generation of therapeutic strategies.

5) Characterisation of Mitochondrial Phenotype in Wild-Type and CMT2A hPSC-derived motor neurons

5.1) Introduction

Patients with CMT2A typically present with muscle weakness and wastage particularly in the distal limbs, the characteristic foot deformity pes cavus is also extremely common (Reilly *et al.*, 2011). Sensory symptoms can include pain and numbness but are less common (Saporta *et al.*, 2011). Patients may have a reduced nerve amplitude though the speed of nerve conduction may not be significantly altered (Bergamin *et al.*, 2014). Aside from this, CMT2A-affected individuals may be of any age, they may have additional symptoms and the severity of their symptoms can be extremely wide-ranging (reviewed in the following: Braathen, 2012; Timmerman, Strickland and Züchner, 2014). Whilst specific mutations are associated with particular presentations and additional symptoms (Chung *et al.*, 2006; Verhoeven *et al.*, 2006; Feely *et al.*, 2011; Choi *et al.*, 2015; Ando *et al.*, 2017) it is clear that the 'typical' CMT2A can be difficult to define and the symptoms patients experience give clues but do not completely explain what is happening in cells.

CMT2A is caused by mutations in MFN2 and, as its name suggests, the most well-known function of MFN2 is its role in the facilitation of mitochondrial fusion. Fusion, and its counterpart fission, play critical roles relevant to the regulation of mitochondrial function and health. Examining fusion directly can be difficult as it is inherently tied to mitochondrial trafficking and distribution (Baloh *et al.*, 2007) therefore it can often be easier to look at the consequences of fusion and fission which is the overall mitochondrial morphology. Morphology can be examined using proteins staining for particular mitochondrial proteins or various MitoTracker™ dyes to visualise mitochondrial structures (Koopman *et al.*, 2005; Luz *et al.*, 2015). Mitochondrial networks are highly complex 3D structures and viewing them on a single plain or stack is not always valuable. Multiple z stacks provide increased information, especially when analysed in 3D, though such software is computationally intensive and expensive meaning maximum intensity projection of z-stacks is often employed (Chen, Chomyn and Chan, 2005). Individual mitochondria can be classified, e.g. aggregated, elongated, mixed, etc (Strickland *et al.*, 2014; Wolf *et al.*, 2019), or given numerical values which describe the shape (Luz *et al.*, 2015). The most common measures applied to mitochondria are aspect ratio (AR) and form factor. Aspect ratio is a normalised measure of length in mitochondria, calculated by the ratio of the major and minor axis of an ellipse for the object. Form factor is $\text{perimeter}^2/4\pi\text{area}$ and is a measure of overall shape and branching of the mitochondria. Both are independent of magnification and have a minimum value of

1. They can be viewed as proxy measures for fusion (Koopman *et al.*, 2005; Luz *et al.*, 2015), where an increase in the value relates to a higher amount of fusion/more elongated complex mitochondria. It is known that disruption of MFN2 can cause alterations in mitochondrial fusion (Chen *et al.*, 2003). In CMT2A, the wide variety of possible MFN2 mutations has led to confusion over whether mitochondrial fusion plays a role in disease pathology. A fly model overexpressing the MFN2 homology *marf* showed that R94Q-like and T105M-like were fusion incompetent but R364W-like was not only fusion-competent but had enhanced fusion compared with wild-type (El Fissi *et al.*, 2018). R94Q and T105M both reside in the GTPase domain of MFN2, meaning a defect in fusion could be due to altered GTPase activity (reviewed in Filadi, Pendin and Pizzo, 2018). R364W is located in HR1 of MFN2 a region not considered to be primarily involved in the mediation of fusion. Altered fusion was seen in several MFN2 mutations in mouse neurons, including R94Q mutation, however, this was not an aspect of all mutations located in the GTPase domain (Detmer and Chan, 2007; Rocha *et al.*, 2018; Wolf *et al.*, 2019). CMT2A patient fibroblasts displayed normal mitochondrial morphology, including in R94Q cells (Loiseau *et al.*, 2007; Amiott *et al.*, 2008; Larrea *et al.*, 2019). The only mutation examined for overall mitochondrial morphology in patient iPSC-derived neurons was R364W which did not show a fusion defect (Saporta *et al.*, 2015). Taken together, the currently available data provide a confusing picture whereby the animal models of R94Q mutation in MFN2 show a fusion defect but human fibroblast harbouring this mutation do not. This discrepancy could be due to either species or cell type differences, highlighting the need to carry out research in not only a human system but in a physiologically relevant cell type as well.

Mitochondria alter their morphology in response to the cellular environment to change their membrane potential, energy production, metabolite production, apoptotic sensitivity and mtDNA (reviewed in Filadi, Pendin and Pizzo, 2018). Disruption of fusion in mitochondria is associated with decreased membrane potential (Chen, Chomyn and Chan, 2005) and depolarisation of mitochondria is associated with autophagy (Twig *et al.*, 2008). In mitochondria, the generation of membrane potential is essential for ATP production via oxidative phosphorylation, meaning disruption of this gradient will lead to decreased energy production through this means. Several MitoTracker™ dyes are sensitive to membrane potential and assays to measure this also exist. Tetramethylrhodamine, ethyl ester (TMRE) is actively sequestered by active mitochondria due to the charge and carbonyl cyanide 4-(trifluoromethoxy) phenylhydrazone (FCCP) is used as a control that uncouples oxidative phosphorylation, therefore depolarising mitochondria. Calculating the difference in these fluorescence measurements can give a reading for mitochondrial membrane potential. Intrinsically linked to mitochondrial membrane potential is the production of ATP. Quantification of cell viability is

possible through ATP measurements using assays such as ATPlite (PerkinElmer) (Gomes, Benedetto and Scorrano, 2011; Perez-Siles *et al.*, 2020) which can be used in combination with respiration inhibitors or compounds to challenge cell viability. A similar principle is used in specialised equipment, such as Seahorse (Agilent), which uses respiration inhibitors to tease apart the specific contribution from different components of respiration. In CMT2A patient fibroblasts, mitochondrial membrane potential was found to be altered, however, this did not result in reduced ATP production despite apparent uncoupling (Loiseau *et al.*, 2007; Guillet *et al.*, 2010; Larrea *et al.*, 2019) indicating this defect was made up for using other energy production means such as increase glycolysis or reclamation of other metabolites. Two rat studies with MFN2^{R94Q/+} neurons found no defects in ATP production (Baloh *et al.*, 2007; Misko *et al.*, 2012), and a mouse model with R94W mutation found defects only in the homozygous version of the model (Strickland *et al.*, 2014). The ability of MFN2 mutant mitochondria to maintain their mitochondrial membrane potential and ATP production capacity is still unclear in CMT2A and further examination in human cells is required to confirm the fitness of CMT2A mitochondria.

Mitochondria contain their own genome which encodes the proteins required for oxidative phosphorylation. Disruption of fusion results in increased mutation burden in mitochondrial DNA (mtDNA) (Chen *et al.*, 2010), additionally fusion allows mitochondria to tolerate a higher mutational burden due to the exchange of mtDNA and compensation mechanisms (Gilkerson *et al.*, 2008). Comparison of mtDNA to genomic DNA (gDNA) can also provide a measure for mitochondrial mass as the number of mtDNA nucleoids is tightly controlled and spaced at regular intervals (Gilkerson *et al.*, 2008). This can be achieved by calculating the ratio of mtDNA and gDNA reference genes whereas assessment of mutational burden requires sequencing of the mitochondrial DNA. Assessment of mtDNA in CMT2A patient fibroblasts showed no alterations in mtDNA quantity (Loiseau *et al.*, 2007; Amiott *et al.*, 2008; Rizzo *et al.*, 2016; Larrea *et al.*, 2019). However, patient-derived iPSC neurons with MFN2^{A383V/+} were found to have significantly more mtDNA than their wild-type counterparts. Patient fibroblasts were unaffected indicating this particular defect may have neuronal specificity (Rizzo *et al.*, 2016). The drosophila CMT2A model did not find an effect in the quantity of mtDNA but found an increased mutational burden for both fusion competent and incompetent mutations (El Fissi *et al.*, 2018). Disruption to mtDNA appears to be a possibility in CMT2A but it is currently unclear how much this contributes to the overall disease phenotype.

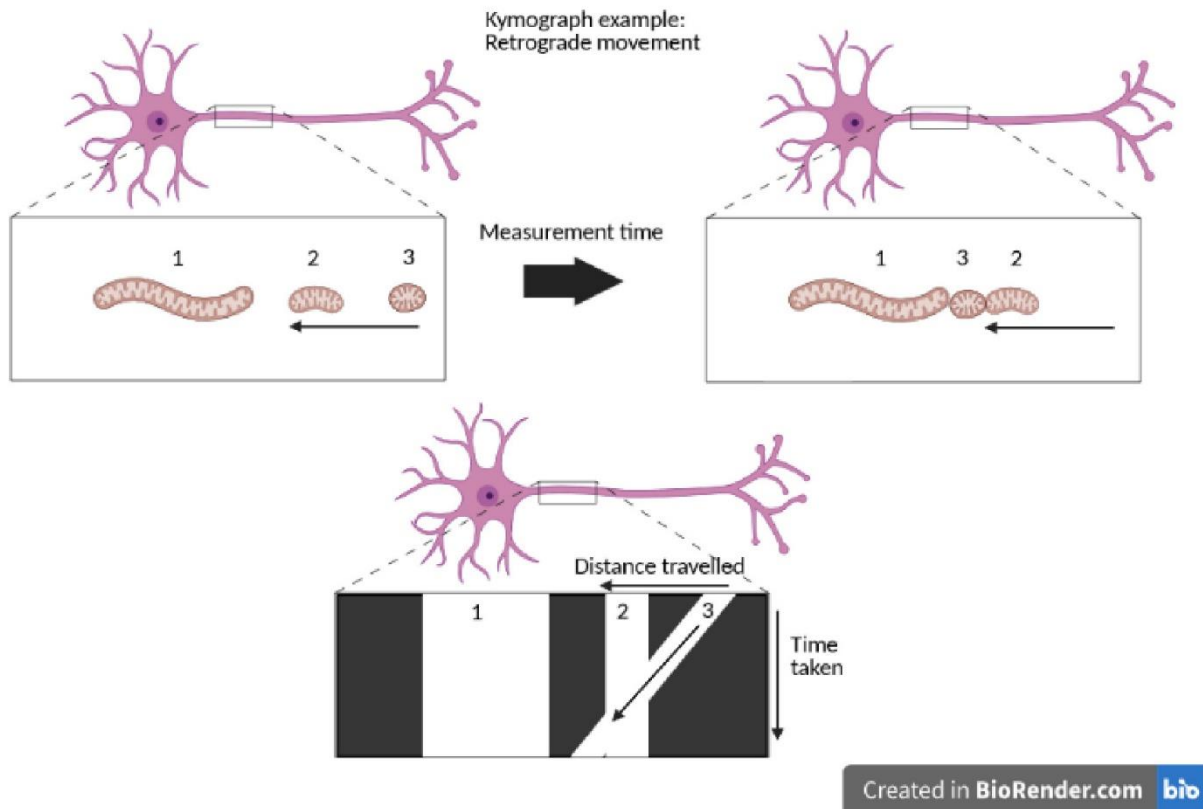


Figure 33: Principles of kymograph generation. The pictured example shows three mitochondria ('1', '2' and '3') that are imaged over time in the neuron. The mitochondrion labelled '3' moves retrograde towards the cell body of the neuron. This can be visualised using the kymograph, a space-time plot, which has corresponding lines indicating the movements of each mitochondrion. Mitochondria '1' and '2' remained stationary during observation, therefore in the kymograph their same position over time results in vertical lines. The movement of the mitochondrion '3' was retrograde (towards the cell body), resulting in a diagonal line towards the left in the kymograph. The distance this mitochondrion moved can be measured as well as the duration of its movement from the kymograph.

MFN2 is known to have a role in mitochondrial trafficking. Trafficking of organelles and specifically mitochondria is an important process for all cells but has unique challenges in neurons due to their architecture. Synapses are the site of intense energy demand meaning mitochondria cluster at these locations (reviewed in Mandal and Drerup, 2019). Mitochondria must therefore be trafficked away from the cell body (anterograde) and return to the cell body (retrograde transport) by the action of motor proteins to fuse and divide with other mitochondria in response to the demands of the cell. MFN2 binds to the MIRO/MILTON complex (Misko *et al.*, 2010) which is involved in binding to Kinesin for anterograde transport and Dynein for retrograde transport (Pilling *et al.*, 2006; reviewed in Schwarz, 2013). This finding helped shed light on why a mutation in KIF1B (a Kinesin) was originally

thought to be the cause of CMT2A before being confirmed to be MFN2 (Zhao *et al.*, 2001; Züchner *et al.*, 2004). Mitochondrial transport can be measured through time-lapse imaging and the production of space-time plots known as kymographs (Figure 33). These plots have distance on the x-axis and time on the y-axis meaning stationary mitochondria shown as vertical lines and mitochondria in motion are displayed as diagonal lines. The direction of travel, therefore motors involved, is also clear as long as the operator notes the direction of the cell body for reference. This allows the contribution or defect of each motor to be fully examined. Whilst measuring transport directly is an option it is also possible to measure the consequences of transport by examining the distribution of mitochondria throughout the cell and the distance between mitochondria. As mentioned, fusion is linked with trafficking as mitochondria must be able to find each other to be able to fuse. Furthermore, in crowded environments like axons, it is known that the action of motor proteins can influence mitochondrial fusion (Henrichs *et al.*, 2020) indicating how linked trafficking is to overall mitochondrial health. It was shown in rat neurons that MFN2^{-/-} and MFN2^{R94Q/+} caused a defect in the transport of mitochondria in both directions of travel and increased time that mitochondria spent paused. Despite this, MFN2 R94Q was still able to interact with MIRO/MILTON and didn't disrupt the interaction of MIRO/MILTON with kinesin proteins. The transport defect was limited to mitochondria and transport of other organelles was not affected (Misko *et al.*, 2010). Following this, other models have examined mitochondrial transport but found varying phenotypes. For example, patient iPSC-derived neurons with A383V mutation showed a transportation defect (Rizzo *et al.*, 2016), but patient-derived iPSC neurons with R364W found no defect (Saporta *et al.*, 2015). Furthermore, a mouse model of R94W found no effect defect in mitochondrial transport, even in the homozygous version of the model (Strickland *et al.*, 2014). Mitochondrial transport defects are a phenotype of CMT2A but the evidence is contradictory in rodent and human models, this may be due to the contribution of particular mutations and must be examined further.

Mitochondrial transport defects are not unique to CMT2A. Other CMT types (Benoy *et al.*, 2018; Mo *et al.*, 2018), certain ALS subtypes (Guo *et al.*, 2017; Moller *et al.*, 2017) and forms of Huntington's (Dompierre *et al.*, 2007) are just a few of the neurodegenerative diseases which are also thought to have this issue. In many of these diseases, inhibition of Histone deacetylase 6 (HDAC6) has been tested as an effort to increase trafficking (Dompierre *et al.*, 2007; Benoy *et al.*, 2017; Guo *et al.*, 2017; Moller *et al.*, 2017; Mo *et al.*, 2018). HDAC proteins are involved in the deacetylation of lysine residues, primarily on histones to alter chromatin folding and access for transcription machinery (reviewed in Simões-Pires *et al.*, 2013). Despite being an HDAC, the majority of HDAC6's targets are cytosolic (reviewed in Batchu, Brijmohan and Advani, 2016). HDAC6 is known to deacetylate tubulin and

preventing deacetylation of tubulin is thought to allow easier binding of motor proteins to microtubules (reviewed in Batchu, Brijmohan and Advani, 2016). This along with a lack of notable defects in HDAC6 knockout mice (Zhang *et al.*, 2008) has made HDAC6 inhibition an attractive target in many systems. Indeed, it has been shown to help in all of the disease models mentioned and increase mitochondrial trafficking to levels comparable to wild-type controls (Dompierre *et al.*, 2007; Benoy *et al.*, 2017; Guo *et al.*, 2017; Moller *et al.*, 2017; Mo *et al.*, 2018). HDAC6 inhibition, with SW-100, has been trialled in a mouse model containing MFN2^{R94Q/+} (Cartoni *et al.*, 2010; Picci *et al.*, 2020) and whilst mitochondrial transport was not directly measured some minor increase in mouse motility and motor function was seen (Picci *et al.*, 2020). As the effect of HDAC6 inhibition was limited, researchers also generated an MFN2^{R94Q/+} HDAC6^{-/-} mouse which showed a restoration to wild-type in many of the defects, thus suggesting that manipulation of HDAC6 is a viable target for alleviation of CMT2A (Picci *et al.*, 2020). More recently, the same researchers developed a novel HDAC6 inhibitor which showed significant improvements in the model (Shen *et al.*, 2021) indicating the need for further development of highly efficacious HDAC6 inhibitors. Another compound known as, ACY738 was previously developed with this in mind and is considered a highly selective and efficacious HDAC6 inhibitor when compared with previous HDAC6 inhibitors such as Tubastatin A (Benoy *et al.*, 2017).

Mitochondria are present in every cell in the body; understandably, a mutation in a mitochondrially resident protein may cause severe disease. What is uncertain in CMT2A is why the impact of MFN2 mutations is only seen in specific cell types, motor and sensory neurons. This is highlighted when CMT2A patient-derived fibroblasts do not necessarily show the same defects as their neuronal counterparts (Rizzo *et al.*, 2016). Patients do not typically display a reduced number of peripheral neurons (Verhoeven *et al.*, 2006), indicating differentiation to this cell type may not be affected and two studies of patient iPSC-derived neurons showed no defects in the number of neurons generated in differentiation (Saporta *et al.*, 2015; Rizzo *et al.*, 2016).

The following chapter describes the characterisation of CMT2A MFN2^{R94Q/+} lines as both hPSC and motor neurons to determine the inherent defect present in different cell types containing the same mutation. Additionally, this chapter describes attempted pharmacological mitigation of a mitochondrial trafficking defect using HDAC6 inhibition.

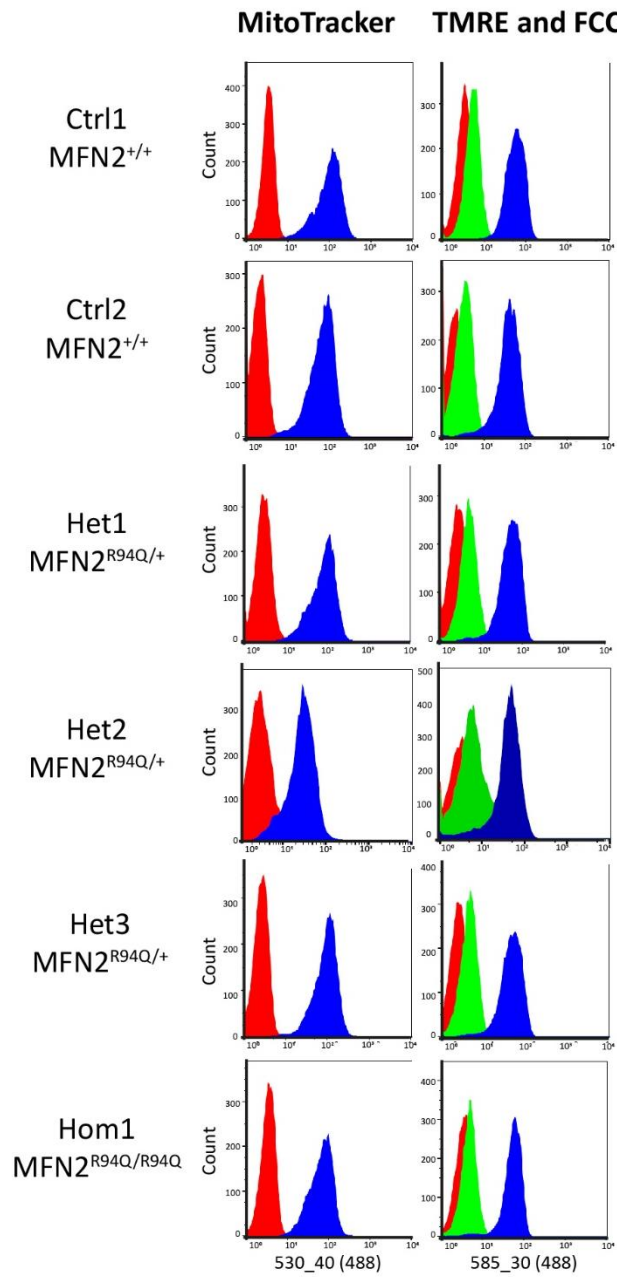
5.2) Results

5.2.1) R94Q hPSC mitochondrial energetics and morphology

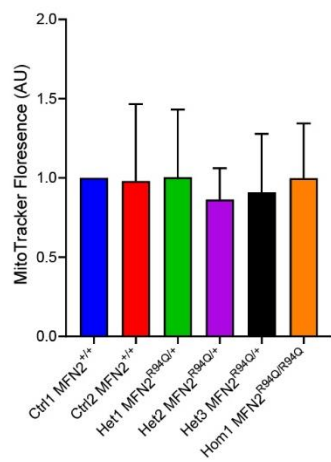
The impact of CMT2A mutations on hPSC has not, to the best of my knowledge, previously been examined. The model I have generated allowed the opportunity to examine if hPSC possess any defects in mitochondrial function that could be affecting their ability to generate motor and sensory neurons.

Studies have previously noted that mutations in MFN2 can alter mitophagy (leading to alterations in mitochondrial mass) and mitochondrial membrane potential, which may or may not lead to altered production of ATP (Loiseau *et al.*, 2007; Guillet *et al.*, 2010; Strickland *et al.*, 2014). I examined if R94Q had altered the mass of mitochondria in hPSC with the use of MitoTracker Green (which is not sensitive to differences in mitochondrial membrane potential) and FACS analysis. No significant difference was found for any of the clones (Figure 34A, 34B), indicating the mitochondria mass was unaffected by the mutation. I also assessed the differences in mitochondrial membrane potential of the lines through the use of a TMRE assay. No significant differences were found for any of the clones (Figure 34A, 34C), indicating the R94Q mutation has not caused mitochondria to lose the ability to generate or maintain membrane potential. Alteration in mtDNA has been seen following MFN2 mutations, especially where mitochondrial fusion deficiencies are seen (Chen *et al.*, 2010; Rizzo *et al.*, 2016) and is an alternate measure of mitochondrial mass (Gilkerson *et al.*, 2008) To investigate I used primers for three different mitochondrial encoded genes MT-ND2 (Mitochondrially encoded NADH2), MT-CO2 (Mitochondrially encoded cytochrome C oxidase 2), MT-RNR1 (Mitochondrially encoded 12S RNA) and comparing them to the nuclear-encoded housekeeping gene GAPDH. No significant differences were found between the clones (Figure 34D). The mitochondrial genes appear to have different copy numbers to each other due to differences in primer binding efficacy (data not shown). I assessed the baseline ATP production using the ATPlite assay where cells generate luminescence for the amount of ATP produced. No significant difference was found between the clones (Figure 34E) indicating that the R94Q does not affect the production of ATP in normal conditions.

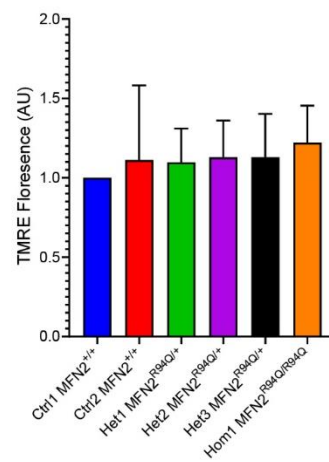
A)



B)



C)



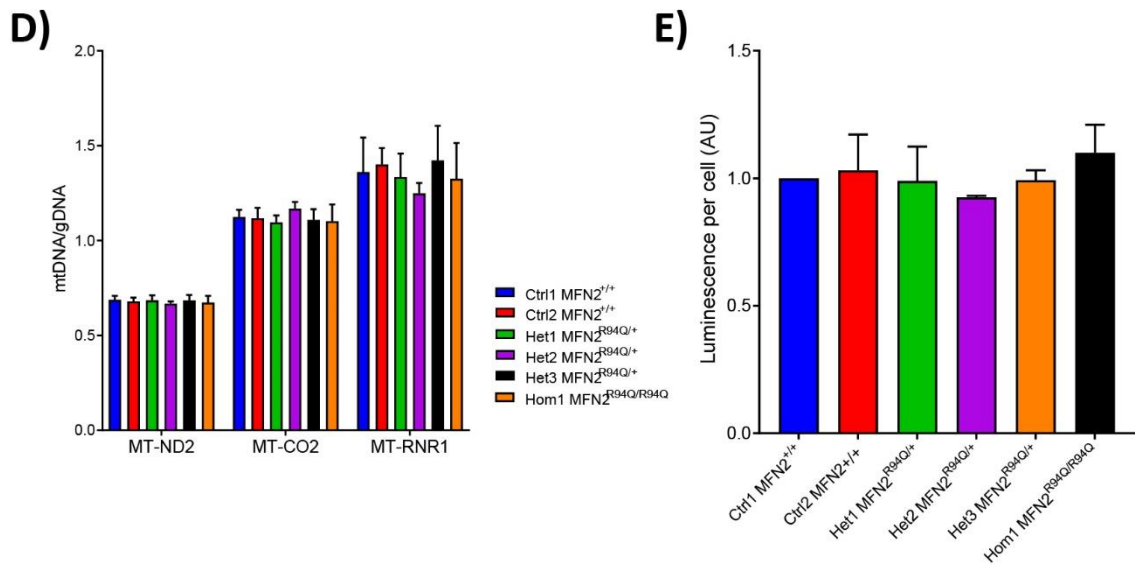
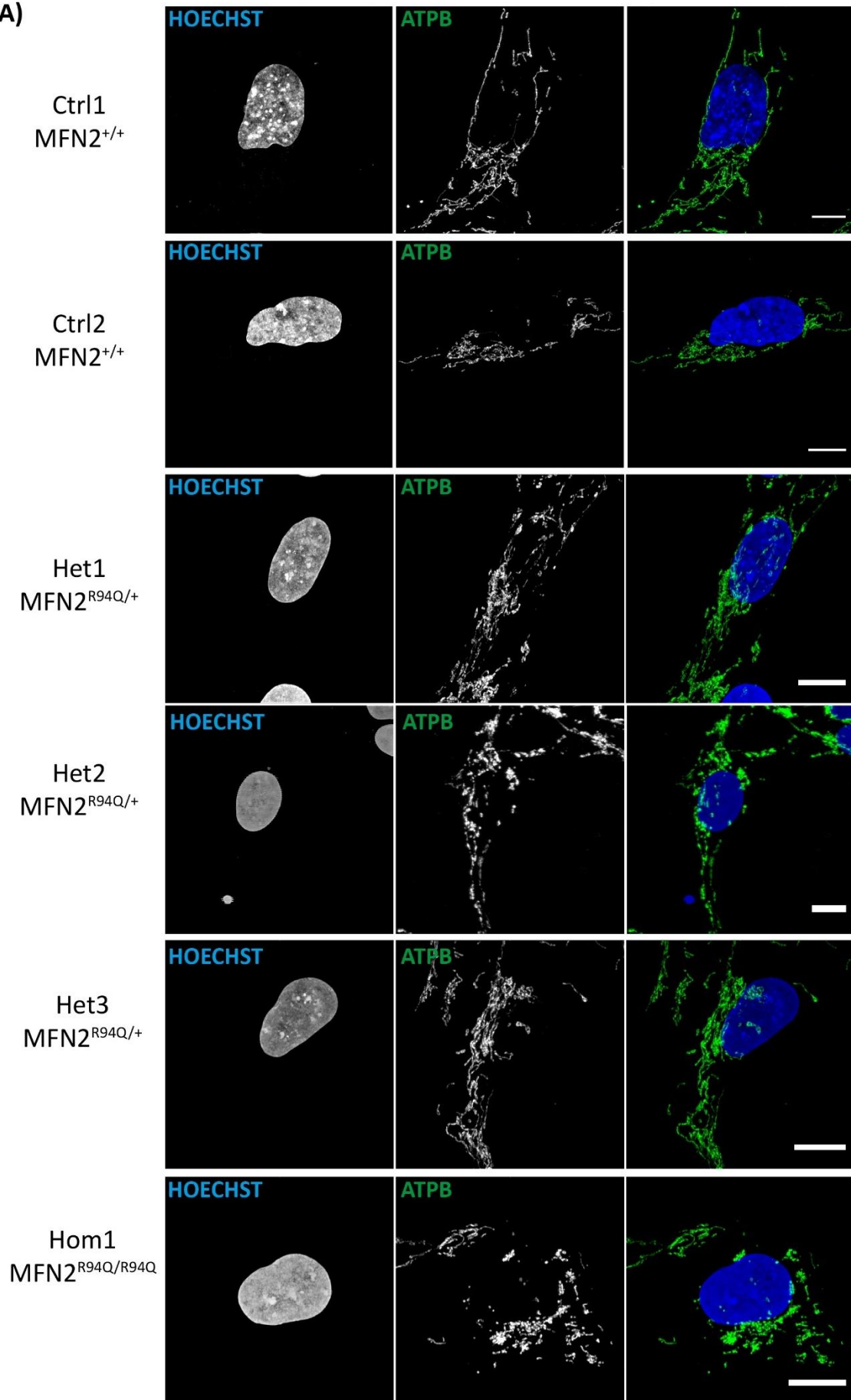


Figure 34: Assessment of mitochondrial content, membrane potential, mtDNA and ATP production in hPSC with MFN2^{+/+} or MFN2^{R94Q/+}. **A)** FACS plots for Mitotracker (blue-left) and TMRE (blue-right) and FCCP-treated (green-right) for wild-type and MFN2 R94Q containing lines. Unstained is represented as red in both sets of plots. **B)** Summary of analysis of Mitotracker fluorescent intensity as determined by flow cytometry in A). Data shown are the mean \pm SD N = 3 biological repeats normalised to Ctrl1 MFN2^{+/+}. **C)** Summary of analysis of TMRE and FCCP-treated fluorescent intensity as determined by flow cytometry in A). Data shown are the mean \pm SD N = 3 biological repeats normalised to Ctrl1 MFN2^{+/+}. **D)** Analysis of mitochondrial content via comparison of mitochondrial encoded genes compared with genome encoded GAPDH. Data shown are the mean \pm SD N = 3 biological repeats. **E)** Analysis of luminescence data from ATPlite assay measuring ATP production. Data shown are the mean \pm SD N = 3 biological repeats normalised to Ctrl1 MFN2^{+/+}.

A)



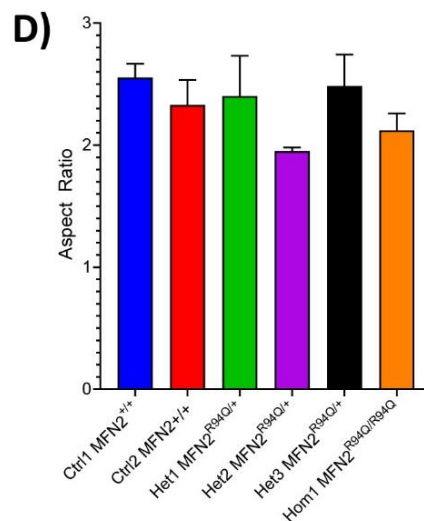
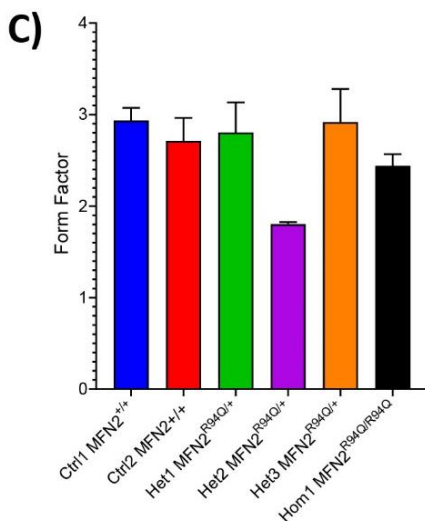
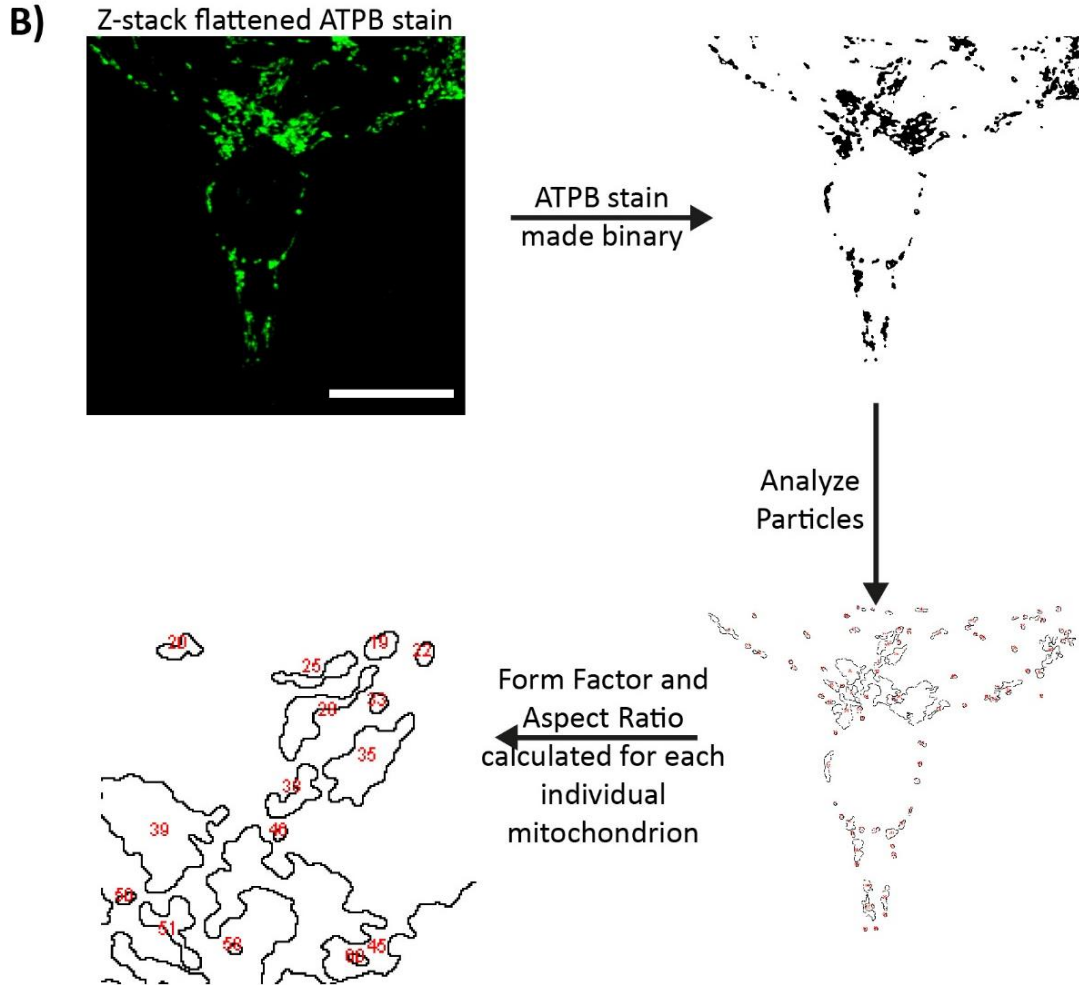


Figure 35: Assessment of mitochondrial morphology in hPSC containing MFN2^{+/+} or MFN2^{R94Q/+}. A)

Staining of mitochondrial marker (ATPB). Nuclei are counterstained with Hoechst33343. Scale bar: 10 μ m. **B)** Steps for analysis of mitochondrial morphology in hPSC stained with ATPB. Scale bar: 20 μ m.

C) Summary of image analysis of mitochondrial data for Form Factor. ...

Cont... Data shown are the mean \pm SD of 3 biological repeats. Each repeat contained N=10 cells analysed. **D)** Summary of image analysis of mitochondrial data for Aspect Ratio. Data shown are the mean \pm SD of 3 biological repeats. Each repeat

The R94Q mutation is particularly associated with poor fusion of mitochondria (Detmer and Chan, 2007; El Fissi *et al.*, 2018), therefore I chose to examine if this had been affected in the hPSC I had edited. Mitochondrial morphology of the panel of clones was assessed by immunocytochemistry examining the expression of ATPB, a subunit of ATP synthase (Figure 35A). Maximum projections were generated from z-stacks and analysed using the 'Analyze particles' function of FIJI (Schindelin *et al.*, 2012) to generate measurements for aspect ratio and form factor (Figure 35C). No significant difference in mean form factor or aspect ratio for the cell lines (Figure 35D, 35E) indicating that R94Q did not significantly affect fusion in stem cells.

In summary, this data suggests as the R94Q mutation does not confer any specific alteration to hPSC mitochondrial mass, membrane potential or fusion.

5.2.2) Comparison of MFN2^{R94Q/+} cells differentiation ability

CMT2A is a progressive neurodegenerative disorder. Even in the most severe conditions, symptoms are not seen until ~3-4 years of age meaning it is unclear if this is a differentiation defect or if axonal degeneration occurs after successful differentiation. The model I have generated allows the ideal setting to study the differentiation of hPSC with CMT2A mutation MFN2^{R94Q/+} and confirm if this may be contributing to disease pathology.

The R94Q and control hPSC lines were differentiated using the protocol optimised in chapter 3 to generate sensory neurons. To confirm that sensory neurons were generated from all of the clones, I assessed differentiation by quantifying the expression of relevant markers of sensory neurons using qPCR. I examined the expression of neural crest markers (*SOX9*, *PAX3*, *TFA2b*, *SNAI1*, *SNAI2*) at day 5 and sensory neuron markers (*POU4F1*, *PRPH*) and nociceptor-specific genes (*SCN9A*, *P2X3*) at day 16 for Ctrl2 MFN2^{+/+}, Het1 MFN2^{R94Q/+} and Het3 MFN2^{R94Q/+} (cell line containing an off-target mutation) (Figure 36A). No significant differences in expression were noted in the cell lines when compared with parental line Ctrl1 MFN2^{+/+} at either the neural crest (day 5) (Figure 36B) or sensory neuron (day 16) (Figure 36C) stages of differentiation.

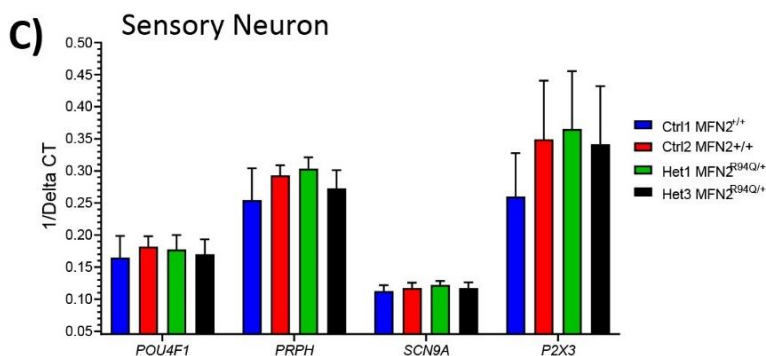
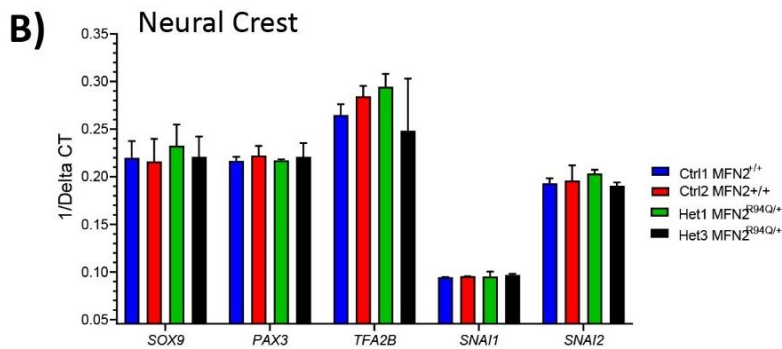
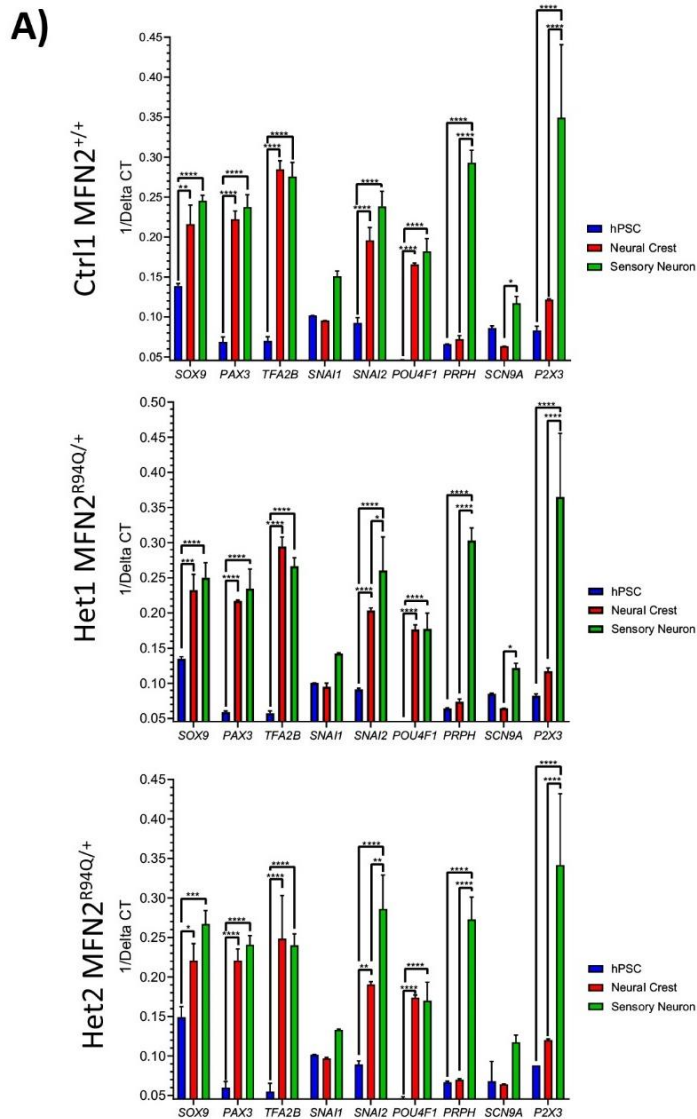
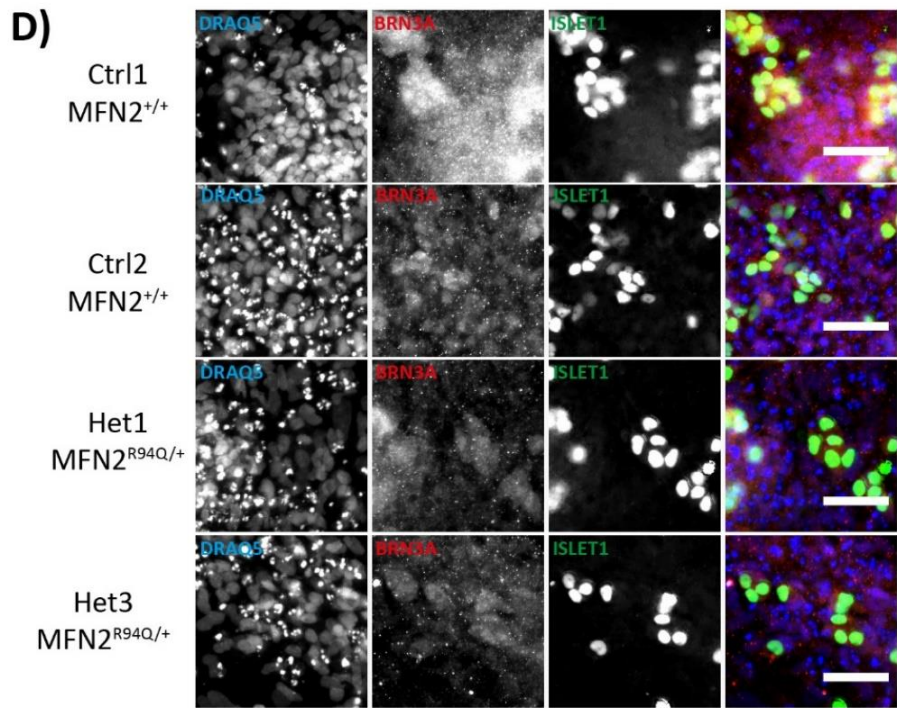
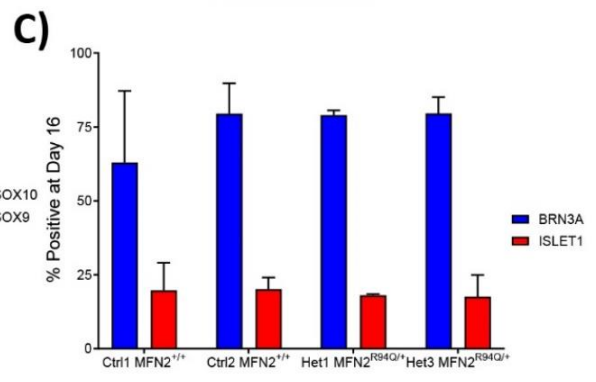
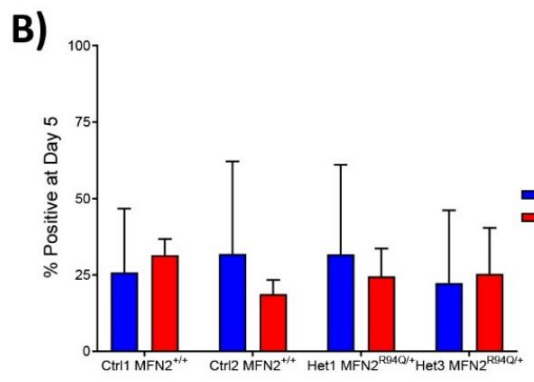
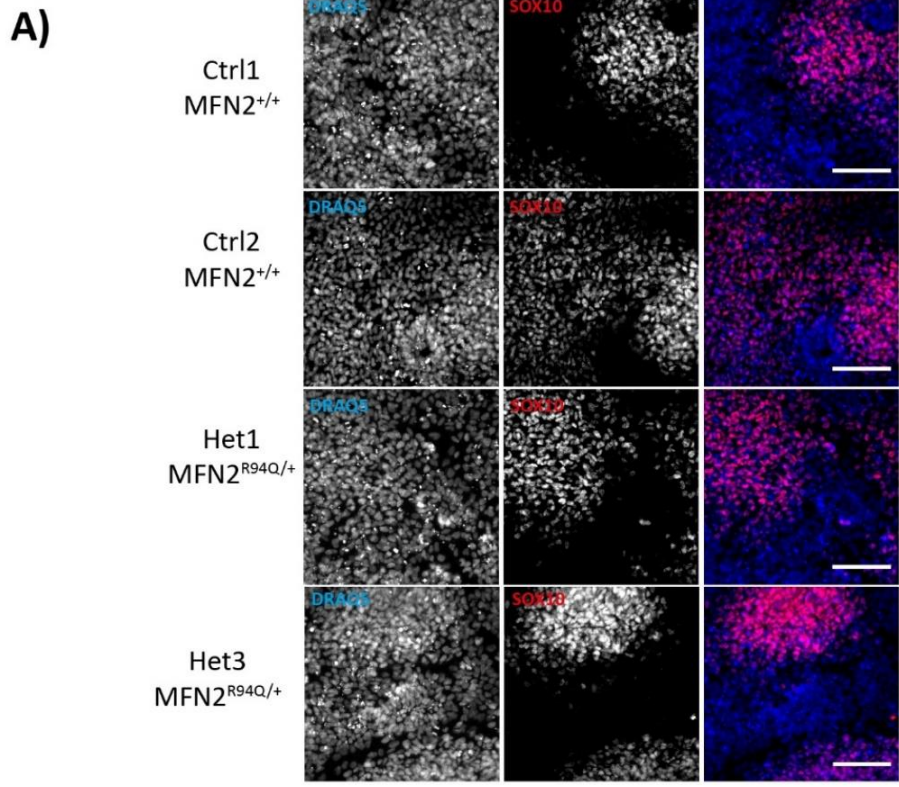


Figure 36: Assessment of MFN2^{+/+} or MFN2^{R94Q/+} lines differentiation to neural crest and sensory neurons via qPCR.

A) Expression of neural crest markers (*SOX9*, *PAX3*, *TFA2B*, *SNAI1*, *SNAI2*), sensory neuron marker (*POU4F1* which encodes for BRN3A), peripheral nervous system axonal marker (*PRPH* which encodes for PERIPHERIN) and nociceptor markers (*SCN9A*, *P2X3*) over the course of differentiation. The data shown are the mean \pm SD. N=3 biological repeats (* - $P \leq 0.05$, ** - $P \leq 0.01$, *** - $P \leq 0.001$, **** - $P \leq 0.0001$, 2-way ANOVA). **B)** Comparison of expression of neural crest markers between wild-type and MFN2 R94Q containing lines at day 5 (neural crest). **C)** Comparison of expression of sensory neuron markers between wild-type and MFN2 R94Q containing lines at day 16 (sensory neuron).



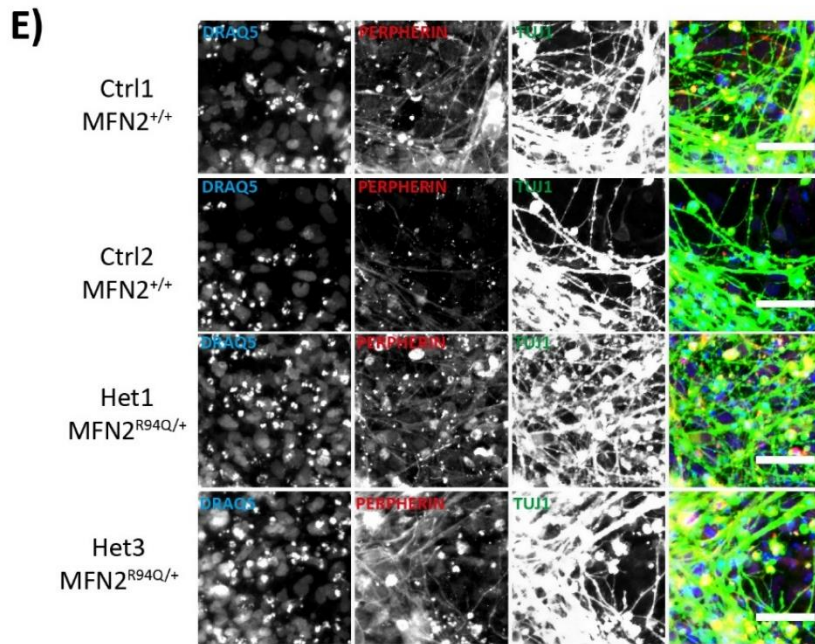
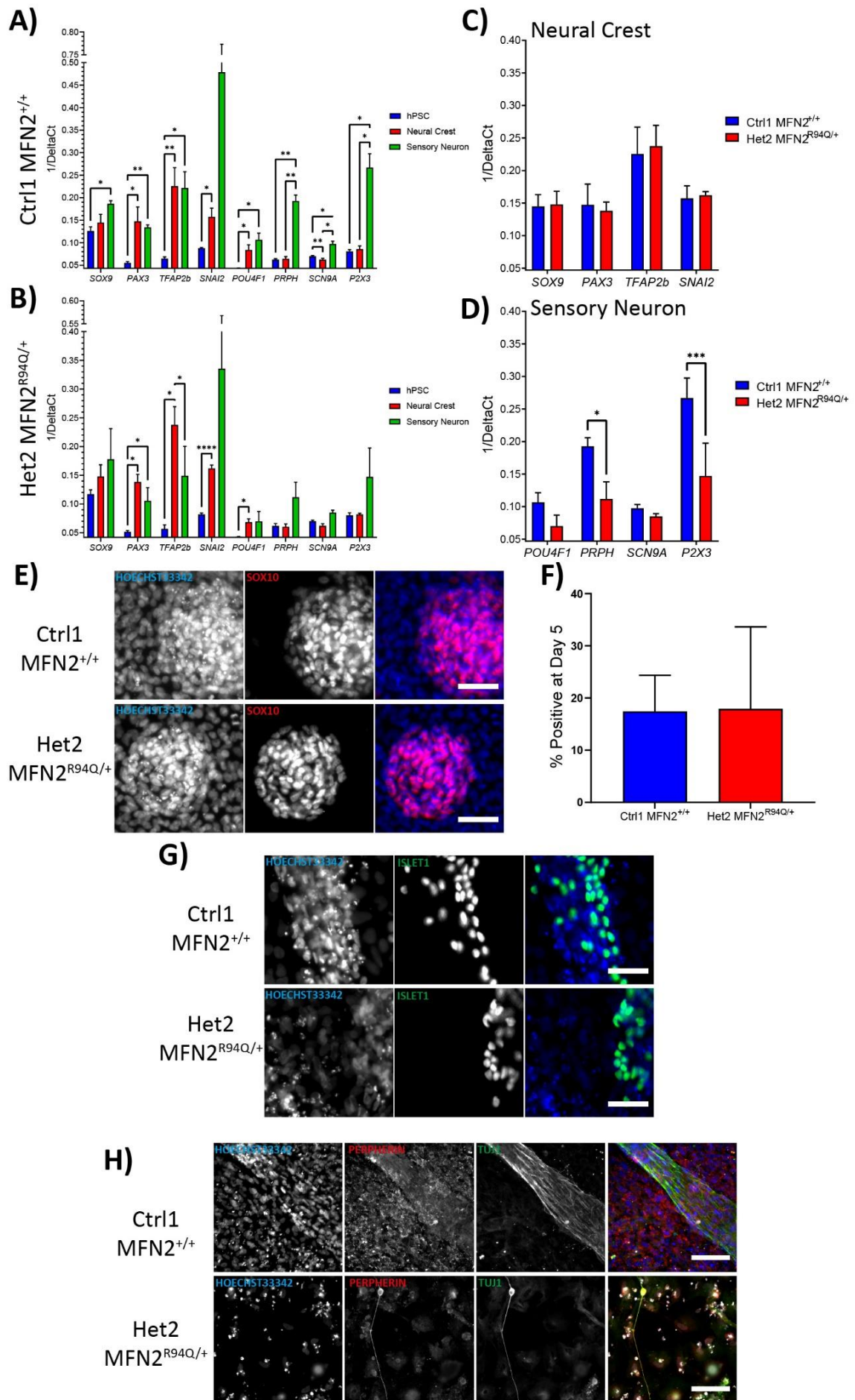


Figure 37: Assessment of MFN2^{+/+} or MFN2^{R94Q/+} lines differentiation to neural crest and sensory neurons via immunofluorescence. A) Neural crest marker staining (SOX10) at day 5 of the differentiation. Nuclei are counterstained with Draq5. Scale bar: 50 μ m. **B)** Summary of image analysis of neural crest markers (SOX9 and SOX10) staining at day 5 of differentiation. The data shown are the mean \pm SD. N=3 biological repeats. **C)** Summary of image analysis of sensory neuron markers (BRN3A and ISLET1) staining at day 16 of differentiation. The data shown are the mean \pm SD. N=3 biological repeats. **D)** Sensory neuron markers staining (BRN3A, ISLET1) at day 15 of the differentiation protocol. Nuclei are counterstained with Draq5. Scale bar: 50 μ m. **E)** Staining of peripheral nervous system axonal marker (PERIPHERIN) and axonal marker (TUJ1) at day 16 of the differentiation protocol. Nuclei are counterstained with Draq5. Scale bar: 50 μ m.

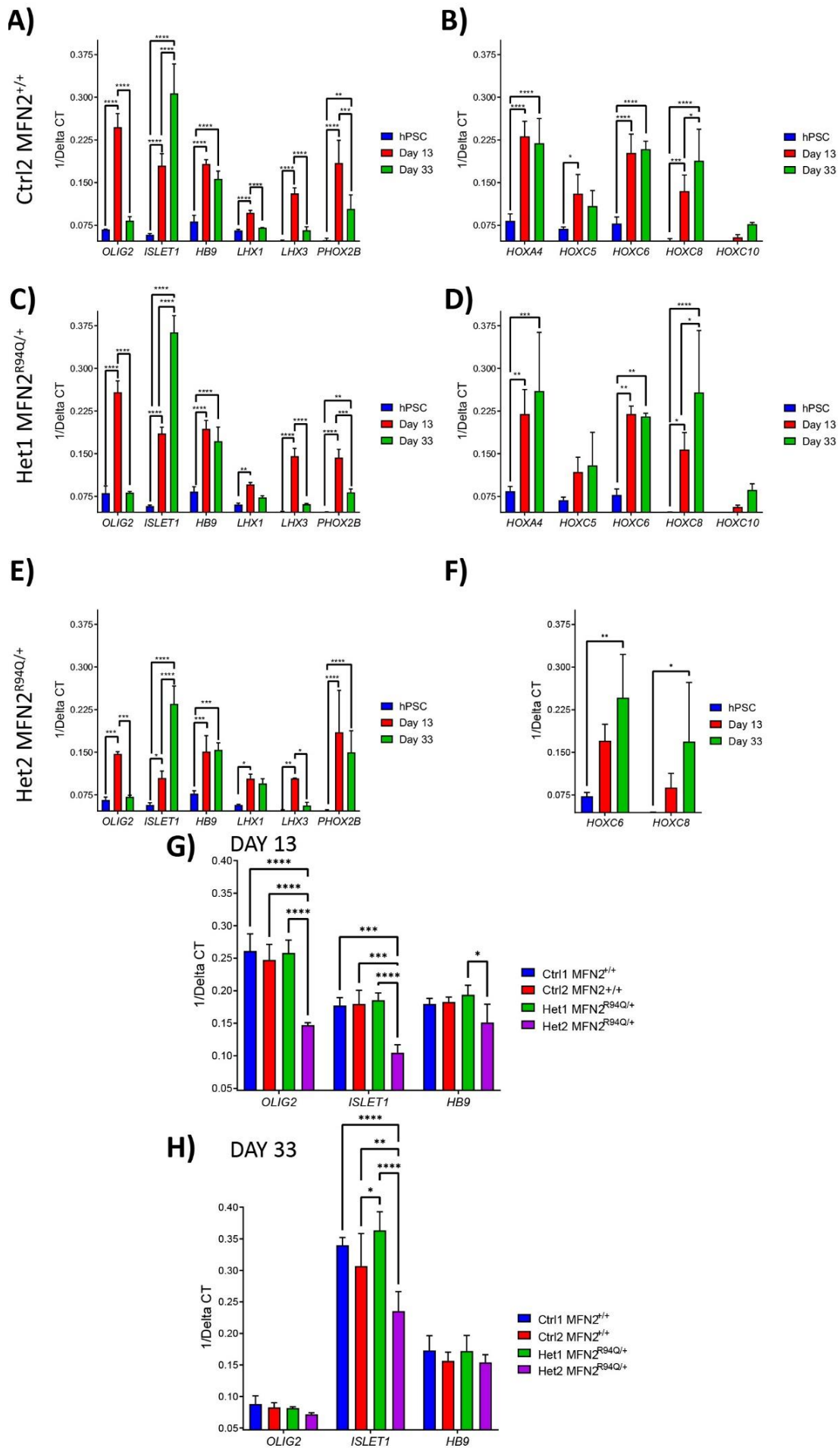
The differentiation efficiency was assessed at day 5 by immunocytochemistry for neural crest markers SOX9 and SOX10 (Figure 37A). All cell lines showed expression of SOX10 (Ctrl1 MFN2^{+/+} 28.8% \pm 20.8, Ctrl2 MFN2^{+/+} 31.8% \pm 30, Het1 MFN2^{R94Q/+} 31.7% \pm 29.3, Het3 MFN2^{R94Q/+} 22.3% \pm 23.8) and SOX9 (Ctrl1 MFN2^{+/+} 31.5% \pm 5.3, Ctrl2 MFN2^{+/+} 18.7% \pm 4.5, Het1 MFN2^{R94Q/+} 24.5% \pm 9.1, Het3 MFN2^{R94Q/+} 25.3% \pm 15.1) with no significant difference seen between the cell lines (Figure 37B). Immunofluorescence was used to confirm protein expression of sensory neuron markers BRN3A, ISLET1, PERIPHERIN and TUJ1 on day 16 of differentiation (Figure 37E, 37F). All cell lines showed staining of BRN3A (Ctrl1 MFN2^{+/+} 62.9% \pm 24.3, Ctrl2 MFN2^{+/+} 79.5% \pm 10.2, Het1 MFN2^{R94Q/+} 79% \pm 1.6, Het3 MFN2^{R94Q/+} 79.6% \pm 5.5) and ISLET1 (Ctrl1 MFN2^{+/+} 19.7% \pm 9.4, Ctrl2 MFN2^{+/+} 20.1% \pm 3.9,

Het1 MFN2^{R94Q/+} 18.1% ± 0.4, Het3 MFN2^{R94Q/+} 17.5% ± 7.4) with no significant difference noted in the percentage of positive cells between cell lines.

Het2 MFN2^{R94Q/+} was assessed for successful generation of sensory neurons alongside parental cell line Ctrl1 MFN2^{+/+} at a later stage than the previous clones. As previously, I examined the expression of neural crest markers (*SOX9*, *PAX3*, *TFA2b SNAI2*) and sensory neuron markers (*POU4F1*, *PRPH*) and nociceptor-specific genes (*SCN9A*, *P2X3*) (Figure 38A, 38B). From the expression of these markers, it is clear the differentiation was not as successful as the previous differentiation attempts due to the comparatively lower levels of *SOX9*, *PAX3* and subsequent sensory neuron markers (Figure 38A, 36A). When the levels of expression are compared within this experiment Het2 MFN2^{R94Q/+} produced a similar expression of neural crest markers as Ctrl1 MFN2^{+/+} (Figure 38C), suggesting the differentiation performed equally in each line. However, Het2 MFN2^{R94Q/+} produced significantly less *PRPH* and *P2X3* expression than Ctrl1 MFN2^{+/+} at the end of the differentiation (Figure 38D), indicating a potential failure in the correct generation of sensory neurons in this cell line. Differentiation was assessed at day 5 for neural crest marker *SOX10* (Figure 38E, 38F) and was found to be under 20% for both lines (Ctrl1 MFN2^{+/+} 17.45% ± 6.9, Het2 MFN2^{R94Q/+} 17.92% ± 15.7), though no significant difference was noted in the percentage of positive cells. Cells were additionally assessed for ISLET1, PERIPHERIN and TUJ1 staining at day 16 of the differentiation (Figure 38G, 38H), where on observation of the images it was clear that Het2 MFN2^{R94Q/+} had not produced as many neuronal cells, with the only neuronal cell found in the differentiation shown in figure 38H.



(Previous page) Figure 38: Assessment of Ctrl1 MFN2^{+/+} and Het2 MFN2^{R94Q/+} differentiation to neural crest. A) Expression of neural crest markers (*SOX9*, *PAX3*, *TFAP2b*, *SNAI1* *SNAI2*), sensory neuron marker (*POU4F1* which encodes for BRN3A), peripheral nervous system axonal marker (*PRPH* which encodes for PERIPHERIN) and nociceptor markers (*SCN9A*, *P2X3*) over the course of differentiation for MShef11 cells. The data shown are the mean \pm SD. N = 3 biological repeats (* - $P \leq 0.05$, - ** - $P \leq 0.01$, 2-way ANOVA) **B)** Expression of neural crest markers (*SOX9*, *PAX3*, *TFAP2b*, *SNAI1* *SNAI2*), sensory neuron marker (*POU4F1* which encodes for BRN3A), peripheral nervous system axonal marker (*PRPH* which encodes for PERIPHERIN) and nociceptor markers (*SCN9A*, *P2X3*) over the course of differentiation for 3E9 cells. The data shown are the mean \pm SD. N = 3 biological repeats (* - $P \leq 0.05$, **** - $P \leq 0.0001$, 2-way ANOVA) **C)** Comparison of expression of neural crest markers between MShef11 and 3E9 MFN2^{R94Q/+}. **D)** Comparison of expression of sensory neuron markers between MShef11 and 3E9 MFN2^{R94Q/+}. **E)** Staining of neural crest marker (SOX10) at day 5 of the differentiation. Nuclei are counterstained with Hoechst33343. Scale bar: 50 μ m. **F)** Summary of image analysis of neural crest marker (SOX10) staining at day 5 of differentiation. The data shown are the mean \pm SD. N=3 biological repeats. **G)** Staining of sensory neuron marker (ISLET1) at day 16 of the differentiation protocol. Nuclei are counterstained with Hoechst33343. Scale bar: 50 μ m. **H)** Staining of peripheral nervous system axonal marker (PERIPHERIN) and axonal marker (TUJ1) at day 16 of the differentiation protocol. Nuclei are counterstained with Hoechst33343. Scale bar: 100 μ m.



((Previous page) Figure 39: Assessment of MFN2^{+/+} or MFN2^{R94Q/+} lines differentiation to motor neurons via qPCR. All data shown are the mean \pm SD. N=3 biological repeats **A)** Expression of motor neuron markers (*OLIG2*, *ISLET1*, *HB9*) and relevant columnar identity markers (*LHX1*, *LHX3*, *PHOX2B*) over the course of differentiation for 3F5 MFN2^{+/+}. (** - $P \leq 0.01$, *** - $P \leq 0.001$, **** - $P \leq 0.0001$, 2-way ANOVA). **B)** Expression of axial markers (*HOX4* – *HOX10*) over the course of differentiation for 3F5 MFN2^{+/+}. (** - $P \leq 0.01$, *** - $P \leq 0.001$, **** - $P \leq 0.0001$, 2-way ANOVA). **C)** Expression of motor neuron markers (*OLIG2*, *ISLET1*, *HB9*) and relevant columnar identity markers (*LHX1*, *LHX3*, *PHOX2B*) over the course of differentiation for 7G7 MFN2^{R94Q/+}. (** - $P \leq 0.01$, *** - $P \leq 0.001$, **** - $P \leq 0.0001$, 2-way ANOVA). **D)** Expression of axial markers (*HOX4* – *HOX10*) over the course of differentiation for 7G7 MFN2^{R94Q/+}. (* - $P \leq 0.05$, ** - $P \leq 0.01$, *** - $P \leq 0.001$, **** - $P \leq 0.0001$, 2-way ANOVA). **E)** Expression of motor neuron markers (*OLIG2*, *ISLET1*, *HB9*) and relevant columnar identity markers (*LHX1*, *LHX3*, *PHOX2B*) over the course of differentiation for 3E9 MFN2^{R94Q/+}. (* - $P \leq 0.05$, ** - $P \leq 0.01$, *** - $P \leq 0.001$, **** - $P \leq 0.0001$, 2-way ANOVA). **F)** Expression of axial markers (*HOXC6* and *HOXC8*) over the course of differentiation for 3E9 MFN2^{R94Q/+}. (* - $P \leq 0.05$, ** - $P \leq 0.01$, 2-way ANOVA). **G)** Comparison of expression of motor neuron markers expressed between wild-type and MFN2 R94Q containing lines at day 13 of differentiation. (* - $P \leq 0.05$, ** - $P \leq 0.01$, *** - $P \leq 0.001$, **** - $P \leq 0.0001$, 2-way ANOVA). **H)** Comparison of expression of motor neuron markers expressed between wild-type and MFN2 R94Q containing lines at day 33 of differentiation. (* - $P \leq 0.05$, ** - $P \leq 0.01$, *** - $P \leq 0.001$, **** - $P \leq 0.0001$, 2-way ANOVA).

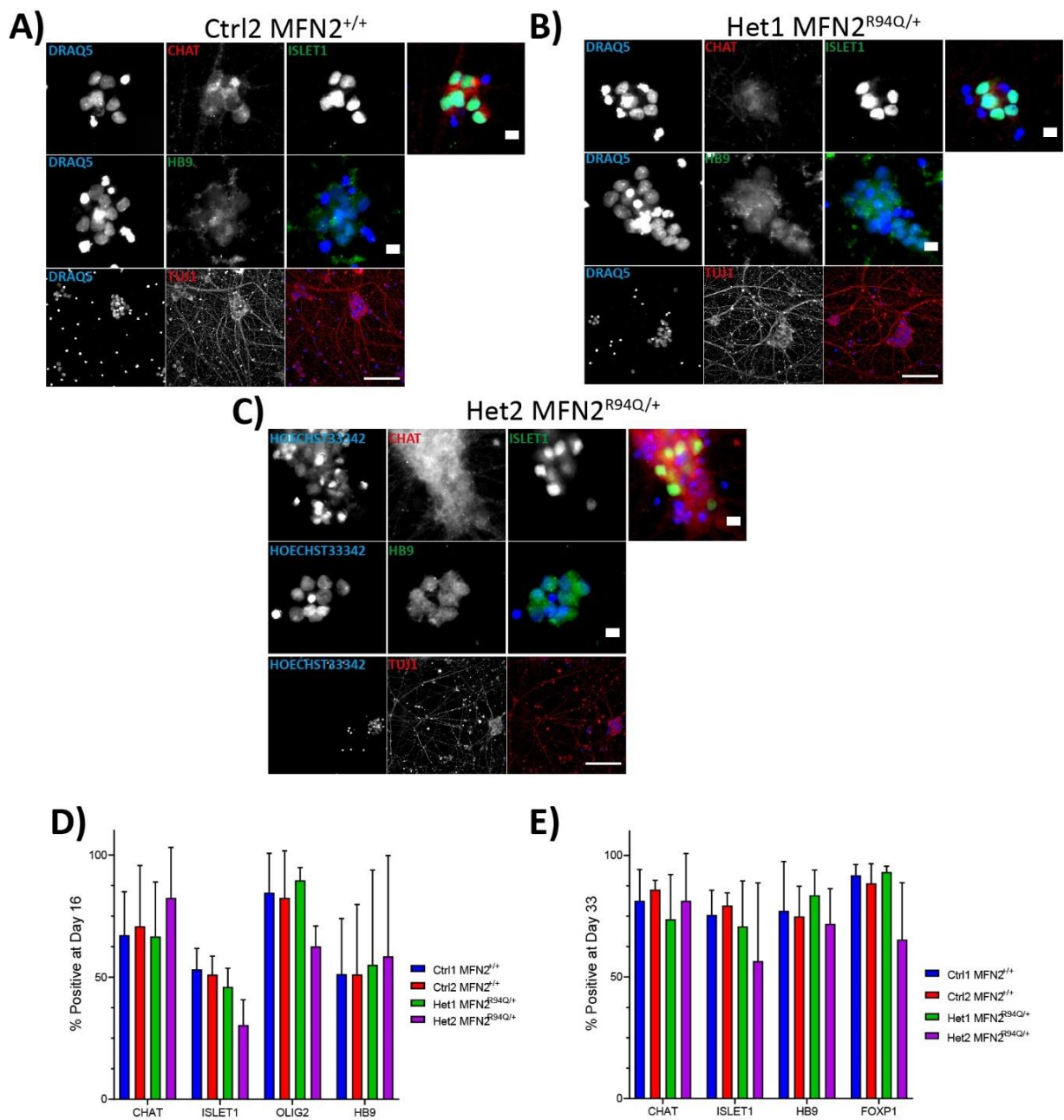


Figure 40: Assessment of MFN2^{+/+} or MFN2^{R94Q/+} lines differentiation to motor neurons via immunofluorescence. A) Staining of motor neuron markers (CHAT, ISLET, HB9) (Scale bar: 10µm) and axonal marker (TUJ1) (Scale bar: 100µm) at day 33 of the differentiation for 3F5 MFN2^{+/+}. Nuclei are counterstained with Draq5. **B)** Staining of motor neuron markers (CHAT, ISLET, HB9) (Scale bar: 10µm) and axonal marker (TUJ1) (Scale bar: 100µm) at day 33 of the differentiation for 7G7 MFN2^{R94Q/+}. Nuclei are counterstained with Draq5. **C)** Staining of motor neuron markers (CHAT, ISLET, HB9) (Scale bar: 10µm) and axonal marker (TUJ1) (Scale bar: 100µm) at day 33 of the differentiation for 3E9 MFN2^{R94Q/+}. Nuclei are counterstained with Hoechst33342. **D)** Summary of image analysis of motor neuron markers (CHAT, ISLET1, OLIG2 and HB9) staining at day 16 of differentiation. The data shown are the mean ±SD. N=3 biological repeats. **E)** Summary of image analysis of motor neuron markers ...

... **cont.** (CHAT, ISLET1, HB9) and limb marker (FOXP1) staining at day 33 of differentiation. The data shown are the mean \pm SD. N=3 biological repeats.

Cells were also differentiated using the previously optimised protocol to generate the predominantly affected cell type of LMC motor neurons (Chapter 3). To assess differentiation, the expression of relevant markers was assessed using qPCR. I examined the expression of motor neuron markers (*OLIG2*, *ISLET1* and *HB9*) as well as columnar markers (*LHX1*, *LHX2* and *PHOX2B*) for the three clones Ctrl1 MFN2^{+/+}, Het1 MFN2^{R94Q/+} and Het2 MFN2^{R94Q/+} (Figure 39A, 39C, 39E). All clones showed similar overall trends in the expression of key genes. When compared at day 13, it can be seen that Het2 MFN2^{R94Q/+} produced significantly less expression of *OLIG2* and *ISLET1* compared with all other clones, additionally produced significantly less expression of *HB9* than the other R94Q clone (Het1 MFN2^{R94Q/+}). At day 33, Het2 MFN2^{R94Q/+} still had significantly reduced expression of *ISLET1* than all other cell lines, however, no difference was noted in the expression of *HB9*. To confirm positional identity, the expression of HOX genes was also examined for the cell lines (Figure 39B, 39D, 39F). All clones showed strong expression of *HOXC6* and *HOXC8* indicating lower brachial identity. No significant differences were noted in the expression of HOX genes across the lines (data not shown). Furthermore, differentiation efficacy was assessed via immunofluorescence for motor neuron markers (CHAT, ISLET1, HB9, OLIG2), an axonal marker (TUJ1) (Figure 40A, 40B, 40C) and limb marker, FOXP1. On day 16 lines showed high staining of neurotransmitter enzyme CHAT (Ctrl1 MFN2^{+/+} 67.2% \pm 17.8, Ctrl2 MFN2^{+/+} 70.8% \pm 24.9, Het1 MFN2^{R94Q/+} 66.7% \pm 22.3, Het2 MFN2^{R94Q/+} 82.4% \pm 20.7) and early marker OLIG2 (Ctrl1 MFN2^{+/+} 84.6% \pm 16, Ctrl2 MFN2^{+/+} 82.5% \pm 19.2, Het1 MFN2^{R94Q/+} 89.6% \pm 5.2, Het2 MFN2^{R94Q/+} 62.5% \pm 8.4) (Figure 40D). Het2 MFN2^{R94Q/+} shows a lower number of cells staining OLIG2⁺ (62.5% \pm 8.4) and ISLET1⁺ (30.4% \pm 10.4) than other lines but these were not significantly different. At day 33 all cell lines showed high percentage CHAT⁺ (Ctrl1 MFN2^{+/+} 81.4% \pm 12.8, Ctrl2 MFN2^{+/+} 85.9% \pm 3.8, Het1 MFN2^{R94Q/+} 73.7% \pm 18.4, Het2 MFN2^{R94Q/+} 81.3% \pm 19.5) and FOXP1⁺ (Ctrl1 MFN2^{+/+} 91.8% \pm 4.5, Ctrl2 MFN2^{+/+} 88.5% \pm 8, Het1 MFN2^{R94Q/+} 93.2% \pm 2.4, Het2 MFN2^{R94Q/+} 65.4% \pm 23.7) indicating a highly motor neuronal population with LMC character (Figure 40E). No significant difference in the percentage of positive cells for the assessed markers.

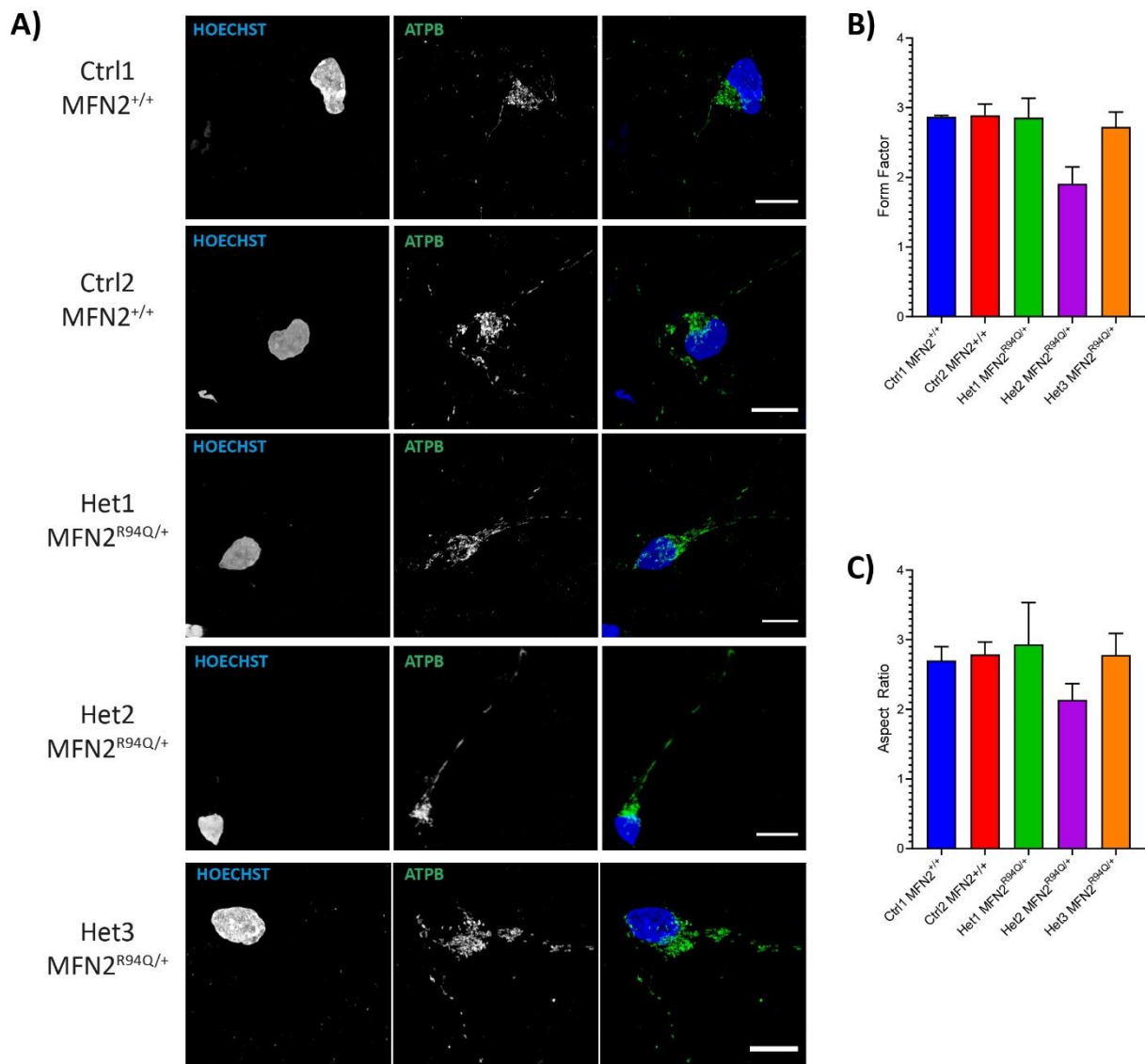


Figure 41: Assessment of mitochondrial morphology for day 16 motor neurons containing MFN2^{+/+} or MFN2^{R94Q/+}. **A)** Staining of mitochondrial marker (ATPB). Nuclei are counterstained with Hoechst33343. Scale bar: 10µm. **B)** Summary of image analysis of mitochondrial data for Form Factor. Data shown are the mean ±SD of 3 biological repeats. Each repeat contained N=10 cells analysed. **C)** Summary of image analysis of mitochondrial data for Aspect Ratio. Data shown are the mean ±SD of 3 biological repeats. Each repeat contained N=10 cells analysed.

In summary, this data shows edited MFN2^{R94Q/+} lines are capable of differentiation to both motor and sensory neurons. However, it was observed that Het2 MFN2^{R94Q/+} had some difficulty differentiating during the sensory protocol and failed to produce as many sensory neurons as Ctrl1 MFN2^{+/+}. Additionally, this clone appeared to have lower expression of key motor neuron markers during the

motor neuron differentiation though this did not result in a decrease in the detected cells staining positive for these markers suggesting the efficiency of differentiation was not significantly altered. For this and other technical reasons relating to the feasibility of individual neuron assessment (see below) the sensory neuron differentiation was not used for further studies.

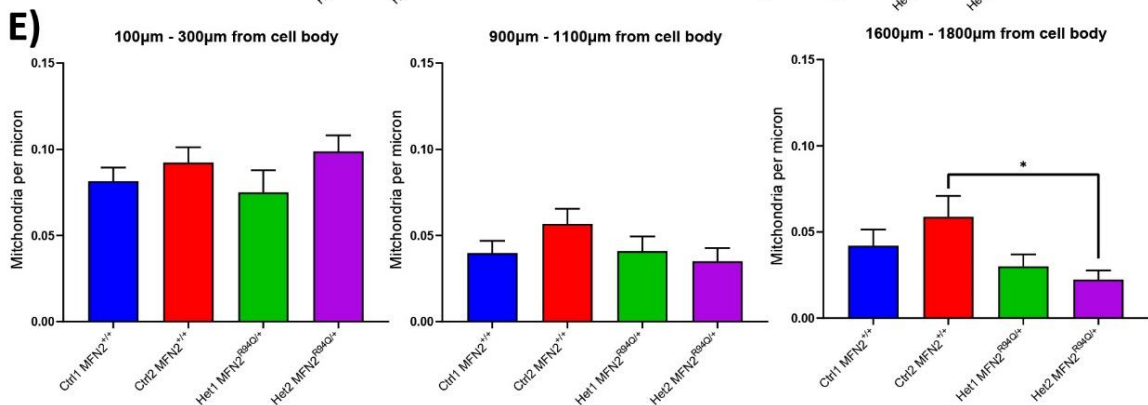
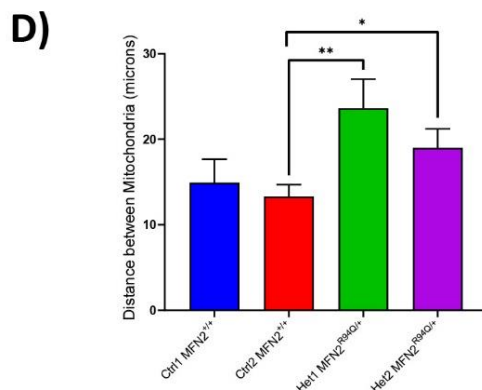
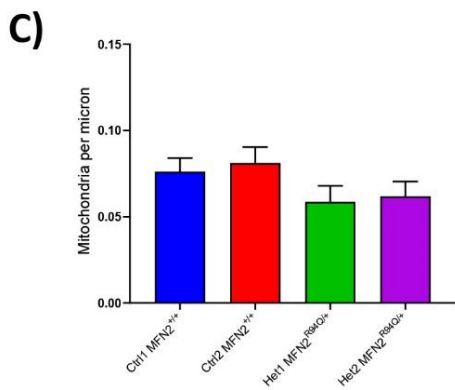
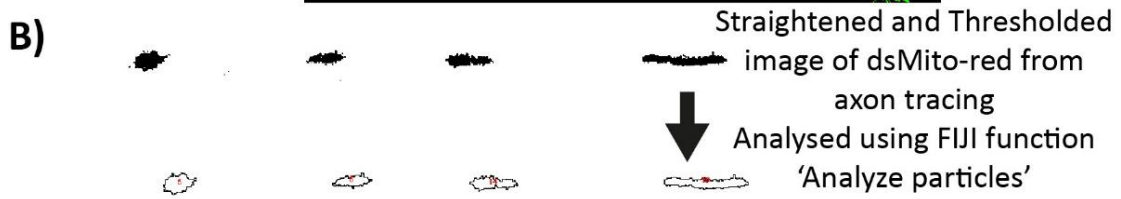
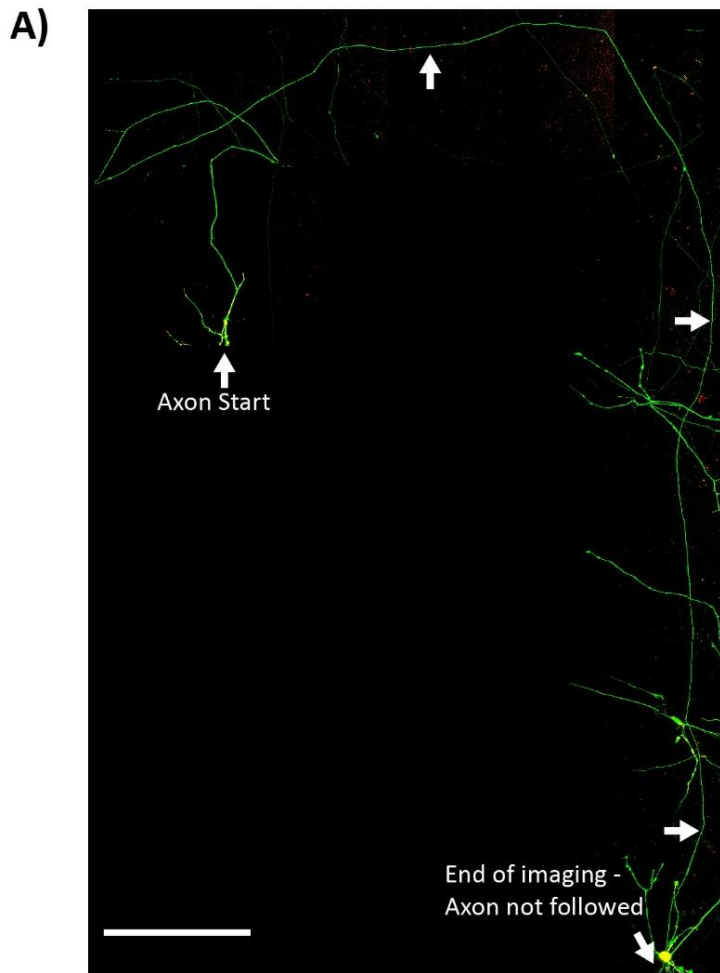
5.2.3) Assessment of Mitochondrial Morphology in MFN2^{R94Q/+} motor neurons

I hypothesised that R94Q motor neurons would be fusion defective in their axons due to the reported axonal phenotypes seen in CMT. Additionally, I believed the R94Q mutation may cause fragmented mitochondria due to a fusion defect and mitochondrial clustering due to transport defects.

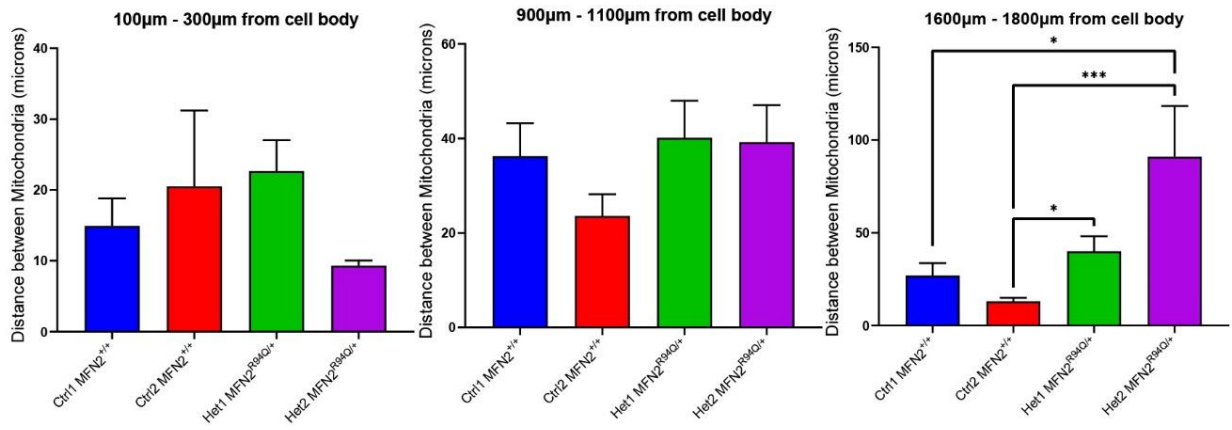
Initially, I chose to focus on day 16, a midpoint of differentiation that may provide insight into the mitochondrial morphology during the process of differentiation into neurons and if this may contribute to later axonal disruption. Mitochondrial morphology of the panel of clones was assessed at day 16 of the motor neuron differentiation by immunocytochemistry examining the expression of ATPB (Figure 41A) similarly as previously (Figure 35C and D). Measurements were calculated from these images for form factor (Figure 41B) and aspect ratio (Figure 41C). No significant difference in mean form factor or aspect ratio for the cell lines indicating that fusion was not significantly affected at day 16 in the cell body measured.

On day 33 neurons assessment of mitochondrial morphology was more difficult due to the density of the axonal network which made it difficult to identify which mitochondrion belonged to which axon. To overcome this, neurons were transfected with two plasmids, one containing ds-RedMito (a red fluorophore with targeting to the mitochondria) under the CMV promoter and the other coding for a green fluorescent protein (GFP) under the CAG promoter, allowing the visualisation of axons and the mitochondria within them. To make neurons easier to identify, this transfection was designed to occur at low efficiency only meaning not all neurons were successfully transfected with plasmids. Subsequently, it was easier to identify individual axons within the network (compare figure 39A TUJ1 with figure 42A). Images of neurons containing both ds-RedMito and GFP were taken along the axon and stitched together to form composite neuron images (Figure 42A) from which mitochondria could be analysed within individual neurons (Figure 42B). Due to the difficulty of imaging these axons over long distances, difficulty identifying individual axons and the extreme length of some, it was not possible to image every axon to its end. Axons were imaged as far as possible or for approximately 12 images which would result in ~2000um of axon length. To identify if mitochondria were disrupted in these axons, I examined the number of mitochondria per micron and the relative spacing between the mitochondria across the whole axon imaged (Figure 42C, 42D). Both R94Q cell lines had significantly

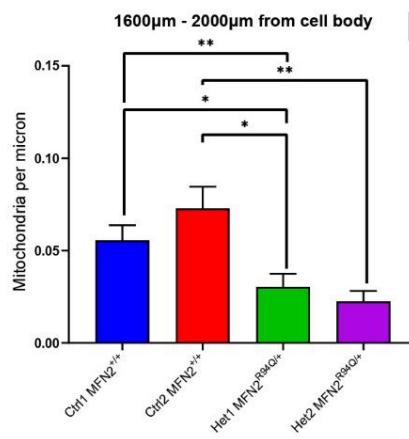
increased distance between mitochondria when compared with Ctrl2 MFN2^{+/+}. Indicating that the number of mitochondria is not different R94Q compared with control but that the space between them has been increased. I noted from the images that this appeared more apparent when viewing specific regions of the neurons. Therefore, I chose to split the analysis of the axon into three regions and see if these were affected differently. The regions are defined as 100μm – 300μm from the cell body, 900μm – 1100μm and 1600μm – 1800μm. Examining the mitochondria per micron using these categories (Figure 10E) it can be seen that there is no significant difference at 100μm – 300μm or 900μm – 1100μm from the cell body. However, in the 1600μm – 1800μm region of the neuron, Het2 MFN2^{R94Q/+} has significantly fewer mitochondria per micron than Ctrl2 MFN2^{+/+}. At both 100μm – 300μm or 900μm – 1100μm from the cell body there is no statistical difference in the distance between the mitochondria (Figure 42F). In the 1600μm – 1800μm region of the neuron, Het2 MFN2^{R94Q/+} has a significantly greater distance between mitochondria than both neurons from control lines, whereas Het1 MFN2^{R94Q/+} is only significantly increase compared with Ctrl2 MFN2^{+/+}. From this data it appears that the number of mitochondria is not affected but there is a greater distance between them, indicating that they may be smaller. However, if the area of analysis is expanded to 1600μm – 2000μm it can be seen that the number of mitochondria per micron is significantly decreased in the R94Q lines compared to both control lines (Figure 42G). Additionally, the space between the mitochondria is still significantly increased (Figure 42H). This suggests that not only are the mitochondria found further from the cell body further apart but that there are also fewer of them further from the cell body than in the wild type. Taken together this data suggests the possibility of a transport defect which may include a potential fusion defect.



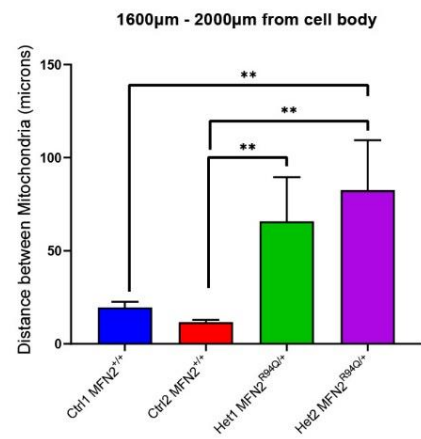
F)



G)



H)



I)

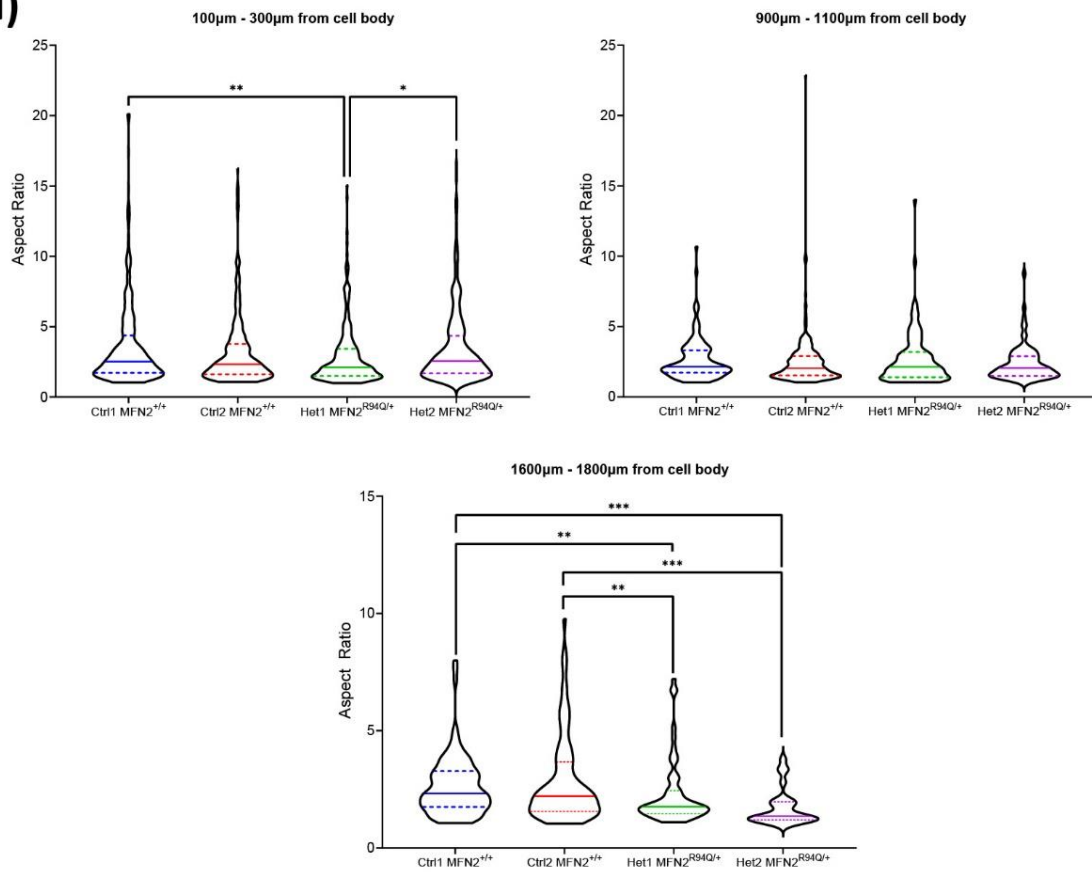


Figure 42: Assessment of mitochondrial spacing and morphology in day 33 neurons containing MFN2^{+/+} or MFN2^{R94Q/+}. **A)** Stitched image of a motor neuron transfected with both GFP and ds-mitochondria plasmids. Axon start and path are indicated using arrows. Scale bar: 200µm. **B)** Steps for analysis of mitochondrial morphology in motor neurons containing ds-mitochondria and GFP plasmids. **C)** The number of mitochondria per micron over the whole axon imaged. The data shown are the mean ±SEM. N = 19+ neurons from 4+ separate differentiations. **D)** Distance between mitochondria over the whole axon imaged. The data shown are the mean ±SEM. N = 19+ neurons from 4+ separate differentiations (* - P ≤ 0.05, Brown-Forsythe and Welch ANOVA tests). **E)** The number of mitochondria per micron for 200µm regions along the axon. The data shown are the mean ±SEM. N = 9+ neurons (* - P ≤ 0.05, Welch's t-test). **F)** Distance between mitochondria measured in 200µm regions along the axon. The data shown are the mean ±SEM. N = 9+ neurons from 4+ separate differentiations (* - P ≤ 0.05, *** - P ≤ 0.001, Kolmogorov-Smirnov test). **G)** The number of mitochondria per micron at 1600µm-2000µm along the axon. The data shown are the mean ±SEM. N = 7+ neurons (* - P ≤ 0.05, Welch's t-test). **H)** Distance between mitochondria measured 1600µm-2000µm along the axon. Data shown are the mean ±SEM. N = 7+ neurons from 4+ separate differentiations (* - P ≤ 0.05, *** - P ≤ 0.001, Kolmogorov-Smirnov test). **I)** Aspect ratio measured in 200µm regions along the axon. Dashed lines indicate interquartile ranges, filled in line indicates mean. Violin plots contain individual data for mitochondrion from at least 18 neurons for each condition from 4+ separate differentiations. (* - P ≤ 0.05, ** - P ≤ 0.01, *** - P ≤ 0.001, **** - P ≤ 0.0001, Kolmogorov-Smirnov test).

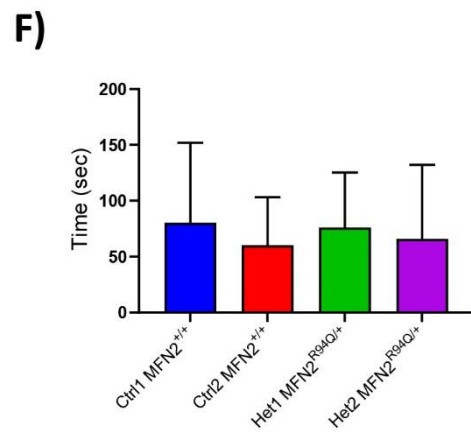
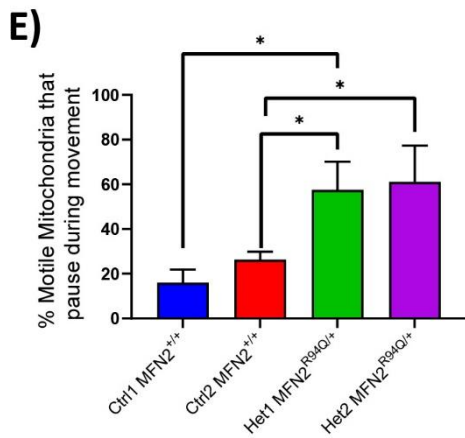
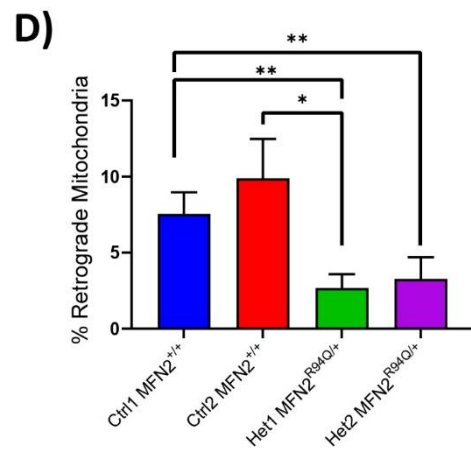
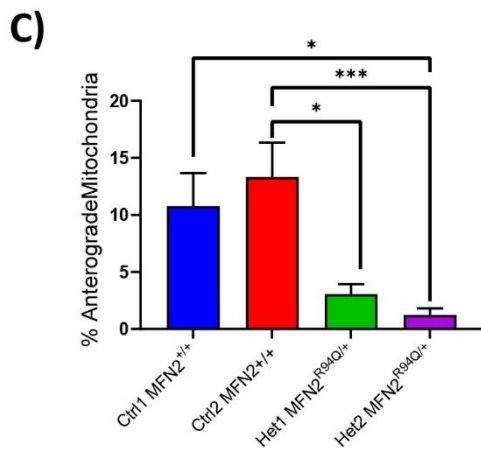
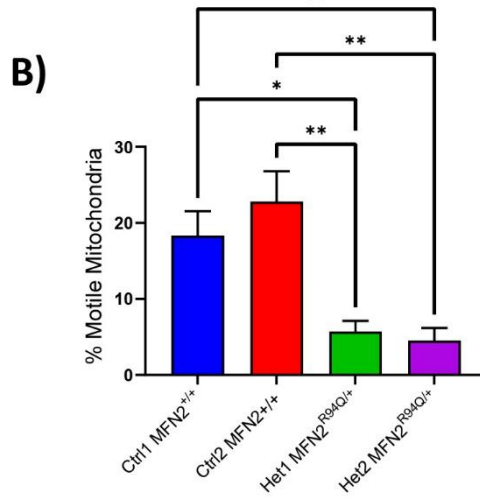
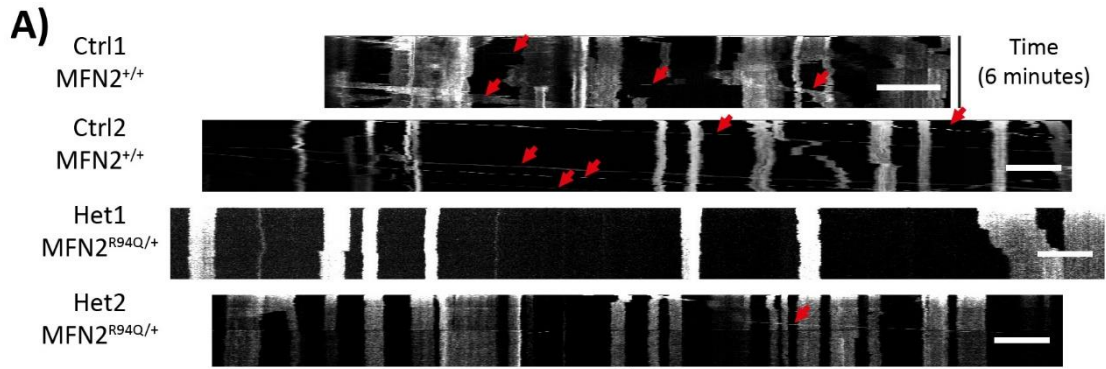
To confirm if the increased distance between mitochondria was indeed indicating smaller mitochondria, I measured the aspect ratio of mitochondria within these regions of the neuron. Form factor was not calculated because due to the width of the axon branching of mitochondria does not occur. This leaves the primary measurement of mitochondrial morphology being aspect ratio. Het1 MFN2^{R94Q/+} appeared to have mitochondria with a significantly decreased aspect ratio compared with Ctrl1 MFN2^{+/+} and Het2 MFN2^{R94Q/+} at 100µm – 300µm (Figure 42I) however this did not appear when mitochondria were examined at 900µm – 1100µm where there was no statistical difference in the aspect ratio of mitochondria. Taken together these pieces of data suggest there is unlikely to be a significant fusion defect in the neuron as the mitochondria are predominantly of a similar distribution of aspect ratios. At 1600µm – 2000µm from the cell body, wild-type lines had significantly larger mitochondrial aspect ratios than the R94Q lines (Figure 42I). This data indicates that further from the cell body mitochondria are smaller in axons of R94Q motor neurons. Whilst this difference indicates a fusion defect, the rest of the neuron appears largely normal suggesting the fusion defect is not due to

the R94Q mutation's impact on fusion but rather on trafficking and lack of fusion partners or reaching fusion partners.

In summary, this data indicates that whilst the mitochondria within the axon appear normal close to the cell body, a difference in mitochondrial spacing and morphology can be found in the distal parts of the axon, which may be suggestive of a trafficking defect.

5.2.4) *MFN2^{R94Q/+} motor neurons have a mitochondrial trafficking defect*

The reduced number of mitochondria found within the distal axon suggested there may be a trafficking defect. I differentiated control and edited lines to motor neurons using the optimised protocol. The day before time-lapse microscopy tracking, cells were transfected with GFP and ds-RedMito plasmids. Kymographs were produced from the time-lapse data (Figure 43A). Moving mitochondria can be seen in these images as diagonal lines, whereas stationary mitochondria are seen as straight lines. During the experiment I noted the direction of the cell body and analysed these images so that the cell body can be found on the left of the kymograph, allowing the distinction between anterograde and retrograde movement. This is important as different motors are involved in each process (Pilling *et al.*, 2006; reviewed in Schwarz, 2013). Motile mitochondria were classified by movements of $>0.3 \mu\text{m/s}$ in either anterograde or retrograde direction as this will exclude any actin-based transport of mitochondria (De Vos *et al.*, 2007). The R94Q neurons showed significantly fewer moving mitochondria than control lines (Figure 43B). This transport was significantly reduced in both anterograde (Figure 43C) and retrograde directions (Figure 43D).



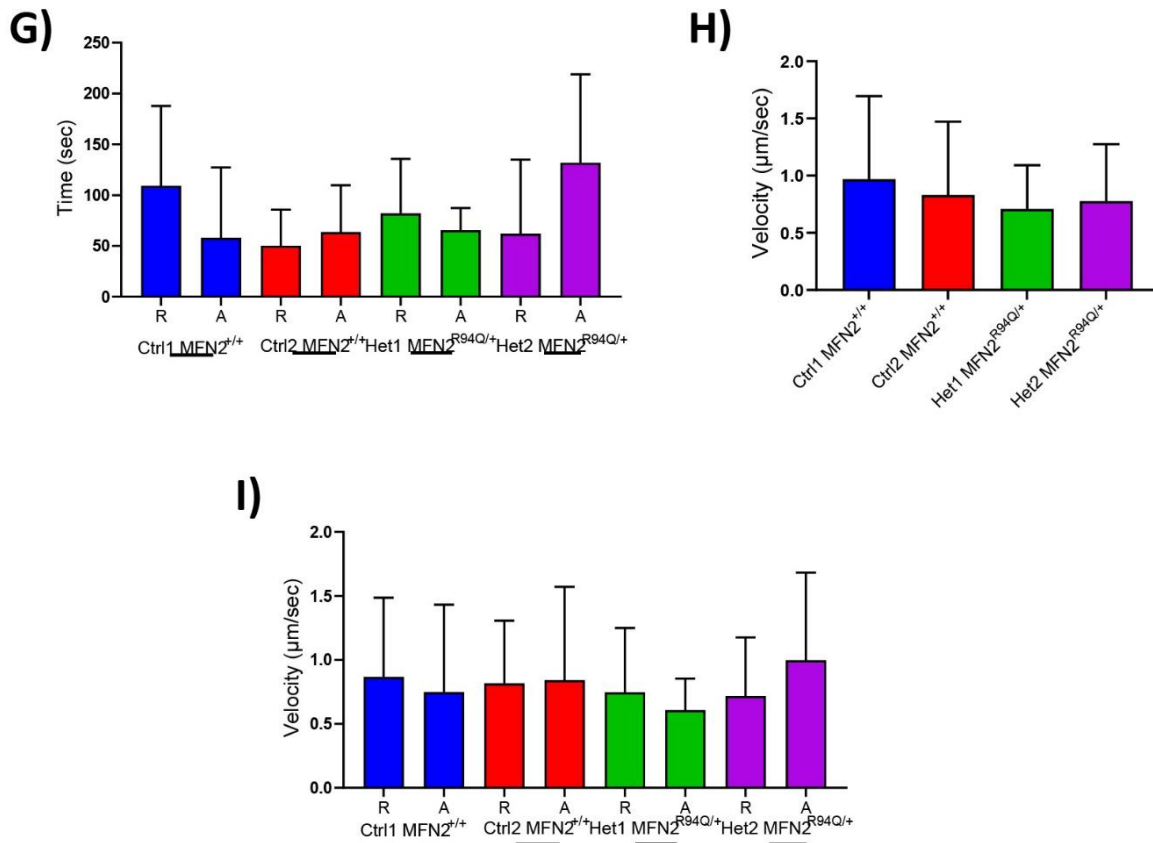


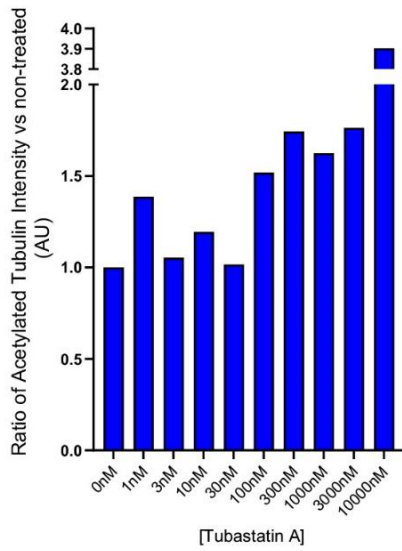
Figure 43: Assessment of mitochondrial transport in day 33 neurons containing MFN2^{+/+} or MFN2^{R94Q/+}. All data shown are mean \pm SEM. N = 15+ neurons for trafficking data from 4+ separate differentiations. **A)** Representative of kymographic space-time plots from wild type and mutant neurons. Stationary mitochondria are visible as straight lines. Mitochondrion in motion is depicted as diagonal lines. Red arrows indicate several mitochondria in motion. Horizontal scale bar 10 μ m, vertical scale 360 seconds. **B)** Overall quantification of tracking data. Motile mitochondria were classified by movements of $>0.3 \mu\text{m/s}$ in either anterograde or retrograde direction. (* - $P \leq 0.05$, ** - $P \leq 0.01$, Kruskal-Wallis test). **C)** Tracking data for anterograde (forward) motion. Motile mitochondria were classified by movements of $>0.3 \mu\text{m/s}$ in anterograde direction. (* - $P \leq 0.05$, ** - $P \leq 0.01$, *** - $P \leq 0.001$, **** - $P \leq 0.0001$, Kolmogorov-Smirnov test). **D)** Tracking data for retrograde (backward) motion. Motile mitochondria were classified by movements of $>0.3 \mu\text{m/s}$ in retrograde direction. (* - $P \leq 0.05$, ** - $P \leq 0.01$, *** - $P \leq 0.001$, **** - $P \leq 0.0001$, Kolmogorov-Smirnov test). **E)** The percentage of mitochondria that pause during movements. Motile mitochondria were classified by movements of $>0.3 \mu\text{m/s}$ in direction. From this, a mitochondrion was classed as paused mitochondria if it was stationary for at least two frames (6 seconds) before becoming motile again (* - $P \leq 0.05$, Kolmogorov-Smirnov test). **F)** The average time mitochondria spend paused. **G)** The average time mitochondria spend paused (as seen in F) separated by direction of movement before pausing. **H)** Mitochondrial velocity. **G)** Mitochondrial velocity (as seen in H) separated by the direction of movement.

For successful mitochondrial trafficking to occur several things must occur. The MIRO/MILTON complex must bind mitochondria (via MFN2), this must then bind to motor proteins which can then bind to microtubules and begin their motion (reviewed in Schwarz, 2013). If these processes cannot happen then mitochondria will not move along microtubules. Additionally, if one of these processes is altered during transport, e.g. motor becomes detached from the microtubules, then trafficking will stop. MFN2 is directly involved in the binding of MIRO/MILTON, meaning the most likely of these three to be disrupted is the binding of this complex to the mitochondria. To gain further information which may help resolve the mechanism, I examined the percentage of motile mitochondria which paused during their movement. A paused mitochondrion was defined as one that moved $>0.3 \mu\text{m/s}$ before stopping for at least two frames and then made a second movement at $>0.3 \mu\text{m/s}$. From the analysis, it can be seen that the motile mitochondria observed in edited lines paused significantly more often than the mitochondria in control lines (Figure 43E), however, the amount of time which each mitochondria spent paused on average was not altered (Figure 43F). The average time spent paused was not significantly different for either direction of movement (Figure 43G). Taken together this data suggests something is interrupting the transportation of mitochondria in the edited lines and that this is causing more pauses. However, it also suggests that no particular motor had specific difficulty binding to the MIRO/MILTON complex as the time spent paused was not altered between control and R94Q lines or direction of travel. To confirm that the motor itself was functional I measured the velocity of the mitochondria being transported. The average velocity of mitochondria was found to be $\sim 1 \mu\text{m/s}$ in all lines (Figure 43H) and was not found to be significantly different between the lines even when separated for the direction (and therefore individual motor action) (Figure 43I). Taken together this suggests that the most likely culprit is the binding of mitochondria to MIRO/MILTON, not the binding or activity of the motor itself or any particular motor binding the MIRO/MILTON complex.

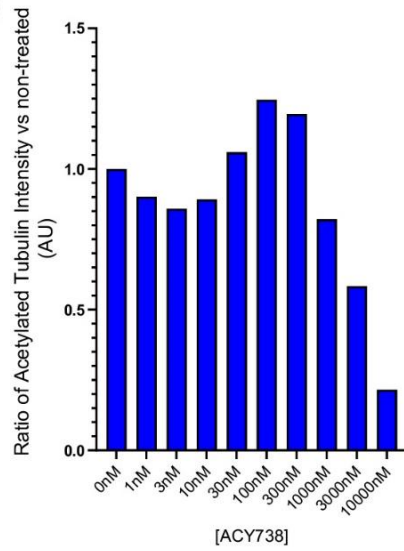
5.2.5) Effect of HDAC6 inhibitor on mitochondrial trafficking and morphology

HDAC6 inhibition has previously been used in other models to alleviate mitochondrial trafficking defects including CMT models types (Benoy *et al.*, 2018; Mo *et al.*, 2018) and has shown benefit in a CMT2A mouse model where transport was not directly examined (Picci *et al.*, 2020; Shen *et al.*, 2021). Based on these findings, I set out to test an HDAC6 inhibitor in the R94Q neurons I generated. I reasoned that inhibition of HDAC6 may help me examine the interactions of motor proteins with mitochondrial transport machinery to investigate mechanisms involved in R94Q dysfunction.

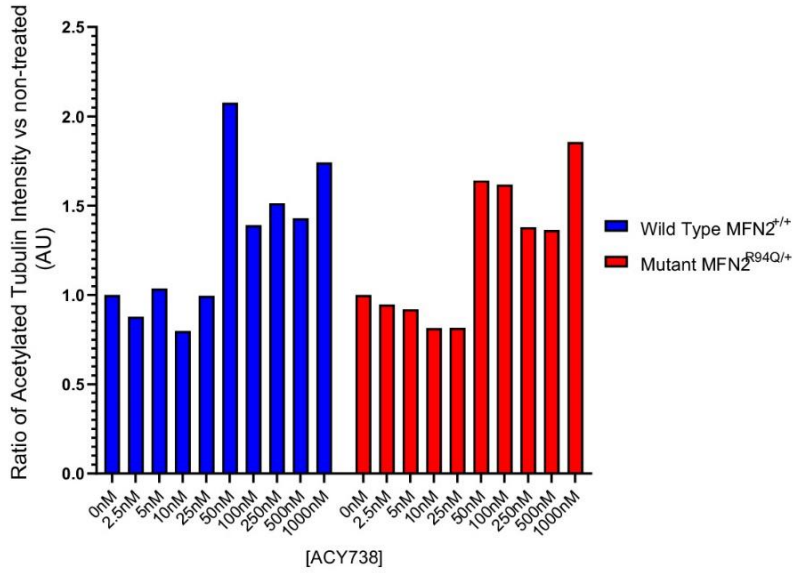
A)



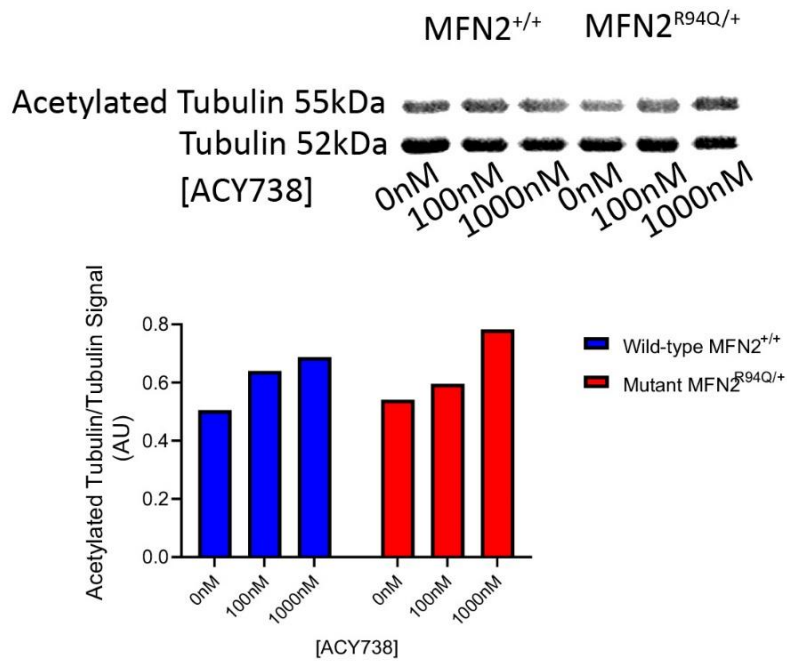
B)



C)

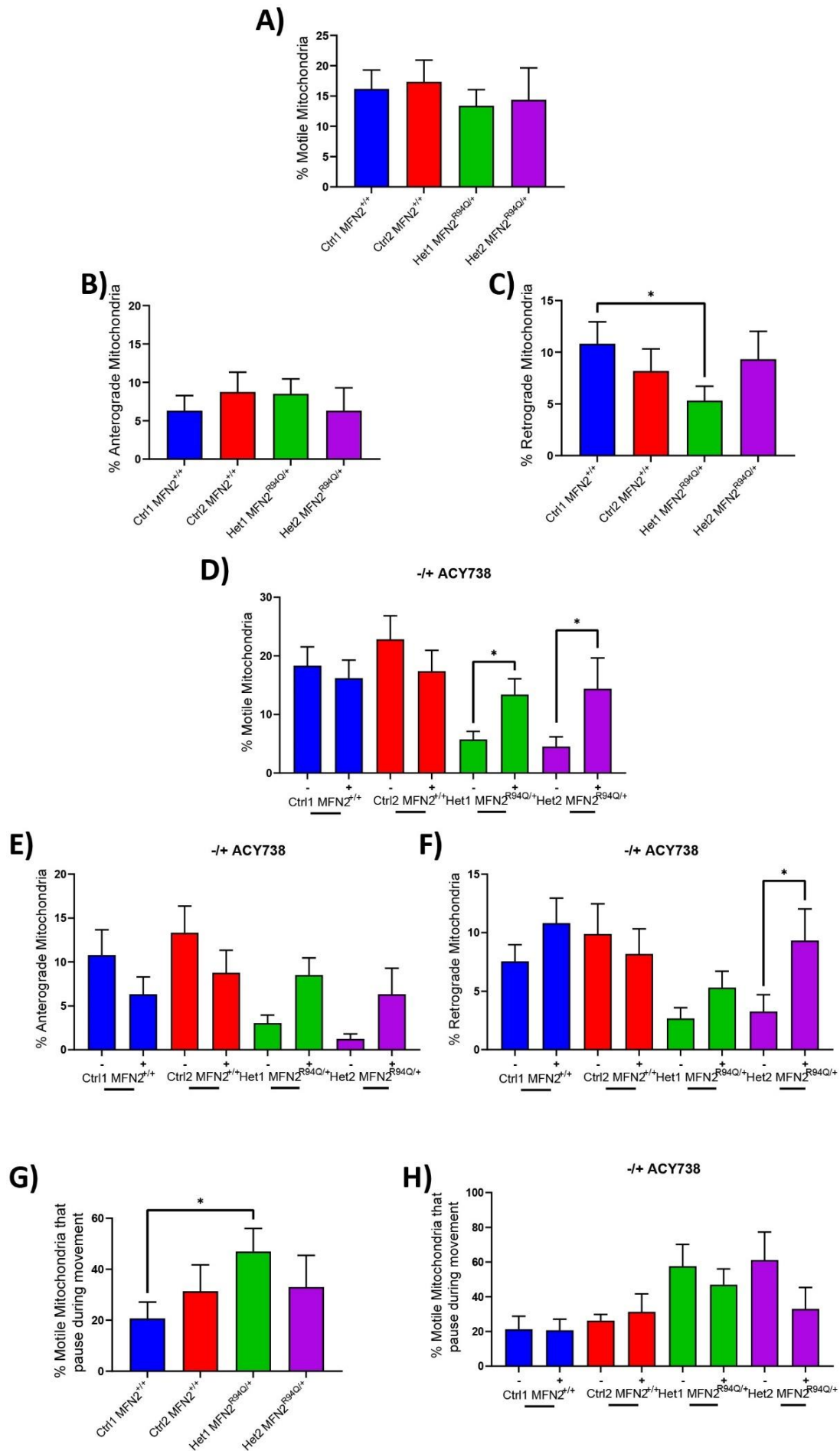


D)



(Previous page) Figure 44: Western Investigation in hPSC and motor neurons to determine the appropriate dose of HDAC6 inhibitors to achieve an increase in acetylated tubulin. Data was from 1 biological repeat. **A)** The ratio of acetylated tubulin in treated versus untreated condition for hPSC dosed with Tubastatin A for 24 hrs. **B)** The ratio of acetylated tubulin in treated versus untreated condition for hPSC dosed with ACY738 for 24 hrs. **C)** The ratio of acetylated tubulin in treated versus untreated condition for motor neurons containing either wild-type MFN2 or R94Q/+ dosed with ACY738 for 24 hrs. **D)** Top) Western blot for tubulin and acetylated tubulin in motor neurons containing either wild-type MFN2 or R94Q/+ at various doses of ACY738. Bottom) Quantification of western blot.

HDAC6 is known to deacetylate tubulin. Preventing the deacetylation of tubulin is thought to allow easier binding of motor proteins to microtubules (reviewed in Batchu, Brijmohan and Advani, 2016). With this in mind, I chose to evaluate the ability of two HDAC6 inhibitors (Tubastatin A and ACY738) to increase the amount of acetylated tubulin in hPSC by analysing staining intensity of acetylated-tubulin staining. I tested both a range of doses of Tubastatin A and ACY738 on hPSC for 24hrs (Figure 44A, 44B). An increase in acetylated tubulin was detected at ~100nM for both compounds. At the highest concentration ranges tested, significant cell death was seen. Using this information, I proceeded to test ACY738 in differentiated motor neurons in a narrower concentration range and used the same method. An increase in acetylated tubulin was detected at 50-100nM (Figure 44C). To confirm this finding, I used western blotting for a smaller range of doses. An increase in acetylated tubulin was detected at all doses (figure 44D). From this data, I concluded that 100nM for 24hrs was an appropriate dose of ACY738 to use for further experiments.



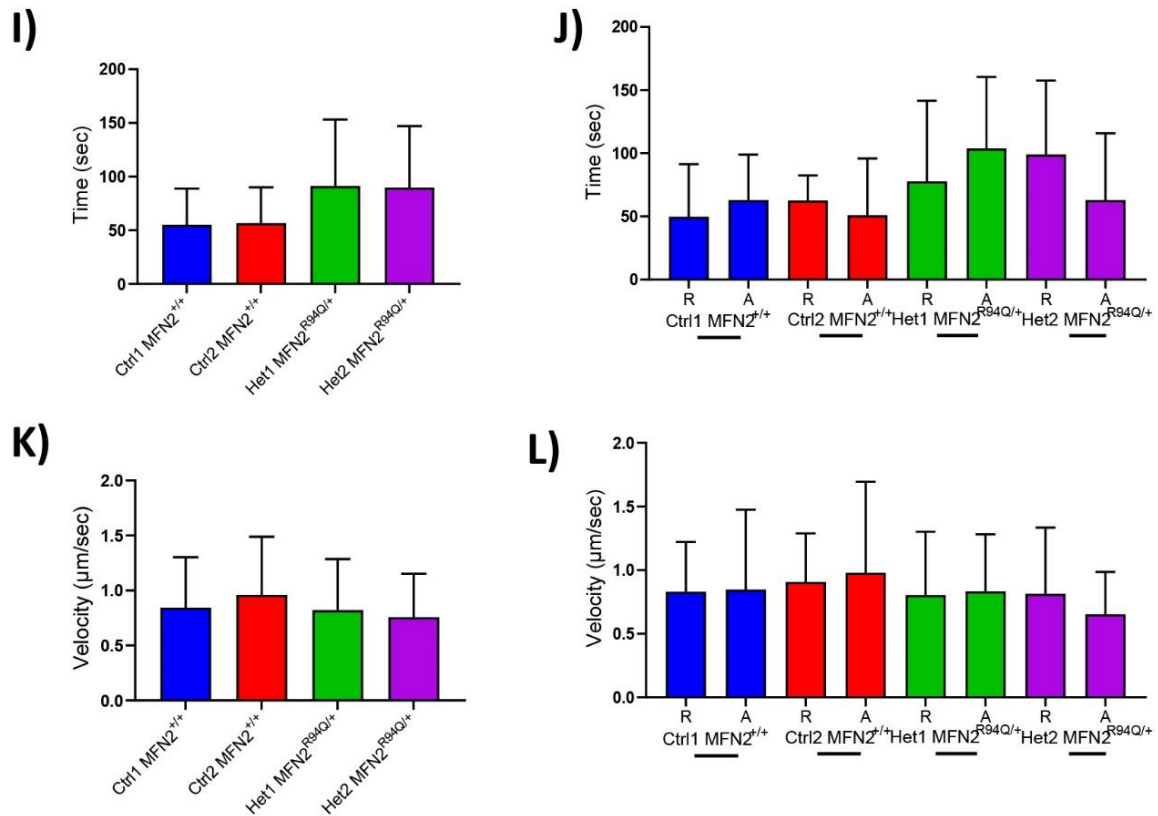
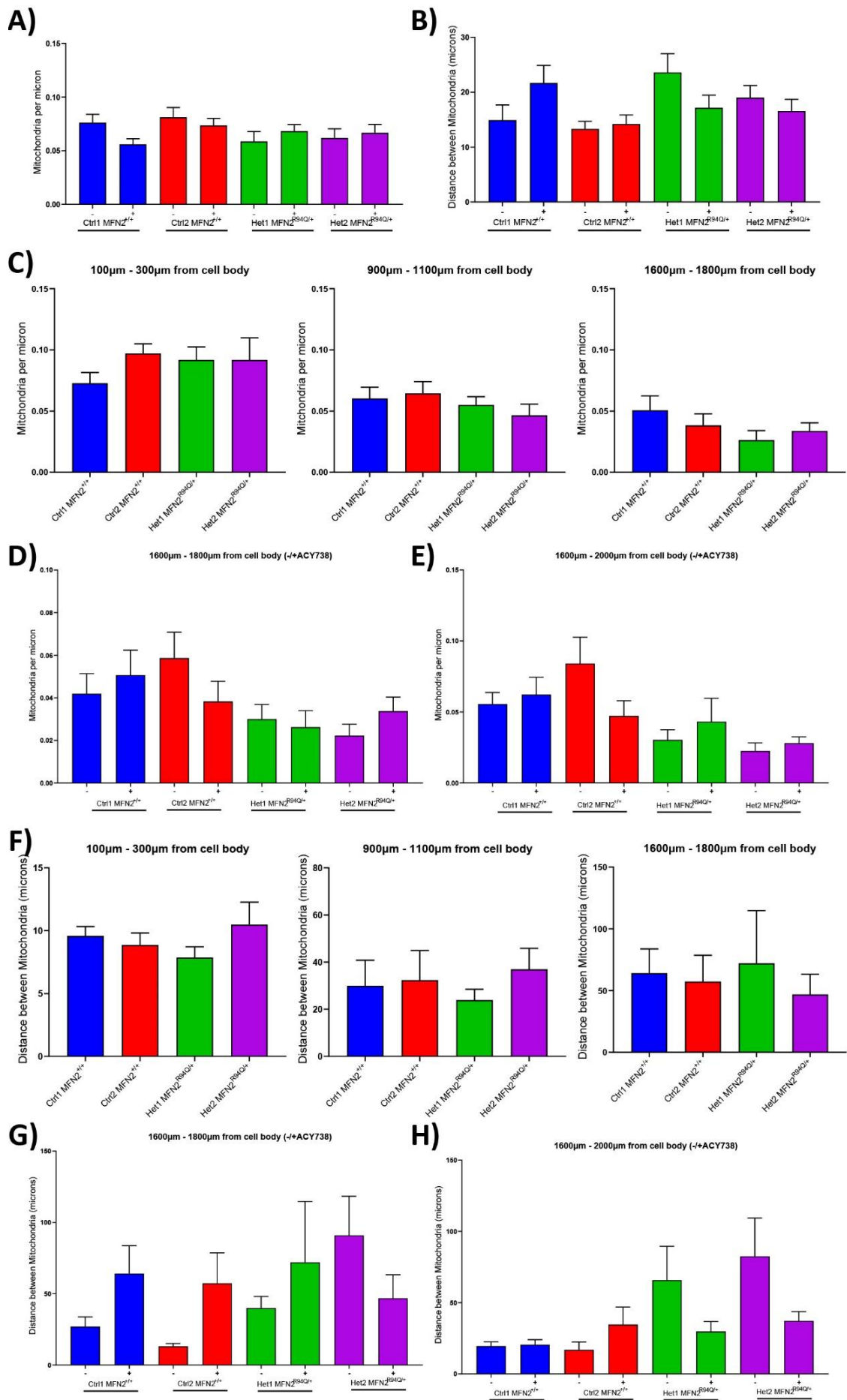


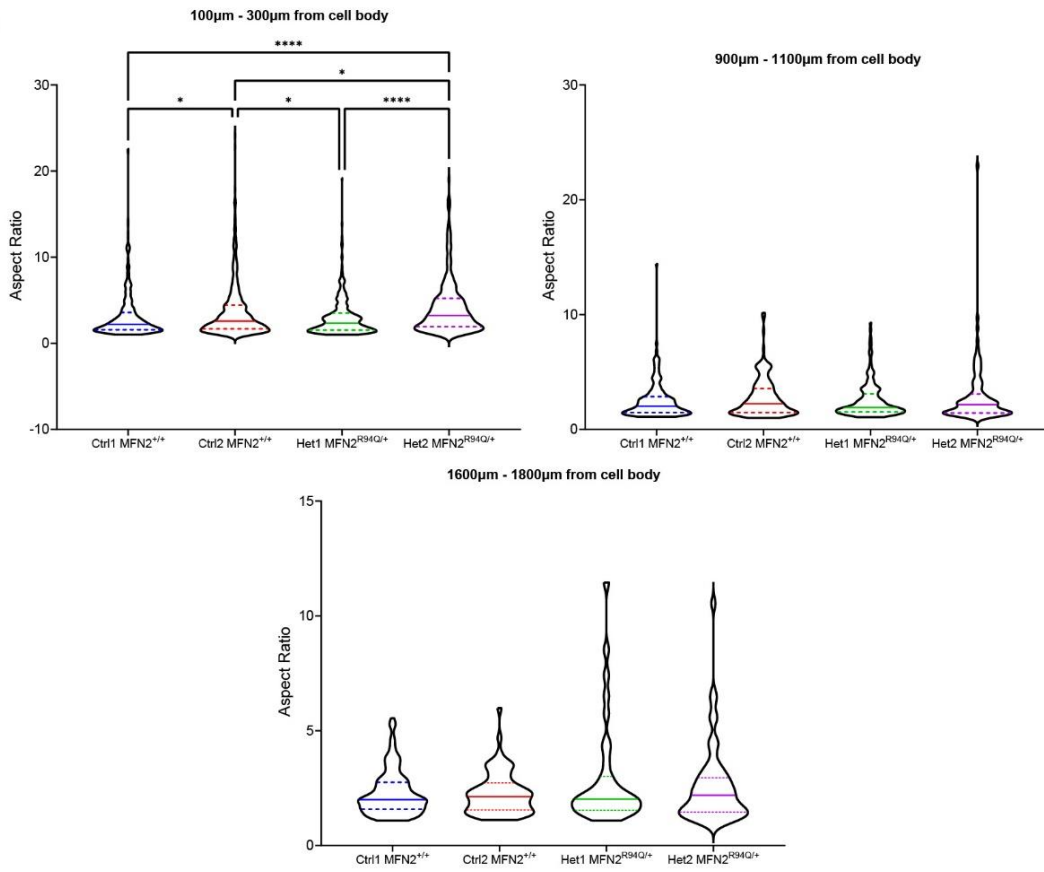
Figure 45: Assessment of mitochondrial transport in day 33 neurons containing MFN2^{+/+} or MFN2^{R94Q/+} in the presence of 100nM HDAC inhibitor ACY738. All data shown are the mean \pm SEM. N = 15+ neurons for trafficking data from 4+ separate differentiations. **A)** Quantification of tracking data. Motile mitochondria were classified by movements of $>0.3 \mu\text{m/s}$ in either anterograde or retrograde direction. **B)** Quantification of tracking data for anterograde (forward) motion. Motile mitochondria were classified by movements of $>0.3 \mu\text{m/s}$ in anterograde direction. **C)** Quantification of tracking data for retrograde (backward) motion. Motile mitochondria were classified by movements of $>0.3 \mu\text{m/s}$ in retrograde direction. **D)** Comparison of overall tracking data in the presence and absence of ACY738. **E)** Comparison of anterograde (forward) tracking data in the presence and absence of ACY738. **F)** Comparison of retrograde (backward) tracking data in the presence and absence of ACY738. (* - $P \leq 0.05$, Kruskal-Wallis test). **G)** Quantification of the percentage of mitochondria that pause during movements. Motile mitochondria were classified by movements of $>0.3 \mu\text{m/s}$ in direction. From this, a mitochondrion was classed as paused mitochondria if it was stationary for at least two frames (6 seconds) before becoming motile again (* - $P \leq 0.05$, Kolmogorov-Smirnov test). **H)** Comparison of the percentage of mitochondria that pause during movements in the presence and absence of ACY738. **I)** Quantification of the average time mitochondria spend paused. **J)** Quantification of the average time mitochondria spend (as seen in I) separated by direction of movement before pausing. **K)** Quantification of mitochondrial velocity. **L)** Quantification of mitochondrial velocity (as seen in K) separated by the direction of movement.

As previously, I differentiated control and edited lines to motor neurons using the optimised protocol. The day before time-lapse microscopy tracking, cells were transfected with GFP and ds-RedMito plasmids and then dosed for 24 hours with 100nM ACY738. Kymographs were produced from the time-lapse data. In the presence of ACY738, the percentage of motile mitochondria in MFN2 R94Q lines was no longer significantly different to the control neurons (Figure 45A). This was true for anterograde (Figure 45B) and retrograde (Figure 45C), aside from Het1 MFN2^{R94Q/+} which was still significantly decreased compared with Ctrl1 MFN2^{+/+}. When compared directly with their no dosed counterparts (Figure 45D, 45E, 45F) it can be seen that overall transport in the edited neurons had been significantly increased, whereas that for the control neurons had not been altered (Figure 45D). This effect is less clear when the movement is separated into the direction of movement, where the anterograde movement of mitochondria was not significantly increased in the edited lines, despite an increase in the trend (Figure 45E). Additionally, treated control neurons appeared to have less anterograde movement than their untreated counterpart but this was not significantly altered. For retrograde movement, the treated control neurons seemed more similar to their untreated counterpart however only Het2 MFN2^{R94Q/+} was significantly increased (Figure 45F). Taken together this data suggests that there has been a significant increase in overall mitochondrial transport in the R94Q lines when treated with ACY738 but this may not be a complete return to wild-type transport levels.

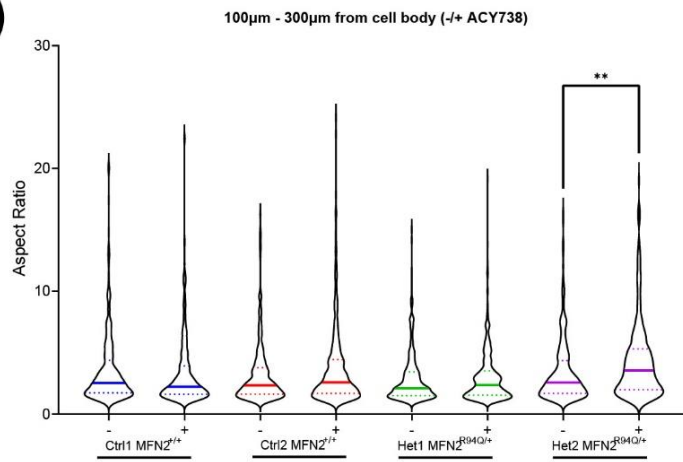
The percentage of motile mitochondria pausing in the treated neurons was now only significant between Ctrl1 MFN2^{+/+} and Het1 MFN2^{R94Q/+} indicating this may have been improved by treatment (Figure 45G). However, when treated and untreated mitochondria are compared directly it can be seen that no significant differences had occurred in the percentage of mitochondria that pause (Figure 45H). Time mitochondrion spend paused was not altered overall (Figure 45I) or in either specific direction (Figure 45J). Overall velocity was unchanged (Figure 45K), still being ~1µm/s in either direction (Figure 45L). Taken together this data suggests that ACY738 had not affected the specific action of either motor.



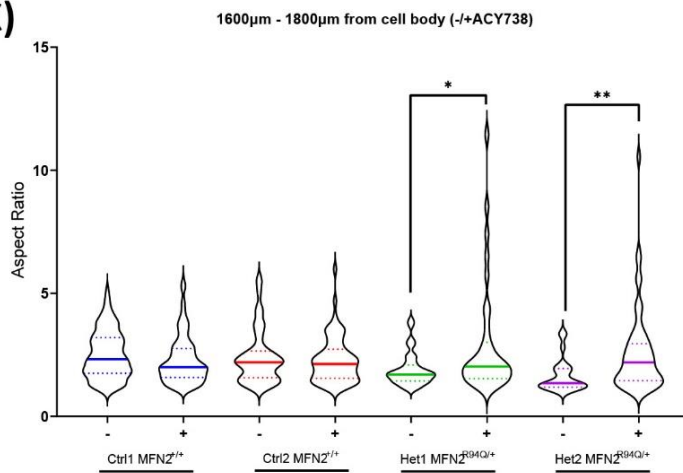
I)



J)



K)

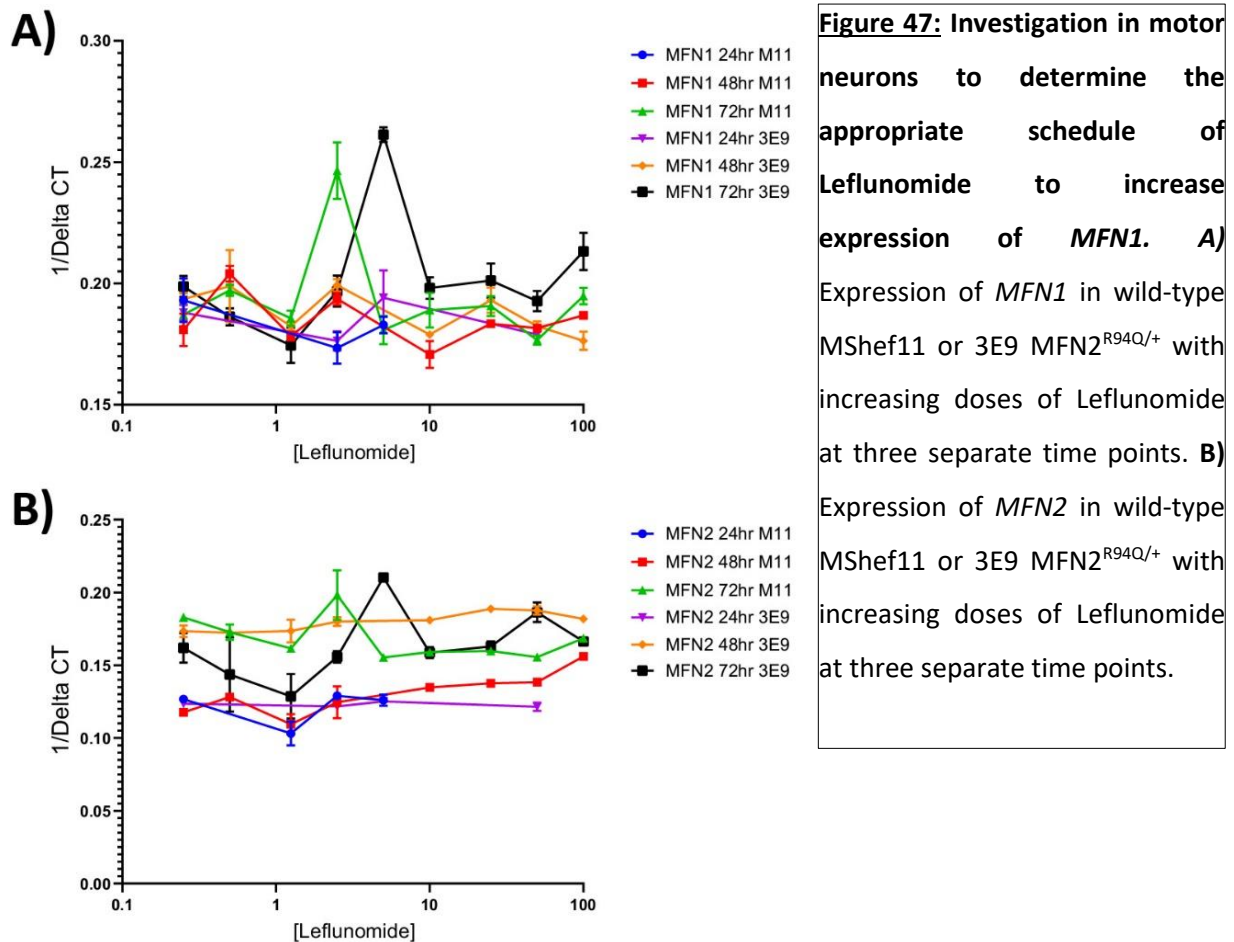


(Previous page) Figure 46: Assessment of mitochondrial spacing and morphology in day 33 neurons containing MFN2^{+/+} or MFN2^{R94Q/+} in the presence of 100nM HDAC inhibitor ACY738. All data shown are the mean \pm SEM. **A)** Comparison of mitochondria per micron over the whole axon imaged in the presence and absence of ACY738. N = 15+ neurons from 4+ separate differentiations. **B)** Comparison of the distance between mitochondria over the whole axon imaged in the presence and absence of ACY738. N = 15+ neurons from 4+ separate differentiations. **C)** The number of mitochondria per micron for 200 μ m regions along the axon. N = 4+ neurons from 4+ separate differentiations. **D)** Comparison of mitochondria per micron at 1600 μ m-1800 μ m along the axon in the presence and absence of ACY738. N = 4+ neurons from 4+ separate differentiations. **E)** Comparison of mitochondria per micron at 1600 μ m-2000 μ m along the axon in the presence and absence of ACY738. N = 4+ neurons from 4+ separate differentiations. **F)** Distance between mitochondria measured in 200 μ m regions along the axon. N = 4+ neurons. **G)** Comparison of the distance between mitochondria at 1600 μ m-1800 μ m along the axon in the presence and absence of ACY738. N = 4+ neurons from 4+ separate differentiations. **H)** Comparison of the distance between mitochondria at 1600 μ m-2000 μ m along the axon in the presence and absence of ACY738. N = 4+ neurons from 4+ separate differentiations. **I)** Aspect ratio measured in 200 μ m regions along the axon. Dashed lines indicate interquartile ranges, the filled-in line indicates mean. Violin plots contain individual data for mitochondrion from at least 15 neurons for each condition. (* - $P \leq 0.05$, ** - $P \leq 0.01$, *** - $P \leq 0.001$, **** - $P \leq 0.0001$, Kolmogorov-Smirnov test). **J)** Comparison of aspect ratio measured at 100 μ m-300 μ m along the axon. Dashed lines indicate interquartile ranges, the filled-in line indicates mean. Violin plots contain individual data for mitochondrion from at least 15 neurons for each condition from 4+ separate differentiations. (* - $P \leq 0.05$, Kruskal-Wallis test). **K)** Comparison of aspect ratio measured at 1600 μ m-1800 μ m along the axon. Dashed lines indicate interquartile ranges, the filled-in line indicates mean. Violin plots contain individual data for mitochondrion from at least 15 neurons for each condition from 4+ separate differentiations. (* - $P \leq 0.05$, ** - $P \leq 0.01$, Kolmogorov-Smirnov test).

The action of ACY738 to increase the overall transport in the mitochondria led me to investigate if the mitochondrial distribution in the axon had been altered. I examined the number of mitochondria per micron (Figure 46A) and spacing between mitochondria (Figure 46B) found throughout the whole axon and found these had not been significantly altered by treatment with ACY738. I also examined the neurons using the previously defined categories to see if the mitochondria had been altered in these specific regions. The number of mitochondria per micron was not different between control and MFN2^{R94Q/+} lines (Figure 46C) in any region measured. When treated and untreated measurements were directly compared for the 1600 μ m-1800 μ m region, it can be seen that no significant differences

are noted between treated and untreated neurons (Figure 46D), indicating that this has not improved with treatment. This was further confirmed when the area examined was expanded to 1600µm-2000µm (Figure 46E). The distance between mitochondria was also found to no longer be significantly different in the regions examined (Figure 46F). However, when comparing control neurons with their non-treated counterparts at 1600µm-1800µm it appeared that the distance between mitochondria was trending towards being increased which may have been why this was no longer significantly different (Figure 46G). When this was expanded to 1600µm-2000µm it was clearer that the mitochondria spacing between treated and untreated controls were no longer appearing different (Figure 46H). It also appeared that the MFN2^{R94Q/+} neurons trended towards having a decreased distance between mitochondria, though this was not statistically different. This data could suggest that the mitochondria were longer in response to treatment with ACY738. To confirm if this was the case, I examined the aspect ratios of the mitochondria. At 100µm-300µm, it can be seen that the aspect ratios of Het2 MFN2^{R94Q/+} are significantly larger than that of the other lines and Ctrl2 MFN2^{+/+} also has a significantly larger aspect ratio than the other two cell lines (Figure 46I). When comparing mitochondrion at 100µm-300µm treated vs untreated aspect ratios, it can be seen that only Het2 MFN2^{R94Q/+} has significantly increased aspect ratio when compared to the untreated neurons (Figure 46J). No significant difference was seen between the aspect ratios between control and R94Q mitochondria at 900µm-1100µm. When comparing the aspect ratio of treated and untreated mitochondria treated at 1600µm-1800µm, it can be seen that the treated R94Q lines have significantly increase compared to their untreated counterparts (Figure 46K) whilst the wild-type lines remain unchanged. Taken together this data indicates that the mitochondria in this region of the axon have significantly increased in size but not in number (Figure 46D) meaning increased fusion may have taken place in this part of the neuron.

Overall, this data suggests, that inhibition of HDAC6 via ACY738 has provided an increase in mitochondrial transport in this system which has led to an increase in the size in mitochondria found 1600µm-1800µm from the cell body.



5.2.6) Effect of increasing *MFN1* expression on Mitochondrial Trafficking

CMT2A has previously been alleviated in animal models by increasing the expression of *MFN1* to compensate for defective *MFN2* (Detmer and Chan, 2007; Zhou *et al.*, 2019). A screen of compound designed to detect an increase in *MFN2* expression found the compound Leflunomide which increased the expression of *MFN1* to a greater extent (Miret-Casals *et al.*, 2018). Therefore, I decided to test this compound in this system to see if increasing *MFN1* expression would alleviate the phenotype. I tested a range of doses across 24hrs, 48hrs and 72hrs and measured the expression of *MFN1* and *MFN2*. *MFN1* expression stayed consistent for the majority of data points, only spiking for one dose in each line in the 72hr time point (Figure 47A). This indicates that the compound was not able to increase the expression of *MFN1*. *MFN2* expression at the 72hr time points as well as on the higher doses of the 48hr time point (Figure 47B). As this compound was unable to achieve a consistent increase in *MFN1* expression in this system, I did not consider it worth trialling in neuron trafficking experiments.

5.3) Discussion

In summary, this chapter discusses the examination of the mitochondrial phenotypes seen in cell lines containing the CMT2A causing mutation, MFN2 R94Q. To my knowledge, this is the first examination of this mutation in human cells. R94Q lines were examined for the phenotypes in their hPSC state, for their efficacy in generating CMT2A affected cell types and for phenotypes in motor neurons.

When examined as hPSC cells, the edited lines showed no detected difference in their mitochondrial morphology, membrane potential, mass, mtDNA content or ATP production capacity. In patients, disease symptoms are predominantly limb specific indicating specificity to the disease pattern despite global genetic changes which have affected a mitochondrial localised protein, MFN2. This indicates hPSCs do not contain the specific vulnerability and suggest that it is gained during differentiation towards these cellular endpoints. ATP production capacity was only measured at a basal level and cells were not challenged using any compounds to inhibit various oxidative phosphorylation complexes which may have highlighted defects in a particular complex. In a mouse embryonic fibroblast CMT2A model, no mitochondrial defects were seen until the cells were pre-treated to cause oxidative stress, indicating that the cells had a heightened sensitivity than the wild-type (Wolf *et al.*, 2019). Furthermore, stem cells are known to rely on glycolysis (Varum *et al.*, 2011) and therefore may not be impacted by a defect in oxidative phosphorylation as strongly as a differentiated cell. Stem cells also have an 'immature' mitochondrial network and do not contain as many long branches as many differentiated cells. However, in patient fibroblasts containing different CMT2A causing mutations basal respiration was altered despite no apparent changes in mitochondrial morphology and ATP production (Loiseau *et al.*, 2007). This indicates that in the hPSC state there may still be an underlying defect or sensitivity caused by the edit which was not detected in these studies but may give insight into the disease mechanism and how it arises.

MFN2^{R94Q/+} motor neurons showed a trend towards an increase in the distance between mitochondria when the neuron was viewed as a whole but was only statistically significant compared with one of the control lines. The number of mitochondria per micron was not found to be significantly altered, which agrees with the data from hPSC. Both these measurements may worsen with age due to the persistence of the most prominent defect noted in the MFN2^{R94Q/+} neurons, the mitochondrial trafficking defect. The neurons tested here were only differentiated for approximately 34 days before testing, whilst care has been taken to replicate a differentiation protocol correctly mimicking the appropriate subtype of neurons it is unreasonable to assume these directly compare to *in vivo* adult or even child motor neurons. Extending the length of time these are allowed to mature, co-culture

with other cell types or perhaps even telomere shortening (Vera, Bosco and Studer, 2016) may help to mimic the ageing phenotype. Despite this, clear defects are seen when the neuron was examined in different regions. At 1600µm-2000µm from the cell body, fewer mitochondria per micron were seen with an increased spacing in between them. This indicates that from an even relevantly juvenile standpoint mitochondria were not getting to this part of the axon to the same extent as control neurons, indicating a trafficking defect. This is likely to cause more severe defects during ageing and can help explain the eventual axon disruption seen in the disease. Furthermore, the mitochondria found further along the axons of edited neurons were significantly smaller than their wild-type counterparts which may result in decreased ATP production or calcium buffering in the synapses of neurons which are typically one of the energy-intensive areas of the neuron meaning mitochondria are usually found there in abundance (reviewed in Mandal and Drerup, 2019). These findings increase understanding around the lack of innervation of distal muscles *in vivo* models (Bernard-Marissal *et al.*, 2019) and suggest the neuron muscular junction may be of particular interest to investigate further. To that end, this model may provide more information if the editing neurons were grown in co-culture with muscle cells and Schwann cells to give a more accurate picture of the defects occurring at the neuromuscular junction.

In the literature, there is disagreement over the extent of transport defect within CMT2A, with some finding a clear defect and others seeing no difference (Baloh *et al.*, 2007; Misko *et al.*, 2012; Strickland *et al.*, 2014; Rizzo *et al.*, 2016). This is the first known study to look at the R94Q mutation in human cells and shows a clear defect in transport. Further study would be required to examine other mutations to confirm if this is a phenotype universal to CMT2A or specific to few mutations. This model provides an ideal background to introduce different mutations and compare them directly with isogenic controls.

As mentioned, the most prominent defect noted in the MFN2^{R94Q/+} cells was a severe reduction in motile mitochondria, in both directions, which was also accompanied by an increase in pausing during trafficking. As average velocity and pausing time were unaffected in either direction the motor function appears unaffected. Given MFN2's role in binding to the MIRO/MILTON complex, there are two likely reasons this may occur. One is that, due to heterozygosity, successful transport is made due to MFN2 without R94Q, but the overall amount is decreased due to ineffective R94Q being unable to carry out the transport. This theory does not explain the increased pausing as control MFN2 mitochondria did not pause as often as R94Q. Additionally, previous work has shown via co-immunoprecipitation that MFN2 containing R94Q was still able to bind MIRO/MILTON and did not

disrupt MIRO/MILTON binding motor proteins (Misko *et al.*, 2010). This suggests that transport is still able to occur with MFN2^{R94Q} protein. Therefore, I propose it is more likely that it is the strength of this interaction that has been altered, making it easier for mitochondrial cargo to be dropped from MIRO and thus halting transport (Figure 48). This would make the initiation of transport harder, as effective binding must take place for motor proteins to bind to microtubules but also explain the increased pausing. Currently, no study has examined the strength of the interaction between R94Q and MIRO which would be required to prove this is the interaction at fault.

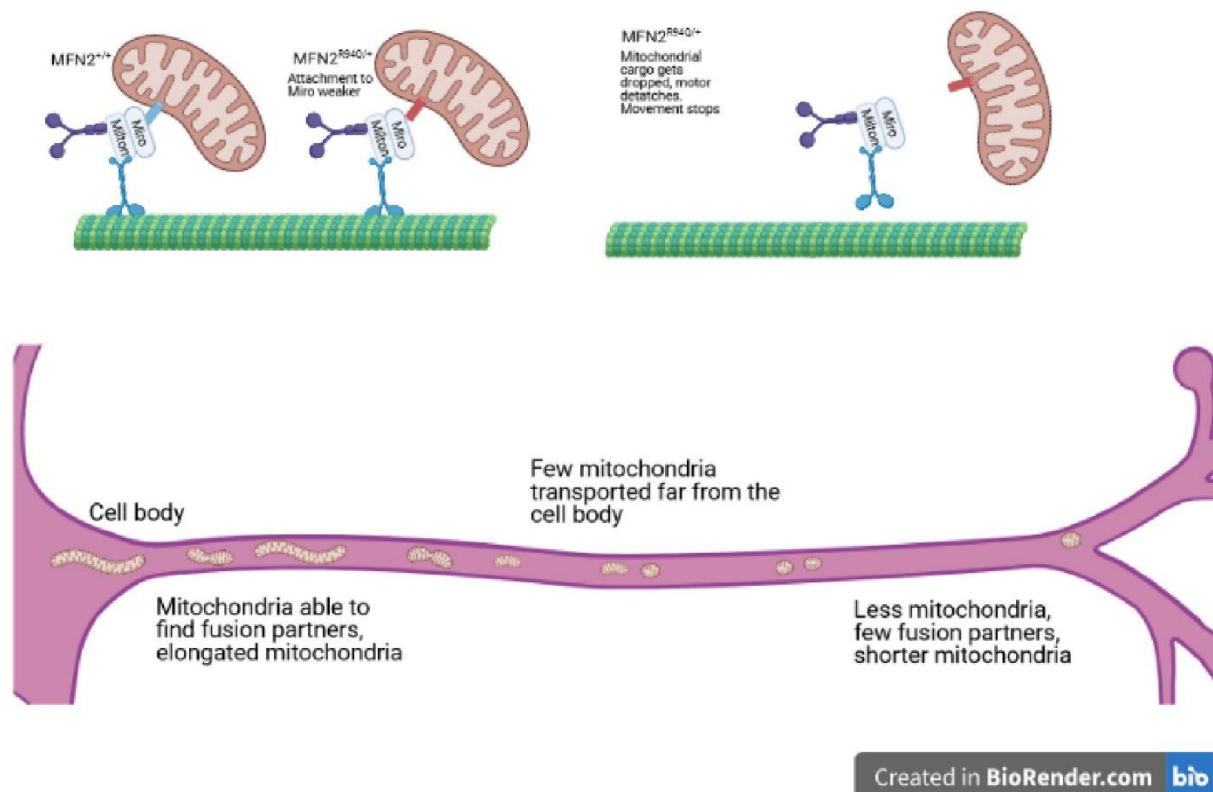


Figure 48: Proposed model for MFN2^{R94Q/+} impact on mitochondrial axonal transport. MFN2 binds to the MIRO/MILTON complex which binds to both Kinesin and Dynein to allow transport in both anterograde and retrograde directions respectively. In the MFN2^{R94Q/+} cells, there is a chance that the MFN2 that binds will contain the R94Q mutation. In this case, the binding to MIRO/MILTON is weaker making it more likely the mitochondria will be dropped. The binding of cargo is required for the motor to bind to microtubules therefore the motor also detaches and transport stops. Ultimately this leads to fewer mitochondria reaching the distal parts of the axon. Subsequently, mitochondria near the cell body can find fusion partners and will be elongated. Further along the neuron, there will come a point only limited mitochondria can reach meaning these mitochondria will have limited fusion partners available. Fission may still take place and mitochondria may still be cleared via normal clearance mechanisms leaving a limited number of small mitochondria.

Analysis of the mitochondria morphology in this model showed no clear defect in mitochondria fusion. This was true both for R94Q hPSC and motor neurons. In motor neurons, smaller mitochondria were seen far from the cell body which could suggest issues in mitochondrial fusion. However, no clear effects were seen in the other regions of the neuron examined, indicating poor fusion was not global and was most likely a symptom of the transport defect (Figure 48). Furthermore, this issue was resolved upon treatment with ACY738, which improved transport and the aspect ratio of mitochondria found far from the cell body without significantly changing the overall number found. If a fusion defect was present, the mitochondria would have increased in number but not in aspect ratio. As the aspect ratio increased it indicates these mitochondria were able to fuse when sufficient partners were provided. The lack of a fusion defect is in contrast to several studies which note this as a prominent phenotype of CMT2A and particularly the R94Q mutation (Detmer and Chan, 2007; El Fissi *et al.*, 2018; Rocha *et al.*, 2018; Wolf *et al.*, 2019). In the drosophila model, Fissi *et al* use the photoconversion method to show fusion defect. However, they also note a reduction of mitochondria at neuromuscular junctions, indicating a mobility defect. This makes it difficult to provide a measure for fusion as mitochondrial movement within the cell must be taken into account. If the mitochondria cannot move to either find fusion partners, this will be interpreted as a fusion defect, or if a photoactivated mitochondrion moves to the other side of the cell during imaging, it could be interpreted as successful fusion. The electron microscope images of mitochondria with R94-like show clustered mitochondria but measurements of the mitochondria are not shown, making it difficult to determine if these mitochondria are more or less fused than wild-type counterparts. Detmer *et al*, use of polyethylene glycol (PEG) method to measure fusion which involves two cell populations, one containing red mitochondria and the other containing green. PEG is used to fuse cells and when mitochondria with opposite colours fuse orange is seen. This method requires the movement of mitochondria across the cells to find fusion partners and therefore in the same way cannot be seen as independent of mitochondria movement. The final two examples mentioned (Rocha *et al.*, 2018; Wolf *et al.*, 2019) initially examine the ability of R94Q to rescue MFN2^{-/-}. Wolf *et al* found that the R94Q mutant was not as effective at the rescue as wild-type MFN2, however, some recovery was seen. Indicating fusion is possible with R94Q but that it may be less efficient. Rocha *et al*, conversely showed R94Q was not capable of rescue. This discrepancy may come about as Wolf *et al* used mitochondrial classification by researchers (conditions blinded) and Rocha *et al* used aspect ratio measurements. In the presence of endogenous MFN2, Rocha *et al* still indicated that R94Q had a significantly decreased aspect ratio in mouse embryonic fibroblasts which is counter to what was seen in this study. Examining all the data and methodologies together, R94Q may not be as effective a fusion partner as wild-type MFN2. As no clear fusion defect was shown in this model it is questionable how much of a phenotype this may have

in human cells and whether this is a primary aspect of CMT2A pathology for R94Q. It is also possible that for different CMT2A causing mutations fusion plays a larger role. Further research is required to confirm the role fusion plays in CMT2A, if it is worthwhile as a targetable treatment option and where it is a symptom of the transport defect.

A further explanation is that another of MFN2's roles is in play in the disruption of transport. In particular, this could be the role MFN2 has in the regulation of the contact of mitochondria with the endoplasmic reticulum. Whilst the exact nature of this role is not entirely understood (De Brito and Scorrano, 2008; Filadi *et al.*, 2015), it is clear that MFN2 has a significant role in mitochondrially associated membranes and such disruption of mitochondrial-ER contacts has previously been seen in CMT2A models (Bernard-Marissal *et al.*, 2019; Larrea *et al.*, 2019). Disruption in mitochondrial-ER contacts has been noted to result in calcium disruption and which has been noted in various CMT2A models (Misko *et al.*, 2012; Saporta *et al.*, 2015; Larrea *et al.*, 2019). Calcium homeostasis is of particular importance in neurons as a second messenger of neurotransmitters but is also a key regulator of transport via Miro, which itself is a calcium sensor, (MacAskill *et al.*, 2009) and will release cargo when it binds with calcium. Mitochondria are halted in transport when high calcium gradients occur as they can act as calcium sinks to control local calcium levels (reviewed in Mandal and Drerup, 2019). Whilst the interplay between the ER-mitochondria and calcium gradients was not looked at in the scope of this work, this model provides a useful tool in which this may be examined further in the future.

The addition of ACY738 showed a significant increase in the percentage of mitochondria that were motile in the MFN2^{R94Q/+} neurons, mirroring what has been seen in other instances of mitochondrial trafficking defect (Dompierre *et al.*, 2007; Benoy *et al.*, 2017; Guo *et al.*, 2017; Moller *et al.*, 2017; Mo *et al.*, 2018). This improvement is thought to arise via the proposed mechanism of increasing the acetylation of tubulin and which makes it easier for the motor to bind to the microtubules to initiate transport. However, treatment with ACY738 did not significantly improve the percentage of mitochondria that pause during transport in the R94Q neurons. If R94Q has altered the strength of MFN2's interaction with MIRO this is not surprising as the HDAC6 inhibition has done nothing to alter this meaning pausing is just as likely as it is before the treatment despite transport being easier to initiate in the presence of the compound. Mitochondrial spacing was also trending towards being increase but was not significant. The consequences of increased trafficking may not have had long enough for the full effect (redistribution of mitochondria) to be seen. Additionally, it is not known how much of an increase in acetylated tubulin is required for these effects to be relevant. As previously

mentioned, it is also possible that there may be other factors limiting mitochondrial transport such as erroneous calcium gradients.

HDAC6 has many other targets in the cytosol, not just tubulin. Notably, MIRO is also a known target of HDAC6 and deacetylation of MIRO can also block mitochondrial transport (Kalinski *et al.*, 2019). This leaves it unclear which effect of HDAC6 inhibition is having the greatest benefit in this system. Persistent acetylation of these targets may be having additional beneficial effects and may be more viable as targets through direct pharmacological manipulation. Further research on HDAC6 inhibition in multiple neurodegenerative diseases is essential to understand the complex interactions at play and whether they may provide benefit.

The use of Leflunomide in this system was unable to replicate previous findings of an increase in *MFN1* expression which made it unsuitable to test in this system. It is possible that the dosing schedule did not allow the increase to be seen and lengthier dosing may see this increase. Despite this, increasing the expression of *MFN1* continues to be an interesting avenue of exploration in treatments for CMT2A and has proved successful in alleviating defects in various models (Detmer and Chan, 2007; Misko *et al.*, 2012; Zhou *et al.*, 2019). Further research on compounds that may produce an increase in *MFN1* expression would be valuable to test in CMT2A and may provide an alternative target for treatment.

In summary, the data presented within this chapter show the first characterisation of an hPSC based model with CMT2A causing mutation *MFN2* R94Q. This model shows a severe mitochondrial transport defect, resulting in a decrease in the number and size of mitochondria found in axon further from the cell body. The addition of HDAC6 inhibitor, ACY738, was successful in increasing the percentage of mitochondria that were motile and in increasing the size of mitochondria found far from the cell body but not the number. Further research will be required to elucidate the full benefit of HDAC6 inhibition in CMT2A and the impact of any further impairments caused by the R94Q mutation.

6) Final discussion and future work

6.1) A novel model of CMT2A

In this project, I created a novel hPSC-based model of CMT2A. To my knowledge, this is the first human *in vitro* model for one of the most common and phenotypically severe CMT2A-causing mutations, MFN2^{R94Q/+}. My work involved genetic editing of wild-type hPSCs to introduce a heterozygous R94Q mutation into *MFN2*, thus obtaining isogenic mutant and wild-type cells. This was a novel approach of generating a human CMT2A model as the mutation was knocked in rather than derived from patient-derived iPSC as in previous studies. To generate disease-relevant cell types, I optimised the differentiation of hPSC to limb innervating motor neurons, the primary affected cell types for CMT2A. Then, I performed phenotypic and functional analyses of motor neurons and neuronal mitochondria in mutant and wild-type cells. This analysis revealed a significant mitochondrial transport defect in MFN2^{R94Q/+} motor neurons, which likely underpins disease pathology. Finally, HDAC6 inhibition was previously shown to rescue mitochondrial trafficking defects in several disease models, including in CMT rodent models (D'Ydewalle *et al.*, 2011; Kim *et al.*, 2016; Benoy *et al.*, 2017; Mo *et al.*, 2018; Shen *et al.*, 2021). I tested HDAC6 inhibition in my CMT2A model. HDAC6 inhibition showed significant alleviation of the mitochondrial transport defect seen in MFN2^{R94Q/+} motor neurons. The novel CMT2A model developed in this study provides a platform for further mechanistic studies and therapeutic discovery.

6.2) Mechanistic insights from hPSC based MFN2^{R94Q/+} CMT2A system

I set out to generate an hPSC model for CMT2A and was able to achieve this using a CRISPR-based strategy to edit hPSC line MShef11 to contain the MFN2^{R94Q/+} mutation. Through analysis of MFN2^{R94Q/+} and wild-type motor neurons, I demonstrated a mitochondrial trafficking defect which resulted in a decrease in the number of mitochondria found further from the cell body of MFN2^{R94Q/+} cells. The work described in this thesis is the first time, to the best of my knowledge, that a mitochondrial trafficking defect has been shown in a human-based CMT2A system. Many previous models have not examined a mitochondrial trafficking phenotype but show phenotypes which may be linked to trafficking. Mitochondrial trafficking phenotypes may be particularly relevant where calcium dysregulation was shown to be involved. CMT2A neurons were shown to be overexcitable due to calcium dysregulation (Saporta *et al.*, 2015). Furthermore, ER-mitochondria contact disruption (Bernard-Marissal *et al.*, 2019; Larrea *et al.*, 2019) was shown to alter the calcium regulation in CMT2A patient fibroblasts. The dysregulation of calcium can interrupt mitochondrial trafficking through disruption of the MIRO/MILTON complex which binds to MFN2 to facilitate binding to motor proteins. MIRO is a calcium

sensor and will release mitochondria (MacAskill *et al.*, 2009), stopping trafficking, in the presence of calcium to allow mitochondria to carry out calcium buffering in that location. Buffering of calcium is particularly necessary at the synapse of neurons where mitochondria are highly resident to control calcium gradients and facilitate energy production. In the presence of disrupted trafficking, as seen in my model, it would be more difficult for mitochondria to make it to these distal locations. Leaving calcium gradients potentially unchecked in at the synapse may lead to neurodegeneration. It is therefore possible that the transport defect observed in my study is a contributing factor to the calcium dysregulation shown in other models and may even be linked to a disruption in ER-Mitochondrial contact. Further work would be required to confirm whether trafficking and/or MAM regulation is affecting calcium management in CMT2A motor neurons. Given that calcium dysregulation is also prevalent in several other neurodegenerative diseases (Alzheimer's (reviewed in Müller *et al.*, 2018), ALS (reviewed in Aufschnaiter *et al.*, 2017)), examination of this model to further understand MAM and calcium control has the potential to be beneficial to numerous diseases.

The work done in this thesis was in contrast to previous studies which have examined patient-derived iPSC. This was done partly due to the lack of availability of CMT2A iPSC lines and as the initial plan was to create an isogenic panel of multiple mutations. Ultimately, the work here confirmed that MFN2^{R94Q/+} alone is capable of introducing severe mitochondrial transport disruptions to motor neurons and may help inform future studies which may look into the modulation of disease between family members.

Mitochondrial trafficking is a known phenotype for multiple forms of CMT2 (Kim *et al.*, 2016; Mo *et al.*, 2018; Reviewed in Rossaert and Van Den Bosch, 2020) and may be a unifying factor by which these diseases are caused. However, it is unknown if the transport defect found in MFN2^{R94Q/+} is common among all CMT2A causing mutations. I initially planned to create separate lines that contained MFN2^{T105M/+} (generally associated with mild CMT2A, a GTPase mutation) and MFN2^{R364W/+} (generally associated with moderate CMT2A, affecting HR1) in addition to the MFN2^{R94Q/+} line. However, editing and establishing each clonal line is a time-consuming procedure, so I chose to focus on the most severe of the mutations, MFN2^{R94Q/+}. The generation of a panel of individual CMT2A mutant lines on the same genetic background would have allowed the examination and comparison of the different phenotypes seen in this disease. Through examination of different CMT2A causing mutations it would be possible to increase understanding of how mutations of various MFN2 domains contribute to the development of disease in CMT2A and whether they act via similar mechanisms. Until further advances in understanding the pathology behind CMT2A is understood it will be difficult to find treatments that

are effective for the majority of the patient population. Given the success of this study in editing and analysis of phenotype and differentiation protocols optimised for hPSC, my model provides a strong foundation on which to examine the contribution each mutation plays in the generation of the CMT2A disease phenotype.

In previous CMT2A studies, MFN2^{R94Q/+} mutations have been associated with significant mitochondrial fusion defects resulting in aberrant mitochondrial morphology (Detmer and Chan, 2007; El Fissi *et al.*, 2018; Rocha *et al.*, 2018; Wolf *et al.*, 2019). In contrast to the previously described CMT2A models, my study shows that the fusion of mitochondria within MFN2^{R94Q/+} hPSCs and motor neurons is not affected. Furthermore, the data presented here suggests that when mitochondria in the distal axon were provided with increased fusion partners (by increasing mitochondrial trafficking through the addition of ACY738), mitochondria increased in size indicating successful fusion. If a fusion defect had been present it would have been expected that the number of mitochondria increased rather than their size. Previous work has indicated that lack of mitochondrial fusion does not necessarily result in axonal degeneration in MFN2^{R94Q/+} CMT2A rodent neurons (Baloh *et al.*, 2007). Furthermore, as the GTPase activity of MFN2 is far less than its counterpart MFN1, it is potentially unlikely that a fusion defect is a primary aspect of CMT2A. Given the interplay between mitochondrial transport and fusion, it is difficult to determine the exact contribution of each defect. Therefore, it is my assertion that many previous fusion defects seen may have been obscured with the defect in mitochondrial mobility and it remains unclear as to whether fusion plays a significant role in the onset of CMT2A disease phenotypes.

The symptoms of CMT2A are primarily observed in patients' limbs and are more prominently seen within legs. Neurons innervating the limbs are considered especially vulnerable in a range of neurodegenerative diseases (Frey *et al.*, 2000). Previous examination of CMT2A has used animal models but many of these models have suffered from a poor representation of disease phenotype. Many human-based studies are in fibroblasts, a relatively unaffected cell type, or in motor neurons that have not been fully characterised. It has been shown that neuron populations show different transcriptomic and metabolomic profiles (reviewed in Nijssen, Comley and Hedlund, 2017) meaning accurate generation of the specific groups of neurons may affect the phenotypes seen. To this end, I developed an optimised differentiation that produced high percentage of limb innervating motor neurons as marked by expression of FOXP1⁺. Further examination of positional identity through *HOX* gene expression in neuronal cultures generated in my optimised protocol showed they were lower brachial neurons which may contribute to the innervation of arms. The specific use of limb innervating

motor neurons in this study may help explain some of the discrepancies between this study and iPSC-based models in regards to the prevalence of mitochondrial trafficking (Saporta *et al.*, 2015). My optimised protocol provides a significant benefit over fibroblasts studies by allowing access to brachial neurons that are difficult to access from humans. Considering difficulty of access and the relative vulnerability of brachial neurons, the differentiation protocol can provide benefit to researchers of ALS and other diseases common to limb-innervating neurons. CMT2A symptoms are more prevalent in the legs therefore further alterations to this protocol would be required to examine neurons capable of targeting this location. Due to the lack of protocols describing the generation of lower motor neurons, it was not possible, in the time scale, to attempt this in addition to the work described. It is likely the mitochondrial trafficking defect seen in my system is still relevant in lower motor neurons and may even be more severe. Furthermore, examination of mitochondrial trafficking in optic motor and sensory neurons would be beneficial as MFN2^{R94Q/+} is attributed to the generation of optic atrophy in patients (Züchner *et al.*, 2006). The use of hPSC to generate a CMT2A model allows the potential to examine multiple different cell types in the same genetic background to examine the contribution of each cell type toward the generation of disease phenotype.

In vivo, neurons exist in concert with a whole host of non-neuronal support cells that in the peripheral nervous system include myelinating Schwann cells. Myelin degeneration is not considered a primary aspect of CMT2, however, it is seen in some patients during later stages of disease (Vallat *et al.*, 2008; Genari *et al.*, 2011). The effect of neuronal support cells and their impact in neuronal degenerative diseases has previously been demonstrated for ALS, wherein the co-culture of astrocytes from ALS patients with unaffected motor neurons resulted in death of the neurons (Haidet-Phillips *et al.*, 2011). To the best of my knowledge, the role of neuron-neuronal support cell interactions has not been extensively examined for CMT2A. Advancement in protocols for differentiating hPSCs to Schwann cells (Kim *et al.*, 2017) would allow examination of the interplay between CMT2A motor neurons and myelinating cells. Furthermore, *in vivo* motor neurons create synapses with muscles to elicit movement. Utilising the MFN2^{R94Q/+} motor neurons from this study, in a combination with a complex environment such as a 3D neuro-muscular junction model (Bakooshli *et al.*, 2019) may provide an insight into how synaptic responses may be altered due to the mitochondrial transport defect and subsequent axonal degeneration in CMT2A patients. Differentiation of MFN2^{R94Q/+} hPSC I have generated can provide the basis for co-culture of multiple cell types to examine the contribution of different cells in the generation of CMT2A disease phenotype.

6.3) Potential for treatments of CMT2A

As a result of the mitochondrial trafficking defect in MFN2^{R94Q/+} motor neurons, I sought to find a compound that could alleviate the defect and may serve as a basis for future therapeutic treatment for patients. Previous work has shown that HDAC6 inhibition can increase mitochondrial axonal transport (Dompierre *et al.*, 2007; Kim *et al.*, 2016; Benoy *et al.*, 2017; Guo *et al.*, 2017; Mo *et al.*, 2018) which is believed to be mediated through increased acetylation of tubulin. I was able to show significantly increased mitochondrial transport in MFN2^{R94Q/+} motor neurons with the addition of ACY738, an HDAC6 inhibitor. In a CMT2A R94Q mouse model SW-101 (a novel HDAC6 inhibitor) showed improvements to rodent rotarod performance (Shen *et al.*, 2021) but axonal mitochondrial transport was not measured, meaning it is unknown by which mechanism this occurred. Given the findings seen in my model, it is likely that mitochondrial transport could be at play in this system and could be how wild-type rodent phenotype was restored. Though the scope of this study did not extend to explore whether the restoration in mitochondrial transport observed would be sufficient to provide a benefit to patient phenotypes the work described with HDAC6 inhibition provides a platform for further studies to evaluate the viability of ACY738 as a CMT2A therapy *in vivo*. The use of ACY738 in this system has continued to highlight the interest in HDAC6 inhibition in the alleviation of mitochondrial transport defects and should be further examined to if this compound can provide benefit to patients.

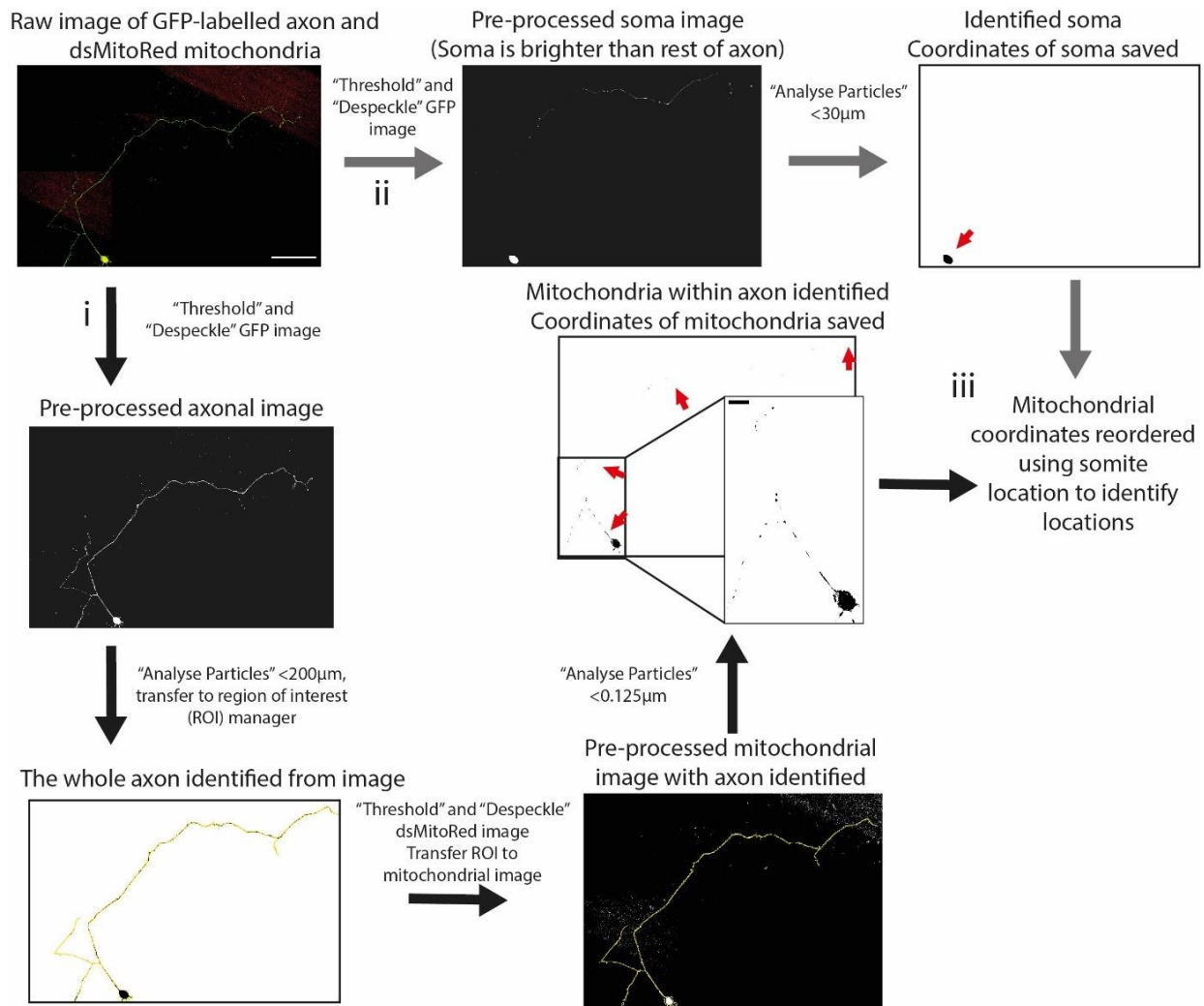


Figure 49: Identifying mitochondria within motor neuron axons using automated image analysis. i) Raw images are analysed using pre-existing functions within FIJI image analysis software. Images of GFP-labelled axons are the process to segment axons within the image. The resulting mask is overlaid on the ds-mitred images to allow accurate detection of mitochondria within the axon. ii) In parallel to axonal segmentation, the soma of the neuron is segmented from the original image. iii) The location of mitochondria identified in (i) are calculated using coordinated of the parental soma identified in (ii). This allows reorganisation of mitochondrial location based on distance from cell body. Raw image of neuron scale bar 100 μm . Mitochondrial particles analysis insert scale bar: 15 μm .

CMT2A differs from many other neurodegenerative diseases by not having any noted aggregation of neurotoxic proteins, though this is present in other forms of CMT (e.g., CMT1C, CMT2E, CMT4B (reviewed in Patzkó and Shy, 2011)). HDAC6 is known to have roles in protein ubiquitination and its expression can help clearance of unfolded proteins (reviewed in Rossaert and Van Den Bosch, 2020). Indeed, HDAC6 was found to be essential for the formation of aggresomes and cell viability in

misfolded protein responses (Kawaguchi *et al.*, 2003). Development of HDAC6 inhibitors for treating neurodegenerative diseases should be carried out with caution as the large number of roles HDAC6 is involved in is not fully understood. The modulation of so many different targets by HDAC6 may result in unintended adverse side effects which have the potential to aggravate disease symptoms. Further examination of HDAC6 activity and the benefits therein may provide more specific druggable targets. This is especially important given the proposed mechanism by which HDAC6 inhibition is inducing benefit in this system. HDAC6 inhibition increases the amount of acetylated tubulin making motor protein binding to microtubules more permissible. However, increased acetylation of tubulin is unlikely to fix what is proposed in this study to be the primary cause of mitochondrial transport defects in MFN2^{R94Q/+}, the poor attachment of mitochondria to motor proteins. Indeed, targeting mitochondrial attachment to motor proteins more specifically may provide significant benefit to transporting without the need for alteration of tubulin. Through examination of the data generated in my work, I believe the CMT2A model I have generated has the potential to be used in a drug screen aimed at finding compounds to alleviate the mitochondrial trafficking defect. To this end, I carried out significant work in planning a drug screen involving my differentiated MFN2^{R94Q/+} motor neurons. Successful restoration of a transport would be examined through examination of mitochondrial spacing and aspect ratio in the axons of motor neurons (Figure 49). CMT2A still has no approved treatments and further therapeutic screening is required to identify further targets which may provide alleviation of disease symptoms for patients.

6.4) Closing remarks

In this body of work, I have described the generation of an hPSC based model for one of the most severe CMT2A mutations, MFN2^{R94Q/+}. By optimising the differentiation of hPSC to limb-innervating motor neurons, I was able to investigate the mechanisms underpinning the most affected subtype of neurons in CMT2A. I found that defects in mitochondrial transport rather than fusion has a significant impact the disease phenotype of CMT2A MFN2^{R94Q/+}. Finally, my model showed mitochondrial transport defects could be alleviated by pharmacological manipulation. Further work should capitalise on the achievements made in this model and continue its examination and characterisation to increase understanding of CMT2A.

Ultimately, it is my hope that the model generated in this work may be of use in further studies of neurodegenerative diseases, such as CMT2A, and may provide a stepping stone in the development of future treatment options for patients.

7) References

- Abril, J. *et al.* (2008) 'Altered expression of 12S/MT-RNRI, MT-CO2/COX2, and MT-ATP6 mitochondrial genes in prostate cancer', *Prostate*, 68(10), pp. 1086–1096. doi: 10.1002/pros.20771.
- Ali, A. T. *et al.* (2019) 'Nuclear genetic regulation of the human mitochondrial transcriptome', *eLife*, 8. doi: 10.7554/elife.41927.
- Amiott, E. A. *et al.* (2008) 'Mitochondrial fusion and function in Charcot-Marie-Tooth type 2A patient fibroblasts with mitofusin 2 mutations', *Experimental Neurology*, 211(1), pp. 115–127. doi: 10.1016/j.expneurol.2008.01.010.
- Amoroso, M. W. *et al.* (2013) 'Accelerated high-yield generation of limb-innervating motor neurons from human stem cells', *Journal of Neuroscience*. Society for Neuroscience, 33(2), pp. 574–586. doi: 10.1523/JNEUROSCI.0906-12.2013.
- Ando, M. *et al.* (2017) 'Clinical and genetic diversities of Charcot-Marie-Tooth disease with MFN2 mutations in a large case study', *Journal of the Peripheral Nervous System*, 22(3), pp. 191–199. doi: 10.1111/jns.12228.
- Andrews, P. W. *et al.* (1984) 'Three monoclonal antibodies defining distinct differentiation antigens associated with different high molecular weight polypeptides on the surface of human embryonal carcinoma cells', *Hybridoma*, 3(4), pp. 347–361. doi: 10.1089/hyb.1984.3.347.
- Angelova, P. R., Esteras, N. and Abramov, A. Y. (2021) 'Mitochondria and lipid peroxidation in the mechanism of neurodegeneration: Finding ways for prevention', *Medicinal Research Reviews*. John Wiley and Sons Inc, pp. 770–784. doi: 10.1002/med.21712.
- Antoniadi, T. *et al.* (2015) 'Application of targeted multi-gene panel testing for the diagnosis of inherited peripheral neuropathy provides a high diagnostic yield with unexpected phenotype-genotype variability.', *BMC medical genetics*, 16, p. 84. doi: 10.1186/s12881-015-0224-8.
- Attarian, S. *et al.* (2014) 'An exploratory randomised double-blind and placebo-controlled phase 2 study of a combination of baclofen, naltrexone and sorbitol (PXT3003) in patients with Charcot-Marie-Tooth disease type 1A', *Orphanet Journal of Rare Diseases*. BioMed Central, 9(1), p. 199. doi: 10.1186/s13023-014-0199-0.
- Audano, M., Schneider, A. and Mitro, N. (2018) 'Mitochondria, lysosomes, and dysfunction: their meaning in neurodegeneration', *Journal of Neurochemistry*. Blackwell Publishing Ltd, pp. 291–309. doi: 10.1111/jnc.14471.
- Auer-Grumbach, M. *et al.* (1998) 'Roussy-Levy syndrome is a phenotypic variant of Charcot-Marie-Tooth syndrome IA associated with a duplication on chromosome 17p11.2', *Journal of the Neurological Sciences*. Elsevier, 154(1), pp. 72–75. doi: 10.1016/S0022-510X(97)00218-9.
- Aufschnaiter, A. *et al.* (2017) 'Mitochondrial lipids in neurodegeneration', *Cell and Tissue Research*.

Springer Verlag, pp. 125–140. doi: 10.1007/s00441-016-2463-1.

Badcock, G. *et al.* (1999) 'The human embryonal carcinoma marker antigen TRA-1-60 is a sialylated keratan sulfate proteoglycan', *Cancer Research*, 59(18), pp. 4715–4719.

Baghbaderani, B. A. *et al.* (2015) 'CGMP-manufactured human induced pluripotent stem cells are available for pre-clinical and clinical applications', *Stem Cell Reports*. Elsevier, 5(4), pp. 647–659. doi: 10.1016/j.stemcr.2015.08.015.

Baker, D. *et al.* (2016) 'Detecting Genetic Mosaicism in Cultures of Human Pluripotent Stem Cells', *Stem Cell Reports*. Cell Press, 7(5), pp. 998–1012. doi: 10.1016/j.stemcr.2016.10.003.

Bakooshli, M. A. *et al.* (2019) 'A 3d culture model of innervated human skeletal muscle enables studies of the adult neuromuscular junction', *eLife*. eLife Sciences Publications Ltd, 8. doi: 10.7554/eLife.44530.

Baloh, R. H. *et al.* (2007) 'Altered Axonal Mitochondrial Transport in the Pathogenesis of Charcot-Marie-Tooth Disease from Mitofusin 2 Mutations', *Journal of Neuroscience*, 27(2), pp. 422–430. doi: 10.1523/JNEUROSCI.4798-06.2007.

Baloh, R. H. (2008) 'Mitochondrial dynamics and peripheral neuropathy', *Neuroscientist*, 14(1), pp. 12–18. doi: 10.1177/1073858407307354.

Banchs, I. *et al.* (2008) 'Two Spanish families with Charcot-Marie-Tooth type 2A: Clinical, electrophysiological and molecular findings', *Neuromuscular Disorders*. Elsevier, 18(12), pp. 974–978. doi: 10.1016/j.nmd.2008.09.006.

Bannerman, P. *et al.* (2016) 'Mice hemizygous for a pathogenic mitofusin- 2 allele exhibit hind limb/foot gait deficits and phenotypic perturbations in nerve and muscle', *PLoS ONE*. Edited by W. D. Phillips. Public Library of Science, 11(12), p. e0167573. doi: 10.1371/journal.pone.0167573.

Bar-Nur, O. *et al.* (2011) 'Epigenetic memory and preferential lineage-specific differentiation in induced pluripotent stem cells derived from human pancreatic islet beta cells', *Cell Stem Cell*. Cell Press, 9(1), pp. 17–23. doi: 10.1016/j.stem.2011.06.007.

Barbaric, I. *et al.* (2014) 'Time-lapse analysis of human embryonic stem cells reveals multiple bottlenecks restricting colony formation and their relief upon culture adaptation', *Stem Cell Reports*. Cell Press, 3(1), pp. 142–155. doi: 10.1016/j.stemcr.2014.05.006.

Batchu, S. N., Brijmohan, A. S. and Advani, A. (2016) 'The therapeutic hope for HDAC6 inhibitors in malignancy and chronic disease', *Clinical Science*, pp. 987–1003. doi: 10.1042/CS20160084.

Beauchamp, P. *et al.* (2020) '3D Co-culture of hiPSC-Derived Cardiomyocytes With Cardiac Fibroblasts Improves Tissue-Like Features of Cardiac Spheroids', *Frontiers in Molecular Biosciences*. Frontiers Media SA, 7, p. 14. doi: 10.3389/fmolb.2020.00014.

Benoy, V. *et al.* (2017) 'Development of Improved HDAC6 Inhibitors as Pharmacological Therapy for

Axonal Charcot–Marie–Tooth Disease’, *Neurotherapeutics*, 14(2), pp. 417–428. doi: 10.1007/s13311-016-0501-z.

Benoy, V. *et al.* (2018) ‘HDAC6 is a therapeutic target in mutant GARS-induced Charcot-Marie-Tooth disease’, *Brain*. Oxford University Press, 141(3), pp. 673–687. doi: 10.1093/brain/awx375.

Bergamin, G. *et al.* (2014) ‘Mutation analysis of MFN2, GJB1, MPZ and PMP22 in Italian patients with axonal Charcot-Marie-Tooth disease’, *NeuroMolecular Medicine*, 16(3), pp. 540–550. doi: 10.1007/s12017-014-8307-9.

Bernard-Marissal, N. *et al.* (2019) ‘Altered interplay between endoplasmic reticulum and mitochondria in Charcot–Marie–Tooth type 2A neuropathy’, *Proceedings of the National Academy of Sciences*. National Academy of Sciences, 116(6), pp. 2328–2337. doi: 10.1073/pnas.1810932116.

Berridge, M. J. (1998) ‘Neuronal calcium signaling’, *Neuron*. Cell Press, pp. 13–26. doi: 10.1016/S0896-6273(00)80510-3.

Bettters, E. *et al.* (2010) ‘Analysis of early human neural crest development’, *Developmental Biology*. Academic Press Inc., 344(2), pp. 578–592. doi: 10.1016/j.ydbio.2010.05.012.

Bhaya, D., Davison, M. and Barrangou, R. (2011) ‘CRISPR-Cas Systems in Bacteria and Archaea: Versatile Small RNAs for Adaptive Defense and Regulation’, *Annual Review of Genetics*. Annual Reviews, 45(1), pp. 273–297. doi: 10.1146/annurev-genet-110410-132430.

Bilic, J. and Belmonte, J. C. I. (2012) ‘Concise Review: Induced Pluripotent Stem Cells Versus Embryonic Stem Cells: Close Enough or Yet Too Far Apart?’, *STEM CELLS*. John Wiley & Sons, Ltd, 30(1), pp. 33–41. doi: 10.1002/STEM.700.

Del Bo, R. D. *et al.* (2008) ‘Mutated mitofusin 2 presents with intrafamilial variability and brain mitochondrial dysfunction’, *Neurology*, 71(24), pp. 1959–1966. doi: 10.1212/01.wnl.0000327095.32005.a4.

Bock, C. *et al.* (2011) ‘Reference maps of human es and ips cell variation enable high-throughput characterization of pluripotent cell lines’, *Cell*. Elsevier, 144(3), pp. 439–452. doi: 10.1016/j.cell.2010.12.032.

Borghese, L. *et al.* (2010) ‘Inhibition of notch signaling in human embryonic stem cell-derived neural stem cells delays G1/S phase transition and accelerates neuronal differentiation in vitro and in vivo’, *Stem Cells*. Wiley-Blackwell, 28(5), pp. 955–964. doi: 10.1002/stem.408.

Braathen, G. J. *et al.* (2010) ‘MFN2 point mutations occur in 3.4% of Charcot-Marie-Tooth families. An investigation of 232 Norwegian CMT families.’, *BMC medical genetics*, 11, p. 48. doi: 10.1186/1471-2350-11-48.

Braathen, G. J. (2012) ‘Genetic epidemiology of Charcot-Marie-Tooth disease.’, *Acta neurologica Scandinavica. Supplementum*, 126(193), pp. iv–22. doi: 10.1111/ane.12013.

- Brini, M. *et al.* (2014) 'Neuronal calcium signaling: Function and dysfunction', *Cellular and Molecular Life Sciences*, 71(15), pp. 2787–2814. doi: 10.1007/s00018-013-1550-7.
- De Brito, O. M. and Scorrano, L. (2008) 'Mitofusin 2 tethers endoplasmic reticulum to mitochondria', *Nature*. Nature Publishing Group, 456(7222), pp. 605–610. doi: 10.1038/nature07534.
- Brockmann, K. *et al.* (2008) 'Cerebral involvement in axonal Charcot-Marie-Tooth neuropathy caused by mitofusin2 mutations', *Journal of Neurology*, 255(7), pp. 1049–1058. doi: 10.1007/s00415-008-0847-1.
- Brooks, C. *et al.* (2007) 'Bak regulates mitochondrial morphology and pathology during apoptosis by interacting with mitofusins', *Proceedings of the National Academy of Sciences of the United States of America*. National Academy of Sciences, 104(28), pp. 11649–11654. doi: 10.1073/pnas.0703976104.
- Calkins, M. J. *et al.* (2011) 'Impaired mitochondrial biogenesis, defective axonal transport of mitochondria, abnormal mitochondrial dynamics and synaptic degeneration in a mouse model of Alzheimer's disease', *Human Molecular Genetics*. Hum Mol Genet, 20(23), pp. 4515–4529. doi: 10.1093/hmg/ddr381.
- Calvo, J. *et al.* (2009) 'Genotype-Phenotype Correlations in Charcot-Marie-Tooth Disease Type 2 Caused by Mitofusin 2 Mutations', *Archives of Neurology*. American Medical Association, 66(12), pp. 1511–1516. doi: 10.1001/archneurol.2009.284.
- Canham, M. A. *et al.* (2015) 'The Molecular Karyotype of 25 Clinical-Grade Human Embryonic Stem Cell Lines', *Scientific Reports*. Nature Publishing Group, 5(1), p. 17258. doi: 10.1038/srep17258.
- Cao, Y. L. *et al.* (2017) 'MFN1 structures reveal nucleotide-triggered dimerization critical for mitochondrial fusion', *Nature*. Nature Publishing Group, 542(7641), pp. 372–376. doi: 10.1038/nature21077.
- Carpenter, A. *et al.* (2006) 'CellProfiler: image analysis software for identifying and quantifying cell phenotypes', *Genome Biology*, 7(R100).
- Cartoni, R. *et al.* (2010) 'Expression of mitofusin 2R94Q in a transgenic mouse leads to Charcot-Marie-Tooth neuropathy type 2A', *Brain*, 133(5), pp. 1460–1469. doi: 10.1093/brain/awq082.
- Casasnovas, C. *et al.* (2010) 'Phenotypic spectrum of MFN2 mutations in the Spanish population', *Journal of Medical Genetics*, 47(4), pp. 249–256. doi: 10.1136/jmg.2009.072488.
- Chambers, S. M. *et al.* (2009) 'Highly efficient neural conversion of human ES and iPS cells by dual inhibition of SMAD signaling', *Nature Biotechnology*. Nature Publishing Group, 27(3), pp. 275–280. doi: 10.1038/nbt.1529.
- Chambers, S. M. *et al.* (2012) 'Combined small-molecule inhibition accelerates developmental timing and converts human pluripotent stem cells into nociceptors', *Nature Biotechnology*. Nature Publishing Group, 30(7), pp. 715–720. doi: 10.1038/nbt.2249.

- Chandrasekaran, A. *et al.* (2017) 'Comparison of 2D and 3D neural induction methods for the generation of neural progenitor cells from human induced pluripotent stem cells', *Stem Cell Research*. Elsevier B.V., 25, pp. 139–151. doi: 10.1016/j.scr.2017.10.010.
- Charcot, J. M. and Marie, P. (1886) 'Sur une forme particulière d'atrophie musculaire progressive souvent familiale débutant par les pieds et les jambes et atteignant plus tard les mains', *Revue de médecine (La)*, 6, pp. 96–138.
- Chen, A. E. and Melton, D. A. (2007) 'Derivation of human embryonic stem cells by immunosurgery', *Journal of Visualized Experiments*. MyJoVE Corporation, (10), p. 574. doi: 10.3791/574.
- Chen, G. *et al.* (2011) 'Chemically defined conditions for human iPS cell derivation and culture', *Nature Methods*, 8(5), pp. 424–429.
- Chen, H. *et al.* (2003) 'Mitofusins Mfn1 and Mfn2 coordinately regulate mitochondrial fusion and are essential for embryonic development', *Journal of Cell Biology*. Rockefeller University Press, 160(2), pp. 189–200. doi: 10.1083/jcb.200211046.
- Chen, H. *et al.* (2010) 'Mitochondrial fusion is required for mtDNA stability in skeletal muscle and tolerance of mtDNA mutations', *Cell*, 141(2), pp. 280–289. doi: 10.1016/j.cell.2010.02.026.
- Chen, H., Chomyn, A. and Chan, D. C. (2005) 'Disruption of fusion results in mitochondrial heterogeneity and dysfunction', *Journal of Biological Chemistry*, 280(28), pp. 26185–26192. doi: 10.1074/jbc.M503062200.
- Chen, H., McCaffery, J. M. and Chan, D. C. (2007) 'Mitochondrial Fusion Protects against Neurodegeneration in the Cerebellum', *Cell*, 130(3), pp. 548–562. doi: 10.1016/j.cell.2007.06.026.
- Chen, J. S. *et al.* (2017) 'Enhanced proofreading governs CRISPR-Cas9 targeting accuracy', *Nature*. Nature Publishing Group, 550(7676), pp. 407–410. doi: 10.1038/nature24268.
- Cho, S. W. *et al.* (2013) 'Targeted genome engineering in human cells with the Cas9 RNA-guided endonuclease', *Nature Biotechnology*, 31(3), pp. 230–232. doi: 10.1038/nbt.2507.
- Choi, B. O. *et al.* (2015) 'A cohort study of MFN2 mutations and phenotypic spectrums in Charcot-Marie-Tooth disease 2A patients', *Clinical Genetics*. Blackwell Publishing Ltd, 87(6), pp. 594–598. doi: 10.1111/cge.12432.
- Choo, Y. S. *et al.* (2004) 'Mutant huntingtin directly increases susceptibility of mitochondria to the calcium-induced permeability transition and cytochrome c release', *Human Molecular Genetics*. Hum Mol Genet, 13(14), pp. 1407–1420. doi: 10.1093/hmg/ddh162.
- Chouhan, S. (2016) 'Normal motor and sensory nerve conduction velocity of radial nerve in young adult medical students', *Journal of Clinical and Diagnostic Research*. JCDR Research & Publications Private Limited, 10(1), pp. CC01–CC03. doi: 10.7860/JCDR/2016/14618.7037.
- Chung, K. W. *et al.* (2006) 'Early onset severe and late-onset mild Charcot-Marie-Tooth disease with

mitofusin 2 (MFN2) mutations', *Brain*, 129(8), pp. 2103–2118. doi: 10.1093/brain/awl174.

Chung, K. W. *et al.* (2008) 'Early-onset stroke associated with a mutation in mitofusin 2', *Neurology*, 70(21), pp. 2010–2011. doi: 10.1212/01.wnl.0000312513.96457.7a.

Chung, K. W. *et al.* (2010) 'Early-onset Charcot-Marie-Tooth patients with mitofusin 2 mutations and brain involvement.', *Journal of neurology, neurosurgery, and psychiatry*, 81(11), pp. 1203–1206. doi: 10.1136/jnnp.2009.181669.

Cockburn, K. and Rossant, J. (2010) 'Making the blastocyst : lessons from the mouse Find the latest version : Review series Making the blastocyst : lessons from the mouse', 120(4), pp. 995–1003. doi: 10.1172/JCI41229.zygotic.

Cohen, D. E. and Melton, D. (2011) 'Turning straw into gold: Directing cell fate for regenerative medicine', *Nature Reviews Genetics*, pp. 243–252. doi: 10.1038/nrg2938.

Cong, L. *et al.* (2013) 'Multiplex genome engineering using CRISPR/Cas systems', *Science*, 339(6121), pp. 819–823. doi: 10.1126/science.1231143.

Cosson, P. *et al.* (2012) 'Mitofusin-2 Independent Juxtaposition of Endoplasmic Reticulum and Mitochondria: An Ultrastructural Study', *PLoS ONE*. Edited by F. G. van der Goot. Public Library of Science, 7(9), p. e46293. doi: 10.1371/journal.pone.0046293.

Cunningham, T. J. *et al.* (2015) 'Wnt8a and Wnt3a cooperate in the axial stem cell niche to promote mammalian body axis extension', *Developmental Dynamics*. John Wiley and Sons Inc., 244(6), pp. 797–807. doi: 10.1002/dvdy.24275.

D'Ydewalle, C. *et al.* (2011) 'HDAC6 inhibitors reverse axonal loss in a mouse model of mutant HSPB1-induced Charcot-Marie-Tooth disease', *Nature Medicine*. Nature Publishing Group, 17(8), pp. 968–974. doi: 10.1038/nm.2396.

Dankwa, L. *et al.* (2018) 'A mutation in the heptad repeat 2 domain of MFN2 in a large CMT2A family', *Journal of the Peripheral Nervous System*. Wiley/Blackwell (10.1111), 23(1), pp. 36–39. doi: 10.1111/jns.12248.

Dasen, J. S. *et al.* (2008) 'Hox Repertoires for Motor Neuron Diversity and Connectivity Gated by a Single Accessory Factor, FoxP1', *Cell*. Cell Press, 134(2), pp. 304–316. doi: 10.1016/j.cell.2008.06.019.

Dasen, J. S., Liu, J. P. and Jessell, T. M. (2003) 'Motor neuron columnar fate imposed by sequential phases of Hox-c activity', *Nature*. Nature Publishing Group, 425(6961), pp. 926–933. doi: 10.1038/nature02051.

Davis-Dusenbery, B. N. *et al.* (2014) 'How to make spinal motor neurons', *Development*. Oxford University Press for The Company of Biologists Limited, 141(3), pp. 491–501. doi: 10.1242/dev.097410.

Deschamps, J. and Duboule, D. (2017) 'Embryonic timing, axial stem cells, chromatin dynamics, and

the Hox clock', *Genes and Development*. Cold Spring Harbor Laboratory Press, pp. 1406–1416. doi: 10.1101/gad.303123.117.

Detmer, S. A. *et al.* (2008) 'Hindlimb gait defects due to motor axon loss and reduced distal muscles in a transgenic mouse model of Charcot - Marie - Tooth type 2A', *Human Molecular Genetics*, 17(3), pp. 367–375. doi: 10.1093/hmg/ddm314.

Detmer, S. A. and Chan, D. C. (2007) 'Complementation between mouse Mfn1 and Mfn2 protects mitochondrial fusion defects caused by CMT2A disease mutations', *Journal of Cell Biology*. Rockefeller University Press, 176(4), pp. 405–414. doi: 10.1083/jcb.200611080.

Ding, Y. *et al.* (2021) 'Derivation of four iPSC lines from a male ASD patient carrying a deletion in the middle coding region of NRXN1α gene (NUIGi039-A and NUIGi039-B) and a male sibling control (NUIGi040-A and NUIGi040-B)', *Stem Cell Research*. Elsevier B.V., 53, p. 102254. doi: 10.1016/j.scr.2021.102254.

Dompierre, J. P. *et al.* (2007) 'Histone deacetylase 6 inhibition compensates for the transport deficit in Huntington's disease by increasing tubulin acetylation', *Journal of Neuroscience*. Society for Neuroscience, 27(13), pp. 3571–3583. doi: 10.1523/JNEUROSCI.0037-07.2007.

Draper, J. S. *et al.* (2004) 'Recurrent gain of chromosomes 17q and 12 in cultured human embryonic stem cells', *Nature Biotechnology*. Nature Publishing Group, 22(1), pp. 53–54. doi: 10.1038/nbt922.

Duan, J. *et al.* (2003) 'Synonymous mutations in the human dopamine receptor D2 (DRD2) affect mRNA stability and synthesis of the receptor', *Human Molecular Genetics*. Oxford Academic, pp. 205–216. doi: 10.1093/hmg/ddg055.

Engelfried, K. *et al.* (2006) 'Charcot-Marie-Tooth neuropathy type 2A: novel mutations in the mitofusin 2 gene (MFN2)', *BMC Medical Genetics*, 7(1), p. 53. doi: 10.1186/1471-2350-7-53.

Estacion, M. *et al.* (2009) 'A sodium channel gene SCN9A polymorphism that increases nociceptor excitability', *Annals of Neurology*. John Wiley & Sons, Ltd, 66(6), pp. 862–866. doi: 10.1002/ana.21895.

Fang, D. *et al.* (2016) 'Mfn2 is required for mitochondrial development and synapse formation in human induced pluripotent stem cells/hiPSC derived cortical neurons', *Scientific Reports*, 6. doi: 10.1038/srep31462.

Fazeli, A. *et al.* (2011) 'Altered patterns of differentiation in karyotypically abnormal human embryonic stem cells', *International Journal of Developmental Biology*. UPV/EHU Press, 55(2), pp. 175–180. doi: 10.1387/ijdb.103177af.

Feely, S. M. E. *et al.* (2011) 'MFN2 mutations cause severe phenotypes in most patients with CMT2A', *Neurology*. American Academy of Neurology, 76(20), pp. 1690–1696. doi: 10.1212/WNL.0b013e31821a441e.

- Filadi, R. *et al.* (2015) 'Mitofusin 2 ablation increases endoplasmic reticulum–mitochondria coupling', *Proceedings of the National Academy of Sciences*, 112(17), pp. E2174–E2181. doi: 10.1073/pnas.1504880112.
- Filadi, R., Pendin, D. and Pizzo, P. (2018) 'Mitofusin 2: From functions to disease', *Cell Death and Disease*. Nature Publishing Group, p. 330. doi: 10.1038/s41419-017-0023-6.
- Filippova, J. *et al.* (2019) 'Guide RNA modification as a way to improve CRISPR/Cas9-based genome-editing systems', *Biochimie*. Elsevier B.V., pp. 49–60. doi: 10.1016/j.biochi.2019.09.003.
- El Fissi, N. *et al.* (2018) 'Mitofusin gain and loss of function drive pathogenesis in *Drosophila* models of CMT2A neuropathy', *EMBO reports*. EMBO Press, 19(8), p. e45241. doi: 10.15252/embr.201745241.
- Freedman, B. S. *et al.* (2015) 'Modelling kidney disease with CRISPR-mutant kidney organoids derived from human pluripotent epiblast spheroids', *Nature Communications*. Nature Publishing Group, 6(1), pp. 1–13. doi: 10.1038/ncomms9715.
- Frey, D. *et al.* (2000) 'Early and selective loss of neuromuscular synapse subtypes with low sprouting competence in motoneuron diseases', *Journal of Neuroscience*, 20(7), pp. 2534–2542. doi: 10.1523/jneurosci.20-07-02534.2000.
- Friedman, J. R. *et al.* (2011) 'ER tubules mark sites of mitochondrial division', *Science*. American Association for the Advancement of Science, 334(6054), pp. 358–362. doi: 10.1126/science.1207385.
- Frith, T *et al.* (2018) 'Human axial progenitors generate trunk neural crest cells in vitro', *eLife*. eLife Sciences Publications Ltd, 7. doi: 10.7554/elife.35786.
- Frith, T. *et al.* (2018) 'Human axial progenitors generate trunk neural crest cells in vitro', *eLife*, 7. doi: 10.7554/eLife.35786.
- Fu, Y. *et al.* (2014) 'Improving CRISPR-Cas nuclease specificity using truncated guide RNAs', *Nature Biotechnology*. Nature Publishing Group, 32(3), pp. 279–284. doi: 10.1038/nbt.2808.
- Fujita, J. *et al.* (2019) 'Concise Review: Genetic and Epigenetic Regulation of Cardiac Differentiation from Human Pluripotent Stem Cells', *Stem Cells*. Wiley-Blackwell, pp. 992–1002. doi: 10.1002/stem.3027.
- Gaj, T., Gersbach, C. A. and Barbas, C. F. (2013) 'ZFN, TALEN, and CRISPR/Cas-based methods for genome engineering', *Trends in Biotechnology*. Elsevier Current Trends, pp. 397–405. doi: 10.1016/j.tibtech.2013.04.004.
- Gall, J. M. *et al.* (2015) 'Conditional knockout of proximal tubule mitofusin 2 accelerates recovery and improves survival after renal ischemia', *Journal of the American Society of Nephrology*. American Society of Nephrology, 26(5), pp. 1092–1102. doi: 10.1681/ASN.2014010126.
- Gaudelli, N. M. *et al.* (2017) 'Programmable base editing of A•T to G•C in genomic DNA without DNA

cleavage', *Nature*. Nature Publishing Group, pp. 1–27. doi: 10.1038/nature24644.

Gegg, M. E. *et al.* (2010) 'Mitofusin 1 and mitofusin 2 are ubiquitinated in a PINK1/parkin-dependent manner upon induction of mitophagy', *Human Molecular Genetics*. Narnia, 19(24), pp. 4861–4870. doi: 10.1093/hmg/ddq419.

Genari, A. B. *et al.* (2011) 'Characterizing the phenotypic manifestations of MFN2 R104W mutation in Charcot-Marie-Tooth type 2', *Neuromuscular Disorders*, 21(6), pp. 428–432. doi: 10.1016/j.nmd.2011.03.008.

Gilkerson, R. W. *et al.* (2008) 'Mitochondrial nucleoids maintain genetic autonomy but allow for functional complementation', *Journal of Cell Biology*. Rockefeller University Press, 181(7), pp. 1117–1128. doi: 10.1083/jcb.200712101.

Glasser, C. E. *et al.* (2018) 'Locally acting ACE-083 increases muscle volume in healthy volunteers', *Muscle and Nerve*. Wiley-Blackwell, 57(6), pp. 921–926. doi: 10.1002/mus.26113.

Gomes, L. C., Benedetto, G. Di and Scorrano, L. (2011) 'During autophagy mitochondria elongate, are spared from degradation and sustain cell viability', *Nature Cell Biology*. Nature Publishing Group, 13(5), pp. 589–598. doi: 10.1038/ncb2220.

Gouti, M. *et al.* (2014) 'In vitro generation of neuromesodermal progenitors reveals distinct roles for wnt signalling in the specification of spinal cord and paraxial mesoderm identity', *PLoS Biology*, 12(8). doi: 10.1371/journal.pbio.1001937.

Greber, B. J. and Ban, N. (2016) 'Structure and Function of the Mitochondrial Ribosome', *Annual Review of Biochemistry*, 85, pp. 103–132. doi: 10.1146/annurev-biochem-060815-014343.

Guillet, V. *et al.* (2010) 'Adenine nucleotide translocase is involved in a mitochondrial coupling defect in MFN2-related Charcot-Marie-Tooth type 2A disease', *Neurogenetics*. Springer-Verlag, 11(1), pp. 127–133. doi: 10.1007/s10048-009-0207-z.

Guo, W. *et al.* (2017) 'HDAC6 inhibition reverses axonal transport defects in motor neurons derived from FUS-ALS patients', *Nature Communications*. Nature Publishing Group, 8(1), p. 861. doi: 10.1038/s41467-017-00911-y.

Gutschner, T. *et al.* (2016) 'Post-translational Regulation of Cas9 during G1 Enhances Homology-Directed Repair', *Cell Reports*. Elsevier B.V., 14(6), pp. 1555–1566. doi: 10.1016/j.celrep.2016.01.019.

Hackland, J. O. S. *et al.* (2017) 'Top-Down Inhibition of BMP Signaling Enables Robust Induction of hPSCs Into Neural Crest in Fully Defined, Xeno-free Conditions', *Stem Cell Reports*, 9(4), pp. 1043–1052. doi: 10.1016/j.stemcr.2017.08.008.

Haidet-Phillips, A. M. *et al.* (2011) 'Astrocytes from familial and sporadic ALS patients are toxic to motor neurons', *Nature Biotechnology*. Nature Publishing Group, 29(9), pp. 824–828. doi: 10.1038/nbt.1957.

- Harris, C. P. *et al.* (2003) 'Comprehensive molecular cytogenetic characterization of cervical cancer cell lines', *Genes Chromosomes and Cancer*, 36(3), pp. 233–241. doi: 10.1002/gcc.10158.
- Harrison, N. J. *et al.* (2009) 'CD30 expression reveals that culture adaptation of human embryonic stem cells can occur through differing routes', *Stem Cells*. John Wiley & Sons, Ltd, 27(5), pp. 1057–1065. doi: 10.1002/stem.41.
- Henrichs, V. *et al.* (2020) 'Mitochondria-adaptor TRAK1 promotes kinesin-1 driven transport in crowded environments', *Nature Communications*. Nature Research, 11(1), pp. 1–13. doi: 10.1038/s41467-020-16972-5.
- Hetz, C. and Saxena, S. (2017) 'ER stress and the unfolded protein response in neurodegeneration', *Nature Reviews Neurology*. Nature Publishing Group, pp. 477–491. doi: 10.1038/nrneurol.2017.99.
- Heyer, W.-D., Ehmsen, K. T. and Liu, J. (2010) 'Regulation of Homologous Recombination in Eukaryotes', *Annual Review of Genetics*. Annual Reviews, 44(1), pp. 113–139. doi: 10.1146/annurev-genet-051710-150955.
- Hikiami, R. *et al.* (2018) 'Charcot-Marie-Tooth disease type 2A with an autosomal-recessive inheritance: The first report of an adult-onset disease', *Journal of Human Genetics*. Nature Publishing Group, 63(1), pp. 89–92. doi: 10.1038/s10038-017-0353-3.
- Hoppins, S. *et al.* (2011) 'The Soluble Form of Bax Regulates Mitochondrial Fusion via MFN2 Homotypic Complexes', *Molecular Cell*, 41(2), pp. 150–160. doi: 10.1016/j.molcel.2010.11.030.
- Hu, B. Y., Du, Z. W. and Zhang, S. C. (2009) 'Differentiation of human oligodendrocytes from pluripotent stem cells', *Nature Protocols*, 4(11), pp. 1614–1622. doi: 10.1038/nprot.2009.186.
- Hye, J. K. *et al.* (2009) 'Targeted genome editing in human cells with zinc finger nucleases constructed via modular assembly', *Genome Research*. Cold Spring Harbor Laboratory Press, 19(7), pp. 1279–1288. doi: 10.1101/gr.089417.108.
- lapadre, G. *et al.* (2018) 'A novel homozygous MFN2 mutation associated with severe and atypical CMT2 phenotype', *European Journal of Paediatric Neurology*. W.B. Saunders, 22(3), pp. 563–567. doi: 10.1016/j.ejpn.2017.12.020.
- Ihry, R. J. *et al.* (2018) 'P53 inhibits CRISPR-Cas9 engineering in human pluripotent stem cells', *Nature Medicine*, 24(7), pp. 939–946. doi: 10.1038/s41591-018-0050-6.
- Ishihara, N., Eura, Y. and Mihara, K. (2004) 'Mitofusin 1 and 2 play distinct roles in mitochondrial fusion reactions via GTPase activity', *Journal of Cell Science*. The Company of Biologists, 117(26), pp. 6535–6546. doi: 10.1242/jcs.01565.
- Jin, S. M. and Youle, R. J. (2012) 'PINK1-and Parkin-mediated mitophagy at a glance', *Journal of Cell Science*. The Company of Biologists Ltd, 125(4), pp. 795–799. doi: 10.1242/jcs.093849.
- Juneja, M. *et al.* (2018) 'PFN2 and GAMT as common molecular determinants of axonal Charcot-

Marie-Tooth disease', *Journal of Neurology, Neurosurgery and Psychiatry*. BMJ Publishing Group Ltd, 89(8), pp. 870–878. doi: 10.1136/jnnp-2017-317562.

Kalinski, A. L. *et al.* (2019) 'Deacetylation of Miro1 by HDAC6 blocks mitochondrial transport and mediates axon growth inhibition', *The Journal of cell biology*. Rockefeller University Press, 218(6), pp. 1871–1890. doi: 10.1083/jcb.201702187.

Kawaguchi, Y. *et al.* (2003) 'The deacetylase HDAC6 regulates aggresome formation and cell viability in response to misfolded protein stress', *Cell*. Elsevier B.V., 115(6), pp. 727–738. doi: 10.1016/S0092-8674(03)00939-5.

Kijima, K. *et al.* (2005) 'Mitochondrial GTPase mitofusin 2 mutation in Charcot-Marie-Tooth neuropathy type 2A', *Human Genetics*, 116(1–2), pp. 23–27. doi: 10.1007/s00439-004-1199-2.

Kim, H. S. *et al.* (2017) 'Schwann Cell Precursors from Human Pluripotent Stem Cells as a Potential Therapeutic Target for Myelin Repair', *Stem Cell Reports*. Cell Press, 8(6), pp. 1714–1726. doi: 10.1016/j.stemcr.2017.04.011.

Kim, J. Y. *et al.* (2016) 'HDAC6 Inhibitors Rescued the Defective Axonal Mitochondrial Movement in Motor Neurons Derived from the Induced Pluripotent Stem Cells of Peripheral Neuropathy Patients with HSPB1 Mutation', *Stem Cells International*, 2016. doi: 10.1155/2016/9475981.

Kim, K. *et al.* (2010) 'Epigenetic memory in induced pluripotent stem cells', *Nature*. Nature Publishing Group, 467(7313), pp. 285–290. doi: 10.1038/nature09342.

Kim, S. *et al.* (2014) 'Highly efficient RNA-guided genome editing in human cells via delivery of purified Cas9 ribonucleoproteins', *Genome research*, 128, pp. 1–32. doi: 10.1101/gr.171322.113.Freely.

Kimchi-Sarfaty, C. *et al.* (2007) 'A "silent" polymorphism in the MDR1 gene changes substrate specificity', *Science*. Science, 315(5811), pp. 525–528. doi: 10.1126/science.1135308.

Kiskinis, E. *et al.* (2014) 'Pathways disrupted in human ALS motor neurons identified through genetic correction of mutant SOD1', *Cell Stem Cell*. Cell Press, 14(6), pp. 781–795. doi: 10.1016/j.stem.2014.03.004.

Kitani-Morii, F. *et al.* (2017) 'Analysis of neural crest cells from Charcot-Marie-Tooth disease patients demonstrates disease-relevant molecular signature', *NeuroReport*, 28(13), pp. 814–821. doi: 10.1097/WNR.0000000000000831.

Kleinstiver, B. P. *et al.* (2016) 'High-fidelity CRISPR-Cas9 nucleases with no detectable genome-wide off-target effects', *Nature*. Nature Publishing Group, 529(7587), pp. 490–495. doi: 10.1038/nature16526.

Klim, J. R. *et al.* (2019) 'ALS-implicated protein TDP-43 sustains levels of STMN2, a mediator of motor neuron growth and repair', *Nature Neuroscience*. Springer US, 22(2), pp. 167–179. doi:

10.1038/s41593-018-0300-4.

Köhler, G. and Milstein, C. (1975) 'Continuous cultures of fused cells secreting antibody of predefined specificity', *Nature*. Nature Publishing Group, 256(5517), pp. 495–497. doi: 10.1038/256495a0.

Koopman, W. J. H. *et al.* (2005) 'Inhibition of complex I of the electron transport chain causes O₂-mediated mitochondrial outgrowth', *American Journal of Physiology - Cell Physiology*. American Physiological Society, 288(6 57-6), pp. 1440–1450. doi: 10.1152/ajpcell.00607.2004.

Kotruchow, K., Kabzińska, D. and Kochański, A. (2015) 'Pathogenic mutations and sequence variants within mitofusin 2 gene in Polish patients with different hereditary motor-sensory neuropathies', *Acta Neurobiologiae Experimentalis*, 75(3), pp. 264–278.

Laing, O., Halliwell, J. and Barbaric, I. (2019) 'Rapid PCR Assay for Detecting Common Genetic Variants Arising in Human Pluripotent Stem Cell Cultures', *Current Protocols in Stem Cell Biology*. John Wiley & Sons, Ltd, 49(1), p. e83. doi: 10.1002/cpsc.83.

Lam, D. *et al.* (2019) 'Tissue-specific extracellular matrix accelerates the formation of neural networks and communities in a neuron-glia co-culture on a multi-electrode array', *Scientific Reports*. Nature Publishing Group, 9(1), pp. 1–15. doi: 10.1038/s41598-019-40128-1.

Larrea, D. *et al.* (2019) 'MFN2 mutations in Charcot–Marie–Tooth disease alter mitochondria-associated ER membrane function but do not impair bioenergetics', *Human Molecular Genetics*. doi: 10.1093/hmg/ddz008.

Lawson, V. H., Graham, B. V. and Flanigan, K. M. (2005) 'Clinical and electrophysiologic features of CMT2A with mutations in the mitofusin 2 gene', *Neurology*, 65(2), pp. 197–204. doi: 10.1212/01.wnl.0000168898.76071.70.

Leach, L. L. and Clegg, D. O. (2015) 'Concise Review: Making Stem Cells Retinal: Methods for Deriving Retinal Pigment Epithelium and Implications for Patients with Ocular Disease', *Stem Cells*. Wiley-Blackwell, 33(8), pp. 2363–2373. doi: 10.1002/stem.2010.

Lee, S. K. and Pfaff, S. L. (2003) 'Synchronization of neurogenesis and motor neuron specification by direct coupling of bHLH and homeodomain transcription factors', *Neuron*. Cell Press, 38(5), pp. 731–745. doi: 10.1016/S0896-6273(03)00296-4.

Li, G. *et al.* (2017) 'Small molecules enhance CRISPR/Cas9-mediated homology-directed genome editing in primary cells', *Scientific Reports*. Nature Publishing Group, 7(1), pp. 1–11. doi: 10.1038/s41598-017-09306-x.

Liang, X. *et al.* (2015) 'Rapid and highly efficient mammalian cell engineering via Cas9 protein transfection', *Journal of Biotechnology*. Elsevier, 208, pp. 44–53. doi: 10.1016/j.jbiotec.2015.04.024.

Liang, X. *et al.* (2017) 'Enhanced CRISPR/Cas9-mediated precise genome editing by improved design

and delivery of gRNA, Cas9 nuclease, and donor DNA', *Journal of Biotechnology*, 241, pp. 136–146. doi: 10.1016/j.jbiotec.2016.11.011.

Lippmann, E. S. *et al.* (2015) 'Deterministic HOX patterning in human pluripotent stem cell-derived neuroectoderm', *Stem Cell Reports*. Cell Press, 4(4), pp. 632–644. doi: 10.1016/j.stemcr.2015.02.018.

Liu, J. P., Laufer, E. and Jessell, T. M. (2001) 'Assigning the positional identity of spinal motor neurons: Rostrocaudal patterning of Hox-c expression by FGFs, Gdf11, and retinoids', *Neuron*, 32(6), pp. 997–1012. doi: 10.1016/S0896-6273(01)00544-X.

Liu, M. *et al.* (2019) 'Methodologies for improving HDR efficiency', *Frontiers in Genetics*. Frontiers Media S.A., p. 691. doi: 10.3389/fgene.2018.00691.

Loiseau, D. *et al.* (2007) 'Mitochondrial coupling defect in Charcot-Marie-Tooth type 2A disease', *Annals of Neurology*, 61(4), pp. 315–323. doi: 10.1002/ana.21086.

Longair, M. H., Baker, D. A. and Armstrong, J. D. (2011) 'Simple neurite tracer: Open source software for reconstruction, visualization and analysis of neuronal processes', *Bioinformatics*. Oxford Academic, 27(17), pp. 2453–2454. doi: 10.1093/bioinformatics/btr390.

Luz, A. L. *et al.* (2015) 'Mitochondrial morphology and fundamental parameters of the mitochondrial respiratory chain are altered in caenorhabditis elegans strains deficient in mitochondrial dynamics and homeostasis processes', *PLoS ONE*. Edited by G. López Lluch. Public Library of Science, 10(6), p. e0130940. doi: 10.1371/journal.pone.0130940.

MacAskill, A. F. *et al.* (2009) 'Miro1 Is a Calcium Sensor for Glutamate Receptor-Dependent Localization of Mitochondria at Synapses', *Neuron*. Elsevier, 61(4), pp. 541–555. doi: 10.1016/j.neuron.2009.01.030.

Magy, L. *et al.* (2018) 'Updating the classification of inherited neuropathies', *Neurology*, 90(10), pp. e870–e876. doi: 10.1212/wnl.0000000000005074.

Mandal, A. and Drerup, C. M. (2019) 'Axonal Transport and Mitochondrial Function in Neurons', *Frontiers in Cellular Neuroscience*. Frontiers Media S.A. doi: 10.3389/fncel.2019.00373.

Markouli, C. *et al.* (2019) 'Gain of 20q11.21 in Human Pluripotent Stem Cells Impairs TGF- β -Dependent Neuroectodermal Commitment', *Stem Cell Reports*. Cell Press, 13(1), pp. 163–176. doi: 10.1016/j.stemcr.2019.05.005.

Martínez-Reyes, I. and Chandel, N. S. (2020) 'Mitochondrial TCA cycle metabolites control physiology and disease', *Nature Communications*. doi: 10.1038/s41467-019-13668-3.

Martinez, J. H. *et al.* (2018) 'Drp-1 dependent mitochondrial fragmentation and protective autophagy in dopaminergic SH-SY5Y cells overexpressing alpha-synuclein', *Molecular and Cellular Neuroscience*. Academic Press Inc., 88, pp. 107–117. doi: 10.1016/j.mcn.2018.01.004.

Maruyama, T. *et al.* (2015) 'Increasing the efficiency of precise genome editing with CRISPR-Cas9 by

inhibition of nonhomologous end joining', *Nature Biotechnology*. Nature Publishing Group, 33(5), pp. 538–542. doi: 10.1038/nbt.3190.

Maury, Y. *et al.* (2015) 'Combinatorial analysis of developmental cues efficiently converts human pluripotent stem cells into multiple neuronal subtypes', *Nature Biotechnology*. Nature Publishing Group, 33(1), pp. 89–96. doi: 10.1038/nbt.3049.

McCorquodale, D. S. *et al.* (2011) 'Mutation screening of mitofusin 2 in Charcot-Marie-Tooth disease type 2', *Journal of Neurology*, 258(7), pp. 1234–1239. doi: 10.1007/s00415-011-5910-7.

Milley, G. M. *et al.* (2017) 'Genotypic and phenotypic spectrum of the most common causative genes of Charcot-Marie-Tooth disease in Hungarian patients', *Neuromuscular Disorders*, 1 January, pp. 38–43. doi: 10.1016/j.nmd.2017.08.007.

Miret-Casals, L. *et al.* (2018) 'Identification of New Activators of Mitochondrial Fusion Reveals a Link between Mitochondrial Morphology and Pyrimidine Metabolism', *Cell Chemical Biology*. Elsevier Ltd, 25(3), pp. 268–278.e4. doi: 10.1016/j.chembiol.2017.12.001.

Mishra, P. and Chan, D. C. (2014) 'Mitochondrial dynamics and inheritance during cell division, development and disease', *Nature Reviews Molecular Cell Biology*. Nature Publishing Group, pp. 634–646. doi: 10.1038/nrm3877.

Misko, A. *et al.* (2010) 'Mitofusin 2 is necessary for transport of axonal mitochondria and interacts with the Miro/Milton complex', *Journal of Neuroscience*. J Neurosci, 30(12), pp. 4232–4240. doi: 10.1523/JNEUROSCI.6248-09.2010.

Misko, A. L. *et al.* (2012) 'Mitofusin2 mutations disrupt axonal mitochondrial positioning and promote axon degeneration', *Journal of Neuroscience*. Society for Neuroscience, 32(12), pp. 4145–4155. doi: 10.1523/JNEUROSCI.6338-11.2012.

Mizuguchi, R. *et al.* (2001) 'Combinatorial roles of Olig2 and Neurogenin2 in the coordinated induction of pan-neuronal and subtype-specific properties of motoneurons', *Neuron*. Cell Press, 31(5), pp. 757–771. doi: 10.1016/S0896-6273(01)00413-5.

Mo, Z. *et al.* (2018) 'Aberrant GlyRS-HDAC6 interaction linked to axonal transport deficits in Charcot-Marie-Tooth neuropathy', *Nature Communications*. Nature Publishing Group, 9(1), p. 1007. doi: 10.1038/s41467-018-03461-z.

Mojica, F. J. M. *et al.* (2009) 'Short motif sequences determine the targets of the prokaryotic CRISPR defence system', *Microbiology*. Microbiology Society, 155(3), pp. 733–740. doi: 10.1099/mic.0.023960-0.

Moller, A. *et al.* (2017) 'Amyotrophic lateral sclerosis-associated mutant SOD1 inhibits anterograde axonal transport of mitochondria by reducing Miro1 levels', *Human Molecular Genetics*, 26(23), pp. 4668–4679. doi: 10.1093/hmg/ddx348.

- Mouilleau, V. *et al.* (2021) 'Dynamic extrinsic pacing of the HOX clock in human axial progenitors controls motor neuron subtype specification', *Development (Cambridge, England)*. NLM (Medline), 148(6), p. 2020.06.27.175646. doi: 10.1101/2020.06.27.175646.
- Mourier, A. *et al.* (2015) 'Mitofusin 2 is required to maintain mitochondrial coenzyme Q levels', *Journal of Cell Biology*. Rockefeller University Press, 208(4), pp. 429–442. doi: 10.1083/jcb.201411100.
- Müller, M. *et al.* (2018) 'Mitochondria and calcium regulation as basis of neurodegeneration associated with aging', *Frontiers in Neuroscience*. Frontiers Media S.A., p. 470. doi: 10.3389/fnins.2018.00470.
- Nakhro, K. *et al.* (2013) 'Missense mutations of mitofusin 2 in axonal Charcot-Marie-Tooth neuropathy: Polymorphic or incomplete penetration?', *Animal Cells and Systems*, 17(4), pp. 228–236. doi: 10.1080/19768354.2013.814587.
- Neusch, C. *et al.* (2007) 'Mitofusin 2 gene mutation (R94Q) causing severe early-onset axonal polyneuropathy (CMT2A)', *European Journal of Neurology*, 14(5), pp. 575–577. doi: 10.1111/j.1468-1331.2006.01688.x.
- NHS England (2016) *Charcot-Marie-Tooth disease - NHS.UK*. Available at: <https://www.nhs.uk/conditions/charcot-marie-tooth-disease/#how-cmt-is-treated> (Accessed: 25 November 2017).
- Nicholson, G. A. *et al.* (2008) 'Severe early-onset axonal neuropathy with homozygous and compound heterozygous mfn2 mutations', *Neurology*, 70(19), pp. 1678–1681. doi: 10.1212/01.wnl.0000311275.89032.22.
- Niederreither, K. *et al.* (1997) 'Restricted expression and retinoic acid-induced downregulation of the retinaldehyde dehydrogenase type 2 (RALDH-2) gene during mouse development', *Mechanisms of Development*. Elsevier, 62(1), pp. 67–78. doi: 10.1016/S0925-4773(96)00653-3.
- Nijssen, J., Comley, L. H. and Hedlund, E. (2017) 'Motor neuron vulnerability and resistance in amyotrophic lateral sclerosis', *Acta Neuropathologica*, pp. 863–885. doi: 10.1007/s00401-017-1708-8.
- Nishizawa, M. *et al.* (2016) 'Epigenetic Variation between Human Induced Pluripotent Stem Cell Lines Is an Indicator of Differentiation Capacity', *Cell Stem Cell*. Cell Press, 19(3), pp. 341–354. doi: 10.1016/j.stem.2016.06.019.
- Nordström, U. *et al.* (2006) 'An early role for Wnt signaling in specifying neural patterns of Cdx and Hox gene expression and motor neuron subtype identity', *PLoS Biology*. PLoS Biol, 4(8), pp. 1438–1452. doi: 10.1371/journal.pbio.0040252.
- O'Driscoll, M. and Jeggo, P. A. (2006) 'The role of double-strand break repair - Insights from human

genetics', *Nature Reviews Genetics*. Nature Publishing Group, pp. 45–54. doi: 10.1038/nrg1746.

Osafune, K. *et al.* (2008) 'Marked differences in differentiation propensity among human embryonic stem cell lines', *Nature Biotechnology*. Nature Publishing Group, 26(3), pp. 313–315. doi: 10.1038/nbt1383.

Pabo, C. O., Peisach, E. and Grant, R. A. (2002) 'Design and Selection of Novel Cys 2 His 2 Zinc Finger Proteins', *Annual Review of Biochemistry*. Annual Reviews 4139 El Camino Way, P.O. Box 10139, Palo Alto, CA 94303-0139, USA, 70(1), pp. 313–340. doi: 10.1146/annurev.biochem.70.1.313.

Patani, R. *et al.* (2011) 'Retinoid-independent motor neurogenesis from human embryonic stem cells reveals a medial columnar ground state', *Nature Communications*. Nature Publishing Group, 2(1), pp. 1–10. doi: 10.1038/ncomms1216.

Patterson, M. *et al.* (2012) 'Defining the nature of human pluripotent stem cell progeny', *Cell Research*. Nature Publishing Group, 22(1), pp. 178–193. doi: 10.1038/cr.2011.133.

Patzkó, Á. and Shy, M. E. (2011) 'Update on Charcot-Marie-Tooth disease', *Current Neurology and Neuroscience Reports*, 11(1), pp. 78–88. doi: 10.1007/s11910-010-0158-7.

Peng, C. *et al.* (2015) 'Mitofusin 2 ameliorates hypoxia-induced apoptosis via mitochondrial function and signaling pathways', *International Journal of Biochemistry and Cell Biology*. Pergamon, 69, pp. 29–40. doi: 10.1016/j.biocel.2015.09.011.

Perez-Siles, G. *et al.* (2020) 'Energy metabolism and mitochondrial defects in X-linked Charcot-Marie-Tooth (CMTX6) iPSC-derived motor neurons with the p.R158H PDK3 mutation', *Scientific Reports*. Nature Research, 10(1), pp. 1–13. doi: 10.1038/s41598-020-66266-5.

PHARNEXT (2018) *Pharnext Announces Positive Topline Results from Pivotal Phase 3 Trial of PXT3003 for Treatment of Charcot-Marie-Tooth Type 1A Disease*. Available at: www.pharnext.com/en/investors/presentation (Accessed: 30 October 2018).

Picci, C. *et al.* (2020) 'HDAC6 inhibition promotes α -tubulin acetylation and ameliorates CMT2A peripheral neuropathy in mice', *Experimental Neurology*. Academic Press Inc., 328, p. 113281. doi: 10.1016/j.expneurol.2020.113281.

Pilling, A. D. *et al.* (2006) 'Kinesin-1 and dynein are the primary motors for fast transport of mitochondria in *Drosophila* motor axons', *Molecular Biology of the Cell*. American Society for Cell Biology, 17(4), pp. 2057–2068. doi: 10.1091/mbc.E05-06-0526.

Plante-Bordeneuve, V. and Said, G. (2002) 'Dejerine-Sottas disease and hereditary demyelinating polyneuropathy of infancy', *Muscle and Nerve*. John Wiley & Sons, Ltd, pp. 608–621. doi: 10.1002/mus.10197.

Polke, J. M. *et al.* (2011) 'Recessive axonal Charcot-Marie-Tooth disease due to compound heterozygous mitofusin 2 mutations', *Neurology*, 77(2), pp. 168–173. doi:

10.1212/WNL.0b013e3182242d4d.

Preibisch, S., Saalfeld, S. and Tomancak, P. (2009) 'Globally optimal stitching of tiled 3D microscopic image acquisitions', *Bioinformatics*. Oxford University Press, 25(11), pp. 1463–1465. doi: 10.1093/bioinformatics/btp184.

Price, C. J. *et al.* (2019) 'Genetically Variant Human Pluripotent Stem Cells Selectively Eliminate Wild-Type Counterparts Through YAP-Mediated Cell Competition', *Cell Stem Cell*. Cold Spring Harbor Laboratory, p. 854430. doi: 10.2139/ssrn.3499745.

Qi, Y. *et al.* (2016) 'Structures of human mitofusin 1 provide insight into mitochondrial tethering', *Journal of Cell Biology*. Rockefeller University Press, 215(5), pp. 621–629. doi: 10.1083/jcb.201609019.

Qu, Q. *et al.* (2014) 'High-efficiency motor neuron differentiation from human pluripotent stem cells and the function of Islet-1', *Nature Communications*. Nature Publishing Group, 5(1), pp. 1–13. doi: 10.1038/ncomms4449.

Ragagnin, A. M. G. *et al.* (2019) 'Motor neuron susceptibility in ALS/FTD', *Frontiers in Neuroscience*. Frontiers Media S.A., p. 532. doi: 10.3389/fnins.2019.00532.

Ramos-Mejia, V. *et al.* (2010) 'Nodal/activin signaling predicts human pluripotent stem cell lines prone to differentiate toward the hematopoietic lineage', *Molecular Therapy*, 18(12), pp. 2173–2181. doi: 10.1038/mt.2010.179.

Ran, F. A. *et al.* (2013) 'Double nicking by RNA-guided CRISPR cas9 for enhanced genome editing specificity', *Cell*. Cell Press, 154(6), pp. 1380–1389. doi: 10.1016/j.cell.2013.08.021.

Rana, P. *et al.* (2017) 'Utilization of iPSC-derived human neurons for high-throughput drug-induced peripheral neuropathy screening', *Toxicology in Vitro*, 45, pp. 111–118. doi: 10.1016/j.tiv.2017.08.014.

Reilly, M. M. *et al.* (2011) 'Charcot-Marie-Tooth disease.', *Journal of the peripheral nervous system : JPNS*. Blackwell Publishing Ltd, 16(1), pp. 1–14. doi: 10.1111/j.1529-8027.2011.00324.x.

Riesenberg, S. and Maricic, T. (2018) 'Targeting repair pathways with small molecules increases precise genome editing in pluripotent stem cells', *Nature Communications*. Nature Publishing Group, 9(1), pp. 1–9. doi: 10.1038/s41467-018-04609-7.

Rieusset, J. (2018) 'The role of endoplasmic reticulum-mitochondria contact sites in the control of glucose homeostasis: An update', *Cell Death and Disease*. Nature Publishing Group, 9(3), pp. 1–12. doi: 10.1038/s41419-018-0416-1.

Rizzo, F. *et al.* (2016) 'Selective mitochondrial depletion, apoptosis resistance, and increased mitophagy in human Charcot-Marie-Tooth 2A motor neurons', *Human molecular genetics*. Oxford University Press, 25(19), pp. 4266–4281. doi: 10.1093/hmg/ddw258.

- Rocha, A. G. *et al.* (2018) 'MFN2 agonists reverse mitochondrial defects in preclinical models of Charcot-Marie-Tooth disease type 2A', *Science*, 360(6386), pp. 336–341. doi: 10.1126/science.aao1785.
- Rodin, S. *et al.* (2014) 'Monolayer culturing and cloning of human pluripotent stem cells on laminin-521-based matrices under xeno-free and chemically defined conditions', *Nature Protocols*. Nature Publishing Group, 9(10), pp. 2354–2368. doi: 10.1038/nprot.2014.159.
- Rosa, F. *et al.* (2020) 'In Vitro Differentiated Human Stem Cell-Derived Neurons Reproduce Synaptic Synchronicity Arising during Neurodevelopment', *Stem cell reports*, 15. doi: 10.1016/j.stemcr.2020.05.015.
- Ross-Thriepland, D. *et al.* (2020) 'Arrayed CRISPR Screening Identifies Novel Targets That Enhance the Productive Delivery of mRNA by MC3-Based Lipid Nanoparticles', *SLAS Discovery*. SAGE Publications Inc., 25(6), pp. 605–617. doi: 10.1177/2472555220925770.
- Ross, A. H. *et al.* (1984) 'Characterization of nerve growth factor receptor in neural crest tumors using monoclonal antibodies', *Proceedings of the National Academy of Sciences of the United States of America*. National Academy of Sciences, 81(21 I), pp. 6681–6685. doi: 10.1073/pnas.81.21.6681.
- Rossaert, E. and Van Den Bosch, L. (2020) 'HDAC6 inhibitors: Translating genetic and molecular insights into a therapy for axonal CMT', *Brain Research*. Elsevier B.V., p. 146692. doi: 10.1016/j.brainres.2020.146692.
- Rouso, D. L. *et al.* (2008) 'Coordinated Actions of the Forkhead Protein Foxp1 and Hox Proteins in the Columnar Organization of Spinal Motor Neurons', *Neuron*. Cell Press, 59(2), pp. 226–240. doi: 10.1016/j.neuron.2008.06.025.
- Saporta, A. S. D. *et al.* (2011) 'Charcot-marie-tooth disease subtypes and genetic testing strategies', *Annals of Neurology*, 69(1), pp. 22–33. doi: 10.1002/ana.22166.
- Saporta, M. A. *et al.* (2015) 'Axonal Charcot–Marie–Tooth disease patient-derived motor neurons demonstrate disease-specific phenotypes including abnormal electrophysiological properties', *Experimental Neurology*. Academic Press, 263, pp. 190–199. doi: 10.1016/j.expneurol.2014.10.005.
- Sassano, M. L., van Vliet, A. R. and Agostinis, P. (2017) 'Mitochondria-associated membranes as networking platforms and regulators of cancer cell fate', *Frontiers in Oncology*. Frontiers Media S.A., p. 174. doi: 10.3389/fonc.2017.00174.
- Schindelin, J. *et al.* (2012) 'Fiji: An open-source platform for biological-image analysis', *Nature Methods*. Nat Methods, pp. 676–682. doi: 10.1038/nmeth.2019.
- Schwarz, T. L. (2013) 'Mitochondrial trafficking in neurons', *Cold Spring Harbor Perspectives in Biology*. Cold Spring Harbor Laboratory Press, 5(6), p. a011304. doi: 10.1101/cshperspect.a011304.
- Scott, T. *et al.* (2019) 'Improved Cas9 activity by specific modifications of the tracrRNA', *Scientific*

- Reports*, 9(1), pp. 1–11. doi: 10.1038/s41598-019-52616-5.
- Sentmanat, M. F. *et al.* (2018) 'A Survey of Validation Strategies for CRISPR-Cas9 Editing', *Scientific Reports*. Nature Publishing Group, 8(1), p. 888. doi: 10.1038/s41598-018-19441-8.
- Sharma, S. and Raghavan, S. C. (2016) 'Nonhomologous DNA End Joining', in *Encyclopedia of Cell Biology*, pp. 451–455. doi: 10.1016/B978-0-12-394447-4.10047-1.
- Shen, S. *et al.* (2021) 'Tetrahydroquinoline-Capped Histone Deacetylase 6 Inhibitor SW-101 Ameliorates Pathological Phenotypes in a Charcot–Marie– Tooth Type 2A Mouse Model', *Journal of Medicinal Chemistry*, p. acs.jmedchem.0c02210. doi: 10.1021/acs.jmedchem.0c02210.
- Shevinsky, L. H. *et al.* (1982) 'Monoclonal antibody to murine embryos defines a stage-specific embryonic antigen expressed on mouse embryos and human teratocarcinoma cells', *Cell*. Elsevier, 30(3), pp. 697–705. doi: 10.1016/0092-8674(82)90274-4.
- Shi, L. *et al.* (2018) 'Modeling the Pathogenesis of Charcot Marie Tooth Disease Type 1A using Patient Specific iPSCs', *Stem Cell Reports*, 10(1), pp. 120–133. doi: 10.1016/j.stemcr.2017.11.013.
- Simões-Pires, C. *et al.* (2013) 'HDAC6 as a target for neurodegenerative diseases: What makes it different from the other HDACs?', *Molecular Neurodegeneration*. doi: 10.1186/1750-1326-8-7.
- Singh, A. M. (2019) 'An Efficient Protocol for Single-Cell Cloning Human Pluripotent Stem Cells', *Frontiers in Cell and Developmental Biology*. Frontiers Media SA, 7, p. 11. doi: 10.3389/fcell.2019.00011.
- Singh, R. *et al.* (2015) 'Cas9-chromatin binding information enables more accurate CRISPR off-target prediction', *Nucleic Acids Research*. Narnia, 43(18), pp. e118–e118. doi: 10.1093/nar/gkv575.
- Sitarz, K. S. *et al.* (2012) 'MFN2 mutations cause compensatory mitochondrial DNA proliferation', *Brain*. doi: 10.1093/brain/aws049.
- Solter, D. and Knowles, B. B. (1975) 'Immunosurgery of mouse blastocyst', *Proceedings of the National Academy of Sciences of the United States of America*. National Academy of Sciences, 72(12), pp. 5099–5102. doi: 10.1073/pnas.72.12.5099.
- Stifani, N. (2014) 'Motor neurons and the generation of spinal motor neuron diversity', *Frontiers in Cellular Neuroscience*, 8. doi: 10.3389/fncel.2014.00293.
- Strickland, A. V. *et al.* (2014) 'Characterization of the mitofusin 2 R94W mutation in a knock-in mouse model', *Journal of the Peripheral Nervous System*, 19(2), pp. 152–164. doi: 10.1111/jns5.12066.
- Stuppia, G. *et al.* (2015) 'MFN2-related neuropathies: Clinical features, molecular pathogenesis and therapeutic perspectives', *Journal of the Neurological Sciences*, 356(1–2), pp. 7–18. doi: 10.1016/j.jns.2015.05.033.
- Sun, X. and Nunes, S. S. (2017) 'Bioengineering approaches to mature human pluripotent stem cell-

derived cardiomyocytes', *Frontiers in Cell and Developmental Biology*. Frontiers Media S.A., p. 19. doi: 10.3389/fcell.2017.00019.

Szigeti, K. and Lupski, J. R. (2009) 'Charcot-Marie-Tooth disease', *European Journal of Human Genetics*. Nature Publishing Group, 17(6), pp. 703–710. doi: 10.1038/ejhg.2009.31.

Takahashi, K. *et al.* (2007) 'Induction of pluripotent stem cells from adult human fibroblasts by defined factors', *Cell*, 131(5), pp. 861–872. doi: 10.1016/j.cell.2007.11.019 SUMMARY.

Takahashi, K. and Yamanaka, S. (2006) 'Induction of Pluripotent Stem Cells from Mouse Embryonic and Adult Fibroblast Cultures by Defined Factors', *Cell*. Elsevier, 126(4), pp. 663–676. doi: 10.1016/j.cell.2006.07.024.

Taylor, R. W. and Turnbull, D. M. (2005) 'Mitochondrial DNA mutations in human disease', *Nature Reviews Genetics*. Nature Publishing Group, pp. 389–402. doi: 10.1038/nrg1606.

Terns, M. P. and Terns, R. M. (2011) 'CRISPR-based adaptive immune systems', *Current Opinion in Microbiology*. Elsevier Current Trends, pp. 321–327. doi: 10.1016/j.mib.2011.03.005.

Thams, S. *et al.* (2019) 'A Stem Cell-Based Screening Platform Identifies Compounds that Desensitize Motor Neurons to Endoplasmic Reticulum Stress', *Molecular Therapy*. Cell Press, 27(1), pp. 87–101. doi: 10.1016/j.ymthe.2018.10.010.

Thompson, O. *et al.* (2020) 'Low rates of mutation in clinical grade human pluripotent stem cells under different culture conditions', *Nature Communications*. Nature Research, 11(1), pp. 1–14. doi: 10.1038/s41467-020-15271-3.

Thomson, J. A. *et al.* (1998) 'Embryonic Stem Cell Lines Derived from Human Blastocysts', *Science*. American Association for the Advancement of Science, 282(5391), pp. 1145–1147. doi: 10.1126/science.282.5391.1145.

Tilokani, L. *et al.* (2018) 'Mitochondrial dynamics: Overview of molecular mechanisms', *Essays in Biochemistry*. Portland Press Ltd, pp. 341–360. doi: 10.1042/EBC20170104.

Timmerman, V., Strickland, A. V and Züchner, S. (2014) 'Genetics of Charcot-Marie-Tooth (CMT) Disease within the Frame of the Human Genome Project Success', *Genes*, 5, pp. 13–32. doi: 10.3390/genes5010013.

Tooth, H. H. (1886) *The peroneal type of progressive muscular atrophy: a thesis for the degree of M.D. in the University of Cambridge*.

Twig, G. *et al.* (2008) 'Fission and selective fusion govern mitochondrial segregation and elimination by autophagy', *EMBO Journal*. EMBO Press, 27(2), pp. 433–446. doi: 10.1038/sj.emboj.7601963.

Vakulskas, C. A. *et al.* (2018) 'A high-fidelity Cas9 mutant delivered as a ribonucleoprotein complex enables efficient gene editing in human hematopoietic stem and progenitor cells', *Nature Medicine*, 24(8), pp. 1216–1224. doi: 10.1038/s41591-018-0137-0.

Vallat, J.-M. *et al.* (2008) 'Histopathological findings in hereditary motor and sensory neuropathy of axonal type with onset in early childhood associated with mitofusin 2 mutations.', *Journal of neuropathology and experimental neurology*. Oxford University Press, 67(11), pp. 1097–1102. doi: 10.1097/NEN.0b013e31818b6cbc.

Varum, S. *et al.* (2011) 'Energy metabolism in human pluripotent stem cells and their differentiated counterparts', *PLoS ONE*. Edited by M. Ludgate. Public Library of Science, 6(6), p. e20914. doi: 10.1371/journal.pone.0020914.

Vera, E., Bosco, N. and Studer, L. (2016) 'Generating Late-Onset Human iPSC-Based Disease Models by Inducing Neuronal Age-Related Phenotypes through Telomerase Manipulation', *Cell Reports*. Elsevier B.V., 17(4), pp. 1184–1192. doi: 10.1016/j.celrep.2016.09.062.

Verhoeven, K. *et al.* (2006) 'MFN2 mutation distribution and genotype/phenotype correlation in Charcot-Marie-Tooth type 2', *Brain*. Oxford University Press, 129(8), pp. 2093–2102. doi: 10.1093/brain/awl126.

De Vos, K. J. *et al.* (2007) 'Familial amyotrophic lateral sclerosis-linked SOD1 mutants perturb fast axonal transport to reduce axonal mitochondria content', *Human Molecular Genetics*, 16(22), pp. 2720–2728. doi: 10.1093/hmg/ddm226.

Voskarides, K. and Deltas, C. (2009) 'Screening for mutations in kidney-related genes using SURVEYOR nuclease for cleavage at heteroduplex mismatches', *Journal of Molecular Diagnostics*. Elsevier B.V., 11(4), pp. 311–318. doi: 10.2353/jmoldx.2009.080144.

Vouillot, L., Thélie, A. and Pollet, N. (2015) 'Comparison of T7E1 and surveyor mismatch cleavage assays to detect mutations triggered by engineered nucleases', *G3: Genes, Genomes, Genetics*. Genetics Society of America, 5(3), pp. 407–415. doi: 10.1534/g3.114.015834.

Wang, C. and Youle, R. J. (2009) 'The role of mitochondria in apoptosis', *Annual Review of Genetics*. NIH Public Access, pp. 95–118. doi: 10.1146/annurev-genet-102108-134850.

Wang, W. *et al.* (2018) 'Exchange factor directly activated by cAMP–PKC ϵ signalling mediates chronic morphine-induced expression of purine P2X3 receptor in rat dorsal root ganglia', *British Journal of Pharmacology*. John Wiley & Sons, Ltd (10.1111), 175(10), pp. 1760–1769. doi: 10.1111/bph.14191.

Watanabe, K. *et al.* (2007) 'A ROCK inhibitor permits survival of dissociated human embryonic stem cells', *Nature Biotechnology*, 25(6), pp. 681–686. doi: 10.1038/nbt1310.

Wesolowska-Andersen, A. *et al.* (2020) 'Analysis of Differentiation Protocols Defines a Common Pancreatic Progenitor Molecular Signature and Guides Refinement of Endocrine Differentiation', *Stem Cell Reports*. Cell Press, 14(1), pp. 138–153. doi: 10.1016/j.stemcr.2019.11.010.

Whitworth, A. J. and Pallanck, L. J. (2017) 'PINK1/Parkin mitophagy and neurodegeneration—what do we really know in vivo?', *Current Opinion in Genetics and Development*. Elsevier Current Trends,

pp. 47–53. doi: 10.1016/j.gde.2017.01.016.

William, C. M. (2003) 'Regulation of motor neuron subtype identity by repressor activity of Mnx class homeodomain proteins', *Development*. The Company of Biologists Ltd, 130(8), pp. 1523–1536. doi: 10.1242/dev.00358.

Williams, B. P. *et al.* (1988) 'Biochemical and genetic analysis of the Oka blood group antigen', *Immunogenetics*. Springer-Verlag, 27(5), pp. 322–329. doi: 10.1007/BF00395127.

Wolf, C. *et al.* (2019) 'The Charcot–Marie Tooth Disease Mutation R94Q in MFN2 Decreases ATP Production but Increases Mitochondrial Respiration under Conditions of Mild Oxidative Stress', *Cells*. MDPI AG, 8(10), p. 1289. doi: 10.3390/cells8101289.

Wong, Y. C., Ysselstein, D. and Krainc, D. (2018) 'Mitochondria-lysosome contacts regulate mitochondrial fission via RAB7 GTP hydrolysis', *Nature*. Nature Publishing Group, 554(7692), pp. 382–386. doi: 10.1038/nature25486.

Xu, L., Wang, X. and Tong, C. (2020) 'Endoplasmic Reticulum–Mitochondria Contact Sites and Neurodegeneration', *Frontiers in Cell and Developmental Biology*. Frontiers Media S.A. doi: 10.3389/fcell.2020.00428.

Yadegari, H. *et al.* (2016) 'Intron retention resulting from a silent mutation in the VWF gene that structurally influences the 5' splice site', *Blood*. American Society of Hematology, 128(17), pp. 2144–2152. doi: 10.1182/blood-2016-02-699686.

Yang, L. *et al.* (2013) 'Optimization of scarless human stem cell genome editing', *Nucleic Acids Research*. Oxford Academic, 41(19), pp. 9049–9061. doi: 10.1093/nar/gkt555.

Ye, J. *et al.* (2017) 'High quality clinical grade human embryonic stem cell lines derived from fresh discarded embryos', *Stem Cell Research and Therapy*, 8(1), p. 128. doi: 10.1186/s13287-017-0561-y.

Yin, H. *et al.* (2017) 'structure-guided chemical modification of guide RNA enables potent non-viral in vivo genome editing', *Nature Biotechnology*. Nature Publishing Group, 35(12), pp. 1179–1187. doi: 10.1038/nbt.4005.

Zeltner, N. *et al.* (2016) 'Capturing the biology of disease severity in a PSC-based model of familial dysautonomia', *Nature Medicine*, 22(12), pp. 1421–1427. doi: 10.1038/nm.4220.

Zhang, J. P. *et al.* (2016) 'Different Effects of sgRNA Length on CRISPR-mediated Gene Knockout Efficiency', *Scientific Reports*. Nature Publishing Group, 6(1), pp. 1–10. doi: 10.1038/srep28566.

Zhang, X. H. *et al.* (2015) 'Off-target effects in CRISPR/Cas9-mediated genome engineering', *Molecular Therapy - Nucleic Acids*. Cell Press, p. e264. doi: 10.1038/mtna.2015.37.

Zhang, Y. *et al.* (2008) 'Mice Lacking Histone Deacetylase 6 Have Hyperacetylated Tubulin but Are Viable and Develop Normally', *Molecular and Cellular Biology*. American Society for Microbiology, 28(5), pp. 1688–1701. doi: 10.1128/mcb.01154-06.

Zhang, Z. *et al.* (2017) 'CRISPR/Cas9 Genome-Editing System in Human Stem Cells: Current Status and Future Prospects', *Molecular Therapy - Nucleic Acids*. Elsevier, pp. 230–241. doi:

10.1016/j.omtn.2017.09.009.

Zhao, C. *et al.* (2001) 'Charcot-Marie-Tooth disease type 2A caused by mutation in a microtubule motor KIF1Bbeta.', *Cell*, 105(5), pp. 587–97. doi: S0092-8674(01)00363-4 [pii].

Zhao, R. Z. *et al.* (2019) 'Mitochondrial electron transport chain, ROS generation and uncoupling (Review)', *International Journal of Molecular Medicine*. Spandidos Publications, pp. 3–15. doi:

10.3892/ijmm.2019.4188.

Zhou, Y. *et al.* (2019) 'Restoring mitofusin balance prevents axonal degeneration in a Charcot-Marie-Tooth type 2A model', *The Journal of Clinical Investigation*, 129(4), pp. 1756–1771. doi:

10.1172/JCI124194.

Züchner, S. *et al.* (2004) 'Mutations in the mitochondrial GTPase mitofusin 2 cause Charcot-Marie-Tooth neuropathy type 2A', *Nature Genetics*. Nature Publishing Group, 36(5), pp. 449–451. doi:

10.1038/ng1341.

Züchner, S. *et al.* (2006) 'Axonal neuropathy with optic atrophy is caused by mutations in mitofusin 2', *Annals of Neurology*, 59(2), pp. 276–281. doi: 10.1002/ana.20797.

8) Appendix 1

Table listing MFN2 mutations which are known to be associated with CMT2A as of May 2021.

Nucleotide Change	Amino Acid Change	Domain	Age at Onset (Years)	Transmission	Reference	Severity
c.299C>G	A100G	GTPase	10	Dominant	(Sitarz et al., 2012),(Verhoeven et al., 2006)	
c.491C>T	A164V+T362M	GTPase	<5	Recessive	(Calvo et al., 2009, Nicholason et al. 2008, Vallat et al, 2008).	Severe
c.1148C>T	A383V	HR1	36, 15		(Sitarz et al., 2012), (Muglia et al., 2007), (Bergamin et al., 2014)	Mild/ Various
c.2146G>A	A716T	HR2	2, 23, 50		(Sitarz et al., 2012), (Geir J Braathen, Sand, Lobato, Høyer, & Russell, 2010), (Feely et al., 2011), (G J Braathen, 2012)	Severe
c.2213C>T	A738V		9		(Bergamin et al., 2014)	Mild
	C390F		1		(Feely et al., 2011)	Severe
c.1168T>C	C390R		3	Dominant	(Vallat et al., 2008)	
c. 629A>T	D210V		Early		(Rouzier et al., 2012)	Severe
c.640G>A	D214N+C390R	GTPase	<5	Recessive	(Calvo et al., 2009, Nicholason et al. 2008, Vallat et al, 2008).	Severe
	D496G				(Sitarz et al., 2012)	
c. 984_986delAGA	E239del		1		(Bergamin et al., 2014)	Severe
c. 865G>C	E288D		29		(Bergamin et al., 2014)	Moderate
	E308Stop	GTPase			(Sitarz et al., 2012)	
c1040A>T	E347V	Linker	childhood		(Engelfried et al., 2006)	Severe
c.1271A>G	E424G		10		(Kijima et al., 2005)	Moderate/ Severe
c.2230G>A	E744K	HR2	8		(Choi et al., 2015)	Moderate
c.671T>C	F216S		6, 13	Recessive	(Vallat et al., 2008)	

c.669T>A	F223L		7		(Kijima et al., 2005)	Severe
C.851T>A	F284Y		4, 9		(Ando et al., 2017), (Kijima et al., 2005)	Severe
c.1994T>C	F665S		<10	Dominant	(Calvo et al., 2009)	Moderate
c.2258_2259insT(L753fs)	FRAMESHIFT		62		(Engelfried et al., 2006)	Mild
c.322G>A	G108R+R707W	GTPase	<10	Recessive	(Calvo et al., 2009)	Moderate
c.380G>A	G127D	GTPase	16, Late	De novo	(Chung et al., 2006), (Choi et al., 2015)	Mild
c.380G>T	G127V	GTPase	48		(Engelfried et al., 2006)	Mild
c.526G>A	G176S		<1	Recessive	(Iapadre et al. 2018)	Severe
	G202A	GTPase			(Sitarz et al., 2012)	
	G280H	GTPase			(Sitarz et al., 2012)	
	G298R	GTPase	<20	Dominant	(Sitarz et al., 2012), (Casasnovas et al., 2010)	Moderate
c.383A>G	H128R	GTPase	<5	De novo	(Calvo et al., 2009), (Ando et al., 2017)	Severe
c.493C>G	H165D	GTPase			(Zhu et al., 2005)	Severe
c.494A>G	H165R	GTPase	Late, 35, 57, 6, 5, 10, 50, 14, 21	De novo, Dominant	(Chung et al., 2006), (Bergamin et al., 2014), (Ando et al., 2017), (Verhoeven et al., 2006) (Choi et al., 2015), (Chung et al., 2010), (Cho, Sung, Kim, & Ki, 2007)	Mild, Moderate, Mild/Moderate
c.494A>G	H165R		21		(Ando et al., 2017), (Verhoeven et al., 2006), (Choi et al., 2015), (Chung et al., 2010), (Zhu et al., 2005)	Moderate
c.493C>T	H165Y	GTPase	12	Dominant	(Sitarz et al., 2012), (Verhoeven et al., 2006)	
c.830A>G	H277R		10; 15	Dominant	(Verhoeven et al., 2006)	
c.829C>T	H277Y		>10	Dominant	(Calvo et al., 2009)	Moderate
c.1081C>T	H361Y		2, 1	De novo	(Verhoeven et al., 2006), (Feely et al., 2011), (Züchner et al., 2006)	Severe
	H750P		6		(Sitarz et al., 2012), (Feely et al., 2011)	Severe
	I203M		<20	Dominant	(Casasnovas et al., 2010)	Moderate

c.638T>C	I213T	GTPase	5, 12		(Lawson, Graham, & Flanigan, 2005)	No mild phenotype all severe.
c.262A>T	I88F				(Antoniadi et al., 2015)	
c.326A>G	K109R		10		(Ando et al., 2017)	
c.559A>G	K187D	GTPase	12		(Choi et al., 2015)	Mild
	K307E		10		(Ando et al., 2017)	
c.1071G>C	K357N		4	de novo	(Kijima et al., 2005)	Severe
c.2194A>G	K732Q				(Antoniadi et al., 2015)	
c.292A>G + c.1168 T>C	K98E +C390R		14	Recessive	(Vallat et al., 2008)	
c.292A>C	K98Q	GTPase	8, 9		(Choi et al., 2015), (Nakhro et al., 2012)	Moderate, Moderate/ Severe
	L248V		1		(Feely et al., 2011)	Moderate/ Severe
c.1134_1142del9	L379_M381del		3	Dominant	(Verhoeven et al., 2006)	
c..1930_1932delCTC	L644del	TM	1		(Choi et al., 2015),(Feely et al., 2011)	
	L673P				(Sitarz et al., 2012)	
c.2096T>6	L699P		<16 and late		(Kang et al. 2019)	Moderate/ Mild
c.2129T>C	L710P	HR2	6, 1-2	Unknown	(Verhoeven et al., 2006), (Ando et al., 2017)	
C.2171T>C	L724P		<20		(Abe et al., 2011)	Severe
c.2222T>G	L741W	HR2	~20	Dominant	(Dankwa et al. 2018)	Mild
C.2234T>C	L745P		<10	Dominant	(Calvo et al., 2009)	Mild
227T>C	L76P		7 to 44	Dominant	(Züchner et al., 2004),(Verhoeven et al., 2006)	

c.275T>C	L92P	GTPase	Early, 1, 1, 1, 3	De novo	(Chung et al., 2006), (Verhoeven et al., 2006),(Choi et al., 2015), (Chung et al., 2010)	Severe, Mild
c.275T>G	L92R		3		(McCorquodale et al., 2011)	Severe
c.809T>C	M270T				(Antoniadi et al., 2015)	
	M375V	HR1			(Sitarz et al., 2012)	
c.1128G>A	M376I	Linker	35, 22, 18-20	Dominant	(Engelfried et al., 2006)(Verhoeven et al., 2006), (Ando et al., 2017)	Moderate/ Severe
c.1125A>C	M376L		26		(McCorquodale et al., 2011)	Moderate/ Severe
c.11247T>C	M376T		39, late	Dominant	(Choi et al., 2015),(Chung et al., 2010)	Mild
c.1126A>G	M376V		4-6, <30	Dominant	(Ando et al., 2017), (Casasnovas et al., 2010), (Antoniadi et al., 2015)	Severe
c.2240T>C	M747T		>10	De novo	(Calvo et al., 2009)	Moderate
	Met376O	HR1			(Sitarz et al., 2012)	
	N252L		<20	Dominant	(Casasnovas et al., 2010),	Severe
c.1709A>G	N570S		63		(G J Braathen, 2012; Geir J Braathen et al., 2010)	
c.368C>T	P123L	GTPase	2, 30	Dominant	(Verhoeven et al., 2006), (Sole et al., 2009)	
751C>G	P251A	GTPase	1, 8		(Züchner et al., 2004)	
c.752C>T	P251L		22		(Sivera et al., 2013)	Moderate
c.752C>G	P251R		2, 1		(Feely et al., 2011), (McCorquodale et al., 2011)	Severe, Moderate/ Severe
c.1397C>T	P456L		47		(Chung et al., 2008)	Moderate
	Q276H		<30	Dominant	(Casasnovas et al., 2010)	Mild
c.827A>G	Q276R		10	Dominant	(Verhoeven et al., 2006),(Züchner et al., 2006), (Calvo et al., 2009)	Mild + optic atrophy, Moderate

c.[1157A>C;1158G>T]	Q386P		1.5	De novo	(Verhoeven et al., 2006)	
	Q65STOP				(Sitarz et al., 2012)	
c.2230G>A	Q744K				(Antoniadi et al., 2015)	
	Q751Stop				(Sitarz et al., 2012)	
c.2251C>T	Q751X		4, 5	De novo, Dominant	(Verhoeven et al., 2006)	
	R104L	GTPase			(Sitarz et al., 2012), (Ando et al., 2017)	
c.310C>T	R104W	GTPase	4, 20, <5, <10, 2-4, 3, 2, 6	De novo, autosomal Dominant	(Choi et al., 2015), (Del Bo et al., 2008), (Calvo et al., 2009), (Brockmann et al., 2008), (Abe et al., 2011), (Ando et al., 2017), (Nakhro et al., 2012), (Chung et al., 2010), (Vallat et al., 2008), (Sitarz et al., 2012), (Genari et al., 2011)	Moderate, Severe
c.749G>A	R250Q	GTPase	21, 12	Unknown	(Verhoeven et al., 2006), (Sitarz et al., 2012), (McCorquodale et al., 2011)	Moderate/ Severe
c.748C>T	R250W	GTPase	4	Unknown	(Verhoeven et al., 2006)	
	R259C	GTPase	1, 11		(Sitarz et al., 2012), (Ando et al., 2017)	
c.776G>A	R259H	GTPase	17, 15		(Wu et al., 2018) (Ando et al., 2017), (Choi et al., 2015)	Mild, Moderate. Also seen with extreme sensory symptoms.
c.820C>T	R274W		59	De novo	(Ando et al., 2017), (Kotruchow, Kabzińska, & Kochański, 2015)	Severe
c.839G>A	R280H	GTPase	11-35, 45, 24, 21, 5, 6, 7, 55, 11-34, 7, 45, 10,	Dominant	(Ando et al., 2017), (Choi et al., 2015), (Nakhro et al., 2012), (Züchner et al., 2004), (Chung et al., 2006)	Mild, Moderate/ Severe, Moderate

			late, 12-32, 7, 45, 8			
c.1029_1032delGAG	R344del				(Antoniadi et al., 2015)	
c1091G>C	R364P	HR1	<5, 2	Dominant	(Sitarz et al., 2012), (Calvo et al., 2009), (Feely et al., 2011)	Severe
c01091G>A	R364Q	HR1	>10, <30, Late and early	Dominant	(Sitarz et al., 2012), (Calvo et al., 2009), (Casasnovas et al., 2010), (Banchs, Casasnovas, Montero, Martínez-Matos, & Volpini, 2008)	Moderate, Mild, Severe
C.1090C>T	R364W	HR1	1, 2, 3, 4, 5, 8, 6, Early	Dominant	(Sitarz et al., 2012), (Chung et al., 2006), (Ando et al., 2017), (Feely et al., 2011), (Züchner et al., 2006)	Severe, Moderate, Mild/ Moderate
c.1190G>C;	R397P	HR1	3-4 males, 7- 8 females	Dominant	(You et al., 2018)	Severe
c.1198C>T	R400X		4	Unknown	(Verhoeven et al., 2006)	
c.1253G>A	R418Q	HR1	37		(Choi et al., 2015)	Mild
C.1252C>T	R418X	Truncation - lacking transmem brane	1, 2		(Züchner et al., 2006), (Chung et al., 2010), (Ando et al., 2017)	Severe
c.1403G>A	R468H	Between TM and coiled coil	26, Childhood, <30, <50	Dominant	(Engelfried et al., 2006), (McCorquodale et al., 2011), (Sitarz et al., 2012), (Casasnovas et al., 2010), (G J Braathen, 2012), (Geir J Braathen, Sand, Lobato, Høyer, & Russell, 2010), (Antoniadi et al., 2015)	Moderate/ Severe, Mild, Moderate
	R519P				(Sitarz et al., 2012)	
c.1894C>T	R632W	Transmem brane	41, 42	Recessive	(Hikiami et al. 2018)	

c.2120delGGGAGAA ACC	R707_N709del		12		(McCorquodale et al., 2011)	Moderate
	R707P	HR2			(Sitarz et al., 2012)	
c.2119C>T	R707W	HR2	44		(Sitarz et al., 2012), (Geir J Braathen et al., 2010), (Antoniadi et al., 2015)	
c.2119C>T	R707W	HR2	3	Recessive	(Nicholson et al 2008)	Severe
	R94G	GTPase	3		(Ando et al., 2017)	
c. 281 G<C	R94P	GTPase	16		(Bergamin et al., 2014)	Severe
281G>A	R94Q	GTPase	1, 4-15, 6-17, 3-15, 4, <10, 7, 5, 3, 2, Early	Dominant, De novo	(Feely et al., 2011), (Ando et al., 2017), (Züchner et al., 2004), (Sitarz et al., 2012), (G J Braathen, 2012), (Casasnovas et al., 2010), (Verhoeven et al., 2006), (Kijima et al., 2005), (Sole et al., 2009), (Geir J Braathen et al., 2010), (Kotruchow et al., 2015), (Neusch et al., 2007)	Moderate/ Severe, Severe
c.280C>T	R94W	GTPase	2, 3, Early, 9, 4, 8, 1, 5, 3- 5, 1-4, <10	De novo, Dominant	(Verhoeven et al., 2006), (Chung et al., 2006), (Choi et al., 2015), (Ando et al., 2017), (Antoniadi et al., 2015), (G J Braathen, 2012), (Feely et al., 2011), (Calvo et al., 2009), (Sitarz et al., 2012), (Casasnovas et al., 2010), (G J Braathen, 2012), (Chung et al., 2010), (Cho, Sung, Kim, & Ki, 2007)	
c.1367C>T	RP456L		12		(Choi et al., 2015)	Mild
c.467G>T	S125I	GTPase	<10		(Calvo et al., 2009)	Moderate
c.476C>T	S249F		<20, 2		(Abe et al., 2011)	Severe
c.787T>C	S263P	GTPase	12, Late, 13	Dominant	(Chung et al., 2006), (Cho et al., 2007), (Ando et al., 2017), (Choi et al., 2015)	Mild, Moderate
c.1048T>C	S350P	GTPase	3		(Choi et al., 2015), (Nakhro et al., 2012), (Chung et al., 2010), (Cho et al., 2007)	Moderate/ Severe, Severe, Mild/ Moderate, Moderate
c.1132T>C	S378P		Early, 44		(Brockmann et al., 2008), (Ando et al., 2017)	Mild

c.152C>T	S51F		56		(Bergamin et al., 2014)	Mild
	T105A	GTPase			(Sitarz et al., 2012)	
c.314C>T	T105M	GTPase	Early, 11, 25, 4, 1	Dominant	(Chung et al., 2006), (Choi et al., 2015), (Ando et al., 2017), (Lawson, Graham, & Flanigan, 2005), (Feely et al., 2011)	Mild
c.371C>T	T124M		50		(Bergamin et al., 2014)	Moderate
c.617C>T	T206I	GTPase	3, 4, 2	De novo	(Verhoeven et al., 2006), (Züchner et al., 2006), (Choi et al., 2015), (Sitarz et al., 2012),	Severe
c.694A>G	T232A		6, 12	Dominant	(Sole et al., 2009)	
	T232N	GTPase			(Sitarz et al., 2012)	
c.707C>T	T236M	GTPase	<10	Dominant	(Calvo et al., 2009), (Kijima et al., 2005)	Moderate, Moderate/ Severe
c.1085>T	T362M		22, 42, Early, 0	Dominant	(Choi et al., 2015), (Chung et al., 2006), (Ando et al., 2017)	Mild, Severe
c.1085C>G	T362R		30		(Ando et al., 2017), (Antoniadi et al., 2015)	
c.2116A>C	T706P		7, 10		(Bergamin et al., 2014), (Ando et al., 2017), (Mathis et al., 2014)	Mild, Severe
c.730G>A	V244M	GTPase	<5, 10		(Calvo et al., 2009), (Kijima et al., 2005)	Moderate, Moderate/ Severe
c.818T>G	V273G	GTPase	1, 5		(Lawson et al., 2005)	Significant variability
c.1525G>C	V509L		37		(Choi et al., 2015)	Mild
c.1717G>A	V573I				(Kotruchow et al., 2015)	
c.205G>T	V69F		1, 5		(Züchner et al., 2004)	
c.2113G>A	V705I	HR2	10, 47, 6, 5		(G J Braathen, 2012; Geir J Braathen et al., 2010), (Kotruchow et al., 2015), (Engelfried et al., 2006), (McCorquodale et al., 2011), (Sitarz et al., 2012)	Severe, Moderate - Benign?

c.2220G>C	W740C		<10, 13	Dominant	(Calvo et al., 2009), (Ando et al., 2017)	Mild, Moderate
c.2219G > C	W740S	HR2	5-52, 5-33	Dominant	(Züchner et al., 2004), (Feely et al., 2011), (Verhoeven et al., 2006)	Mild/ Moderate
	Y752Stop				(Sitarz et al., 2012)	
	Y752X		14		(Feely et al., 2011)	Severe
c.1287+50G>T					(Kotruchow et al., 2015)	
c.1392+2T>C			50		(Bergamin et al., 2014)	Severe
IVS5-1G>C		Affects splice site	Early, 7		(Brockmann et al., 2008), (Chung et al., 2010)	Moderate/ Severe
c.617C>T			7		(Oh et al. 2014)	Severe - optic atrophy